Advanced Imaging of Congenital Chiasmal Malformations

Thesis

for the degree of

doctor rerum naturalium (Dr. rer. nat.)

approved by the Faculty of Natural Sciences

of Otto von Guericke University Magdeburg

by M.Sc. Robert Jerzy Puzniak

born on 2. September 1989 in Stockholm, Sweden

Examiner: apl. Prof. Dr. Michael Hoffmann

Prof. Dr. Peter König

submitted on: 28. January 2021

defended on: 1. December 2022

Zusammenfassung

Achiasmie und Albinismus sind die beiden wichtigsten Fälle von angeborenen Störungen, bei denen eine Fehlentwicklung des Chiasma opticums zu einem erheblich gestörten Signalfluss im visuellen System führt. Neben dem klinischen Interesse an ihrer Diagnostik sind chiasmale Störungen auch für die wissenschaftliche Forschung von Bedeutung, denn sie ermöglichen die durch den veränderten Signalfluss hervorgerufenen neuronalen Kompensationsmechanismen zu untersuchen, um letztendlich das Ausmaß plastischer Prozesse im visuellen Gehirn des Menschen zu verstehen. Sowohl klinische als auch wissenschaftliche Studien zu chiasmalen Störungen erfordern eine universelle Methode zur Bewertung der Integrität des Chiasmas, idealerweise aufgrund anatomischer Informationen, welche noch nicht etabliert ist. Das Ziel der hier vorgestellten Dissertation war es, dieses Defizit zu beheben, indem (i) Methoden der diffusionsgewichteten Magnetresonanztomographie (dMRT) in (ii) einen Auswerteprozess integriert wurden, der die Quantifizierung der Konnektivitätsänderungen am Chiasma bei Albinismus ermöglicht, und in einem separaten (iii) Fall von Chiasma-Hypoplasie anzuwenden. Die weiteren Arbeiten umfassten (iv) Konzeptnachweise zur Deep-Learning-basierten (DL-basierten) Erkennung von Chiasma-Anomalien aus anatomischen Bildern und (v) die Veröffentlichung von MRT-Daten von Patienten mit angeborenen chiasmalen Störungen. Explizit umfasst die Arbeit folgende Studien:

(i) **Empfehlungen für die Traktographie des visuellen Systems**
Die Rekonstruktion neuronaler Verbindungen im Gehirn durch Traktographie, wie bei dMRT, ist ein leistungsstarkes aber komplexes Werkzeug. Um seine Verwendung in klinischen und experimentellen Studien zu fördern und zu erleichtern, wurde einen Review (Puzniak et al., 2021b) mit Empfehlungen zur Etablierung einer dMRT-basierten Analyse, Akquisition, Vorverarbeitung und Modellierung von dMRT sowie eine Diskussion über Algorithmen zur Rekonstruktion neuronaler Verbindungen verfasst. Es wird erwartet, dass dieser Review die Einbeziehung der dMRT in bestehende und zukünftige Projekte fördert und ermöglicht.

(ii) **dMRT-basierte Quantifizierung abnormaler neuronaler Projektionen am Chiasma opticum**
In Anbetracht der Tatsache, dass eine Fehlentwicklung des Chiasmas dessen Konnektivität verändert, wurde untersucht, ob solche bei Albinismus beobachteten Veränderungen mit dMRT-basierter Traktographie erkannt und quantifiziert werden können (Puzniak et al., 2019). Die Analyse wurde mit anatomischen MRT- (aMRT) und dMRT-Daten von gesunden Kontrollprobanden (n=8) und Menschen mit Albinismus (PWA[1]; n=9) durchgeführt. Diese wurden vorverarbeitet und mit Diffusionstensor- (DT) und Constrained

[1] People with Albinism

Spherical Deconvolution- (CSD) Ansätzen modelliert und für die Traktographie verwendet. Die erhaltenen Schätzungen des prozentualen Anteils der kreuzenden Fasern im Chiasma zeigten signifikante Unterschiede zwischen PWA und Kontrollen sowohl für DT- (p=0.014) als auch für CSD-Modelle (p=0.0009). Die Bewertung der Unterscheidungskraft mittels ROC AUC[2] zeigte eine bessere Leistung des CSD-Modells (0.75 gegenüber 0.61 für DT), was durch die Korrelation zwischen CSD- und fMRT-basierten Schätzungen der Kreuzung (R2=0.83, p=0.012) zusätzlich unterstützt wurde. Diese Ergebnisse zeigen, dass insbesondere die CSD-basierte Traktographie einen effizienten Ansatz zur Erkennung von chiasmalen Anomalien darstellt und somit einen neuartigen anatomie-basierten Ansatz für die Diagnostik von chiasmalen Anomalien darstellt.

(iii) **Weitere Anwendungen des entwickelten dMRT-basierten Frameworks**
Der obige dMRT-Auswerteprozess wurde in einer separaten Fallstudie zur Chiasma Hypoplasie angewandt, um die Symmetrie der Projektionen aus den nasalen Netzhäuten zu bewerten (Ahmadi et al., 2020). Die durchgeführte Analyse bestätigte die Verringerung der Kreuzungsstärke und zeigte die asymmetrischen Projektionen beider nasaler Hemiretinae (73% vom rechten Auge und 27% vom linken Auge), die von denen bei Kontrollen abwichen (39-68% bzw. 32-61%), während die Projektionen der temporalen Hemiretinae in die normal beobachteten Werte fielen. Diese Ergebnisse bestätigten die Robustheit des obigen Auswerteprozesses und zeigten die komplementäre Nutzung von funktioneller und Diffusions-MRT.

(iv) **DL-basierter Nachweis von chiasmalen Fehlbildungen**
Trotz ihrer Wirksamkeit ist der Nutzen der dMRT-basierten Diagnostik durch die Kosten der zeitaufwändigen Datenerfassung stark eingeschränkt. Dies motivierte zur Erforschung alternativer, kosteneffizienter Methoden, die die Erkennung von Fehlbildungen aus klinischen T1-gewichteten (T1w) Standarddaten ermöglichen. Zu diesem Zweck wurde getestet, ob ein neuronales Faltungsnetzwerk (CNN[3]), das für die Segmentierung normaler Sehnerven aus T1w-Bildern trainiert wurde, ebenso genau die für menschlichen Albinismus typischen Fehlbildungen des Sehnervs segmentiert (Puzniak et al., 2021c). Die Netzwerkleistung wurde anhand des Dice Similarity Coefficient (DSC) bestimmt, der die Ähnlichkeit zwischen den CNN-Vorhersagen und den manuell definierten Sehnervenmasken angibt. Die Ergebnisse zeigten, dass das trainierte CNN zwar eine stabile Leistung für Kontrollen aus zwei unabhängigen Datensätzen - HCP und CHIASM[4], hatte (Mittelwert ± SEM des DSC gleich 79±2% bzw. 75±3%, FWE-korrigierter p-Wert von 1.0), seine Leistung für Daten von PWA aus dem CHIASM-Datensatz jedoch deutlich geringer war [44±8%; Vergleiche mit HCP- und CHIASM -Kontrollen führten zu p-Werten (FWE-korrigiert) von 0.004 bzw. 0.04]. Die Diskrepanz, die zu einer ROC AUC von 0.89 (CHIASM-Kontrollen vs. PWA aus CHIASM) und 0.84 (HCP-Kontrollen vs. PWA aus CHIASM) führt, liefert einen proof-of-concept für eine DL-basierte Diagnostik chiasmaler Fehlbildungen, die in klinischem Umfeld breit angewendet werden kann.

[2] Receiver Operator Characteristics Area Under Curve
[3] Convolutional Neural Networks
[4] (Puzniak et al., 2021a), Artikel (v)

(v) **Veröffentlichung von MRT-Daten zu angeborenen chiasmalen Störungen**
Eine der größten Herausforderungen bei der Erforschung von Chiasmenfehlbildungen ist die Knappheit der Daten. Um dieses Hindernis zu beseitigen, wurde der Datensatz von T1- und diffusionsgewichteten Bildern einer Kontrollgruppe (n=8) sowie PWA (n=9), Chiasmenhypoplasie (n=1) und Achiasma (n=1) (Puzniak et al., 2021a) veröffentlicht. Der Datensatz enthielt zusätzlich fMRT-Daten einer Untergruppe von 4 Kontrollen und 6 PWA, zu kortikalen Antworten auf die monokulare visuelle Reizung beider Augen, sowie manuell bearbeitete Masken zur Unterstützung der Traktographie des Chiasma opticums und Skripte zur Vorverarbeitung und Qualitätsbewertung. Es wird erwartet, dass die auf der Cloud-Computing-Plattform brainlife.io veröffentlichten Daten die Erkennung von angeborenen Chiasma-Störungen verbessern und eine Vielzahl von Studien erleichtern werden, die von diesen einzigartigen Daten profitieren können.

Abstract

Achiasma and albinism are the two primary cases of congenital chiasm disorders, where ill-development of the optic chiasm results in a substantially disrupted signal flow in the visual system. Apart from the clinical interest in their diagnostics, the chiasmal disorders are also of importance for scientific research that aims to study compensatory mechanisms evoked by altered signal flow to ultimately understand the scope of plasticity in the human visual brain. Both clinical and scientific studies on chiasmal disorders require a universal method of assessment of chiasm integrity, ideally based on anatomy, which is not fully established yet. The objective of work presented in this thesis was to address this need through the incorporation of (i) diffusion Magnetic Resonance Imaging (dMRI) methods into (ii) a framework capable of quantifying connectivity changes at chiasm in albinism, which was applied in a separate (iii) case of chiasm hypoplasia. The further works covered (iv) demonstration of proof-of-concept for Deep Learning-based (DL-based) detection of chiasmal abnormalities from anatomical images and (v) the publication of MRI data of patients with congenital chiasmal disorders. Specifically, the thesis covers following studies:

(i) **Recommendations for tractography of the visual system**
Reconstruction of neural connections within the brain through tractography, as provided by dMRI, is a powerful, yet complex tool. To promote and facilitate its use in clinical and research studies, a review with recommendations for establishing dMRI-based analysis was published (Puzniak et al., 2021b), which discussed acquisition, preprocessing and modelling of dMRI, as well as algorithms used for reconstruction of neural connections. As such, the review is expected to promote and enable incorporation of dMRI in existing and upcoming projects.

(ii) **dMRI-based quantification of abnormal chiasmal crossing**
Considering that maldevelopment of the chiasm alters its connectivity, it was investigated whether such changes observed in albinism can be detected and quantified with dMRI-based tractography (Puzniak et al., 2019). The analysis was performed on anatomical MRI (aMRI) and dMRI data of controls (n=8) and people with albinism (PWA; n=9), which was preprocessed, modelled with Diffusion Tensor (DT) and Constrained Spherical Deconvolution (CSD) approaches and used for tractography. The obtained estimates of percentage of crossing fibers in the chiasm revealed significant differences between PWA and controls for both DT (p=0.014) and CSD (p=0.0009) models. The assessment of discriminative power with ROC AUC[5] revealed better performance of the CSD model (0.75 as opposed to 0.61 for DT), which was further reinforced by correlation between CSD- and functional MRI-based estimates of crossing

[5]Receiver Operator Characteristics Area Under Curve

(R^2=0.83, p=0.012). These results demonstrate that especially CSD-based tractography provides an efficient approach to detection of chiasmal abnormalities, thus providing a novel anatomy-driven approach for diagnostics of chiasmal abnormalities.

(iii) **Further applications of developed dMRI-based framework**
The developed dMRI-based framework was applied in a separate case study on chiasm hypoplasia to assess the symmetry of projections from the nasal retinas (Ahmadi et al., 2020). The conducted analysis confirmed the reduction of crossing strength, as well as revealed the asymmetrical projections from the nasal retinas (73% from the right eye and 27% from the left) which fell beyond ranges observed in controls (39–68% and 32–61%, respectively), while the projections from temporal retinas fall into normally observed values. These results validated the robustness of previously developed framework, as well as demonstrated complementary use of functional and diffusion MRI.

(iv) **DL-based detection of chiasmal malformations**
Despite its effectiveness, the utility of dMRI-based diagnostics is severely limited by costs of time-consuming data collection. This motivated the exploration of alternative, cost-efficient methods that enables detection of malformations from clinically standard T1-weighted (T1w) data. For this aim it was tested whether convolutional neural network (CNN) trained to segment normal optic chiasm from T1w images will equally accurately segment the malformed optic chiasm as typical for human albinism (Puzniak et al., 2021c). The performance of the network was measured by the Dice Similarity Coefficient (DSC), which denoted the similarity between CNN predictions and manually defined optic chiasm masks. The results revealed that while trained CNN showed stable performance for controls from two independent datasets – HCP and CHIASM[6] (mean $\pm$ SEM of DSC equal to 79$\pm$2% and 75$\pm$3%, respectively, FWE-corrected p-value of 1.0), its performance for data of PWA from CHIASM dataset was significantly lower (44$\pm$8%, with comparisons against HCP and CHIASM controls yielding FWE-corrected p-values of 0.004 and 0.04, respectively). The observed discrepancy, translating into ROC AUC of 0.89 (controls from CHIASM vs PWA from CHIASM) and 0.84 (controls from HCP vs PWA from CHIASM) provides proof-of-concept for DL-based diagnostics of chiasmal malformations that can be widely applied in clinical settings.

(v) **Publication of MRI data on congenital chiasmal disorders**
One of the major challenges of research on chiasmal malformations is the scarcity of the data. To address this obstacle, the dataset of T1- and diffusion-weighted images from a control group (n=8), PWA (n=9), chiasm hypoplasia (n=1) and achiasma (n=1) was published (Puzniak et al., 2021a). The dataset furtherly included fMRI data from a subset of 4 controls and 6 PWA which contained recordings of the cortical response to the monocular stimulation of both eyes, as well as manually edited masks supporting the tractography of the optic chiasm and scripts for preprocessing and quality assessment. The data, published on the cloud computing platform brainlife.io, is expected to increase recognition of the congenital chiasmal disorders and to facilitate wide range of studies that may benefit from this unique data.

[6](Puzniak et al., 2021a), paragraph (v)

Contents

List of Figures

Chapter 1

Introduction

"*A disease is never a mere loss or excess. There is always a reaction on the part of the organism or individual to restore, replace or compensate for and to preserve its identity, however strange the means may be.*"

(Sacks, 1987)

As much as can be learned about the human brain and its functioning from the control population, it is the disease that often grants unique insights into well described systems. Investigations on neurological disorders not only allow for understanding their causes and effects, but may also reveal new and key information about mechanisms underlying brain functioning (Poldrack et al., 2012).

This applies as well to congenital disorders of visual system, as in achiasma (Apkarian et al., 1994; Apkarian et al., 1995) and albinism (Kolb et al., 1995). Although the patho-physiology and mechanisms behind the afore-mentioned disorders differ, they both result in ill-development of the visual system and misrouting of nerves forming the optic chiasm. Notably, although such alterations disrupt the normal flow of signal in the visual system, the functional integrity of vision is mainly preserved (Wolynski et al., 2010; Klemen et al., 2012; Hoffmann and Dumoulin, 2015). This surprising finding extends the importance of albinism and achiasma beyond their clinical profile, as they may serve as scientific models for understanding the coupling between structure and function of visual system, or for neuroplasticity mechanisms preserving the integrity of the visual system (Ahmadi et al., 2019b). These potential applications of albinism and achiasma, together with detailed descriptions of both diseases and their impact on the visual system, are provided in the Chapter 2 (Background).

Naturally, the diagnostics and investigations on chiasmal malformations require robust methods for the assessment of the chiasm's properties. Currently, this is being standardly achieved with functional measurements, such as Visual Evoked Potentials [VEPs; (Hoffmann et al., 2015)] or functional Magnetic Resonance Imaging [fMRI; (Hagen et al., 2008)]. The performance of these techniques is however dependent on quality of visual functions and compliance of the participants, which limits their applicability in cases of significant visual deficits, as observed in albinism or achiasma (Sami et al., 2005). This motivates a need for development of alternative imaging methods, such as anatomical measurements of chiasm with Computer Tomography (CT) or Magnetic Resonance Imaging (MRI), which would allow for a direct and independent assessment of the optic chiasm. Interestingly, such methods have not yet been definitely established. There are several reasons for this, (1) The small and complex shape of the optic chiasm is poorly visible on CT images,

which has been reported as early as 1984 (Daniels et al., 1984), and continues to affect present studies (Ibragimov and Xing, 2017; Duanmu et al., 2020). This issue is also present with MRI images of chiasm, which despite their sufficiently high resolution and contrast cannot effectively process with conventional methods, such as atlas-based segmentation of MRI images (Isambert et al., 2008). These general problems can be further enhanced in case of particular MRI acquisition sequences, such as Echo-Planar Imaging [EPI; (Stehling et al., 1991)], where chiasm's image is affected by geometry-induced distortions (Andersson and Skare, 2012). (2) Errors in the quantitative measures derived from diffusion MRI [(Basser et al., 1994)] caused by the presence of crossing populations of fibers (Jones et al., 2013). (3) Development of methods for imaging malformed chiasms is limited by data scarcity, an effect resulting from the low prevalence of both albinism [approximately 1:20000 according to (Marçon and Maia, 2019)] and achiasma (fewer than 50 reported cases).

The purpose of the work presented in this thesis was to aid researchers and clinicians in overcoming the challenges discussed above, and thus facilitate future studies on chiasmal malformations. Specifically, I addressed the research questions, presented in detail in Chapter 3 (Research Questions), which pertained to:

(1) limited literature on analysis of connectivity of the visual system and optic chiasm,

(2) absence of validated framework for assessment of chiasmal misrouting,

(3) lack of anatomy-based methods for detection of malformations of chiasm,

(4) scarcity of imaging data on chiasmal disorders.

The aims of the thesis have been pursued using two non-invasive imaging techniques i.e. anatomical MRI (aMRI) and diffusion MRI (dMRI), suited to the task of imaging of the optic chiasm. These imaging modalities have been combined with two distinct computational approaches. The first used neuroimaging algorithms and models designed specifically for analysis of aMRI and dMRI data. The second one involved the application of generalizable data-driven Neural Networks (NN) models to aMRI data. The detailed description of employed methods is provided in Chapter 4 (Methods).

The resulting works gathered in this thesis consist of a:

- Review article on dMRI-based tractography of the visual system (Puzniak et al., 2021b)(Chapter 5), addressing (1),
- Scientific article demonstrating a dMRI framework capable of robust quantification of nerve decussation in chiasm (Puzniak et al., 2019)(Chapter 6), which was successfully applied in further studies (Ahmadi et al., 2020)(Chapter 7), addressing (2),
- Scientific article providing a proof-of-concept for novel detection of chiasmal malformations from aMRI images (Puzniak et al., 2021c)(Chapter 8), addressing (3),
- Data descriptor of the first publicly available MRI dataset on chiasmal publications (Puzniak et al., 2021a) (Chapter 9), addressing (4).

The impact and importance of the above listed scientific findings and contributions are summarized in Chapter 10 (General Discussion), which also includes the outlook and concluding remarks.

Chapter 2

Background

This chapter starts with an overview of visual system [subchapter 2.1 (Structural and functional organization of the primary visual pathway)] in order to provide a wider context into understanding the nature and impact of chiasmal malformations. Subsequently, a comprehensive description of albinism and achiasma with their causes, phenotypes and their impact on the integrity of the human visual system are discussed [subchapter 2.2 (Congenital chiasmal disorders)]. Finally, I discuss the relevance of the studying chiasmal malformations for clinical and research purposes.

2.1 Structural and functional organization of the primary visual pathway

While the human visual system consists of multiple visual pathways (Kelts, 2010; De Moraes, 2013), this thesis focuses on the one that is fundamental for vision, the geniculo-striate pathway. The basic purpose of this primary visual pathway is to capture and process visual information, which is then being transmitted through a system of inter-connected brain structures (**Figure 1)**. The structural organization of those structures is presented in detail in subsequent series of paragraphs depicting the flow of signal through visual system, specifically:

- subchapter 2.1.1 (Visual signal processing in the eye)
- subchapter 2.1.2 (Routing of signal in the optic chiasm)
- subchapter 2.1.3 (Organization of the lateral geniculate nucleus)
- subchapter 2.1.4 (Visual cortex organization)

2.1.1 Visual signal processing in the eye

The processing of a visual scene starts when the light, upon entering the eye, reaches 120 million rods and 20 million cones, the two types of photoreceptors located in the outermost part of the retina [the third type of photoreceptors, melanopsin, is not involved in conscious vision and is therefore not a part of the primary visual pathway (Güler et al., 2008)]. This initiates the phototransduction in the photoreceptors, where through a series of chemical reactions started by conformational changes in the photopigment, the input photons are translated into electrical signal (Wald, 1968). The outcome signal is subsequently transmitted to bipolar cells and the retinal ganglion cells (RGC) which are the first neurons of visual pathway located in the innermost retinal layers. There are several classes of RGC, with the parasol (magnocellular) and midget (parvocellular) cells being the most distinctive ones (Kim et al.,

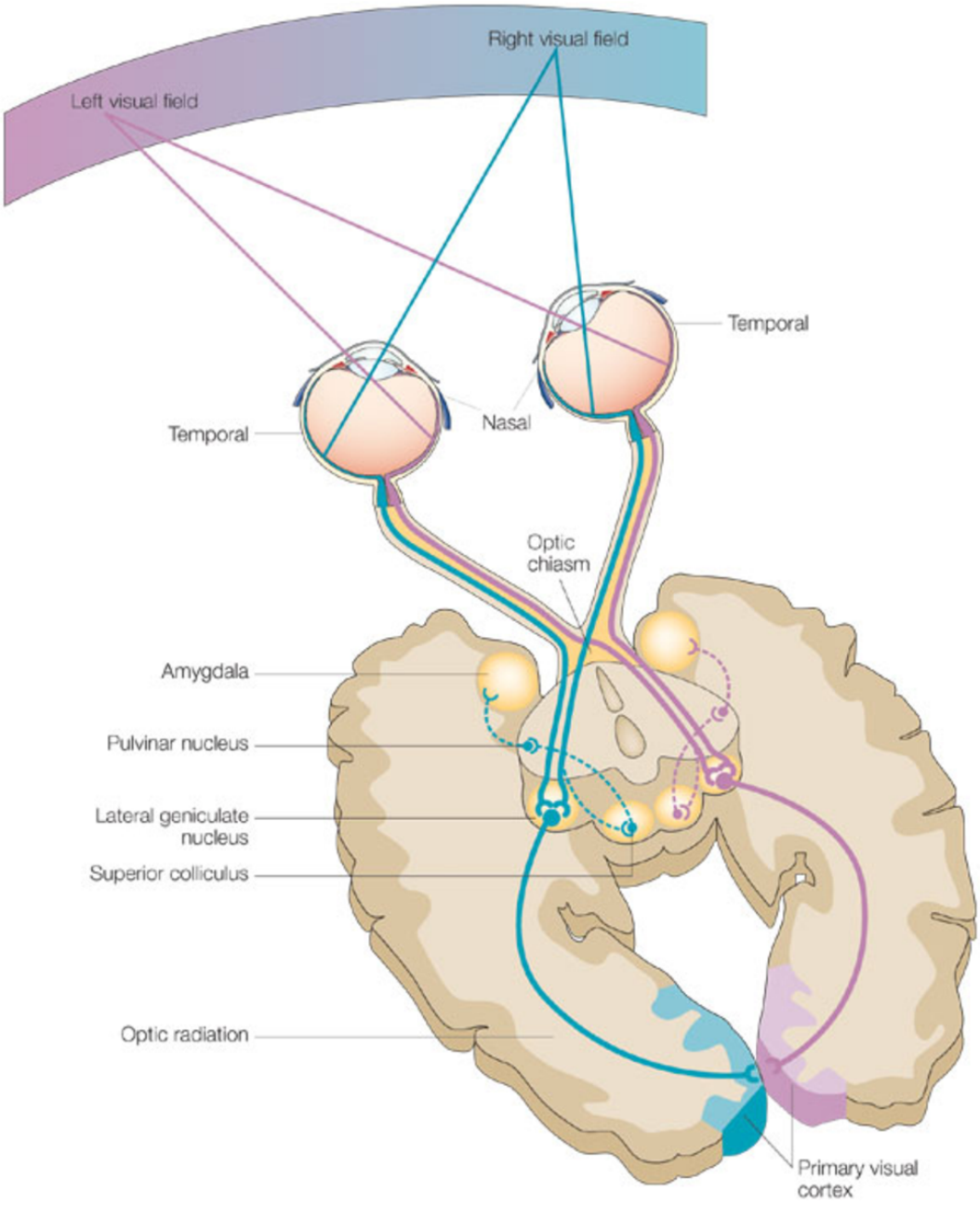

FIGURE 1: **Flow of visual signal through the structures of primary visual pathway.** The projection of visual scene is projected onto the retina, where it is translated into electrical signal. The signal propagates along optic nerve and enters the optic chiasm. Here, depending whether it originates from temporal or nasal retina, the signal either remains on the same brain hemisphere or crosses to contralateral, respectively. The signal travels further along the optic tract and reaches via synaptic connection to lateral geniculate nucleus. From the nucleus it propagates along optic radiation and reaches the primary visual cortex – the first of several visual areas involved in processing the visual signal.

2021). Due to their extensive branching the parasol cells have larger receptive fields, and captures high level information about stimuli, such as motion or depth of objects (Atkinson, 1992). The midget RGCs with smaller receptive field provide more detailed information about stimuli, such as color. The axons of 1.2 million RGCs reach the retinal nerve fiber layer and converge to form the optic nerve (Ogden, 1984), which leads the signal further along the visual pathway.

Importantly, the resulting representations of the visual field is characterized by two features, which are critical for its further processing and, effectively, for vision (a) cortical magnification and (b) retinotopic organization of the signal. Specifically:

(a) The term "cortical magnification" refers to the fact, that the number of neurons in the visual cortex representing a visual stimulus of given size is not constant, but is rather dependent on the location of stimulus in the visual field (Rovamo and Virsu, 1979). The largest cortical representation, and consequently highest visual acuity, is observed for the central visual field [e.g. the central 2° of visual field drive 50% of the visual cortex (Kandel et al., 1991)], whereas acuity at periphery is about 50 times lower (Frisén and Glansholm, 1975). This effect is a consequence of far greater density of cones and RGCs in the fovea than in the periphery (Hendrickson, 2005) and is further enhanced by the presence of foveal pit, which increases the amount of cortical surface per degree of the visual field (Rodieck, 1998). The qualitative depiction of cortical magnification is presented in the **Figure 2**.

(b) The term "retinotopic organization" refers to the fact, that the spatial continuity of visual field is preserved upon its projection onto the retina. Effectively, the adjacent RGCs encode adjacent portions of the visual field, whereas their spatial relationships encode the organization of visual field. This important information on the organization of signal is preserved at all stages of signal processing in the visual system, including lateral geniculate nucleus [LGN; (Schneider et al., 2004)] and visual cortex (Horton and Hoyt, 1991), as qualitatively depicted in the **Figure 2**. Effectively, the retinotopic organization guides the retinal mapping of the signal onto neurons, enabling retinotopic organization of visual cortex (Inouye, 1909), which plays a critical role in the integration of signal in the cortex.

2.1.2 Routing of signal in the optic chiasm

The optic chiasm is a relatively small structure [mean width reportedly in the range of 13-15 mm (Parravano et al., 1993; Wagner et al., 1997; Schmitz et al., 2003)] formed by the crossing and non-crossing RGC axons. Specifically, the optic nerve bundles split in the chiasm in two separate groups of axons corresponding to nasal and temporal retina (**Figure 3**). The axons of the nasal RGCs cross in the optic chiasm to the contralateral brain hemisphere, while the axons from temporal retina project to the visual cortex of the ipsilateral hemisphere. This anatomical pattern formed by the crossing and non-crossing axons [of ratio 53:47, respectively (Kupfer et al., 1967)] ensures that processing of each visual hemifield is limited to a single (contralateral) brain hemisphere only, where the visual representations from both eyes are being integrated (**Figure 2**). Lastly, the nerves exit the chiasm forming the optic tracts, eventually transmitting the signal to LGN.

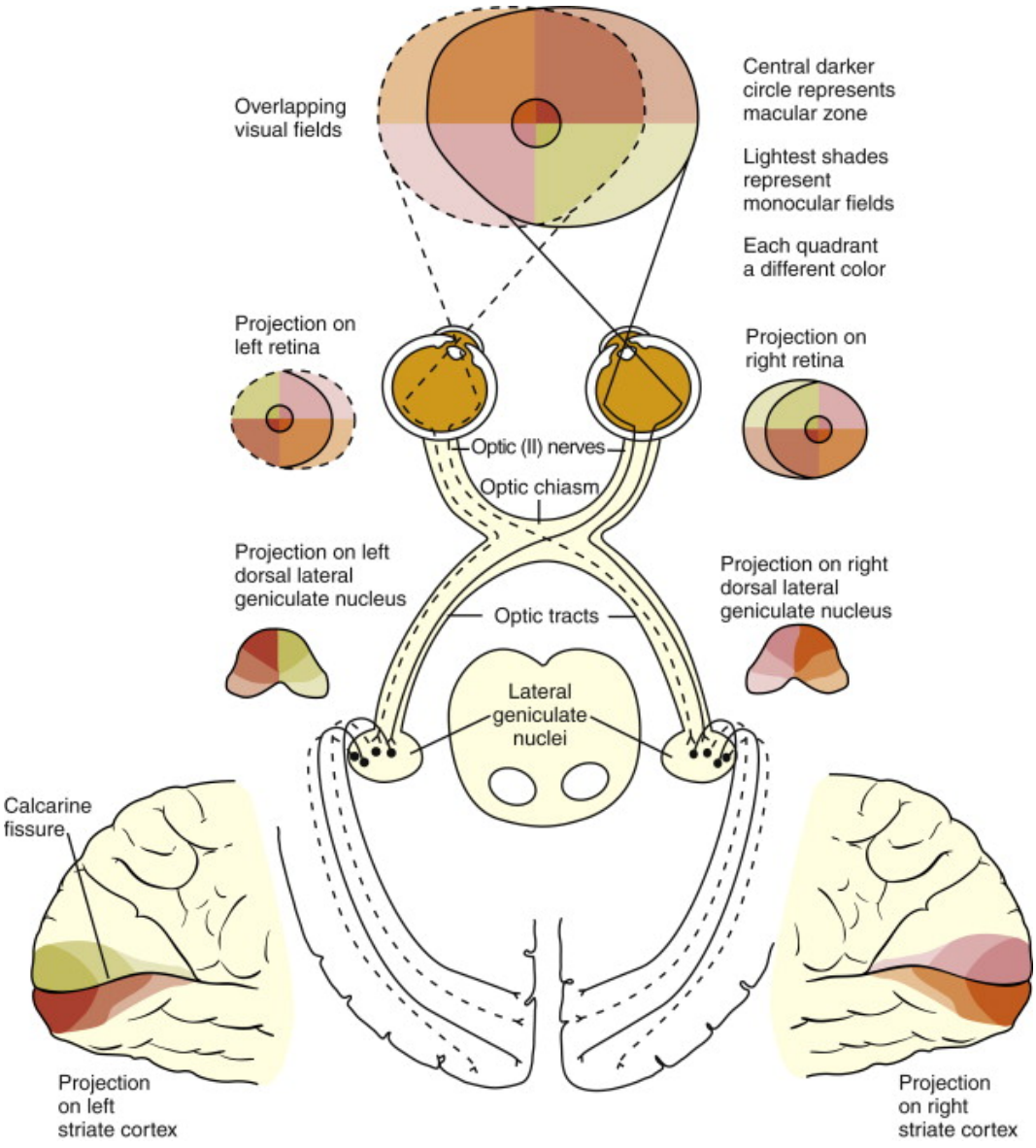

FIGURE 2: **Representations of visual signal throughout the visual system.**
The visual field is asymmetrically projected onto left and right retina. In the chiasm the RGC axons from temporal and nasal retina are being split between ipsi- and contralateral brain hemispheres, respectively. The post-chiasmal segments of RGC axons, optic tracts, end with synaptic connection to LGN. From the retinotopically organized LGN the signal is projected to the striate cortex. Here, the significantly large portion of cortex is driven by relatively small central portion of visual field, whereas large peripheral visual areas have comparatively small representations.

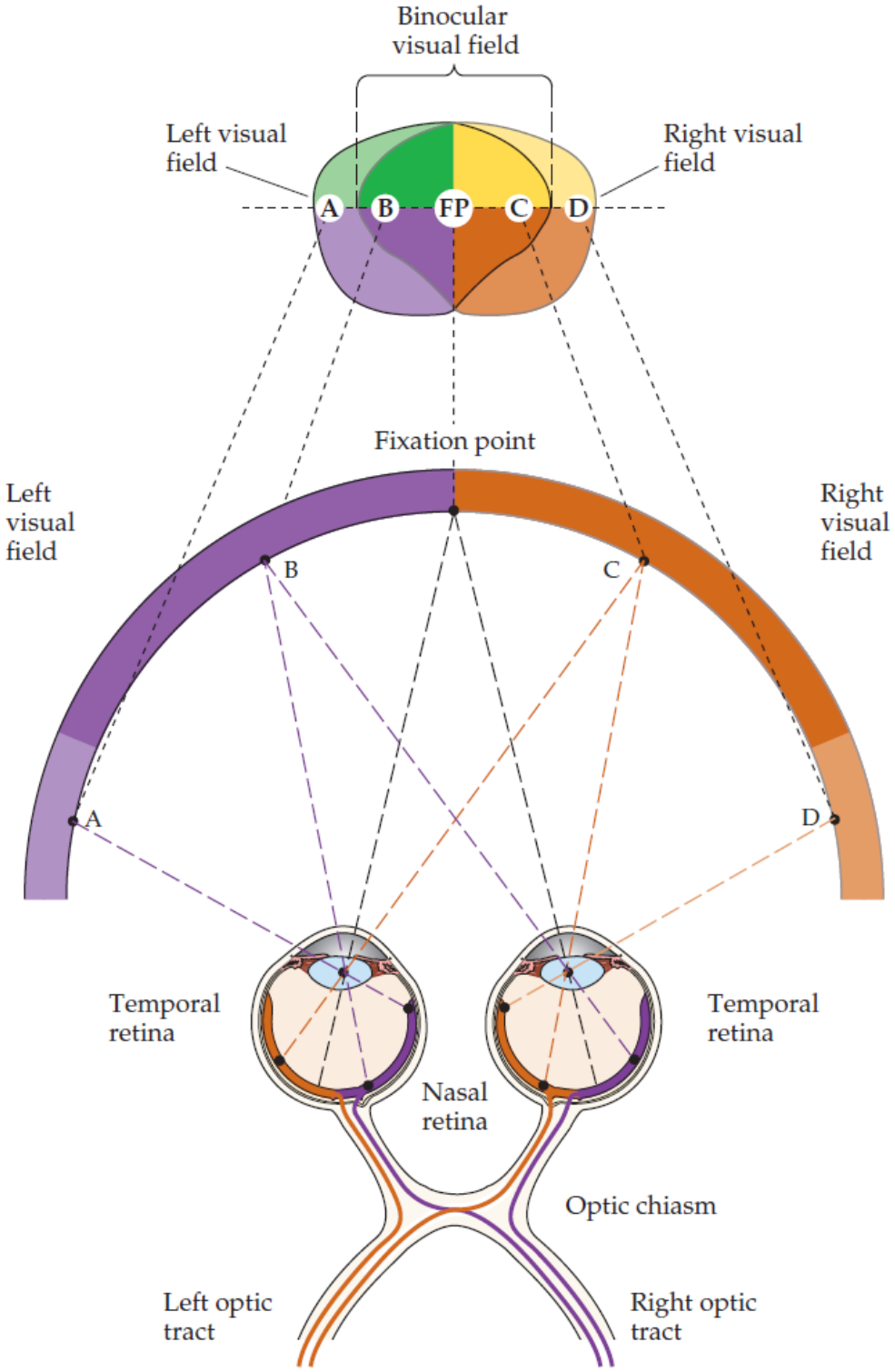

FIGURE 3: **Schematic of the optic nerve crossing in the optic chiasm.**
The left visual field (point B) is projected onto nasal retina of the left eye and the temporal retina of the right eye. In the optic chiasm, the axons of nasal RGCs cross to the contralateral (right) brain hemisphere, while the ones from nasal retina remain on the same (right) brain hemisphere. Consequently, the representations of left visual field from both eyes are projected to the right brain hemisphere.

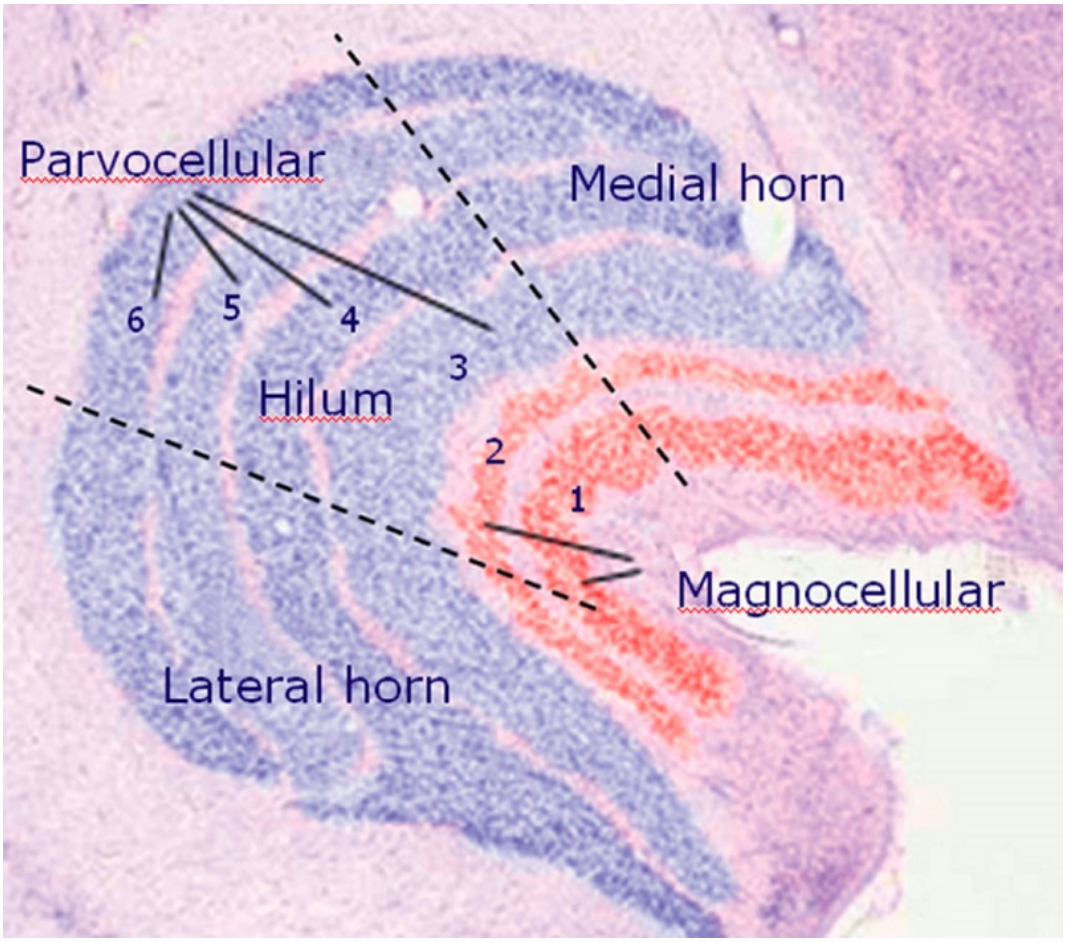

FIGURE 4: **Coronal section through the LGN of the rhesus monkey.**
The red staining indicates layers receiving signal from magnocellular RGCs (with layer 1 receiving signal from contra- and layer 2 from ipsilateral eye). The blue staining indicates parvocellular layers (with layers 4 and 6 receiving signal from contra- and layers 3 and 5 from ipsilateral eye). The dotted lines mark approximate border between hilum and horns. Reprinted by permission from Wolters Kluwer Health, Inc., Journal of Glaucoma; Anatomy of the Visual Pathways. De Moraes C.; Copyright © 2015.

2.1.3 Organization of the lateral geniculate nucleus

The optic tract ends with synaptic connections, which transmit the signal to the neurons of the primary visual pathway that are located in the lateral geniculate nucleus (LGN). Anatomically, LGN is divided into 6 layers, with layers 2, 3 and 5 receiving signal from temporal retina of the ipsilateral eye, while layers 1, 4 and 6 receive signal from nasal retina of the contralateral eye. Further, the layers can be divided into magnocellular layers (1, 2) and parvocellular layers (3-6), receiving signal from parasol and midgets RGCs, respectively (**Figure 4**). Notably, the spatial organization of LGN preserves the retinotopic organization. Here, the visual signal from the macula (central part of retina containing the fovea) is reaching the central area of LGN (hilum), while the signal from inferior and superior parts of retina reaches lateral and medial horns, respectively (Chacko, 1948). Upon reaching the LGN, the visual signal is projected via the optic radiation to the occipital lobe, where the visual cortex is located.

2.1.4 Visual cortex organization

The visual cortex is a component of the visual system, where the sensory signal is being integrated and processed. Functionally, the visual cortex comprises numerous visual field maps which capture distinct features of visual input, and are located in several distinct brain areas, such as occipital lobe, dorsal cortex, lateral occipital cortex or ventral cortex (Wandell et al., 2007).

The visual area that receives the signal from the LGN is the V1, also referred to as *"primary visual cortex"*, Brodmann area 17 or the striate cortex, which is located around the calcarine fissure of the occipital lobe. Specifically, the visual signal is projected to the layer 4 (out of 6 functional layers of the V1), with sub-layer 4Cα receiving mainly magnocellular input, while the sub-layer 4Cβ receives parvocellular input (Hubel and Wiesel, 1972). Importantly, V1 of each hemisphere receives two representations of contralateral visual field which demonstrate cortical magnification and are retinotopically organized (Inouye, 1909), as presented in **Figure 2**. The first of those two features allow for high visual acuity for the central portion of visual field, whereas the second is essential for organization and integration of visual signal.

From V1, the visual signal is processed down through two separate streams. The first one, the ventral stream (also known as *"What Pathway"*) is relevant for object representation, and comprises V2, V4 and inferior temporal cortex. The second, dorsal stream or the *"Where Pathway"* is responsible for motion and localization of objects and involves V2, dorsomedial area of V6, medial temporal area of V5 and the posterior parietal cortex (Mishkin et al., 1983).

2.2 Congenital chiasmal disorders

The presented structural, and consequently functional organization of the visual system can be changed in differential ways by disorders, diseases and trauma. Particularly remarkable classes of those are congenital chiasmal disorders, described in detail in subchapters 2.2.1 (Achiasma) and 2.2.2 (Albinism). Here, the abnormal development of the visual system results in a seemingly subtle, yet very impactful malformation of the optic chiasm, disrupting the flow of signal in the visual system (Hoffmann and Dumoulin, 2015). Remarkably, such significant changes do not harm the fundamental integrity of the visual system, apart from their clinical relevance, described in the subchapter 2.2.3 (Clinical challenges). As such, the congenital chiasmal disorders provide valuable opportunities for research, as detailed in the subchapter 2.2.4 (Research challenges).

2.2.1 Achiasma

Achiasma is a disorder of the visual system characterized by the absence or lack of crossing fibers in the optic chiasm (Hoffmann et al., 2012; Hoffmann and Dumoulin, 2015). While the name *"achiasma"* is a generic term for a broad spectrum of chiasmal abnormalities, some authors suggest to use more precise terms, such as *"chiasmal aplasia"* for complete absence of chiasm (Taylor, 2007) and *"chiasm hypoplasia"* for reduced crossing (Ahmadi et al., 2020). The mechanisms and phenotype of the achiasma, as well as its consequences for the visual system and diagnostics are described in next subchapters.

2.2.1.1 Mechanisms

Due to the extreme rarity of achiasma [fewer than 50 reported cases since it was first reported by (Apkarian et al., 1994; Apkarian et al., 1995)], the underlying causes and mechanisms are primarily unknown. Studies on animal models however suggest, that the disorder is underpinned by genetic factors (Williams et al., 1994; Seth et al., 2006).

2.2.1.2 Phenotype

Existing evidence indicates a correlation of achiasma with nystagmus, usually see-saw (Apkarian et al., 1995; Thompson et al., 1999), which is usually included along the VEP documentation of abnormal chiasmal connectivity and reduced size of chiasm on aMRI images in achiasma's diagnostic criteria (Sami et al., 2005; Hoffmann and Dumoulin, 2015). Furthermore, achiasma is reported together with general developmental delay and optic disc abnormalities (Sami et al., 2005), but is not in principle associated with significant abnormalities e.g. of the optic disc (Victor et al., 2000; Jansonius et al., 2001; Korff et al., 2003). Generally, achiasma can be classified into 3 types (Sami et al., 2005):

- Type A: reduced decussation accompanied by apparently normal optic nerves and visual fields. Possible see-saw (Apkarian and Bour, 2001) or purely horizontal (Jansonius et al., 2001) nystagmus, as well as abnormal head posture and strabismus. The only known anatomical abnormality is reduction of the chiasm's size (Sami et al., 2005).
- Type B: reduced decussation accompanied by chiasmal hypoplasia and midline symptoms of septo-optic dysplasia (Thompson et al., 1999).
- Type C: reduced decussation accompanied by chiasmal hypoplasia and clefts (abnormal fissures or openings, effects of abnormal embryonic development) and encephaloceles (sac-like protrusions of the brain and its membranes through openings in the skull) of the skull base (Hodgkins et al., 1998).

2.2.1.3 Consequences for the visual system's integrity

The main consequence of achiasma is mis-routing of the signal in the visual pathways (Davies-Thompson et al., 2013). Here, the signal from nasal retina, instead of crossing thorough the chiasm to other brain hemisphere, is partially or completely redirected to the same brain hemisphere. As such, the LGN receives signal from two opposite hemifields instead of one, which influences its representation. The abnormal mapping is propagated further down to the visual cortex. Here, instead of the usual pattern, where a single visual hemifield is represented on the contralateral brain hemisphere, each hemisphere receives an input from both the contra- and the ipsilateral visual field. Interestingly, these opposing hemifields are superimposed over each other, such that the same cortical region is driven by stimuli in two distinct visual field locations (Victor et al., 2000; Hoffmann et al., 2012; Purington et al., 2012; Davies-Thompson et al., 2013). Consistently, it has been shown that each cortical location has two populations of receptive fields – one for each hemifield that are mirrored across the vertical meridian (Hoffmann et al., 2012). Furthermore, current evidence indicates that the specific pattern of overlaid representations of opposing hemifields also propagates across the visual hierarchy, responsible for high level

processing of visual stimuli (Davies-Thompson et al., 2013; Kaule et al., 2014). Surprisingly, despite the high degree of abnormalities of the cortical representations and further limitations such as nystagmus, reduced acuity or lack of stereovision, achiasmatic patients are being reported to demonstrate strikingly normal behavioural vision (Thompson et al., 1999; Victor et al., 2000).

2.2.1.4 Diagnostics

Diagnosis of achiasma requires confirmation of an absence or a reduction of chiasmal crossing, which can be achieved by either electrophysiology or MRI imaging. The former relies on confirmation of positive contralateral asymmetry of the monocular VEP response to flash (Hoffmann et al., 2015), but is susceptible to noise and may suffer from limited reproducibility. Such limitations are absent in the alternative MRI imaging, used to detect reduced size of chiasm, which however may encounter problems caused by insufficient resolution and ambiguities in chiasmal sizes. Consequently, a certain diagnostic is achieved by combination of both VEPs and MRI imaging (Korff et al., 2003; Sami et al., 2005; Taylor, 2007).

2.2.2 Albinism

Albinism (from lat. *"albus" –"white"*) is a rare [estimated prevalence of 1:20 000 (Marçon and Maia, 2019)] condition characterized by visual system deficits in association with hypopigmentation (Montoliu et al., 2014). The heterogenous spectrum of albinism is classically divided into:

- Oculocutaneous albinism (OCA), the most commonly recognizable form due to the visible impact on hair and skin pigmentation, which is divided into 7 subtypes OCA1 – OCA7;
- Ocular albinism (OA) in the form of OA1 where the shortage of melanin alters the visual system only;
- Syndromic albinism, which covers i.e. Hermansky-Pudlak or Chediak-Higashi syndromes (Scheinfeld, 2003).

The discussion on albinism requires also mentioning the Fovea Hypoplasia, Optic Nerve Decussation defect Anterior segment syndrome [FHONDA; (Pal et al., 2004; Al-Araimi et al., 2013)], which shares several features with albinism (such as fovea hypoplasia or abnormal nerve decussation), but due to different underlying mechanisms is not considered to belong to albinism's spectrum (Poulter et al., 2013; Ahmadi et al., 2019a).

The mechanisms and phenotype of albinism, as well as its consequences for the visual system and diagnostics are described in next subchapters.

2.2.2.1 Mechanisms

The underlying cause of all forms of albinism are genetic mutations that impair melanocytes, rendering them unable to either synthetize melanin or distribute it properly (notably, the total number of melanocytes remains unchanged, unlike in piebaldism and vitiligo). Normally, melanocytes are derived from neural crest (Cramer, 1991) and migrate through the developing embryo to specific locations, such as skin, eyes, hair and inner ear. There, melanocytes, in their specialized organelles called melanosomes, synthetize melanin (Videira et al., 2013). However,

the melanogenesis can be impaired in cases of specific genetic mutations, thereby inducing a deficiency of melanin and effectively cause albinism. Until recently mutations in 19 genes (inherited in autosomal recessive inheritance pattern) have been reported to cause albinism – 6 out of 7 causing 7 forms of OCA (1 mutation still remains unidentified), 1 causing OA1, 10 genes causing Hermansky-Pudlak syndrome and 1 responsible for Chediak-Higashi syndrome (Lasseaux et al., 2018).

Importantly, the consequences of melanin deficits extend beyond increased susceptibility to UV radiation, as this pigment, or rather precursors, also guides the development of the visual system. This important feature explains the co-occurrence of two characteristic albinism's features, i.e. pigmentation and visual system deficits, since it is the hypopigmentation that drives visual system's abnormalities. Specifically, the visual system alterations involve:

- Foveal hypoplasia: The foveal pit is typically located in the avascular zone and shows increased density of cone photoreceptors (Hendrickson, 2005). This is however not the case in albinism, as the PWA often lack the avascular zone (Gregor, 1978; Abadi and Pascal, 1989) and the foveal pit [chiasm hypoplasia; (Kinnear et al., 1985; Oetting et al., 1994)]. This outcome is explained by the lack of developmental molecular barrier securing the future foveal avascular zone (Provis and Hendrickson, 2008).

- RGC genesis: Reduced number of RGCs in albinism, as demonstrated on albinotic animals (Guillery et al., 1984; Leventhal and Creel, 1985). This leads to thinner peripapillary nerve fiber layer (Mohammad et al., 2015) and smaller optic nerves and chiasm width (Schmitz et al., 2003; Hagen et al., 2005; Mcketton et al., 2014).

- Optic nerve misrouting: Enhanced crossing in the optic chiasm by the portion of axons from temporal RGC abnormally projecting to contralateral brain hemisphere (Guillery et al., 1975). This is attributed to the disruption of molecular mechanisms at the retina that guide axons at the chiasm (Prieur and Rebsam, 2017), most likely due to delayed neurogenesis (Rachel et al., 2002; Bhansali et al., 2014). Specifically, the gathered evidence suggests that the crossing or non-crossing of an axon is dependent on the moment at the developmental stage when it reaches the chiasm, with "earlier" axons being more likely to stay ipsilateral (Baker and Reese, 1993). In albinism, the lack of melanin's precursor, L-Dopa in the retinal pigment epithelium delays the development of RGCs in the retina (Ilia and Jeffery, 1999; Kralj-Hans et al., 2006) and, consequently, the time point their axons reach the optic chiasm, which translates into a higher probability of projecting to the contralateral brain hemisphere (Erskine and Herrera, 2014).

- Reduced volume of the visual cortical areas in case of albinism (Hagen et al., 2005). Alterations to the visual cortex furtherly investigated on the geometric models of cortical surfaces (Bridge et al., 2014) demonstrated that albinism is associated with reduced gyrification in the occipital cortex (explaining the reduction of cortical volume observed by Hagen et al.), as well as increased cortical thickness at the occipital pole. These changes were attributed to the absence of post-natal neuronal pruning, which was the effect of foveal underdevelopment and effective lack of high-resolution input to the visual cortex.

2.2.2.2 Phenotype

The phenotype of albinism covers both dermatological and ophthalmological features, and is significantly varied according to the form of albinism (Kruijt et al., 2018). The dermatological features include hypopigmentation of hair, skin, eyebrows and eyelashes, which may be complete (as in one of the forms of OCA – OCA1A), partial (other forms of OCA: OCA2-OCA7) or absent (as in OA).

The ophthalmological features may include refractive errors (astigmatism, myopia, hyperopia), foveal hypoplasia, fundus hypopigmentation, nystagmus, strabismus, reduced binocular vision, reduced iris pigmentation, iris trans-illumination and misrouting in the optic chiasm (Federico and Krishnamurthy, 2021). Importantly, although the retrospective cohort study on over 500 patients by (Kruijt et al., 2018) revealed that some of the aforementioned features are only rarely absent in patients with albinism, such as nystagmus (absent in 8%), iris translucency (9%), fundus hypopigmentation (4%), foveal hypoplasia (1%) and chiasmal misrouting (16%), none of these features were consistently present in the cohort.

2.2.2.3 Consequences for the visual system's integrity

The structural abnormalities of visual system clearly bear consequences for its function:

- Deficiency of pigment in the retinal pigment epithelium, which normally absorbs most of the incoming light, enhances the ocular straylight [scattering of light on parts in the eye which creates glare; (Kruijt et al., 2011)] and induces photophobia.
- Foveal hypoplasia combined with limited stability of vision (due to nystagmus) and possible light-induced retinal damage effectively reduces visual acuity.
- The optic nerve misrouting in chiasm causes re-direction of signal flow in the visual system. As a consequence, both the LGN and visual cortices receive abnormal input, which in addition to the typical representation of contralateral visual field also contains signal from the ipsilateral visual field (Schmitz et al., 2004; Hagen et al., 2008). The resulting retinotopic maps of two opposing visual hemifields were found to be superimposed (Hoffmann et al., 2003; Kaule et al., 2014; Ahmadi et al., 2019b), which disrupts the integration of visual information and, consequently, stereovision (Hoffmann and Dumoulin, 2015). Importantly, despite the highly disruptive nature of the observed alterations, the fundamental aspects of vision are still preserved (Wolynski et al., 2010; Klemen et al., 2012; Hoffmann and Dumoulin, 2015). This surprising effect is accounted to the presence of adaptive mechanisms mitigating the disruptions, which include re-wiring of cortico-cortical connections in the extrastriate cortex (Ahmadi et al., 2019b).

2.2.2.4 Diagnostics

In general, the wide heterogeneity of the albinism's spectrum and graduation of symptoms poses a considerable challenge for development of diagnostic methods. These can be divided in 3 categories, described in detail below:

- Identification of gene mutations underlying albinism enabled the diagnostics of albinism through **gene testing** (Arveiler et al., 2020). In principle, this approach offers the most certain diagnosis, but is not universal due to still incomplete information about mutations causing specific types of albinism, such as OCA5. Effectively, the most recent studies on molecular characterization of PWA reported successful molecular diagnosis for approx. 73% out of 990 index patients (Lasseaux et al., 2018). Additionally, due to its relatively high costs, genetic testing is more suited as a confirmation of suspected albinism rather than a method for common application (e.g. screening).
- **Dermatological examinations**, despite its relative simplicity offers ambiguous results and as such cannot be relied upon (Federico and Krishnamurthy, 2021).
- Considering the causal relationship between the hypopigmentation and visual system's abnormalities, which translates into their co-occurrence (Kruijt et al., 2018), **ophthalmological evaluation** is a highly relevant tool for diagnostics. This approach is, however, still limited by albinism's heterogeneity. To address this challenge, the Krujit et al. proposed a comprehensive approach to albinism diagnostics, which uses a combination of major (major foveal hypoplasia, ocular hypopigmentation and chiasm misrouting) and minor (nystagmus, hypopigmentation of skin and hair, fundus hypopigmentation, minor foveal hypoplasia) clinical criteria to determine the albinism.

2.2.3 Clinical challenges

Clearly, due to their negative impact on individual's functioning, both achiasma and albinism are relevant targets for clinical studies. This chapter focuses on the clinical aspects of both disorders, which are presented in the subchapters 2.2.3.1 (Diagnostics) and 2.2.3.2 (Treatment).

2.2.3.1 Diagnostics

In the case of achiasma diagnostics, the recommended approach involves a combination of functional and anatomical methods Sami et al., 2005. The functional assessment is typically done using electrophysiology methods, such as VEPs (Hoffmann et al., 2015), but can be also achieved using functional MRI (Bao et al., 2015) and is well established in the clinical routine. The complementary anatomical measurements, standardly based on MRI (Korff et al., 2003), usually provide more robust estimates, but may not be able to resolve the borderline cases, such as partial achiasma (*"chiasm hypoplasia"*) and requires an examination by the radiologists, which is an increasingly more resource expensive (Rimmer, 2017). This highlights a need for a more automated and objective method of assessment of misrouting from anatomical MRI images, or more advanced imaging techniques. A promising alternative measuring technique is the diffusion MRI [(Basser et al., 1994); described in detail in chapter 4 (Methods)], which is capable of capturing the neural fibers of the brain and can be used for direct assessment of absence of crossing (Hoffmann et al., 2012). Utility of this approach for diagnostic purposes requires a thorough testing, however, which has not yet been resolved.

The challenges of diagnostics are even more expressed in case of the more heterogenous spectrum of albinism. Here, between the two extremes of highly accurate and highly expensive genetic testing on one side, and the low cost and low precision dermatological examination on the other, ophthalmological assessment offers a sound

balance between those two worlds. Furthermore, the proposal of using multiple diagnostic criterions (Kruijt et al., 2018) allows to offset the limitations of uni-modal techniques (Park and Oh, 2013; McCafferty et al., 2015), but at the same time highlights the need for using a wide range of robust diagnostic techniques. This is particularly important for the assessment of chiasm's integrity, since this is the only structure that cannot be directly measured during ophthalmological examination. Currently, the assessment of misrouting is being performed with VEPs (Hoffmann et al., 2005; Hagen et al., 2008; Hoffmann et al., 2015), which is used to track the cortical response to monocular simulation in order to identify misrouting. This approach, however, is susceptible to noise, limiting the reproducibility (Sami et al., 2005), and is furthermore dependent of the participant's visual function, which is of particular issue given that low visual acuity and nystagmus are inherent characteristics in albinism. Similarly, in achiasma, this challenge can be addressed by using direct measurements of chiasm's integrity, which can be done using either aMRI or dMRI. Unfortunately, despite the past attempts, none of these techniques were shown to be capable of the individual diagnostics. Specifically, the first study using MRI to compare morphological features of chiasm in controls and people with albinism reported no inter-group differences (Brodsky et al., 1993). While those findings were later contradicted by three independent reports that demonstrated significant group-level differences in the width of optic nerves and chiasm (Schmitz et al., 2003; Hagen et al., 2005; Mcketton et al., 2014), but did not attempt to evaluate the relevance of these anatomical biomarkers in the individual diagnostics. As such, the possibility of detection of abnormally enhanced crossing in the chiasm from aMRI images is still unresolved. Additionally, the chiasmal misrouting observed in albinism was also investigated with the dMRI, which attempted to directly measure portions of crossing and non-crossing fibers in the chiasm (Ather et al., 2018). Interestingly, while dMRI also revealed group-level differences, the testing of its potential for individual diagnostics showed a performance that is insufficient for clinical applications. This aspect of dMRI can be, however, potentially improved with use of newly developed acquisition protocols and modelling approaches, which are yet to be tested for this purpose.

2.2.3.2 Treatment

Due to the congenital nature of both disorders, their effective treatment is possible only during the developmental phase of the visual system and is until now unavailable. Apart from isolated pioneering attempts on reversing some of their aspects [such as increasing melanin content in individuals with albinism (Adams et al., 2019)], majority of therapeutic approaches involves mitigating the disorder's consequences. Those actions are critical, however, as e.g. the individuals with albinism are more susceptible to UV radiation and require increased protection from sun to avoid skin cancer. As such, this highlights the importance of awareness of one's condition and, consequently, the high relevance of robust and widely available diagnostics.

2.2.4 Research challenges

Notably, the relevance of congenital chiasmal disorders extends beyond the clinical context. The significantly altered, yet in principle functional organization of the visual system in achiasma and albinism represents a unique biological model that can be utilized in a wide range of studies. Generally, these can be divided into basic

research, aimed at gaining deeper understanding of structure-function coupling in the brain [subchapter 2.2.4.1 (Basic research)] and methods development, using the unique organization of visual system to design and test novel neuroimaging methods [subchapter 2.2.4.2 (Methods development)].

2.2.4.1 Basic research

In terms of basic research, the biological model provided by congenital chiasmal disorders grants insight into fundamental aspects of brain organization. A prime example here is the understanding of structure-function coupling, which can be studied in novel ways by analysing the properties of chiasmal malformations and their impact on structural and functional organization of the rest of visual system (e.g. definition of disrupted cortical maps). As such, this kind of analyses may provide new information about the principles guiding the development and organization of visual system (Hoffmann and Dumoulin, 2015). However, what truly distinguishes albinism and achiasma from other visual system diseases is the fact, that despite their highly disruptive nature for the visual system, the fundamental integrity of vision is mainly intact (Wolynski et al., 2010; Klemen et al., 2012). This highly surprising finding suggests the presence of unexplored neuroplasticity mechanisms, capable of adjusting to the congenitally disrupted input (Hoffmann and Dumoulin, 2015). While existing evidence suggests that cortico-cortical rewiring may play an important role in the observed adaptation (Ahmadi et al., 2019b), the understanding of this potentially highly valuable plasticity mechanisms requires further studies.

2.2.4.2 Methods development

The chiasmal congenital disorders may be, however, also placed in an interesting perspective where they represent the two extremes of the chiasmal connectivity, absence (or severe reduction) in case of achiasma, and enhanced crossing in albinism. As such, the chiasmal malformations combined with "neutral" crossing observed in the control group (Kupfer et al., 1967) represent a range of gradually varying (both structurally and functionally) visual systems. This unique setup provides an excellent testbed for development of neuroimaging methods. The prime example here is the development of retinotopic mapping, where new methods can be tested and validated on the highly varied biological retinotopic maps. This approach is particularly relevant in the case of development of methods requiring little a priori information, as it was demonstrated with micro-probing (Carvalho et al., 2020). Importantly, the utility of chiasmal malformation models extends beyond functional methods, as they also offer a prime testing dataset for methods of structural imaging, such as diffusion MRI-based tractography (Mori and Zijl, 2002). Here, the information about diffusivity of water in brain, captured by diffusion MRI (Basser et al., 1994), is used to reconstruct the neural fibers. This method, although highly successful in a wide range of applications (Rokem et al., 2017), suffers from several limitations, with one of those being the "crossing fibers problem" (Tournier et al., 2004; Staempfli et al., 2006; Descoteaux et al., 2007; Descoteaux et al., 2009; Thomas et al., 2014; Reveley et al., 2015). This term refers to the problem of poor performance of tractography when performed in brain regions where multiple fibers are crossing (Oouchi et al., 2007; Jones et al., 2013), which is estimated to be the case for to up to 90% of brain's volume (Jeurissen et al., 2012). Accordingly, the data on chiasmal malformations capturing a full range of configurations of two crossing fibers populations offers an

excellent asset for validation and development of diffusion MRI and tractography methods.

Chapter 3

Research questions and steps taken to address them

Robust imaging of chiasmal malformations is a critical component of both clinical and research studies on albinism and achiasma. However, currently available methods offer only limited insights, particularly in the case of direct anatomical measurements. Considering this, the primary goal of my work was to develop and evaluate novel methods designed for anatomy-based detection and assessment of chiasmal malformations. Ideally, this would facilitate further scientific research on chiasm's properties, encourage use of data on chiasmal malformations in methods development and enable novel diagnostics of visual system disorders. In order to achieve these goals, I have contributed to answering 4 research questions as detailed below:

3.1 How to image the visual system with dMRI?

Chapter 5 presents a review paper on the basics and intricacies of dMRI-based imaging of the visual system (Puzniak et al., 2021b). The primary motivation behind this work was to increase awareness about the relevance and clinical applications of dMRI methods, and to provide guidance for dMRI imaging of visual system. Specifically, the review covered discussion on:

- importance and application of dMRI in epilepsy,
- acquisition and modalities of MRI images required of visual system imaging,
- software available and data processing pipeline for dMRI analysis,
- delineation of visual system structures,
- computational models applicable to dMRI data,
- reconstruction of neural connections (tractography) from dMRI data.

The published review provided a comprehensive link between dMRI methods and studies on epilepsy/visual system, which will hopefully facilitate further research in those directions.

3.2 Is it possible to detect and quantify chiasmal malformations?

Chapter 6 presents a scientific article on the quantification of nerve decussation in normal and abnormal (albinotic) chiasms using dMRI (Puzniak et al., 2019). The

primary motivation behind this work was to test the capabilities of advanced dMRI tools, assess the detectability of enhanced nerve crossing with dMRI and design a robust framework serving this purpose. To accomplish this, the following steps were taken:

- acquisition of high quality aMRI and dMRI data from controls and patients with albinism,
- establishing and validation of state-of-the-art preprocessing and modelling-steps of dMRI data,
- tractography within the chiasm and post-processing of the resulting streamlines,
- calculation of the index of decussation (ID) from the tractography data,
- assessment of obtained IDs via:
  - group-level inferences,
  - evaluation of ID-based classification of individuals,
  - comparison of ID with fMRI-based estimates of misrouting,
- evaluation of the techniques used for tractography validation.

Importantly, the developed dMRI-based framework allowed not only for detection of group differences in the calculated IDs, but also demonstrated a robust separation of individuals from both groups, indicating the potential of the dMRI-based diagnostics. Those important findings were additionally reinforced by the cross-validation of dMRI-based results with fMRI-based estimates of misrouting calculated in a separate study (Ahmadi et al., 2019b). Furthermore, the study demonstrated the strengths and limitations of a range of post-processing methods for tractography. Consequently, the presented study is expected to benefit future attempts on tractography of the chiasm (and in general tractography of crossing fibers populations).

Furthermore, the robustness of developed framework allowed for its application in an additional study, presented in the chapter 7, where it was used in a case study of chiasmal hypoplasia to detect asymmetric chiasmal connectivity (Ahmadi et al., 2020). Specifically, my contribution involved:

- preprocessing and modelling of dMRI data,
- tractography within the chiasm and postprocessing of the resulting streamlines.

The results of the conducted dMRI analysis provided a complementary proof for fMRI-based results indicating a surprising presence of three superimposed cortical maps. As such, this study provided novel insights into the organization of the human visual cortex.

3.3 Is it possible to detect chiasmal malformations in aMRI images?

The scientific article presented in chapter 8 investigated a possibility of detection of chiasmal malformations directly from aMRI with deep learning (DL) methods

(Puzniak et al., 2021c). The primary motivation behind this work was development of a direct, anatomy-based diagnostic method suitable for clinical setting. For this purpose, the following steps were taken:

- gathering of publicly available MRI data of a large cohort of controls and patients with albinism,
- generation of accurate optic chiasm masks by combination of atlas-based segmentation with custom correction algorithm,
- implementation and supervised training of the convolutional neural network (CNN) for the purpose of segmentation of optic chiasm from whole-brain aMRI images,
- deployment of the trained network on the aMRI brain images of controls and participants with albinism,
- evaluation of the performance of the CNN.

The obtained results demonstrated that the accuracy of segmentation varies between control and patient groups, which indicate a differential spatial organization of normal and abnormal chiasms. Consequently, this finding provides a proof-of-concept for development of novel tools for detection of chiasmal malformations.

3.4 How to facilitate future research on chiasmal misrouting?

The article presented in chapter 9 describes a publication of anatomical MRI, diffusion MRI and functional MRI data from rare patients showing a wide range of chiasmal malformations (Puzniak et al., 2021a). The primary motivation behind this work was to enable incorporation of rare data on chiasmal malformations into datasets for public use enabling its usage in a wide range of studies. For this purpose, the following steps were taken:

- collection of the previously gathered aMRI, dMRI and fMRI data on chiasmal malformations,
- preprocessing and anonymization of the collected data,
- extensive assessment of the data quality,
- publication of the raw and preprocessed data on the online computational platform,
- publication of the accompanying supplementary data files and scripts on two further online platforms.

The provided data was published on a specialized computational platform brainlife.io (Avesani et al., 2019), where it can be processed online using available cloud-based services or downloaded for offline preprocessing. As such, the published data is expected to benefit researchers working on modeling of diffusion MRI signal, development of tractography algorithms and deep learning methods, basic research of visual system and plasticity, as well as clinicians investigating albinism.

Chapter 4

Methods

In principle, the main techniques available for non-invasive imaging of the human brain anatomy are Computed Tomography (CT) and MRI. Given that, CT imaging involves exposure to radiation and its contrast is reportedly insufficient for chiasm's imaging (Daniels et al., 1984; Ibragimov and Xing, 2017; Duanmu et al., 2020), the optimal imaging technique for the outlined task is the MRI (Lauterbur, 1973), which is devoid of the above listed limitations. Furthermore, MRI supports a range of specialized modalities providing valuable information which is otherwise unavailable with CT imaging. The overview of employed imaging methods is provided in the subchapter 4.1 (Principles of Magnetic Resonance Imaging), which focuses on the two modalities designed for structural imaging – T1-weighted (T1w) and diffusion-weighted (DW) imaging (Basser et al., 1994).

The acquired data has been analysed with two kinds of computational approaches based on, respectively, dMRI and aMRI. The first involved specialized algorithms, tools and models designed exclusively for the purpose of dMRI data analysis, as described in the subchapter 4.2 (Analysis of the MRI Data). The second approach instead used aMRI data in combination with DL techniques (LeCun et al., 1989; Krizhevsky et al., 2012), which are well generalizable, data-driven models excelling at a wide range of medical imaging tasks (Lundervold and Lundervold, 2019), as described in the subchapter 4.3 (Deep Learning models).

4.1 Principles of Magnetic Resonance Imaging

Magnetic Resonance Imaging (MRI) is a non-invasive technique that uses strong magnetic fields to image anatomy and physiological processes of the body (Rabi et al., 1938). At its core lies the magnetic resonance, a phenomenon where atomic nuclei placed in external magnetic field are able to absorb and emit radio frequency (RF) energy (Bloch, 1946). Inducing, controlling and measuring an outcome of this process, as it is done during MRI measurements, reveals the properties of tissue composed of measured nuclei, ultimately allowing for creation of 3D images of desired structure (Pooley, 2005; Currie et al., 2013). Importantly, the parameters of the acquisition can be tuned to capture specific types of interactions that influence the property of magnetic resonance. Effectively, this allows for the development of several MRI techniques, with the most notable being anatomical, diffusion and functional MRI (aMRI, dMRI and fMRI, respectively). The purpose of this subchapter is to describe the former two, which were used for anatomy imaging – subchapter 4.1.1 (Analysis of the T1-weighted images) and subchapter 4.1.2 (Analysis of the Diffusion-weighted Images), unlike fMRI which is used for measurements of brain's neuronal activity (Soares et al., 2016).

4.1.1 T1-weighted images

The aMRI is a broad term for MRI sequences (Rabi et al., 1938) which provide insights into the anatomical organization of the body. As for each MRI measurement, the aMRI sequence starts with placing the participant in a scanner's strong, constant magnetic field $\mathbf{B_0}$. While the magnetic field affects magnetic moments of all particles, the effects are particularly pronounced in protons, due to their distinctively high magnetic moment (Frisch and Stern, 1933) and their high concentration in tissues. Consequently, the MRI measurements are driven by protons, and as such are most sensitive to tissues with high concentration of protons, such as water and fats. In the presence of strong magnetic field the magnetic moments of protons will tend to be aligned in either parallel or anti-parallel direction to the $\mathbf{B_0}$ direction, with the probabilities given by the Boltzmann distribution (Boltzmann, 1868; Hanson, 2008). Effectively, this leads to most of the spins being in the lower energy state (parallel alignment), which altogether contribute to net magnetization vector $\mathbf{M}$, parallel (longitudinal) to $\mathbf{B_0}$. Importantly, considering that MRI is majorly driven by protons contributing to $\mathbf{M}$, in the rest of this section only their role will be considered.

In principle, the nuclei placed in an external magnetic field precess with a specific cyclic frequency f_0, also known as Larmor's frequency, which is given by Larmor's equation:

$$f_0 = \frac{\gamma}{2\pi} B_0 \qquad \text{(Equation 1)}$$

where the γ denotes gyromagnetic ratio. This applies also to the protons contributing to $\mathbf{M}$, which Larmor's frequency in 3 T field equals 127.74 MHz. Importantly, the net magnetization vector $\mathbf{M}$ can be altered by an additional rotating magnetic field $\mathbf{B_1}$, provided that the rotational frequency matches (resonates with) the Larmor's frequency of protons (Hanson, 2008). This is commonly being realized with a perpendicular radiofrequency (RF) field $\mathbf{B_1}$, which tips $\mathbf{M}$ from its primary longitudinal direction by desired angle α. The typically used α is 90°, so that vector of magnetization will be in perpendicular, or transversal, plane while longitudinal magnetization will be equal 0, or 180°. After the RF pulse, the net magnetization M will start returning to its initial state (regrowing its longitudinal magnetization) where it was parallel to $\mathbf{B_0}$ in a process of "relaxation" (Hahn, 1950). In this process, the protons that were excited by the RF pulse dispose of the excess energy by transferring it to nearby nuclei in the form of kinetic energy (heat). The speed of this process is described by the value of T1, the time required for longitudinal magnetization to regrow from 0 to 63% of its nominal value (Bloch, 1946). Most importantly, T1 captures the dynamics of energy flow between the spins and their external environment, which varies between tissues and is a source of image's contrast (e.g. white matter has short T1, while the cerebrospinal fluid requires long relaxation). Effectively, the T1-weighted brain images provide contrast between different types of tissues such as white and gray matter of cerebrospinal fluid. This allows for multiple highly relevant applications, such as diagnostics of injuries (contrast), tracking the development of potential diseases (morphology) or locating critical structures for the purpose of surgery planning. Those properties make T1w images also invaluable for combinations with other modalities, such as dMRI, as it provides detailed information about regions of interest (ROIs) identified by other modalities.

Notably, T1-weighting is one of the several available contrasts, such as T2-weighting or the proton density maps. Although detailed explanation of T1-weighting and other contrasts extends beyond the scope of this chapter, for more elaborative information please refer to (Pooley, 2005; Currie et al., 2013; Elster, 2021).

4.1.2 Diffusion-weighted images

While aMRI enables localization and delineation of brain tissues, it does not offer any further insight into structural organization of the brain. This gap can be filled by dMRI (Basser et al., 1994), a MRI modality excelling at revealing the connectivity and microstructural properties of the brain. For this purpose, dMRI utilizes the phenomenon of diffusion, a random motion of molecules caused by their kinetic energy, which was first described by Robert Brown (hence *"Brownian motion"*) and later studied by Albert Einstein (Einstein, 1956). Initially, diffusion was perceived as an undesirable factor in the studies on spin echo (Hahn, 1950), which prompted extension of Bloch's MR formalism by additional terms related to diffusion (Torrey, 1956). This provided a fundament for the breakthrough work by Stejskal and Tanner (Stejskal and Tanner, 1965), who suggested improvements to the existing spin echo sequences, which greatly improved measurements of diffusion of water molecules. The proposed sequence for measuring diffusion along a specific direction given by vector **x** **(Figure 5)** involves application of magnetic field gradient along **x**. Since the frequency of the spin precession is dependent on the effective magnetic field **(Equation 1)**, the presence of gradient field will alter the frequencies of the nuclei's precession based on their location. Importantly, after the gradient pulse ends, the nuclei from different locations along **x** will regain their original precession frequency, but they won't be in the same phase anymore. Effectively, the phases of precession are used to label water molecules along the **x**. After a short delay (typically 20-50 ms) a second gradient of opposed polarity (-**x**) is applied, which is used for phase rewinding (refocusing). If the molecules haven't moved between the pulses, the phases will be perfectly refocused and the total signal will remain unchanged. However, in case of motion of water molecules along the **x** (due to diffusion), the phase refocusing will be imperfect, what will be indicated by an attenuation of the MR signal.
Mathematically, this process can be described by the Stejskal-Tanner equation (which was derived by solving the Bloch-Torrey partial differential equations for a symmetric pair of pulsed gradients):

$$S = S_0 \cdot e^{-bD} \qquad \text{(Equation 2)}$$

where S denotes the signal strength in a discussed pulse sequence, S_0 denotes the signal strength in analogical experiment but without the diffusion gradient pair, D denotes coefficient of diffusion along the chosen direction and b is a collective term controlling for the sensitivity to diffusion. Specifically, b is defined as:

$$b = \gamma^2 G^2 \delta^2 (\tau - \frac{1}{3}\delta) \qquad \text{(Equation 3)}$$

where γ denotes gyromagnetic ration of nuclei, G - strength of gradients, δ - their duration and τ - interval between them. Notably, the parameters G, δ, τ and consequently b can be controlled during the acquisition and adjusted to the problem e.g. by setting high b-value to measure slow diffusion (which would be undetectable in case of low b-values) or low b-value to measure quick diffusion (since dMRI measures loss of signal, application of high b-value in such scenario leads to complete attenuation of signal).

Given that S and S_0 can be measured and b can be controlled for, from the two separate measurements of signals S_1 and S_2:

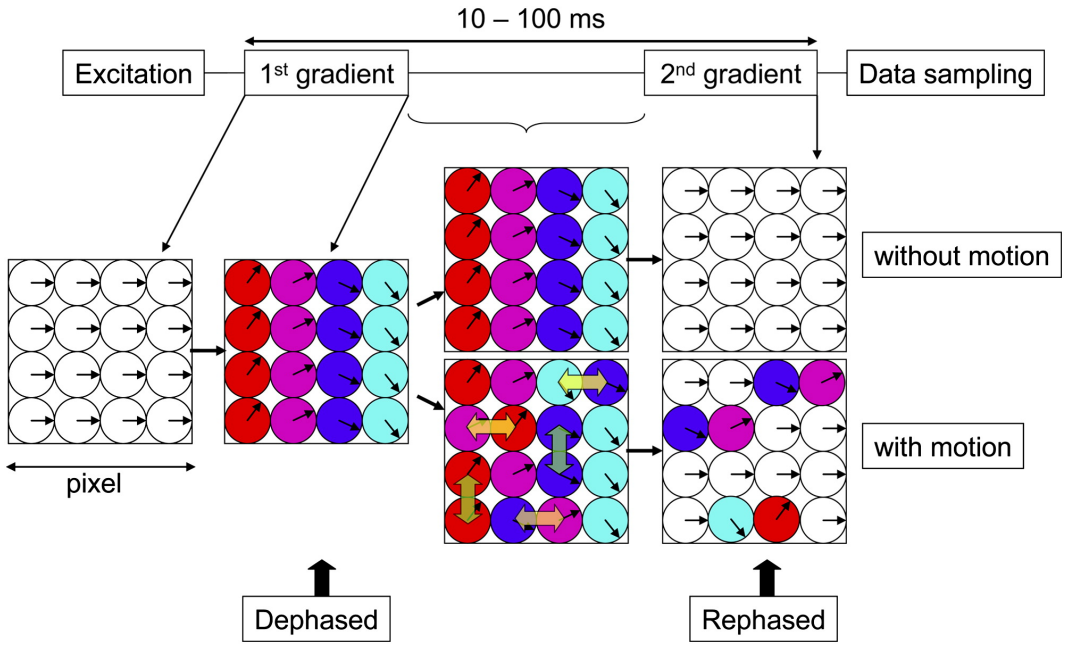

FIGURE 5: **A schematic diagram depicting the idea of diffusion-weighted measurement.** Each circle depicts a water molecule at different locations, with the arrows inside indicating the phase of the local signal. If the molecules are stationary between the two gradient pulses, the 2nd gradient refocuses signal perfectly. However, in case of the diffusion-induced movement of water molecules the rephasing will lead to loss of signal. Notably, only the movement in the direction parallel to that of gradient pulses (here – horizontal) will affect refocusing.

$$S = S_1 \cdot e^{-b_1 D} \quad \text{(Equation 4)}$$

and

$$S = S_2 \cdot e^{-b_2 D} \quad \text{(Equation 5)}$$

The diffusion coefficient D can be calculated as:

$$D = \frac{-\ln(\frac{S_2}{S_1})}{b_2 - b_1} \quad \text{(Equation 6)}$$

Importantly, this rationale applies to diffusion that is free from any barriers. The water in the brain is however bound by cellular walls, which effectively restrict the diffusion and limit the attenuation of signal as compared to free diffusion. As such, measurements of restricted diffusion reveal presence and orientation of objects such as nerve membranes, and are used to identify the orientation of neural fibers in the brain. Notably, despite the increased complexity of mathematical model of restricted diffusion, Equation 2 and Equation 3 are still used for calculations, with the most fundamental difference lying in requirement of measurement of diffusion along at least 6 non-collinear directions in order to use simplest models of restricted diffusion (Bammer, 2003; Mori and Zhang, 2006; Hrabe et al., 2007; Mueller et al., 2015).

While the breakthrough work by Stejskal and Tanner laid foundations for modern dMRI, the method itself was first established on the clinical scanners nearly 35 years later by Le Bihan and colleagues (Le Bihan, 1990). As of now, thanks to numerous advances, the dMRI is a widely used imaging technique that grants insight into microstructural parameters of the brain (Basser and Pierpaoli, 1996), as well as enables imaging of the neural fibers with tractography (Mori and Zijl, 2002), a technique that uses information about local diffusivity to reconstruct the neural pathways.

4.2 Analysis of the MRI Data

The analysis of the MRI can be divided into 2 primary steps – preprocessing and modeling. The prime objective of the data preprocessing is to evaluate and ensure the quality of acquired images. This typically involves corrections for typical artifacts and distortions that are specific to chosen modalities, MRI acquisition sequences and their parameters. The secondary purpose of preprocessing is to prepare the data for further analysis, which may involve co-registration of acquired images (e.g. in case of studies using multiple modalities) or derivation of specific information that will be later required (e.g. segmentation of T1-weighted images into different types of tissues). Since these afore-mentioned steps reflect the general needs shared across a wide range of projects, the preprocessing is commonly done with widely recognized tools such as FSL (Smith et al., 2001; Jenkinson et al., 2012) or FreeSurfer (Fischl, 2012) and with respect to well-established preprocessing pipelines acknowledged as a golden standard, such as Human Connectome Project (HCP) preprocessing pipeline (Glasser et al., 2013). The modeling step involves the application of computational models and tools to previously preprocessed data, allowing for organization of information and extraction the meaningful features from the input data. Similar to preprocessing, modeling of MRI data is also highly dependent on the type and properties of the data to be modelled.

Accordingly, the overview of the aMRI and dMRI data divided into two separate subchapters: 4.2.1 (Analysis of the T1-weighted images) and 4.2.2 (Analysis of the Diffusion-weighted images), respectively.

4.2.1 Analysis of the T1-weighted images

Typically, the handling of T1w data follows the standardized approach based largely on the HCP pipelines (Glasser et al., 2013), which aims to correct the acquired structural images, co-align them (in case of multiple structural scans from a single individual) and transform the images to space of choice to support cross-subjects and -studies comparisons, such as standard MNI152 space (Brett et al., 2002). This subchapter provides a brief overview of selected steps in T1w data analysis, including the steps present in HCP pipelines as well as other approaches.

Generally, the first recommended step is to perform correction for gradient nonlinearity-induced distortions, which are inherent to MRI data acquisition. Notably, while several scanners apply this online during image acquisition, this step can, or in case of specific vendors *must*, be also done offline using the information files provided by the MRI scanner vendors (Jovicich et al., 2006).

Standardly, the next step involves linear or non-linear transformation of T1-weighted image to the space of choice. The linear, or rigid-body, transformations usually have 6 degrees of freedom (3 for translation and 3 for rotation) in order to transform the image to the space of choice, such as anterior commissure – posterior commissure space, one of the standardly defined spaces [e.g. Talairach space (Talairach et al., 1997)] or custom space (e.g. a chosen image's). As such, linear transformations are generally used to standardize orientation of the images in the dataset (which eases future handling) and to match different images of the same subject (e.g. T1-weighted and diffusion-weighted images). The non-linear transformations [performed either to a user-defined template, or one of the standardly defined templates such as the MNI152 (Mazziotta et al., 2001)] allow for effective matching of brain regions across all datasets, at the cost of deformation of individual images.

Typically, after transforming to the desired space, the T1-weighted images are segmented into different regions. Depending on the objective, this may involve only stripping the skull from the image, resulting in a brain mask [e.g. by using BET tool (Smith, 2002) from FSL software], segmentation of the T1-weighted image into white matter, grey matter and cerebrospinal fluid or full-scale segmentation of image into a wide range of brain structures and parcellation of cortex (Fischl, 2012). Notably, the obtained data derivatives can be used for standalone analysis e.g. for the purpose of morphological studies, as done by (Bridge et al., 2014), or be combined with other modalities e.g. dMRI in order to improve the tractography by limiting it to white matter only (Smith et al., 2012).

Finally, it is worth to consider inclusion of data anonymization steps, where both sensitive metadata, as well as notable facial features [such as face and ears; (Bischoff-Grethe et al., 2007; Jeong et al., 2020)] are removed from T1-weighted image to protect participant's identity (Ravindra and Grama, 2019). Although this step is generally optional, it is a critical requirement for sharing MRI data in public domain, the relevance of which increases together with the spread of the Open Science values (Vicente-Saez and Martinez-Fuentes, 2018).

4.2.2 Analysis of the Diffusion-weighted images

In contrast to the standardized T1-weighted images, the analysis of dMRI is in principle a complex topic. The main reason for this is a wide range of applications of dMRI and controllable dMRI acquisition parameters [e.g. number and value of *b*-values (Tuch et al., 2002; Jbabdi et al., 2012; Tournier et al., 2013), number and orientation of directions, spatial resolution]. These choices determine the specific applicable preprocessing methods and models [Diffusion Tensor, or DT, (Basser et al., 1994); Constrained Spherical Deconvolution, or CSD, (Tournier et al., 2004; Tournier et al., 2007); Diffusion Spectrum Imaging, or DSI, (Wedeen et al., 2008); Q-Ball imaging (Tuch, 2004) or Composite Hindered and Restricted Model of Diffusion (Assaf and Basser, 2005)], which in turn define a range of furtherly available computational methods (Mori and Zijl, 2002; Smith et al., 2006; Descoteaux et al., 2009; Dhollander et al., 2021). Considering that dMRI analysis should additionally take into account the choice of software [e.g. FSL (Smith et al., 2001; Jenkinson et al., 2012), MRtrix (Tournier et al., 2012; Tournier et al., 2019)] and avoidance of commonly observed ill-advised practices (Jones et al., 2013), there's a clear gap between proper introduction to dMRI methods and the space available for their comprehensive description (as witnessed in this chapter). This gap can be however addressed with practical reviews, as the one presented in the chapter 5 (Tracking the visual system—from the optic chiasm to primary visual cortex), which covers the basics of data acquisition, preprocessing, data modeling and tractography necessary to a degree that is sufficient for this thesis (Puzniak et al., 2021b). For further information, please refer to reviews of (Tournier et al., 2011; Soares et al., 2013) and an excellent work by (Jones et al., 2013).

4.3 Deep Learning models

Machine Learning (ML) is a broad term for computer algorithms that are able to improve from experience or data, namely: regression analysis, genetic algorithms, support-vector machines, Bayesian networks, decision trees and artificial neural networks (ANNs). The last category describes computing systems inspired by biological neural networks. Accordingly, the ANNs consists of multiple nodes, *"artificial neurons"*, which are able to receive signal from other neurons, compute it and send it to further neurons through connections mimicking synapses. Typically, the modern ANNs are composed of thousands of neurons that are grouped in the input layer, output layer and multiple hidden layers in between. This organization led to coining the term Deep Neural Networks (DNN) that represents ANNs with multiple hidden layers, and Deep Learning (DL) for this subfield of ML.

Although after almost 80 years of development the DL became a complex (and rapidly growing) subfield of ML, its fundamental ideas can be well understood by following the history of DNN. While the fundaments for DNN were laid first by novel discoveries of Santiago Ramon y Cajal (Cajal, 1910), the first recorded model of artificial neurons was proposed by McCulloch and Pits in 1943 (McCulloch and Pitts, 1943) and is presented on the **Figure 6**.

In principle, the model uses multiple binary inputs X_i, which are weighted either by a corresponding W_i of 1 (for excitatory inputs) or -1 (for inhibitory inputs). The signal from all input connections is summarized in a neuron and input to thresholding

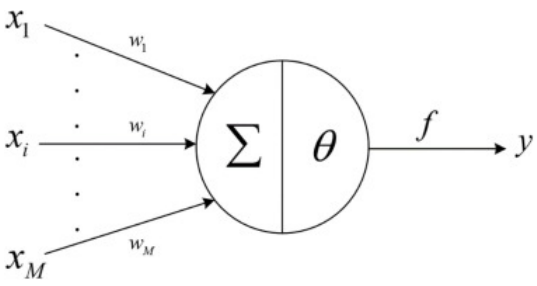

FIGURE 6: **A schematic diagram depicting the McCulloch-Pits neuron.**
The binary inputs X_i are multiplied by corresponding weights w_i and summed in the neuron. The summarized signal is compared against the arbitrary value θ, if the threshold value is reached, the neurons activates and outputs 1, otherwise 0.
Reprinted from Neurocomputing, 465, He J. et al.. Neural networks based on vectorized neurons, pp. 63-70, Copyright 2021, with permission from Elsevier.

function f, which compares it against parameter θ. If the sum exceeds the thresholding parameters, the neuron is activated and outputs signal y equal to 1, otherwise 0. Mathematically, the McCulloch-Pits (MP) neuron is described by equations:

$$y = f\left(\sum_{i=1}^{M} X_i W_i\right) \qquad \text{(Equation 7)}$$

where f, generally referred to as *activation function*, performs thresholding (similarly to the Heaviside step function), such that for any input A:

$$f(A) = 1 \text{ if } A \geq \theta \text{ and } 0 \text{ otherwise} \qquad \text{(Equation 8)}$$

Notably, despite the simplistic model the MP neuron can represent a subset of Boolean logical functions, such as AND, OR or NOT. The simplicity of MP neuron was however also its main limitation, as it was able to operate only on binary inputs and outputs.

The next vital step in the development of artificial neurons was done by David Hebb, who postulated that *"When an axon of cell A is near enough to excite a cell B and repeatedly or persistently takes part in firing it, some growth process or metabolic change takes place in one or both cells such that A's efficiency, as one of the cells firing B, is increased"* and that this is fundamental for learning and memory (Hebb, 1949). Application of this *"Hebbian rule"*, later paraphrased as *"what fires together, wires together"* (Shatz, 1992), to the MP neuron model led to the development of the first *"perceptron"* (Rosenblatt, 1961). The novelty of the perceptron lied in fact, that the weights Wi were non-binary and could be adjusted to different values, which enabled the networks of stacked perceptrons to learn in a Hebbian sense. At the same time, the perceptrons were inherently limited to solving problems, where both classes were linearly separable (and could not be resolved by stacking layers of perceptrons, since the combination of linear functions is a linear function itself). The further (later proven to be unjust) strong criticism by Minsky and Papert, who pointed out that training of multi-layer perceptron networks in a finite time is nearly impossible (Minsky and Papert, 1969) effectively halted all the research in this direction, thus starting a so-called *"AI Winter"*. It took a new generation of scientists to resume the research on neural networks and introduce new, critical concepts, such as backpropagation algorithm (Lecun, 1985; Rumelhart et al., 1986), which enabled effective training of the

multi-layer neural networks, or universal approximation theorem (Cybenko, 1989), that laid theoretical foundations for modernly used non-linear activation functions. This, combined with further method (Robbins, 2007) and hardware developments provided foundations for modern DL models (Vaswani et al., 2017) which set state-of-the-art techniques for Natural Language Processing (Brown et al., 2020) and computer vision tasks (O'Mahony et al., 2020). Importantly, the latter is realized by a specialized subset of ANN known as Convolutional Neural Networks (CNNs), which, due to their high relevance for medical imaging and presented studies, is described in more detail in next subchapter 4.3.1 (Convolutional Neural Networks).

4.3.1 Convolutional Neural Networks

Analogous to the ANNs they stem from, the design of CNNs was based on the biological visual system. Specifically, the inspiration for the development of CNNs were works by Hubel and Wiesel, who showed on cats that individual neurons of visual cortex respond to small areas of the visual field, termed as receptive fields (Hubel and Wiesel, 1959). This finding was followed by the discovery of simple and complex cells (Hubel and Wiesel, 1968), which, respectively, are specialized in detection of straight lines of particular orientation within their receptive field (simple cells) and which have larger receptive field, but are less sensitive to edges' orientations (complex cells). The discoveries of Hubel and Wiesel inspired the first implementation of CNN known as *"neocognitron"* (Fukushima, 1980). Technically, the neocognitron consisted of two types of layers – convolutional and downsampling layers. The convolutional layers, analogous of simple cells, were built from multiple units whose receptive fields covered a patch from the previous layer. The sensitivity of units to patterns was determined by sets of adaptive parameters (filters) that were shared across units. The downsampling layers, analogous of complex cells, were built from multiple units which covered patches of previous convolutional layers. The purpose of those layers was to average local responses from convolutional layers, thus improve network's shift-invariance. Importantly, it was the congnitron that inspired the first modern CNN, which aggregated simpler features into model complex patterns in order to successfully recognize hand-written digits (LeCun et al., 1998). This and other developments of CNNs, such as the introduction of the concept of max-pooling, where the downsampling layers use only maximal activation from their receptive field instead of average (Riesenhuber and Poggio, 1999) or proposal to use backpropagation for filters' training, furtherly unlocking CNNs' capabilities. The most notable display of this emerging technique is dated back to 2012, when the CNN reached the state-of-the-art performance in the ImageNet challenge (Krizhevsky et al., 2012). This started the surge of interest in the CNN, which helped in establishing the CNNs as the state-of-the-art model in the computer vision tasks. As of now, the capabilities of CNNs are successfully utilized in a wide range of fields, including medical imaging (Lundervold and Lundervold, 2019), which was one of the motivations for establishing DL-based diagnostics of chiasmal malformations, as presented in this thesis.

Chapter 5

Tracking the visual system— from the optic chiasm to primary visual cortex

This chapter contains the permitted reprint of the study **"Tracking the visual system—from the optic chiasm to primary visual cortex"** published in *Zeitschrift für Epileptologie*:

Puzniak, R. J., Prabhakaran, G. T., Buentjen, L., Schmitt, F. C., and Hoffmann, M. B. (Feb. 2021). "Tracking the visual system—from the optic chiasm to primary visual cortex". In: *Zeitschrift für Epileptologie* 34.1, pp. 57–66. DOI: 10.1007/s10309-020-00384-y

Zeitschrift für
Epileptologie

Review

Z. Epileptol. 2021 · 34:57–66
https://doi.org/10.1007/s10309-020-00384-y
Accepted: 2 December 2020
Published online: 21 December 2020

Robert J. Puzniak[1] · Gokulraj T. Prabhakaran[1] · Lars Buentjen[2] · Friedhelm C. Schmitt[3] · Michael B. Hoffmann[1,4]

[1] Department of Ophthalmology, Otto-von-Guericke University, Magdeburg, Germany
[2] Department of Stereotactic Neurosurgery, Otto-von-Guericke University, Magdeburg, Germany
[3] Department of Neurology, Otto-von-Guericke University, Magdeburg, Germany
[4] Center for Behavioral Brain Sciences, Magdeburg, Germany

Tracking the visual system—from the optic chiasm to primary visual cortex

Introduction

While epilepsy is a complex and not thoroughly understood phenomenon of brain malfunction, the key to its understanding is in some cases actually hidden in the structure of the brain. This applies, for instance, to acquired causes of epilepsy, such as serious brain trauma, strokes, tumors, and other lesions [5], as well as to observed interactions between structure and function [24]. The comprehensive and accurate description of brain anatomy and connectivity is even more important for surgical interventions, particularly those with a high risk of causing damage to the integrity of the visual system (e.g., anterior temporal lobe resections and amygdalohippocampectomy, see **Fig. 1b**). These examples demonstrate that research on and treatment of epilepsy greatly benefits from the integration of brain imaging techniques, such as diffusion magnetic resonance imaging [23]. Diffusion MRI is a noninvasive imaging technique capable of capturing microstructural tissue properties and of mapping the fiber architecture, e.g., trajectories of neural pathways, which has been demonstrated to significantly contribute to the field of epilepsy. Its capability of capturing the microstructural properties has made it possible to link the structural compromise of fibers tracts in temporal lobe epilepsy (TLE) with memory and language impairments [24] and, as demonstrated in some cases of focal cortical dysplasias, to reveal thinning of white matter fibers and reduced connectivity between subcortical gray matter and the dysplastic cortex [10]. The latter study employed also the second feature of dMRI, i.e., its capability of reconstruction of trajectories of neural pathways. This process, referred to as "tractography" or "fiber or streamline tracking" [26], uses estimates of local fiber orientations (calculated from dMRI data) to produce a tractogram, i.e., the reconstruction of the given pathways in the brain.

The inherent risk of surgical interventions for visual function is well known in standard procedures, such as anterior temporal lobectomy and amygdalohippocampectomy. Although mostly nondisabling, a significant numbers of visual field defects were reported (respectively 78% and 73%; [14]), as for temporal lobe resections, where postoperative upper quadrant visual field deficits were reported for 29 of 38 patients [36]. Between the aforementioned resective approaches, there is no significant difference concerning the risk for visual field deficit [14]. The indicated need for more tailored surgical approaches can be addressed by incorporating tractography in the routine [32, 45], which is known to predict postoperative visual field deficits based on pre- and postoperative tractography [8, 20]. Apart from resective interventions, dMRI can also be integrated for the prevention of visual function deficits in minimally invasive approaches, such as laser interstitial thermal therapy (LiTT; also known as "MRI-guided laser ablation" or "stereotactic laser-thermoablation"; [7]), e.g., for amygdalohippocampectomies in mesial temporal lobe epilepsies ([11, 31]; see **Fig. 1a**) or parieto-occipital lesionectomies typically performed for periventricular heterotopias ([44]; see **Fig. 1b**). At least for mesial temporal lobe epilepsies, more definitive information on risk can be awaited by larger prospective studies in the near future. However, initial results from consecutive case series suggest that the surgical risk for a visual field deficit after LiTT is less than that with the aforementioned resective procedures, particularly if an initial technical learning curve is acknowledged [17].

One risk-posing structure for all temporal surgical approaches is the individual anatomy of Meyer's loop. Nilsson et al. examined the intra- and interindividual variability of Meyer's loop in seven healthy volunteers and two patients undergoing anterior temporal lobe resection by measuring the distance between the anterior edge of the loop and the temporal lobe: the distance varied considerably between 34 and 51 mm (mean 44 mm; [27]) indicating the need for an individual approach during the presurgical planning (see section "Primary visual cortex").

Tractography allows for the visualization and assessment of the connectivity between brain regions [10] and thus can also provide vital information for surgi-

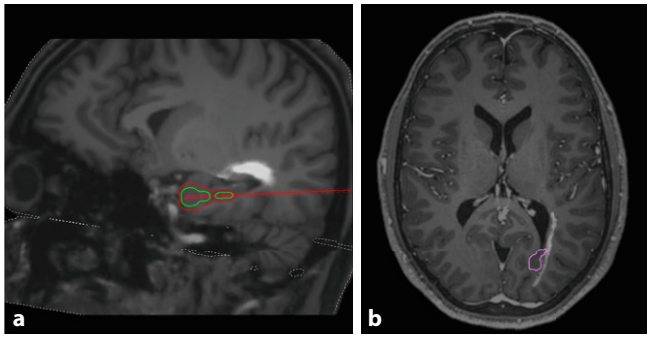

Fig. 1 ▲ Relevance of visual system imaging in clinical routines. **a** Presurgical planning for LiTT on T1-weighted image in pseudo-sagittal view. Stereotactic trajectory (*red line*) and the aimed for lesion zone depicted by a brachytherapy planning tool (arbitrarily chosen: *red contour* resembles 50 Gy Isodose as desired limit of the irreversible damage zone, *green contour* resembles 100 Gy Isodose as core heat zone which needs to be monitored for peak temperatures). Neither trajectory nor lesion zone interfere with the visual tract (as defined by deterministic tractography; *white area* above trajectory), thus minimizing the risk of visual field loss. **b** Periventricular heterotopia (*pink contour*) adjacent to superimposed optic radiation (as defined by deterministic tractography; *white streak* adjacent to the *pink contour*) on T1-weighted image with gadolinium contrast. (Image courtesy of Dept. for Stereotactic Neurosurgery/Otto von Guericke University Magdeburg)

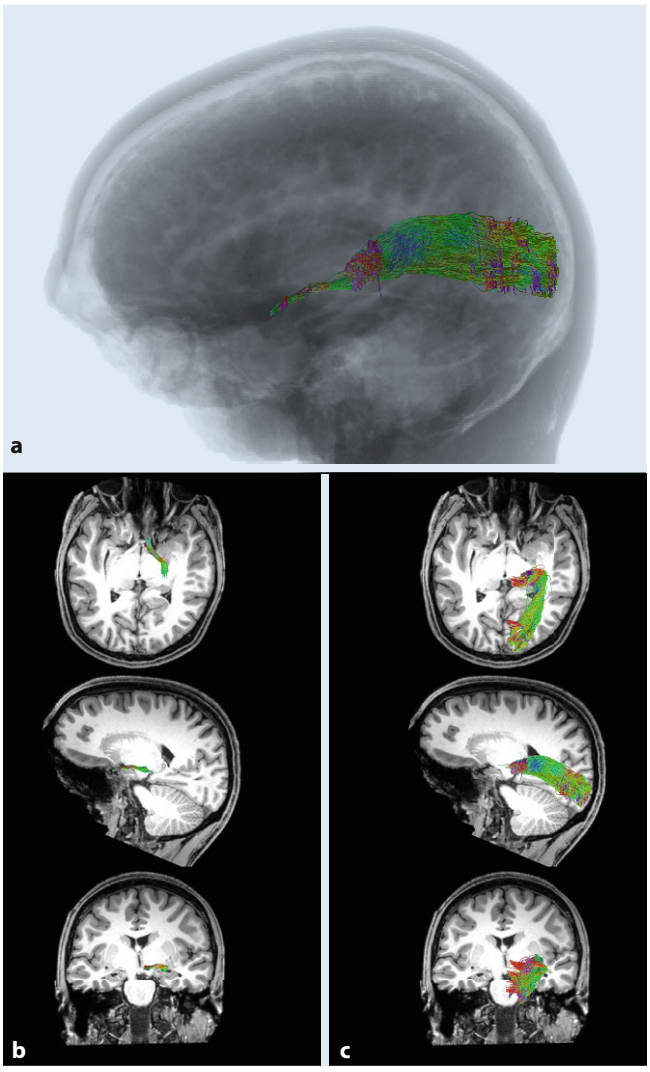

Fig. 2 ▲ Tractography of the visual pathways. **a** A 3D graphic in sagittal view displaying orientation of right optic tract and optic radiation streamlines. **b** T1-weighted images including optic tract (*left*) and optic tract streamlines (*right*) in false color (color code describes streamline orientation: *green* anterior–posterior; *red* left–right; *blue* inferior–superior). Streamlines are not cropped to the shown slices. (Image courtesy of Otto von Guericke University Magdeburg)

cal intervention planning and risk assessment in epilepsy. In the following, the different concepts of imaging the visual system using dMRI are introduced.

Methods

In order to generate the tractogram of the visual system (**Fig. 2**), it is necessary to acquire data, select the analysis tools, preprocess the diffusion-weighted (DW) data, segment the structures of the visual system defining starting and ending points of reconstructed streamlines, fit the model to DW images, and perform the tractography. While each of these steps will be discussed separately, it should be noted that they should not be perceived as separate entities, but rather as interconnected and dependent.

Overview of required MRI data

The optimal MRI dataset acquired for the purpose of tracking of the visual system should comprise (a) T1-weighted (**Fig. 3a**), and optionally a proton density (PD) map, to allow for the comprehensive delineation of brain tissue and structures, and (b) DW images necessary for the tractography (**Fig. 3b**). In the dMRI analysis, the T1-weighted images and PD maps are used in order to identify and segment regions of interest (ROIs) and white matter mask, which enhances tractography. The DW images provide information about microstructural properties (**Fig. 3c**) and what is critical for tractography, spatial organization of neural fibers (additionally, tractography may also provide its own contrast as shown in **Figure 3d**). The basic underlying concept is the measurement of dephasing of excited protons along the given direction simultaneously in all of the brain voxels [37]. The contrast in a DW image depends on the properties of diffusion processes occurring in the tissue and is controlled by two parameters set for MR scanning: b-value (determines the sensitivity to diffusion; b0 is the lowest, where b-value equal to, e.g., 3000 s/mm^2 is considered high) and b-vector (describes the direction along which the diffusion is measured). The selection of DW acquisition parameters is a complex issue, as one needs to consider MRI scanner capabilities, the focus of study (imaging of the whole brain or a single structure), data quality requirements (signal-to-noise ratio, spatial resolution, number of b-values, and gradient directions) and external

Abstract · Zusammenfassung

Z. Epileptol. 2021 · 34:57–66 https://doi.org/10.1007/s10309-020-00384-y

R. J. Puzniak · G. T. Prabhakaran · L. Buentjen · F. C. Schmitt · M. B. Hoffmann

Tracking the visual system—from the optic chiasm to primary visual cortex

Abstract

Epilepsy surgery is a well-established method of treatment for pharmacoresistant focal epilepsies, but it carries an inherent risk of damaging eloquent brain structures. This holds true in particular for visual system pathways, where the damage to, for example, the optic radiation may result in postoperative visual field defects. Such risk can be minimized by the identification and localization of visual pathways using diffusion magnetic resonance imaging (dMRI). The aim of this article is to provide an overview of the step-by-step process of reconstructing the visual pathways applying dMRI analysis. This includes data acquisition, preprocessing, identification of key structures of the visual system necessary for reconstruction, as well as diffusion modeling and the ultimate reconstruction of neural pathways. As a result, the reader will become familiar both with the ideas and challenges of imaging the visual system using dMRI and their relevance for planning the intervention.

Keywords

DTI · Diffusion MRI · dMRI · Tractography · Epilepsy surgery

Traktographie des Sehsystems – vom Chiasma opticum zum primären visuellen Kortex

Zusammenfassung

Epilepsiechirurgische Interventionen sind etablierte Ansätze zur Behandlung pharmakoresistenter fokaler Epilepsien, bergen jedoch das Risiko der Schädigung eloquenter Hirnstrukturen. In Bezug auf die Sehbahn kann dies, beispielsweise bei Läsionen im Bereich der Sehstrahlung, zu postoperativen Gesichtsfelddefekten führen. Die Identifikation und Lokalisierung der Sehbahnstrukturen mittels Diffusionsbildgebung (diffusionsgewichtete Magnetresonanztomographie, dMRT) ermöglicht es, diese Risiken einzuschätzen und zu reduzieren. Der vorliegende Artikel vermittelt eine Schritt-für-Schritt-Darstellung der Prozesse, die der dMRT-basierten Sehbahnrekonstruktionen zugrunde liegen. Dies umfasst die Datenakquise, Vorverarbeitung, Identifikation essenzieller Schlüsselstrukturen sowie die Diffusionsmodellierung und abschließend die Rekonstruktion der Sehbahn. So wird dem Leser ein Verständnis sowohl der Möglichkeiten und Herausforderungen der Bildgebung des Sehsystems mittels dMRT als auch ihrer Relevanz für die Interventionsplanung vermittelt.

Schlüsselwörter

Visuelles System · Diffusionsgewichtete Magnetresonanztomographie · dMRT · DTI · Epilepsiechirurgie

factors, e.g., scanning time (detailed in: [22, 40]). An efficient alternative solution is the adaptation of already validated and well-established protocols such as the Human Connectome Project (HCP) acquisition protocols [42]. Publicly available datasets should also be considered an option to tune the analysis procedures (see **Table 1**).

Processing

Apart from the data acquisition parameters, it is important to consider the choice of tools for data preprocessing and tractography (see **Table 2**). Diffusion-weighted data preprocessing is an important stage, as it determines the data quality and may affect the final outcome of the study. While the applicability and/or necessity of constituent preprocessing steps depends on parameters of the data and specifics of the study, the preprocessing pipelines applied in the HCP project [16] are a commonly recognized standard. **Table 3** provides a list of recommended preprocessing steps, created by extending the HCP preprocessing pipeline by more recent utilities, which result in a corrected DW dataset aligned to the T1-weighted image (**Fig. 4**). A recently emerging alternative to data preprocessing and analysis on local machines are online platforms, such as BrainLife [1]. BrainLife allows one to upload one's own data, or to use existing publicly available datasets (which are either stored directly on BrainLife or can be downloaded from other repositories) and perform neuroimaging analysis in the cloud using online services.

Segmentation of visual system structures

While the previous sections can be generalized for any study involving dMRI data, the selection of regions of interest (ROIs) is determined individually for each study. In the case of tractography of the visual system, it is required to delineate at least the optic chiasm, lateral geniculate nucleus (LGN), and the primary visual cortex (V1), as depicted in **Fig. 5**. The idea here is to localize the structures being connected by visual pathways and to perform the tractography in order to reconstruct these connections. It should be noted that while tractography directly between the optic chiasm and V1 is theoretically possible, in practice it is extremely challenging due to its length and complexity. Therefore, it is recommended to incorporate the LGN in the tractography.

In terms of segmentation there are two main approaches—manual, where the structures are identified and marked by hand by a trained user, or automated, which is performed by designated software. For the latter, the FreeSurfer segmentation software (**Table 2**) is widely used and functions as a semi-standard of automated segmentation. It should also be noted that recent rapid developments in deep learning (DL) methods, although not yet widely established, resulted in new emerging tools that are of great promise.

Optic nerves

If required, the currently recommended strategy would be a manual delineation based on T1-weighted images. This may change with emerging DL-based meth-

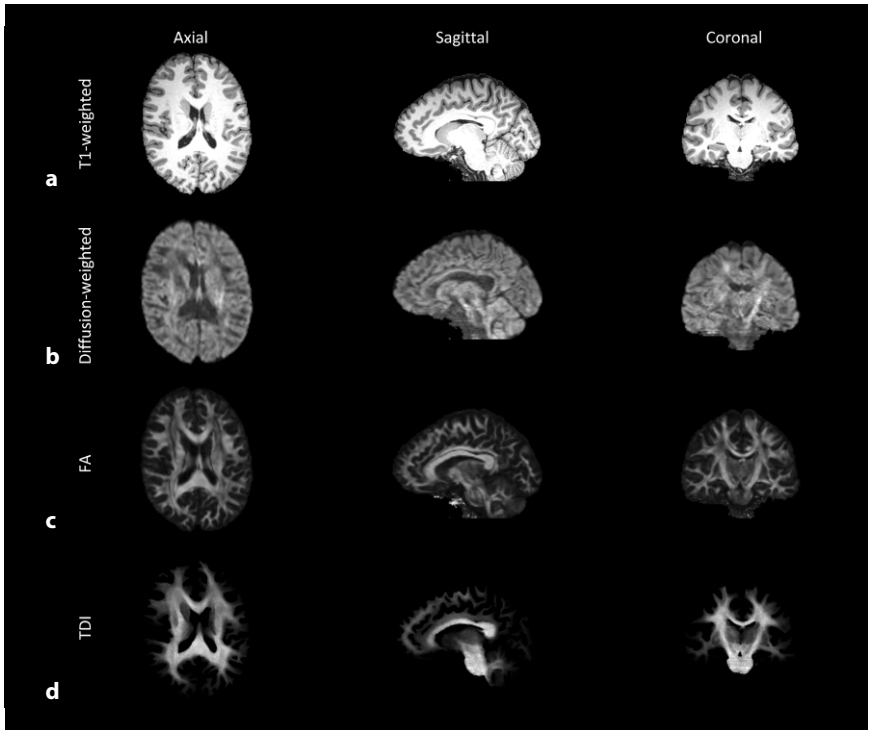

Fig. 3 ▲ T1-weighted and dMRI-derived sample images. **a** T1-weighted images. **b** Single post-processed diffusion-weighted volume acquired with b-value = 1600 s/mm^2. **c** Map of fractional anisotropy (*FA*) describing anisotropy of local diffusion. **d** Track-density imaging (*TDI*), tractography-derived contrast obtained by mapping density of streamlines. (Image courtesy of Otto von Guericke University Magdeburg)

ods, which demonstrate good performance [25], but are not yet widely available.

Optic chiasm

A FreeSurfer software, regarded as a standard tool in automated brain segmentation, is capable of segmenting the optic chiasm, yet its results can be suboptimal (**Fig. 5b,** top). As such it is recommended to segment the optic chiasm manually in order to achieve optimal accuracy (**Fig. 5b**, bottom)—an approach widely used in optic chiasm imaging [30]. Similar to optic nerves, current DL developments allow for the segmentation of the optic chiasm, but they are still not widely tested and available—especially in the case of optic chiasm malformations.

Lateral geniculate nucleus

The segmentation of the LGN is particularly challenging, as this structure does not stand out in T1-weighted images. While it is possible to use automated segmentation tools (e.g., FreeSurfer, SPM, FSL, GIF, MALP-EM, Mipav) to this end, this approach has limitations, e.g., LGN segmentation can even vary between versions (as shown for FreeSurfer in **Fig. 5c**). Furthermore, the lack of validation undermines the study's reliability. Therefore, it is recommended to obtain PD maps during the data acquisition, as their contrast allows for an LGN identification. In the absence of this information, an alternative strategy is the tractography-based identification of the LGN [28]. We propose that this strategy would be even further improved by simultaneous tractography from both the optic chiasm and V1 with the target in the thalamus. The intersection of the streamline endpoints might serve to identify the LGN, which can be combined with the previously introduced FreeSurfer segmentation.

Primary visual cortex

For the identification of the primary visual cortex (V1), three approaches are available: (1) the use of automated segmentation tools, (2) individualized retinotopic mapping, and (3) the estimation of retinotopic maps from anatomical priors. (1) Automated segmentation tools in principle allow for an estimation of V1; however, individual differences from the general template introduce errors in the results of the V1 ROI definition. Further, this approach does not provide an estimate of the retinotopy of V1. (2) The alternative is to obtain retinotopic maps of the visual cortex specifically for the respective individuals with dedicated functional magnetic resonance imaging (fMRI) measurements [32]. Due to the retinotopic organization of the visual cortex, visual areas can be identified via fMRI-based retinotopic mapping (reviewed in [18, 19, 43]). T2*-weighted BOLD gradient-EPI sequences are acquired in fMRI scans during visual stimulation, typically with a contrast-inverting or moving checkerboard pattern section that travels through the visual field in a systematic manner to create a specific spatiotemporal response pattern on the visual cortex. Conventional phase-encoded retinotopic mapping [33] or the neuro-computationally more demanding population receptive field mapping [13] can be applied to obtain cortical maps of the eccentricity and polar angle representations of the visual field. These are typically visualized on the computationally inflated or flattened surface of the visual cortex as derived from high-resolution T1 images. Visual area boundaries can be delineated from these maps [33] as depicted in **Fig. 5d** (top row) for the primary visual cortex (V1). (3) Based on the evidence of qualitatively consistent organization of primary (V1) and extra-striate (V2 and V3) visual area topography [12], Benson et al. [4] demonstrated the ability of an anatomical template to predict the retinotopic organization of the visual cortex with high accuracy using only a participant's brain anatomy, i.e., the patterns of the gyral and sulcal curvatures. In the absence of retinotopic mapping data, a viable alternative is therefore the use of Benson's atlas, which utilizes known anatomical priors in order to estimate V1 location, as well as polar

Table 1 Sample of online, publicly available repositories offering dMRI datasets

Source	Modality	Sample size	Link
Human Connectome Project (HCP; [42])	dMRI, T1w	1206 controls	http://www.humanconnectomeproject.org/
Beijing Normal University data	dMRI, T1w	180 controls	http://fcon_1000.projects.nitrc.org
Image & Data Archive (IDA; 138 studies)	Various	Various	https://ida.loni.usc.edu
Information eXtraction from Images (IXI)	dMRI, T1w, PD	500 controls	http://brain-development.org

dMRI diffusion magnetic resonance imaging, ***PD*** proton density, ***T1w*** T1-weighted

Table 2 Sample list of neuroimaging tools used in DW and T1w data processing

Name	Format conversion	T1w processing	DW processing	Analysis of microstructural properties	Tractography	Function and remarks
dcm2niix	X	–	–	–	–	Well-established converter from Digital Imaging and Communications in Medicine format (DICOM; scanner output) to Neuroimaging Informatics Technology Initiative format (NIfTI; neuroimaging standard)
FSL [21]	–	X	X	X	X	Well-established, high-quality distortion correction tools
FreeSurfer [15]	–	X	–	–	–	Well-established standard in T1-weighted image segmentation
mrDiffusion	X	X	X	X	X	MATLAB-dependent, part of VISTASOFT package
MRtrix [41]	X	X	X	X	X	Notable software for processing, analysis and visualization of dMRI data
Trekker [2]	–	–	–	–	X	Uses state-of-the-art parallel transport tractography algorithm
FiberNavigator	–	–	–	–	X	Supports real-time tractography from the data
DIPY	X	X	X	X	X	Python library for analysis of dMRI data

DW diffusion weighted, ***dMRI*** diffusion magnetic resonance imaging, ***PD*** proton density, ***T1w*** T1-weighted

Table 3 Suggested DW preprocessing pipeline

Name	Software	Purpose	Comments
Conversion from DICOM	dcm2niix	Converting the scanner's DICOM to format standardly handled by neuroimaging software (NIfTI)	Diffusion image in NIfTI format is accompanied by files storing information on b-values (.bvals) and gradient directions (.bvecs)
Denoising	MRtrix	Removal of noise	Requires unmodified data, therefore must be first in the preprocessing
Gibbs rings	MRtrix	Removal of Gibbs ringing artifacts from image	Must be run before any interpolation is performed on the data
Topup	MRtrix/FSL	Estimation of motion in the images	Benefits from low b-value volumes interspersing the DW series (**Fig. 4a**)
Eddy	MRtrix/FSL	Correction of motion, geometry-induced and eddy current distortions	Acquisition of at least portion volumes with opposite phase-encoding direction is recommended (**Fig. 4b**)
Gradient non-linearity correction	FSL	Correction of gradient non-linearity of diffusion gradients	Recommended if not performed automatically during data acquisition
Bias field correction	MRtrix/ANTS	Removes bias field in order to normalize voxels intensities	MRtrix function interacting with ANTs software
Alignment	MRtrix/FSL	Aligns the DW and T1w and PD maps in order to ensure match between images on the voxel scale	Any transformations of DW image must also be applied to gradient directions (.bvecs file) (**Fig. 4c**)
Upsampling	MRtrix	Optional step allowing data to be interpolated to increase resolution	Optional, in some cases recommended

DW diffusion weighted, ***dMRI*** diffusion magnetic resonance imaging, ***PD*** proton density, ***T1w*** T1-weighted

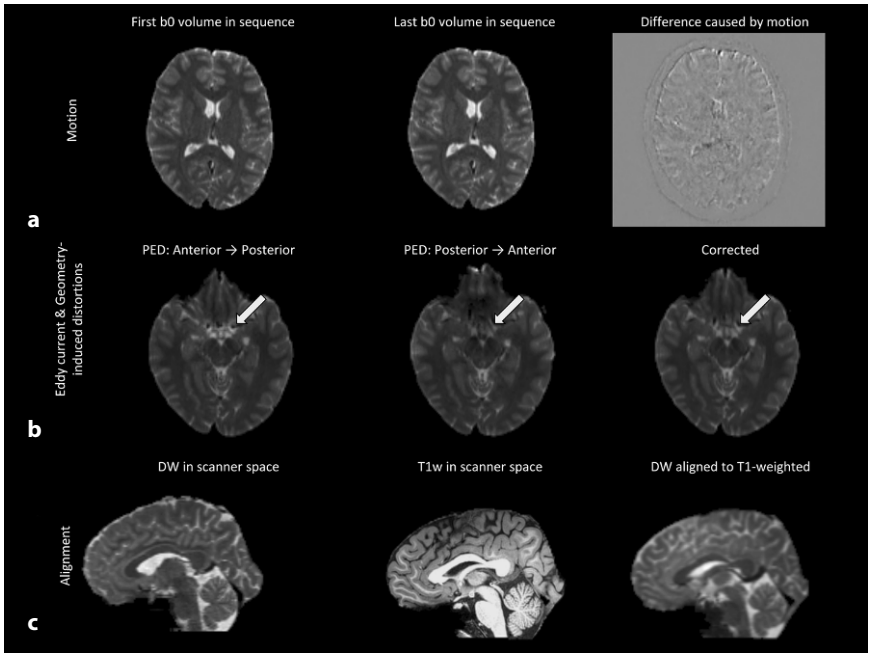

Fig. 4 ▲ Exemplary distortions affecting the quality of the diffusion-weighted (*DW*) b0 images. **a** Example of motion-induced distortions. First (*left*) and last (*middle*) b0 image in the DW series. Calculation of voxel-wise difference between volumes reveals displacement introduced by motion. **b** Example of Echo-Planar Imaging (EPI) distortions. Discontinuity of the medium causes the inhomogeneity of the magnetic field, which warps the image. These distortions are particularly pronounced in the region of the optic chiasm (*white arrows*) and near the ear canals, and depending on the phase-encoding direction (*PED*) are manifested either by squeezing (*left*) or stretching (*middle*). Images acquired with opposite PEDs can be combined in order to unwarp the distortion (*right*). **c** Alignment of the T1-weighted (*T1w*; *middle*) and DW image (*left*) ensures the correspondence between voxels (*right*). (Image courtesy of Otto von Guericke University Magdeburg)

angle and eccentricity map (see ◘ **Fig. 5d**, middle row). This information can be used to specify ROIs for the purpose of tractography.

White matter

In order to enhance the accuracy of the tractography it is recommended to use the known anatomical priors, such as the limitation of the reconstructed pathways to white matter only. Such white matter masks can be extracted using, e.g., FSL or FreeSurfer software. This approach can be further extended by taking into account other types of tissues, such as in five-tissue-type segmentation (implemented in MRtrix), which is a critical component in their proposed anatomically constrained tractography (ACT; [34]).

DW data modeling

Subsequent to DW data preprocessing, it is necessary to fit the diffusion model to the data (◘ **Fig. 6b**). The available modeling approaches depend on the quality and properties of DW data, such as the number of gradient directions, number of shells etc. As the in-depth discussion of available models is beyond the scope of this paper, the following section will cover a sample of two well-established models.

Diffusion tensor

Basic, yet successful and well-established, is the DT [3] model (◘ **Fig. 6b**, *right*), which's popularity caused confusion of Diffusion Tensor Imaging (DTI; application of DT model) with the general dMRI term (covering all models). The DT model represents diffusion as a 3×3 matrix with six independent terms (i.e., from at least six volumes with unique gradient directions), which can be graphically represented as an ellipsoid. This model has limitations, as it models only one diffusion direction per voxel, and as such fails to represent more complex structures, such as the optic chiasm (due to the presence of crossing fibers), Meyer's loop (due to its curvature), or posterior parts of optic radiation (due to fanning).

Constrained spherical deconvolution

Among other alternatives (such as Q-ball imaging, diffusion spectrum imaging), we would like to discuss in detail CSD [39], which treats signal in each voxel as a convolution of the response from a single fiber population and distribution of the local fiber's orientations. As such, CSD is capable of resolving multiple fiber bundles crossing a single voxel, which are described by orientation distribution functions (ODFs). The fitting of the CSD model requires more than six gradient directions (typically 30–60), which grants noise reduction and higher angular resolution at the cost of longer scanning time.

Tractography

In addition to the chosen diffusion model, the outcome tractogram depends on multiple parameters governing the tracking process (◘ **Fig. 6**). These options are introduced and briefly discussed here.

Probabilistic vs. deterministic algorithms

Generally, there are two classes of tracking algorithms—deterministic and probabilistic. Deterministic algorithms assume that fibers in each voxel are oriented in only one direction as determined by the given model (see ◘ **Fig. 6c**)—as such they offer robust results, but fail to grasp complex architectures. Alternative probabilistic algorithms at each step of tracking sample the final direction from the distribution of all possible directions. This approach makes it possible to uncover connections missed by the deterministic algorithms (◘ **Fig. 6c**) and has been proven to be superior to deter-

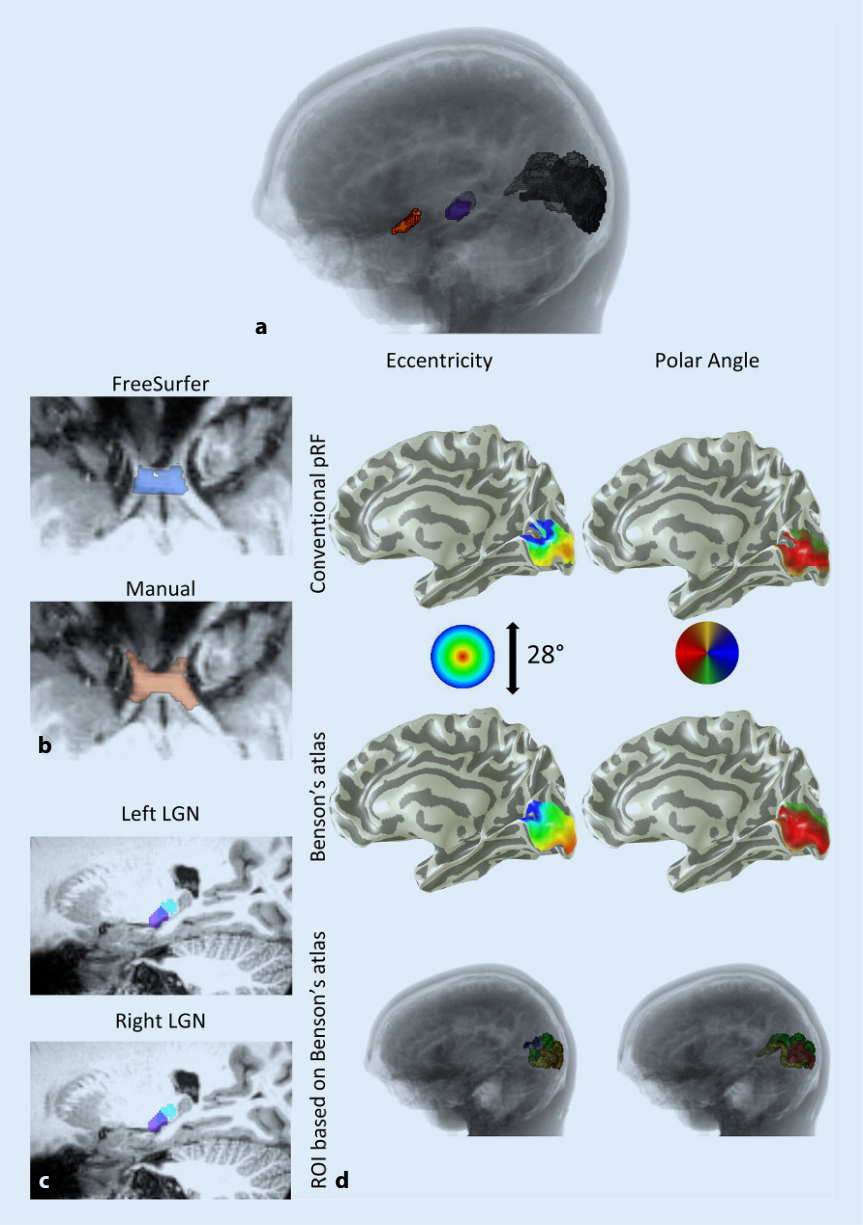

Fig. 5 ▲ Segmentation of visual system structures. **a** A sagittal view of the 3D graphic displaying the optic chiasm (*orange*), *left* and *right* lateral geniculate nucleus (*LGN*; *purple*) and primary visual cortex (*dark gray*) and their location in the T1-weighted image. **b** Tilted axial slices displaying comparison of the optic chiasm masks obtained via FreeSurfer software (*top*) and manual segmentation (*bottom*). **c** Axial slices comparing LGN masks from FreeSurfer v6.0 (*purple*) or FreeSurfer v7.1 (*cyan*; *overlap in blue*). **d** Correspondence of the functional magnetic resonance imaging (fMRI)-derived retinotopic maps, their estimates derived from anatomy using Benson's atlas and the volumetric representation of the latter. *Left* and *right* columns depict eccentricity and polar angle maps, respectively. *Top row* displays surface representation of retinotopic maps of the right hemisphere derived from fMRI data using population Receptive Field (pRF) models. *Middle row* displays analogical representation derived directly from T1-weighted image using Benson's atlas. The *bottom row* displays Benson's prediction in a volumetric representation. It should be noted that the representation is limited to the central visual field (14° radius). (Image courtesy of Otto von Guericke University Magdeburg)

ministic tracking. Consequently, modern tracking algorithms relying on advanced models, such as CSD, employ probabilistic tracking algorithms.

Algorithm types

Even within the class of probabilistic algorithms, there exists a wide range of possible choices, which impacts the outcome tractogram. The difference between two probabilistic algorithm—iFOD2 (implemented in MRtrix) and parallel transport tractography (implemented in Trekker)—is demonstrated in **Fig. 6c**.

Seeding region

The term "seed" refers to locations chosen as starting points for reconstructed streamlines. Global seeding describes allowance to track from any brain voxel (usually white matter voxel), while ROI seeding refers to limiting seeds to defined ROIs. Global seeding allows for the reconstruction of all possible pathways, which is important in studies on the connectivity within the whole brain, but at the same time is much more computationally demanding. It also does not guarantee that the pathways of interest will indeed be reconstructed. The ROI seeding limits the tractography only to the selected structures, which is faster, but may, at the same time, limit the application of streamline post-processing options (see next section).

Target ROIs

For the recommended probabilistic algorithms, the generated streamlines will not only be limited to the "true" pathways between seeds, but will also cover a wide range of positive, but anatomically implausible, connections (**Fig. 6d**). In order to limit the tractography outcome to only valid streamlines, it is advised to employ information about the destination of the streamlines, known as a "target." A combination of information about start (seed) and end (target) ROIs greatly improves the accuracy of tractography (**Fig. 6d**).

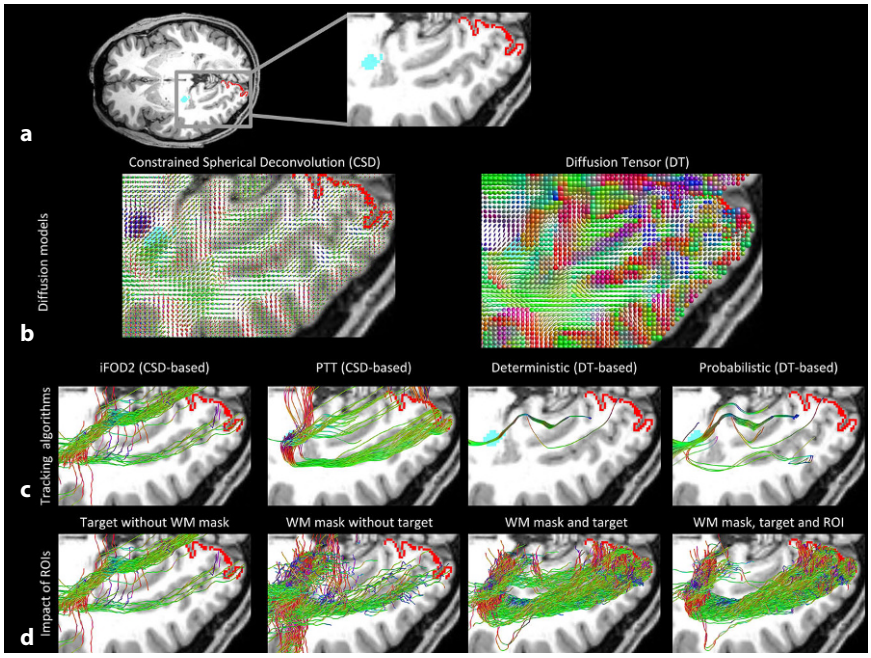

Fig. 6 ▲ Exemplary diffusion models, tractography algorithms, and tracking strategies. **a** The axial slice of the T1-weighted image with highlighted LGN (*cyan*) and V1 (*red*). **b** Two exemplary models fit to the data: constrained spherical deconvolution (*CSD*; *left*) and diffusion tensor (*DT*; *right*). **c** Sample streamlines connecting LGN and V1 generated using different tracking algorithms (from *left* to *right*): second-order Integration over Fiber Orientation Distrbutions (iFOD2) based on CSD model, Parallel Transport Tractography (PTT) based on CSD model, deterministic algorithm based on DT, and probabilistic algorithm based on DT. **d** Impact of incorporating regions of interest (*ROIs*) in the iFOD2-based tractography. *From left to right*: streamlines connecting LGN to V1, but not limited to white matter (*WM*); streamlines generated in LGN and limited to white matter but not requested to reach V1; streamlines connecting LGN and V1 and limited to white matter; streamlines connecting LGN and V1, limited to white matter and requested to pass through user-defined ROI (enforcing anatomical plausibility of streamlines). (Image courtesy of Otto von Guericke University Magdeburg)

Additional inclusion/exclusion ROIs

Still, the definition of seed and target ROIs does not necessarily unambiguously determine the reconstructed streamlines, especially in the case of complex neural connections, such as the optic radiation. Therefore, it is necessary to always visually inspect the tractography results. For uncertain results, it is recommended to introduce further inclusion or exclusion ROIs (based on anatomical knowledge) in order to impose other restrictions on generated streamlines and remove implausible connections (**Fig. 6d**). A good and widely used example of the incorporation of anatomical priors in tractography is using the white matter mask as a limitation for the tractography. This option is supported in all tracking software, as well as its extensions to tissue types other than WM (such as in ACT; [34]).

Other parameters and ensemble tractography

Apart from the aforementioned points, it is also necessary to choose the parameters governing tracking, such as the number of steps, maximal angle between consecutive steps, and possible thresholds preventing tractography from entering false regions etc. A detailed discussion of this topic requires a separate study, as the selection of fixed parameters introduces tracking bias. A solution to this problem is the repetition of tractography multiple times (using different algorithms, sets of parameters, and possibly even models) and combining all these into one outcome [38]. This will, however, naturally extend the complexity of the analysis and its duration.

Streamline post-processing—editing and filtering

Once the tractogram is generated, it can be subjected to further editing and adjustments. All approaches can generally be grouped into two classes: (a) User-informed tractograms can be merged, divided with respect to the number of streamlines or their properties (such as length), split using newly defined ROIs, transformed to different templates etc. The common denominator here is the user-made decision about the action. (b) Signal-informed tractograms are automated methods that refine the selection of streamlines using initially measured signal as a reference, a validation process referred to as filtering. As an example, linear fascicle evaluation (LiFE; [29]) calculates the predicted signal based on generated streamlines and compares it with the currently measured signal. Redundant streamlines with zero contribution to the currently measured signal are subsequently discarded. Other filtering methods include, e.g., Spherical-deconvolution Informed Filtering of Tractograms (SIFT; [35]) or Convex Optimization Modeling for Microstructure Informed Tractography (COMMIT; [9]).

Outlook

The previous sections presented the procedure involved in the tractography of the visual system and its relevance for presurgical planning. From a more general viewpoint, dMRI with its unparalleled capability of capturing the architecture and microstructural properties is a versatile tool also in research on epilepsy, or any kind of neuroscientific research involving brain anatomy. Neurosurgery is continuously seeking to be less invasive, yet attempts in this direction are often hindered by limitations in knowledge, e.g., of the function of higher-order visual cortices. This is expected to eventually change with the scientific progress regarding structure–function relationships in the visual system and thus foster its integration with clinical applications and presurgical planning. A fine example of such developments are research initia-

tives aiming to design visual prosthesis by microelectrode stimulation of the V1 [6]. Here, it is anticipated that dMRI will be of assistance in deciphering retinal projection fields in V1 a priori to the application of the high-resolution stimulation grids. As such, this would be a meaningful step in the development of visual prosthesis, even though it is still a long way from creating phosphenes capable of inducing meaningful visual impressions by neuronal stimulation.

Practical conclusion

- **Surgical planning and risk assessment in epilepsy benefit greatly from an individualized reconstruction of the visual pathways.**
- **Integrated diffusion magnetic resonance imaging (dMRI)-based tractography allows for the individualized identification of the visual pathways, including optic tracts and optic radiation.**
- **To acquire the information essential for successful tractography and to cope with imaging artifacts, dMRI requires careful consideration of data acquisition settings and preprocessing tools.**
- **Tractography requires the segmentation of seed structures, i.e., optic chiasm, lateral geniculated nucleus, primary visual cortex, and white matter masks.**
- **The choice of the correct dMRI data modeling framework is critical for the successful tractography-based reconstruction of the visual pathways.**

Corresponding address

Prof. Michael B. Hoffmann
Department of Ophthalmology, Otto-von-Guericke University
Magdeburg, Germany
michael.hoffmann@med.ovgu.de

Funding. This work was supported by European Union's Horizon 2020 research and innovation programme under the Marie Sklodowska-Curie grant agreement (No. 641805) and by the German Research Foundation (DFG, HO 2002 10-3) to M.B.H.

Funding. Open Access funding enabled and organized by Projekt DEAL.

Compliance with ethical guidelines

Conflict of interest. R.J. Puzniak, G.T. Prabhakaran, L. Büntjen and M.B. Hoffmann declare that they have no competing interests. F.C. Schmitt received reimbursement for expenses and travel from Medtronic Inc.

All procedures performed in studies involving human participants or on human tissue were in accordance with the ethical standards of the institutional and/or national research committee and with the 1975 Helsinki declaration and its later amendments or comparable ethical standards. Informed consent was obtained from all individual participants included in the study.

References

1. Avesani P, McPherson B, Hayashi S et al (2019) The open diffusion data derivatives, brain data upcycling via integrated publishing of derivatives and reproducible open cloud services. Sci Data 6:69. https://doi.org/10.1038/s41597-019-0073-y
2. Aydogan DB, Shi Y (2019) A novel fiber-tracking algorithm using parallel transport frames
3. Basser PJ, Mattiello J, LeBihan D (1994) MR diffusion tensor spectroscopy and imaging. Biophys J 66:259–267
4. Benson NC, Butt OH, Brainard DH, Aguirre GK (2014) Correction of distortion in flattened representations of the cortical surface allows prediction of V1-V3 functional organization from anatomy. PLoS Comput Biol 10:e1003538. https://doi.org/10.1371/journal.pcbi.1003538
5. Berkovic SF, Mulley JC, Scheffer IE, Petrou S (2006) Human epilepsies: interaction of genetic and acquired factors. Trends Neurosci 29:391–397. https://doi.org/10.1016/j.tins.2006.05.009
6. Bosking WH, Beauchamp MS, Yoshor D (2017) Electrical stimulation of visual cortex: relevance for the development of visual cortical prosthetics. Annu Rev Vis Sci 3:141–166. https://doi.org/10.1146/annurev-vision-111815-114525
7. Büntjen L, Voges J, Heinze HJ et al (2017) Stereotaktische Laserablation – Technische Konzepte und klinische Anwendungen. Z Epileptol 30:152–161. https://doi.org/10.1007/s10309-016-0099-5
8. Chen X, Weigel D, Ganslandt O et al (2009) Prediction of visual field deficits by diffusion tensor imaging in temporal lobe epilepsy surgery. Neuroimage 45:286–297. https://doi.org/10.1016/j.neuroimage.2008.11.038
9. Daducci A, Dal Palù A, Lemkaddem A, Thiran J-P (2015) COMMIT: convex optimization modeling for microstructure informed tractography. IEEE Trans Med Imaging 34:246–257. https://doi.org/10.1109/TMI.2014.2352414
10. Diehl B, Tkach J, Piao Z et al (2010) Diffusion tensor imaging in patients with focal epilepsy due to cortical dysplasia in the temporo-occipital region: electro-clinico-pathological correlations. Epilepsy Res 90:178–187. https://doi.org/10.1016/j.eplepsyres.2010.03.006
11. Donos C, Rollo P, Tombridge K et al (2020) Visual field deficits following laser ablation of the hippocampus. Neurology 94:e1303–e1313. https://doi.org/10.1212/WNL.0000000000008940
12. Dougherty RF, Koch VM, Brewer AA et al (2003) Visual field representations and locations of visual areas V1/2/3 in human visual cortex. J Vis 3:586–598. https://doi.org/10.1167/3.10.1
13. Dumoulin SO, Wandell BA (2008) Population receptive field estimates in human visual cortex. Neuroimage 39:647–660. https://doi.org/10.1016/j.neuroimage.2007.09.034
14. Egan RA, Shults WT, So N et al (2000) Visual field deficits in conventional anterior temporal lobectomy versus amygdalohippocampectomy. Neurology 55:1818–1822. https://doi.org/10.1212/wnl.55.12.1818
15. Fischl B, Salat DH, Busa E et al (2002) Whole brain segmentation: automated labeling of neuroanatomical structures in the human brain. Neuron 33:341–355. https://doi.org/10.1016/s0896-6273(02)00569-x
16. Glasser MF, Sotiropoulos SN, Wilson JA et al (2013) The minimal preprocessing pipelines for the Human Connectome Project. Neuroimage 80:105–124. https://doi.org/10.1016/j.neuroimage.2013.04.127
17. Gross RE, Stern MA, Willie JT et al (2018) Stereotactic laser amygdalohippocampotomy for mesial temporal lobe epilepsy. Ann Neurol 83:575–587. https://doi.org/10.1002/ana.25180
18. Hoffmann MB, Dumoulin SO (2015) Congenital visual pathway abnormalities: a window onto cortical stability and plasticity. Trends Neurosci 38:55–65. https://doi.org/10.1016/j.tins.2014.09.005
19. Hoffmann MB, Kaule F, Grzeschik R et al (2011) Retinotopic mapping of the human visual cortex with functional magnetic resonance imaging—basic principles, current developments and ophthalmological perspectives. Klin Monatsbl Augenheilkd 228:613–620. https://doi.org/10.1055/s-0029-1245625
20. James JS, Radhakrishnan A, Thomas B et al (2015) Diffusion tensor imaging tractography of Meyer's loop in planning resective surgery for drug-resistant temporal lobe epilepsy. Epilepsy Res 110:95–104. https://doi.org/10.1016/j.eplepsyres.2014.11.020
21. Jenkinson M, Beckmann CF, Behrens TEJ et al (2012) FSL. Neuroimage 62:782–790. https://doi.org/10.1016/j.neuroimage.2011.09.015
22. Jones DK, Knösche TR, Turner R (2013) White matter integrity, fiber count, and other fallacies: the do's and don'ts of diffusion MRI. Neuroimage 73:239–254. https://doi.org/10.1016/j.neuroimage.2012.06.081
23. Le Bihan D, Breton E, Lallemand D et al (1986) MR imaging of intravoxel incoherent motions: application to diffusion and perfusion in neurologic disorders. Radiology 161:401–407. https://doi.org/10.1148/radiology.161.2.3763909

24. McDonald CR, Ahmadi ME, Hagler DJ et al (2008) Diffusion tensor imaging correlates of memory and language impairments in temporal lobe epilepsy. Neurology 71:1869–1876. https://doi.org/10.1212/01.wnl.0000327824.05348.3b
25. Mlynarski P, Delingette H, Alghamdi H et al (2020) Anatomically consistent CNN-based segmentation of organs-at-risk in cranial radiotherapy. J Med Imaging 7:14502. https://doi.org/10.1117/1.JMI.7.1.014502
26. Mori S, van Zijl PCM (2002) Fiber tracking: principles and strategies—a technical review. NMR Biomed 15:468–480. https://doi.org/10.1002/nbm.781
27. Nilsson D, Starck G, Ljungberg M et al (2007) Intersubject variability in the anterior extent of the optic radiation assessed by tractography. Epilepsy Res 77:11–16. https://doi.org/10.1016/j.eplepsyres.2007.07.012
28. Ogawa S, Takemura H, Horiguchi H et al (2014) White matter consequences of retinal receptor and ganglion cell damage. Invest Ophthalmol Vis Sci 55:6976–6986. https://doi.org/10.1167/iovs.14-14737
29. Pestilli F, Yeatman JD, Rokem A et al (2014) Evaluation and statistical inference for living connectomes. Nat Methods 11:1058–1063. https://doi.org/10.1038/nmeth.3098
30. Puzniak RJ, Ahmadi K, Kaufmann J et al (2019) Quantifying nerve decussation abnormalities in the optic chiasm. Neuroimage Clin 24:102055. https://doi.org/10.1016/j.nicl.2019.102055
31. Schmitt FC, Büntjen L, Schütze H et al (2020) Stereotaktische Laserthermoablation bei mesialer Temporallappenepilepsie mit Hippocampussklerose rechts – Patientenentscheidung, Durchführung und Visualisierung von Gedächtnisfunktion. Z Epileptol 33:42–49. https://doi.org/10.1007/s10309-020-00313-z
32. Schmitt FC, Kaufmann J, Hoffmann MB et al (2014) Case report: practicability of functionally based tractography of the optic radiation during presurgical epilepsy work up. Neurosci Lett 568:56–61. https://doi.org/10.1016/j.neulet.2014.03.049
33. Sereno MI, Dale AM, Reppas JB et al (1995) Borders of multiple visual areas in humans revealed by functional magnetic resonance imaging. Science 268:889–893. https://doi.org/10.1126/science.7754376
34. Smith RE, Tournier J-D, Calamante F, Connelly A (2012) Anatomically-constrained tractography: improved diffusion MRI streamlines tractography through effective use of anatomical information. Neuroimage 62:1924–1938. https://doi.org/10.1016/j.neuroimage.2012.06.005
35. Smith RE, Tournier J-D, Calamante F, Connelly A (2013) SIFT: spherical-deconvolution informed filtering of tractograms. Neuroimage 67:298–312. https://doi.org/10.1016/j.neuroimage.2012.11.049
36. Steensberg AT, Olsen AS, Litman M et al (2018) Visual field defects after temporal lobe resection for epilepsy. Seizure 54:1–6. https://doi.org/10.1016/j.seizure.2017.11.011
37. Stejskal EO, Tanner JE (1965) Spin diffusion measurements: spin echoes in the presence of a time-dependent field gradient. J Chem Phys 42:288–292. https://doi.org/10.1063/1.1695690
38. Takemura H, Caiafa CF, Wandell BA, Pestilli F (2016) Ensemble tractography. PLoS Comput Biol 12:e1004692. https://doi.org/10.1371/journal.pcbi.1004692
39. Tournier J-D, Calamante F, Connelly A (2007) Robust determination of the fibre orientation distribution in diffusion MRI: non-negativity constrained super-resolved spherical deconvolution. Neuroimage 35:1459–1472. https://doi.org/10.1016/j.neuroimage.2007.02.016
40. Tournier J-D, Calamante F, Connelly A (2013) Determination of the appropriate b value and number of gradient directions for high-angular-resolution diffusion-weighted imaging. NMR Biomed 26:1775–1786. https://doi.org/10.1002/nbm.3017
41. Tournier J-D, Smith R, Raffelt D et al (2019) MRtrix3: a fast, flexible and open software framework for medical image processing and visualisation. Neuroimage 202:116137. https://doi.org/10.1016/j.neuroimage.2019.116137
42. Van Essen DC, Smith SM, Barch DM et al (2013) The WU-Minn Human Connectome Project: an overview. Neuroimage 80:62–79. https://doi.org/10.1016/j.neuroimage.2013.05.041
43. Wandell BA, Winawer J (2015) Computational neuroimaging and population receptive fields. Trends Cogn Sci 19:349–357. https://doi.org/10.1016/j.tics.2015.03.009
44. Whiting AC, Bingaman JR, Catapano JS et al (2020) Laser interstitial thermal therapy for epileptogenic periventricular nodular heterotopia. World Neurosurg 138:e892–e897. https://doi.org/10.1016/j.wneu.2020.03.133
45. Winston GP, Mancini L, Stretton J et al (2011) Diffusion tensor imaging tractography of the optic radiation for epilepsy surgical planning: a comparison of two methods. Epilepsy Res 97:124–132. https://doi.org/10.1016/j.eplepsyres.2011.07.019

Chapter 6

Quantifying nerve decussation abnormalities in the optic chiasm

This chapter contains the permitted reprint of the study **„Quantifying nerve decussation abnormalities in the optic chiasm"** published in *Neuroimage: Clinical*:

Puzniak, R. J., Ahmadi, K., Kaufmann, J., Gouws, A., Morland, A. B., Pestilli, F., and Hoffmann, M. B. (Jan. 2019). "Quantifying nerve decussation abnormalities in the optic chiasm". In: *NeuroImage: Clinical* 24, p. 102055. DOI: 10.1016/j.nicl.2019.102055

NeuroImage: Clinical 24 (2019) 102055

Contents lists available at ScienceDirect

NeuroImage: Clinical

journal homepage: www.elsevier.com/locate/ynicl

Quantifying nerve decussation abnormalities in the optic chiasm

Robert J. Puzniak[a], Khazar Ahmadi[a], Jörn Kaufmann[b], Andre Gouws[c], Antony B. Morland[c,d], Franco Pestilli[e,1], Michael B. Hoffmann[a,f,1,*]

[a] Department of Ophthalmology, Otto-von-Guericke-University Magdeburg, Magdeburg, Germany
[b] Department of Neurology, Otto-von-Guericke-University Magdeburg, Magdeburg, Germany
[c] York Neuroimaging Centre, Department of Psychology, University of York, York, United Kingdom
[d] York Biomedical Research Institute, University of York, York, United Kingdom
[e] Department of Psychological and Brain Sciences, Program in Neuroscience and Program in Cognitive Science, Indiana University, Bloomington, USA
[f] Center for Behavioral Brain Sciences, Magdeburg, Germany

ARTICLE INFO

Keywords:
Optic chiasm
Albinism
Diffusion MRI
Functional MRI
Crossing nerves

ABSTRACT

Objective: The human optic chiasm comprises partially crossing optic nerve fibers. Here we used diffusion MRI (dMRI) for the in-vivo identification of the abnormally high proportion of crossing fibers found in the optic chiasm of people with albinism.

Methods: In 9 individuals with albinism and 8 controls high-resolution 3T dMRI data was acquired and analyzed with a set of methods for signal modeling [Diffusion Tensor (DT) and Constrained Spherical Deconvolution (CSD)], tractography, and streamline filtering (LiFE, COMMIT, and SIFT2). The number of crossing and non-crossing streamlines and their weights after filtering entered ROC-analyses to compare the discriminative power of the methods based on the area under the curve (AUC). The dMRI results were cross-validated with fMRI estimates of misrouting in a subset of 6 albinotic individuals.

Results: We detected significant group differences in chiasmal crossing for both unfiltered DT ($p = 0.014$) and CSD tractograms ($p = 0.0009$) also reflected by AUC measures (for DT and CSD: 0.61 and 0.75, respectively), underlining the discriminative power of the approach. Estimates of crossing strengths obtained with dMRI and fMRI were significantly correlated for CSD ($R^2 = 0.83$, $p = 0.012$). The results show that streamline filtering methods in combination with probabilistic tracking, both optimized for the data at hand, can improve the detection of crossing in the human optic chiasm.

Conclusions: Especially CSD-based tractography provides an efficient approach to detect structural abnormalities in the optic chiasm. The most realistic results were obtained with filtering methods with parameters optimized for the data at hand.

Significance: Our findings demonstrate a novel anatomy-driven approach for the individualized diagnostics of optic chiasm abnormalities.

1. Introduction

The optic chiasm is a core component of the human visual system. Here the fate of the axons is decided, such that fibers from the nasal retina cross to the contralateral hemisphere, while those from the temporal retina do not cross and remain on the ipsilateral hemisphere. This partial decussation of the optic nerves guarantees that each hemisphere receives binocular input from the contralateral visual hemifield. Beyond its clinical relevance (Hoffmann and Dumoulin, 2015) and its relevance as a model for neuronal pathfinding in basic neuroscience (Prieur and Rebsam, 2017; Petros et al., 2008) the optic chiasm can be used as a powerful test-bed for the development of methods that allow the in-vivo-reconstruction of fiber tracts in the human brain. A common tool for this purpose is diffusion MRI (dMRI), which uses random thermal motion of water molecules (Stejskal and Tanner, 1965) to identify markers of the neuronal tissue organization. This approach, initially using the Diffusion Tensor model [DT; Basser et al., 1994], was, however, proven to be confounded by tissues with a complex microstructure comprising a mixture of crossing and non-crossing nerves (Alexander et al., 2002; Tuch et al., 2002). This leads to misestimations of microstructural parameters (Oouchi et al., 2007) and the underlying fiber distribution (Jones et al., 2013).

* Corresponding author at: Department of Ophthalmology, Otto-von-Guericke-University Magdeburg, Leipziger Str. 44, 39120 Magdeburg, Germany.
E-mail address: michael.hoffmann@med.ovgu.de (M.B. Hoffmann).
[1] Shared senior authorships.

https://doi.org/10.1016/j.nicl.2019.102055
Received 16 May 2019; Received in revised form 14 October 2019; Accepted 22 October 2019
Available online 01 November 2019

Moreover, this is particularly relevant in areas with crossing fibers, which may affect as much as 90% of the brain volume (Jeurissen et al., 2013), making it an important challenge for dMRI. In order to address this challenge new models were developed, such as Q-Ball imaging (Tuch, 2004), Diffusion Spectrum Imaging [DSI; (Wedeen et al., 2005)] or Constrained Spherical Deconvolution [CSD; Tournier et al., 2007; Descoteaux et al., 2006]. Those and other emerging approaches, however, require a sound testing model.

The optic chiasm reflects the complex microstructure of other brain structures and has the decisive advantage that (i) the ratio of crossing and non-crossing nerve fibers is a well-known ground truth and that (ii) human diseases are known, where this ratio is significantly altered. Based on previous work (Kupfer et al., 1967), we have a clear understanding that in the neurotypical case 53% of nerve fibers in the optic chiasm travel across the optic chiasm to the contralateral lateral geniculate nucleus (LGN), while 47% project to the ipsilateral LGN. The optic chiasm was investigated in several studies evaluating the accuracy of dMRI, such as the qualitative evaluation of tracking algorithms (Staempfli et al., 2007) or the quantification of fiber crossing strength in ex-vivo chiasms (Roebroeck et al., 2008). While both studies were successful in capturing qualitative features of the optic chiasm, neither provided an accurate quantitative estimation of crossing strength that was in agreement with expected values; Staempfli et al. (2007) performed qualitative analyses only and Roebroeck et al. (2008) estimated only up to 5% of nerve fibers to cross to the contralateral hemisphere.

The optic chiasm as a test-bed for differentiating crossing and non-crossing fibers can be extended further by the inclusion of known neuropathies affecting the human optic chiasm that reveal clear abnormalities. The most frequent of these rare conditions is albinism, which is associated with an enhanced crossing of the optic nerve fibers (Guillery 1986; Morland et al., 2002; von dem Hagen et al., 2005). Here the line of decussation that separates the retinal ganglion cells with a crossed projection from those with an uncrossed projection and which is normally aligned with the fovea, is shifted by on average 8° into the temporal retina (Hoffmann et al., 2005; von dem Hagen et al., 2007; von dem Hagen et al., 2008). As a result, the crossing of the optic nerves is enhanced (Hoffmann and Dumoulin, 2015). Recently, the first study to report group differences in chiasm tractography between albinism and controls was published (Ather et al., 2019). It used the DT model and demonstrated that dMRI can be used to identify, at the group level, differences in chiasmal connectivity between albinism and controls.

The dMRI approach can be extended beyond the DT model (Basser et al., 1994), by incorporating an additional Constrained Spherical Deconvolution model [CSD; Tournier et al., 2007], as well as the state-of-the-art tractography evaluation: Linear Fascicle Evaluation [LiFE; Pestilli et al., 2014b; Caiafa and Pestilli, 2017], Convex Optimization Modeling for Microstructure Informed Tractography [COMMIT; Daducci et al., 2013, 2015], and Spherical-deconvolution Informed Filtering of Tractograms [SIFT2; Smith et al., 2015]. In the present study, we compared the efficacy of these methods in identifying and quantifying optic nerve fiber misrouting at the optic chiasm in albinism and its relation to fMRI-based estimates of misrouting extent.

2. Methods

2.1. Participants

Nine participants with diagnosed albinism (5 females) and eight control subjects (6 females) were recruited for the study. The controls had no neurological or ophthalmological history, normal decimal visual acuity [≥1.0, Freiburg Visual Acuity Test (Bach, 1996)] and normal stereo vision (Lang and Lang 1988; Donzis et al., 1983). Each participant was instructed about the purpose of the study and the methods involved and gave written informed study participation and data sharing consents. The study was approved by the Ethics Committee of the Otto-von-Guericke University Magdeburg, Magdeburg, Germany.

2.2. Data acquisition

All MRI data was acquired with a Siemens MAGNETOM Prisma 3 Tesla scanner with *syngo* MR D13D software and a 64-channel head coil. Diffusion and functional data was acquired in separate scanning sessions. During both sessions additional T1-weighted images were acquired.

2.2.1. T1-weighted data acquisition

T1-weighted images, obtained during both dMRI and fMRI scanning sessions, were collected in sagittal orientation using a 3D-MPRAGE sequence resolution [$0.9 \times 0.9 \times 0.9\,mm^3$, FoV 230×230 mm, TR 2600 ms, TE 4.46 ms, TI 1100 ms, flip angle 7°, image matrix: $256 \times 256 \times 176$, acquisition time 11 min 6 s; Mugler and Brookeman 1990].

2.2.2. dMRI data acquisition

The dMRI acquisition protocol was initiated with a localizer scan, followed by a T1-weighted MPRAGE scan and two diffusion-weighted scans [one with anterior-posterior ($A > > P$) and the other with posterior-anterior ($P > > A$) phase-encoding direction]. All data was collected during a single continuous scanning session. dMRI images were acquired with Echo-Planar Imaging (EPI) [b-value 1600 s/mm^2, resolution $1.5 \times 1.5 \times 1.5\,mm^3$, anterior to posterior ($A > > P$) phase-encoding direction, FoV 220×220 mm, TR 9400 ms, TE 64.0 ms, acquisition time 22 min and 24 s]. The b-value was chosen with regard to the reported range of b-values optimal for resolving two-way crossing [for single shell acquisition: 1500–2500 s/mm^2 (Sotiropoulos et al., 2013)]. Each scan was performed with 128 gradient directions, therefore the obtained diffusion-weighted data could be described as High Angular Resolution Diffusion Imaging [HARDI; Tuch et al., 2002] data. The high number of gradient directions, while excessive for angular contrast allowed by b-value of 1600s/mm^2, enhanced the effective signal-to-noise-ratio (SNR) and thus supported residual bootstrapping. This is of importance for diffusion-MRI of the optic chiasm with its reduced SNR. The gradient scheme, initially designed for 3 shell acquisition, was generated using Caruyer's tool for q-space sampling (Caruyer et al., 2013). Due to the acquisition time constraints, however, we limited the set of directions to single shell only. Diffusion-weighted volumes were evenly intersected by 10 non-diffusion weighted volumes for the purpose of motion correction. The second diffusion-weighted series was acquired with a reversed phase-encoding direction relative to the previous scan, i.e., posterior to anterior ($P > > A$). Apart from that, all scan parameters were identical to those corresponding to the preceding acquisition. The acquisition of two diffusion-weighted series with opposite phase-encoding directions enhanced the correction of geometrically induced distortions (Andersson et al., 2003). Furthermore, the additional scans provided a boost of the effective SNR in the dMRI data.

2.2.3. fMRI data acquisition

Functional T2*-weighted images were acquired with EPI [resolution $2.5 \times 2.5 \times 2.5\,mm^3$; 54 axial slices covering the whole brain, FoV 210×210 mm, TR 1500 ms, TE 30.0 ms, flip angle 70°] during the course of a different study (Ahmadi et al., 2019), where methods are detailed. Briefly, the fMRI scanning session consisted of 6 functional scans, 168 time-frames each, resulting in a scan length of 252 s. The dominant eye of the albinotic participants was stimulated with moving bars that appeared within a circular aperture of 9.5° radius covering either the left or the right visual hemifields (three repetitions per hemifield stimulation). All data was acquired in a single continuous scanning session.

2.3. Data analysis

2.3.1. dMRI data analysis

2.3.1.1. dMRI data preprocessing. The data was preprocessed using a combination of software toolboxes: MRtrix 3.0 (http://www.mrtrix.org/), FMRIB's FSL 5.0.9 (https://fsl.fmrib.ox.ac.uk/fsl/fslwiki), FreeSurfer 6.0.0 (https://surfer.nmr.mgh.harvard.edu/), ANTS 2.1.0 (http://stnava.github.io/ANTs/) and MrDiffusion (https://github.com/vistalab/vistasoft/tree/master/mrDiffusion). The preprocessing of the dMRI data from DICOM involved converting it to .mif format (compatible with MRtrix) [mrconvert command], denoising of the dMRI data [dwidenoise command; Veraart et al., 2016a, 2016b], removal of Gibbs ringing in the dMRI data [dwidegibbs command; Kellner et al., 2015], estimation of the susceptibility induced field in the dMRI data [topup command; Andersson et al., 2003] using FSL (Smith et al., 2004), correction for geometry-induced, eddy current and motion distortions in the dMRI data [eddy command; Andersson and Sotiropoulos, 2016; Andersson and Sotiropoulos, 2016], and correction for the bias field (low frequency intensity inhomogeneities caused by uneven absorption of RF power across scanned tissue) in the dMRI data [ANTS, N4 algorithm; Tustison et al., 2010]. Finally, the dMRI data was coregistered to the T1-weighted images aligned to the Anterior Commissure - Posterior Commissure (AC-PC) space (mrAnatAverageAcpcNifti command from https://github.com/vistasoft/vistalab). Notably, this step also required the application of an exact transformation to the gradient table, since the gradient vectors were defined in the space of the dMRI data. The T1-weighted image was segmented into white, grey and subcortical grey matter and cerebrospinal fluid using FSL [FIRST command; Patenaude et al., 2011]. The white matter masks were additionally manually corrected in the region of the optic chiasm using the T1-weighted images (Fig 1A, left and middle image).

2.3.1.2. dMRI data modeling and tractography. Two distinct diffusion signal models were applied to the dMRI data - Diffusion Tensor [DT; Basser et al., 1994] and Constrained Spherical Deconvolution [CSD; Tournier et al., 2007; Descoteaux et al., 2011]. The DT model was selected in order to compare our results with previous studies that used this model alone (Roebroeck et al., 2008; Ather et al., 2019). Due to the limited performance of the DT model for populations of crossing fibers, an additional model, CSD, was also tested. The rationale behind this choice was to investigate whether the results can be improved by using a model that is more sensitive to crossing fiber populations and at the same time benefits from the high angular resolution of collected dMRI data. The modeling for DT was performed with MRtrix tool tckgen (Tensor_Prob algorithm), where dMRI data in each voxel for each streamline was residually bootstrapped, prior to DT fitting (Jones, 2008), such that tracking along the principal eigenvectors of tensors was probabilistic. For the purpose of CSD modeling, an estimation of a response from voxels containing only single fiber population (single fiber response, SFR) was acquired using Tournier's approach [dwi2response tool with -tournier option (Tournier et al., 2013)] for a maximum harmonic order (L_{max}) of 6. The fibre orientation distribution functions [fODFs; Jeurissen et al., 2014] were obtained for 3 different maximum harmonic orders $L_{max} = 6$, 8 and 10 (command dwi2fod using msmt_csd algorithm, as its hard constraints prevents the estimation of negative peaks).

For the purpose of tracking for both DT and CSD, four regions of interest (ROIs) were manually drawn on T1 images for each individual data set - two covering intersections of left and right optic nerves and two covering intersections of left and right optic tracts. ROIs were placed to be as close to the optic chiasm as possible without intersecting it (Fig 1A, right image). ROI widths and heights (in coronal view) had the minimal values required to fully cover the optic nerves or tracts, and each of the ROIs was 3 voxels (4.5 mm) thick to ensure proper termination of streamlines during tractography. In total there were four pairs of ROIs connecting optic nerves and optic tracts. For each model, tracking was performed between 2 ROIs, one of two optic-nerve ROIs and one of the two optic tract ROIs (Fig 1B), such that the created streamline groups could be either classified as crossing or non-crossing. For each pair of ROIs the streamlines were generated twice, with a switched definition of seed and target ROI, and merged into a single group of streamlines, such that the tracking results were not biased towards the direction of tracking. The tracking was limited to previously obtained and manually corrected white matter masks [following Anatomically-Constrained Tractography framework; Smith et al., 2012]. In addition, to reduce a potential bias in tractography caused by the specific choice of tracking parameters, Ensemble Tractography (Takemura et al., 2016) was used for all analyses. Accordingly, the tractography was performed multiple times, with each run using a different set of parameters. The modified parameters were, specifically: fractional anisotropy threshold (FA_{thresh}) and maximum curvature angle between consecutive tracking steps ($Curv_{max}$). In case of CSD this list was extended by the maximal harmonics order (L_{max}) of the fitted fODFs. Notably, the CSD used the SFR obtained for only a single $L_{max} = 6$. The values of the parameters applied are summarized in Table 1.

For each subject, for a given combination of parameters the tractography was performed for the 4 distinct seed-target ROI pairs, and for each pair of ROIs it was performed twice (reversal of seed-target definitions), with 139 000 seeds (random locations within the seed ROI, which served as starting points for tracking) and 1000 tracking attempts per seed. This resulted in a total of 6.672×10^9 tracking attempts per subject for the DT-based analysis and 20.016×10^9 attempts for the CSD-based analysis. The DT-based tracking used the Tensor_Prob algorithm (Jones, 2008), the CSD-based was performed with the iFOD2 algorithm (Tournier et al., 2010).

The tracking with a fixed number of attempts resulted in unevenly populated streamline groups, where the count depended on the overall success ratio of tracking for (Smith et al., 2012) given set of parameters and ROIs. The tractograms were therefore biased toward the underlying structural connectivity, which allowed them to be used for the estimation of crossing strength. Furthermore, the resulting tractograms can be used as an input to filtering, where the input streamlines are modeled forward in order to explain the measured diffusion signal. This, in turn, allows for the estimation of the contribution of each generated streamline to the original signal, thus addressing the stochasticity of tracking. It is of interest to investigate how well filtering performs, if the initial tractogram does not accurately represent the underlying microstructure, i.e., when it contains high-levels of noise. In order to answer this question, a second set of tractograms was created, where all the parameters were identical with the previous tractography, except for the restriction to a fixed number of streamlines per combination of groups and parameters. Precisely, the generated tractograms, further referred to as “streamline number targeted” (SNT) tractograms, were restricted to the generation of 139 streamlines or reaching 139 000 seeds with 1000 attempts per seed, with the latter condition preventing excessively long computations in cases of very low success ratio of tractography.

2.3.1.3. Tractography filtering. To further investigate the robustness of the results on intra-study level, tractograms, both normally generated and SNT tractograms, were filtered with 4 separate algorithms: (1) Linear Fascicle Evaluation [LiFE; Pestilli et al., 2014b; Caiafa and Pestilli 2017; Takemura et al., 2016], (2) Convex Optimization Modeling for Microstructure Informed Tractography [COMMIT-SZB; Daducci et al., 2013, 2015)] using the Stick-Zeppelin-Ball model, (3) COMMIT using the Stick-Ball model [COMMIT-SB; Daducci et al., 2015, 2013], and (4) Spherical-deconvolution Informed Filtering of Tractograms [SIFT2; Smith et al., 2015]:

LiFE (Pestilli et al., 2014b; Caiafa and Pestilli, 2017; Takemura et al., 2016; Avesani et al., 2019). LiFE evaluates the

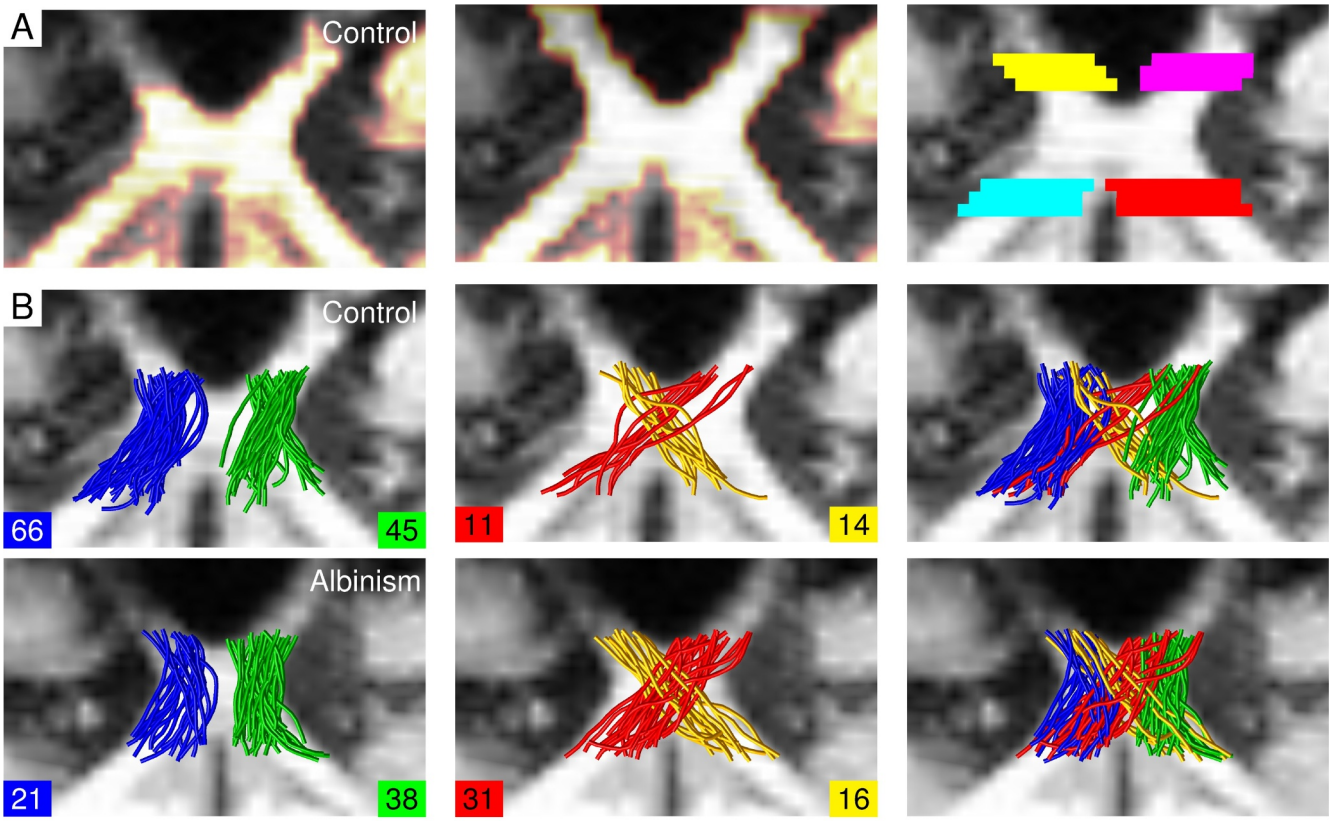

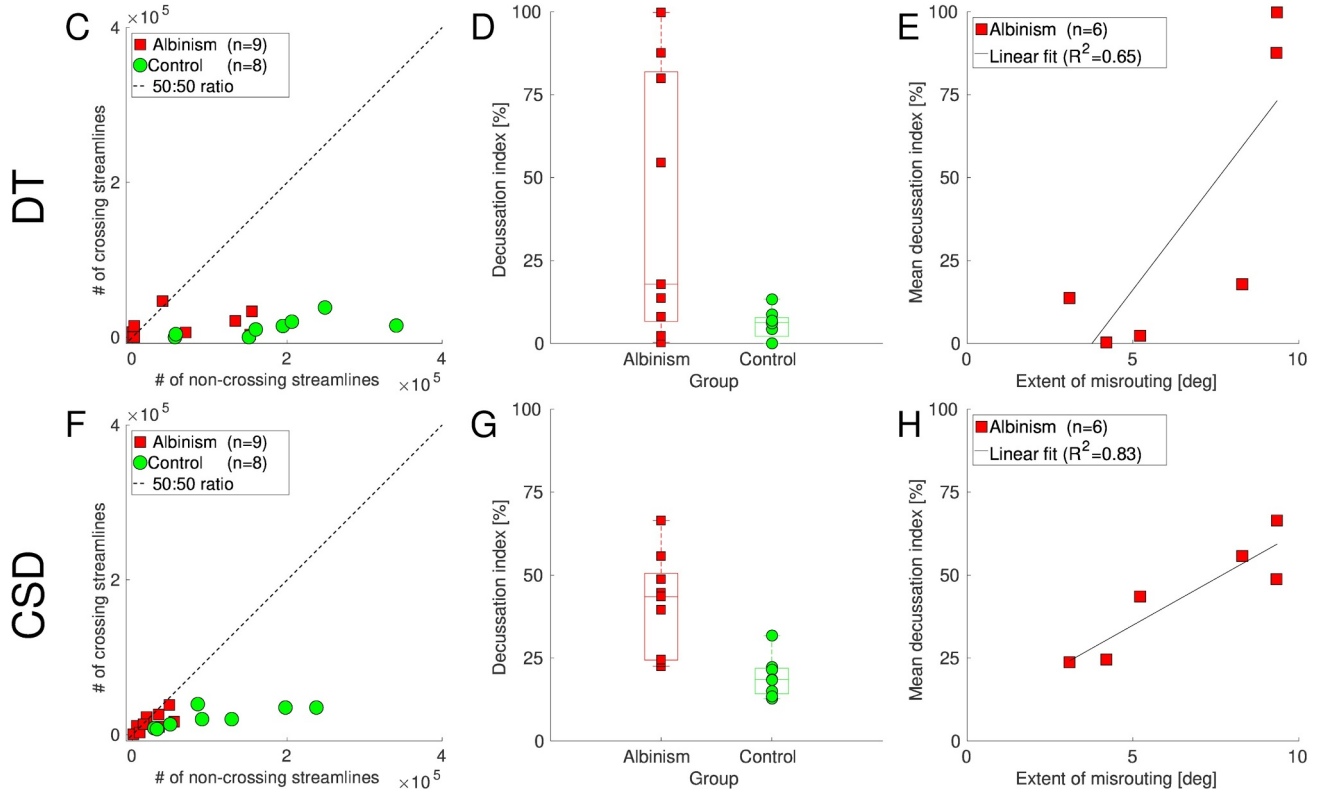

(caption on next page)

Fig. 1. Optic chiasm – white matter mask, ROI definitions, example of tractography and quantitative results. A. T1-weighted image of a representative control subject overlaid with the automatically generated white matter mask (left column), manually corrected mask (middle column) and ROIs covering the intersections of the ends of optic nerves and the beginnings of the optic tracts (right column). B. Representative subsets of tractograms (0.125% of the total number of streamlines) created using the CSD signal model for a control (top row) and a participant with albinism (bottom row), i.e., streamlines projecting through the chiasm ipsilaterally (non-crossing; left column), contralaterally (crossing; middle column), and a combination of both streamlines (right column). C. Numbers of crossing vs non-crossing streamlines calculated from tractograms based on the DT model. D. Numbers of crossing and non-crossing streamlines calculated from tractograms based the on DT model expressed as I_D. E. Correlation between the estimates of the extent of crossing obtained with dMRI using the DT model and fMRI-based pRF mapping. F. Numbers of crossing streamlines plotted vs non-crossing streamlines calculated from tractograms based on the CSD model. G. Numbers of crossing and non-crossing streamlines calculated from tractograms based on the CSD model expressed with I_D. H. Correlation between the estimates of crossing obtained with dMRI, using the CSD model, and fMRI-based pRF mapping.

Table 1
Tractography parameters. Sets of parameters used in generating DT- (left column) and CSD-based (right column) tractograms. The rows correspond to different parameters, from top to bottom, respectively, the cut-off FA threshold (FA_{thresh}), maximum angle between consecutive tracking steps ($Curv_{max}$), maximal harmonic order of SFR (SFR L_{max}) and fODF (fODFs L_{max}).

	DT	CSD
FA_{thresh}	0.04, 0.08	0.04, 0.08
$Curv_{max}$ [°]	30, 45, 60	30, 45, 60
SFRs L_{max}	–	6
fODFs L_{max}	–	6, 8, 10

individual streamline paths by scoring their contribution (expressed as weights assigned to each individual streamline) to predict the measured diffusion signal across the brain white matter voxels; good streamlines positively contribute to predicting the dMRI signal (non-zero weights, higher value represents higher contribution), poor streamline paths do not contribute positively to predicting the measured dMRI signal (zero weights).

COMMIT-SZB (Daducci et al., 2013, 2015) using a Stick-Zeppelin-Ball model. The COMMIT framework follows a similar rationale as LiFE (as well outputting weights for the whole tractogram), extending the range of model parameters that can be used for predicting the dMRI signal (i.e., it adds additional parameters in order to model both intra- and extra-axonal cellular contributions to the dMRI signal prediction). The Stick-Zeppelin-Ball model, as in (Panagiotaki et al., 2012), describes one anisotropic intra-axonal (here implemented with a tensor with axial diffusivity equal to 1.7×10^{-3} mm^2/s and null radial diffusivity), one anisotropic extra-axonal (implemented with axial diffusivity equal to 1.7×10^{-3} mm^2/s and radial diffusivity calculated as such, that according to tortuosity model the intra-cellular volume fractions are equal to 0.7) and one isotropic extra-axonal (implemented with tensors with isotropic diffusivities equal to 1.7×10^{-3} and 3.0×10^{-3} mm^2/s) compartment contributing to modeling and predicting the dMRI signal for each segment of analyzed streamlines. This model was chosen due to its overall good previous performance, as demonstrated in Panagiotaki et al. (2012).

COMMIT-SB (Daducci et al., 2013, 2015) using a Stick-Ball model. Although simpler, this multi-compartment model is a more fitting match for our acquired single shell dMRI data. While the single shell data allows for the discrimination between anisotropic and isotropic contributions to the signal, it severely limits the distinction of extra- and intra-axonal signals. Therefore a model using one anisotropic intra-axonal compartment and one isotropic extra-axonal compartment is expected to be optimal for our data and was implemented using the corresponding components from the COMMIT-SZB approach.

SIFT2 (Smith et al., 2015). SIFT2 filters a tractography solution by assigning weights to the streamlines in order to optimize a model that matches the densities generated from the weighted streamline counts with the size of the modelled fiber Orientation Distribution Functions (fODFs) estimated from the signal within the individual voxels (Smith et al., 2015).

While the filtering used only a subset of whole-brain tractograms and a subset of voxels from diffusion-weighted images, the information was complete, i.e., tractograms covered all anatomically connecting regions and all white matter voxels within the region we analyzed. This feature of input tractograms allows for the application of filtering – if this criterion is not fulfilled, filtering leads to erroneous results, i.e. is not applicable. It should be noted that two of the methods, i.e. LiFE and SIFT2, were applied with their default parameters, while in the case of COMMIT a wider range of parameters was tested. This, in combination with the established knowledge, demonstrates that the better the model fit to the data, the better the evaluation (Pestilli et al., 2014b; Takemura et al., 2016; Rokem et al., 2015, 2017).

2.3.2. fMRI data analysis

The fMRI data analysis is detailed in (Ahmadi et al., 2019). Briefly, the functional data was preprocessed using FreeSurfer 6.0.0, FMRIB's FSL 5.0.9, Vistasoft (https://github.com/vistalab/vistasoft) and a toolbox developed by Kendrick Kay (https://github.com/kendrickkay/alignvolumedata). The T1-weighted images were automatically segmented into white matter volume and cortical surface using FreeSurfer. The fMRI data was corrected for motion with FSL, averaged across runs for each participant and subsequently aligned to the T1-weighted image with Vistasoft and Kendrick Kay's alignment toolbox. The cortical surface reconstruction at the white and grey matter boundary as well as rendering of the smoothed 3D mesh (Wandell et al., 2000) was performed with Vistasoft.

The estimation of the pRF properties, the delineation of the visual areas, and the visualization on the smoothed mesh surface were performed using Vistasoft, as described in (Ahmadi et al., 2019a, b). Polar angle and eccentricity maps were extracted and the misrouting extent was measured by calculating the mean eccentricity value [in degrees of visual angle] for the most eccentric abnormal representation in a ROI drawn at the fundus of the calcarine sulcus that coincided with the representation of the horizontal meridian. The maximal extent that could be determined was limited to the stimulus size of 9.5°. In accordance with the well-known variability of misrouting in albinism, particularly evident in cortical measures of the representation in albinism (Hoffmann et al., 2003, 2005), these values ranged between 3.0° and 9.3° (Ahmadi et al., 2019).

2.4. Quantitative and statistical analysis

The crossing strength was expressed using either the weights provided by tractogram filtering or, in the case of unfiltered tractograms, the number of the obtained streamlines (which is equivalent to the assumption that all weights are equal). For both metrics, the crossing strength was described by a pair of values - sums of streamlines/weights of streamlines that cross at the optic chiasm to the other brain hemisphere (crossing streamlines) or that remain on the same side (non-crossing streamlines). In order to reduce the dimensionality of the results, as well as to allow for cross-study comparison (Ather et al., 2019), the decussation index (I_D) was calculated:

$$I_D = \frac{\sum weights_{crossing}}{\sum weights_{crossing} + \sum weights_{non-crossing}}$$

where the $weights_{crossing}$ and $weights_{non\text{-}crossing}$ for each streamline were

Table 2
Results derived from original and filtered tractograms. The rows describe different filtering techniques. The columns describe separate estimates including the p-values derived from statistical testing of equality of the IDs for albinism and controls. Each column is divided into two sub-columns, corresponding to the two signal models, i.e., DT and CSD.

	mean I_D for albinism [%]		mean I_D for controls [%]		p-value for I_D		AUC		R^2	
	DT	*CSD*	DT	*CSD*	*DT*	*CSD*	*DT*	*CSD*	*DT*	*CSD*
Unfiltered	40.5 ± 40.1	41.1 ± 15.2	5.8 ± 4.4	19.2 ± 6.2	0.014	0.00009	0.61	0.75	0.65	0.83
LiFE	37.0 ± 33.4	42.3 ± 10.0	11.0 ± 7.1	35.9 ± 5.4	0.024	0.0635	0.60	0.74	0.52	0.51
COMMIT - SB	42.0 ± 27.2	41.3 ± 6.0	20.3 ± 8.4	28.6 ± 4.2	0.024	0.00008	0.56	0.94	0.34	0.32
COMMIT- SZB	46.3 ± 29.8	44.8 ± 8.4	22.5 ± 11.0	30.6 ± 5.0	0.025	0.0004	0.58	0.92	0.29	0.63
SIFT2	40.2 ± 35.3	39.1 ± 12.9	8.9 ± 4.5	20.5 ± 5.3	0.013	0.0009	0.61	0.94	0.64	0.79

either used according to the filtering results (for filtered tractograms) or set to 1 (for unfiltered tractograms).

The I_Ds obtained for each group (control and albinism), signal model (DT or CSD) and applied filtering model (none, LiFE, COMMIT-SB, COMMIT-SZB, and SIFT2) were tested for normality using the Kolmogorov–Smirnov test. As all the data samples were normally distributed, the equality of means was tested with one-tailed, two-sample t-tests at an alpha level of 5%. Additionally, for better comparability of our estimates, we calculated mean, median and standard deviation values of I_Ds.

The calculated I_Ds were subsequently entered into a Receiver Operating Characteristic (ROC) curve analysis, which returned the Area Under Curve (AUC) measure for a given combination of signal model (DT or CSD) and applied various filtering methods (none, LiFE, COMMIT-SB, COMMIT-SZB, and SIFT2). It should be noted that the estimated values were derived from the classification of the training data. As such, the obtained AUCs reflect the ability to separate already measured groups.

Finally, we tested whether the variability in the fMRI-based extent of misrouting was related to the estimates of misrouting derived from dMRI. This was tested by correlating the I_Ds derived from dMRI with the fMRI-based extent of misrouting. The results were expressed with the coefficient of determination R^2, which describes the proportion of variance in the dependent variable (dMRI-based I_D) explained by the independent (fMRI-based extent of misrouting). It should be noted that the fMRI-based eccentricity measures were available only for a subset of six albinotic participants.

3. Results

In order to compare different dMRI-based approaches to assess optic chiasm integrity, we assessed (i) non-validated DT-based tractograms, (ii) non-validated CSD-based tractograms, (iii) the impact of filtering techniques on the identification of chiasmal abnormalities at both the group and the individual level and (iv) its robustness to noise in the tractograms.

3.1. Efficacy of non-validated DT-based tractograms for the detection of chiasma abnormalities

In analogy to Ather et al. (2019) we quantified the crossing strength by comparing the streamline counts for crossing and non-crossing streamlines as depicted in Fig 1B and **C**. In order to compare different dMRI-based approaches to assess optic chiasm integrity, we further expressed the extent of crossing at the optic chiasm in the albinotic and the control group via I_D (Fig 1D) as detailed in Methods. In accordance with Ather et al., 2019, our results demonstrated a significant I_D difference between the albinism and the control group [$t = -2.43$; $p = 0.014$; median (mean ± SEM) I_D: 17.9% (40.5% % ± 40.1) and 6.4% (5.8% % ± 4.4), respectively]. A ROC analysis to assess the accuracy of the detection of chiasmatic abnormalities at an individual level, yielded an AUC of 0.61, i.e., short of that reported by Ather et al., 2019 (AUC = 0.73).

3.2. Comparison of non-validated CSD- and DT-based tractograms

The CSD-based approach also allowed for the detection of differences in the chiasm crossing at the group level [$t = -3.78$; $p = 0.0009$; median (mean ± SEM) decussation index 43.5% (41.1% % ± 15.2) and 18.5% (19.2% % ± 6.2)], between the albinism and the control group, respectively as depicted in (Fig 1F and G). Importantly, the ROC analysis yielded a higher AUC, i.e. 0.75, than the DT-based approach, which underlines a greater discriminative power at the individual level for CSD derived streamlines. Interestingly, I_Ds vary across the albinotic subjects, for both the CSD and for the DT model. We now tested whether this variability in I_D across albinotic subjects was related to the well-known variability of the extent of misrouting in albinism, which is particularly evident in the cortical measures of the representation abnormality in albinism (Hoffmann et al., 2003, 2005). For this purpose, we correlated the dMRI-derived I_D of six albinotic participants with the strength of their misrouting as determined from fMRI-based pRF mapping [see Methods]. There was a clearly significant positive correlation for the CSD model ($R^2 = 0.83$; $p = 0.012$; Fig 1H), while there was only a non-significant trend of a positive correlation for the DT model ($R^2 = 0.65$, $p = 0.052$; Fig 1E). This indicates a remarkable precision of the dMRI-based detection of misrouting in reflecting the extent of misrouting in albinism.

3.3. Relevance of tractography filtering

While the previous analyses were exclusively performed for unfiltered tractograms, we now assessed the effect of tractography filtering as detailed in Methods for the DT and the CSD modeling approaches. As for the above analyses, their outcome is quantified via the ROC-derived AUC values and the R^2 values for the correlation of ID and fMRI-based extents of misrouting (Table 2 and Supplementary Fig A.1).

3.3.1. DT-based approach

For each filtering technique the group differences in the mean ID values were detected. However, only for SIFT2 the actual p-value was lower than for the original unfiltered tractogram (0.013 versus 0.014, respectively) - all other techniques showed higher values. The original, non-filtered, tractogram also returned similar results to the filtered ones with regard to the AUC values (0.61, the highest values for filtering were obtained for SIFT2 and LiFE, 0.61 and 0.60, respectively) and to the R2 values (0.65 for non-filtered, with SIFT2 and LiFE returning 0.64 and 0.52, respectively, neither being significant). It should be noted, however, that the derived ID values were generally improved, i.e. closer to the known ground truth in comparison to their non-filtered ID counterparts (where estimates of crossing are lower; Table 2 and Supplementary Fig A.1).

3.3.2. CSD-based approach

For the CSD-based approaches, except for LiFE, all filtered techniques yielded significant group differences for ID and, including LiFE, higher IDs for both albinism and controls closer to the ground truth, compared to the unfiltered approaches. The good performance of

filtering was also reflected in the highly increased AUC values (with non-filtered tractograms yielding an AUC of 0.75, the COMMIT-SB, COMMIT-SZB and SIFT2 returned AUCs of 0.94, 0.92 and 0.94, respectively). Surprisingly, filtering did not improve the correlation between dMRI and fMRI. Out of 4 tested filtering techniques only SIFT2 returned a significant correlation (R2 = =0.79). The best results (highest R2 and AUC) were obtained for SIFT2, with COMMIT-SZB being the second best.

3.4. Robustness of tractography filtering

Given the remarkable similarity of the unfiltered tractograms and the SIFT2-filtered tractograms, it was tested whether applied filtering models are robust to noise in input tractograms. For this purpose, the filtering techniques were applied to SNT ("Streamline Number Targeted", see Methods) tractograms with forcibly equalized numbers of streamlines as detailed in Methods. This effectively caused for the unfiltered tractograms an overrepresentation of the crossing streamlines, especially in the control population (Supplementary Table C.1). The group mean I_Ds were not significantly different, neither for the DT- [median (mean ± SEM) I_D = =36.8% (46.9% % ± 33.3) and 34.7% (28.4% % ± 18.2), for albinism and controls respectively; $p = 0.093$] nor for the CSD-based approaches [median (mean ± SEM) decussation index 48.7% (44.2% % ± 7.9) and 48.3% (46.2% % ± 5.4), for albinism and controls respectively; $p = 0.726$]. Subsequent filtering and analysis of filtered SNT tractograms resulted in the following results for the DT- and CSD-based approaches (Supplementary Table C.1):

3.4.1. DT-based approach

Already prior to filtering there was a tendency to group differences in the initial mean I_D values, which turned significant for all filtered SNT tractograms. With regard to the AUC values, all filtering techniques returned increased AUC values with respect to the unfiltered tractogram. The filtering, however, did not improve the R^2 values, neither made it the correlation statistically significant.

3.4.2. CSD-based approach

The initial mean I_D values were much less distinguishable between groups than for the DT-based approach. This made the group differences after filtering more meaningful. In agreement with the above results (Suppl. Table C.1), LiFE failed to detect group differences ($p = 0.58$), but this also applied to the SIFT2 results ($p = 0.68$). SIFT2 also returned a lower AUC than without filtering. In contrast, for the COMMIT-SB and the COMMIT-SZB model the group I_D differences were significant (0.006 and 0.024, respectively), and the reported AUC values were higher than without filtering (0.83 and 0.78, respectively). All filtering methods failed to detect strong and significant correlations between dMRI and fMRI estimates.

4. Discussion

We used diffusion weighted imaging to identify decussation abnormalities at the optic chiasm and compared different tractography methods (DT and CSD) and filtering schemes (LiFE, COMMIT-SZ, COMMIT-SZB, and SIFT2). Even in the case of unfiltered tractograms we reported a significant difference of the decussation index (I_D) between albinism and controls, which was more pronounced for the CSD than for the DT model. This result is consistent with previous reports that CSD-based tracking can return valuable results that outperform DT-based methods (Pestilli et al., 2014). The ROC analyses for the CSD model suggested its potential as an aid for individualized diagnostics. This was further supported by the better linear correlation of the CSD-derived I_D values with the extent of misrouting estimated from fMRI. Further analyses for the tested models and filtering methods consistently confirmed that the CSD model yields better classification accuracies for all investigated approaches. We used two filtering methods with default parameters (LiFE and SIFT2), and a third one that varied in the parameters set to fit the diffusion kernel that optimally matches the dMRI data (COMMIT-SB and -SZB). We replicated previous results demonstrating that the choice of parameters matters (Takemura et al., 2016). We demonstrate that even a single implementation of an evaluation method (COMMIT in our case) can return very different results depending on the choice of parameter set and corresponding quality of fit to the data. Indeed, COMMIT-SB was comparable in performance to the default LiFE and SIFT2. Instead, COMMIT with a kernel model that returned a better fit to the diffusion signal (the -SZB kernel) improved results, with both increased evaluation performance and decreased NRMSE (Supplementary Fig. B.1.). These findings are consistent with established knowledge; the better the model fit to the data, the better the evaluation (Pestilli et al., 2014b; Takemura et al., 2016; Rokem et al., 2015, 2017).

4.1. Comparison of results for DT with the literature

Our results are in accordance with those reported by Ather et al. (2019) demonstrating that dMRI can detect structural abnormalities of the optic chiasm at a group level. Notably, the findings were reproduced despite several differences in the study design, e.g. acquisition protocols, preprocessing pipeline, implementation of the DT model, tracking algorithms and sample size, which indicates the robustness of the effect. However, the numerical values of mean I_D we obtained differ from those previously reported (Ather et al., 2019). While Ather et al. (2019) report mean I_D for albinism and controls of 42.0% % ± 18.7 and 27.8% % ± 17.5, respectively, we note that, while our estimates of crossing in albinism show similar values (40.5% ± 40.1), we underestimate crossing in the control group (5.8% ± 4.4). Our values for controls, however, correspond very well with those reported by Roebroeck et al. (2008). In their study, a ultra-high field (9.4 T) and sub-millimetre resolution (156 × 156 × 312 μm) dMRI analysis of 3 ex-vivo human chiasms using the DT model, they also reported values corresponding to $I_D \approx 5\%$. The discrepancy of the results across studies appears to be linked to different b-values – while Ather et al., 2019 used b-value of 1000 s/mm^2, Roebroeck et al. used b-value of 1584 s/mm^2, similar to our study (1600 s/mm^2). Generally speaking, lower b-values preserve more signal originating from extra-axonal compartments, which results in more isotropic tensors. This, in turn, eases tractography and results in the generation of a higher number of streamlines. Those differences would be expected to particularly impact on challenging conditions, such as the mixture of crossing and non-crossing streamlines in the chiasm of controls. Higher b-values, in turn, would severely impair the success ratio of tracking in such conditions, as observed here. More generally, it should be noted that all the estimates of I_D inferred from DT analyses of dMRI which were reported thus far (Roebroeck et al., 2008; Ather et al., 2019) heavily underestimate the actual ground truth ratio of crossing to non-crossing nerves in the optic chiasm (53:47, respectively) as reported by Kupfer et al. (1967). One of the causes of this is an intrinsic limitation of the DT model, as it assumes only one, dominant direction per voxel and as such is ill-defined for populations of crossing fibers. Consequently, the application of DT in those cases leads to the neglect of valid fibers and erroneous estimates of the primary direction (Wiegell et al., 2000).

4.2. Comparison of results between CSD and DT

Given the established limitations of DT for the crossed fibers as in the chiasm, we extended our study by incorporating a CSD model. This model is believed to be superior to DT in resolving crossing fibers and additionally benefits from the HARDI protocol we used for the acquisition of our data. Accordingly, we found that for non-filtered CSD-based tractograms the mean I_D values for albinism and control (41.1 ± 15.2 and 19.2 ± 6.3%, respectively) were higher and closer to the biological ground truth than those we reported for DT. This is further supported by the cross-modality validation with fMRI-estimated

misrouting [R^2_{CSD} vs R^2_{DT} : 0.83 (p = 0.012) and 0.65 (n.s., p = 0.052)] and by the ROC-based classification (AUC_{CSD} vs AUC_{DT}: 0.75 and 0.61). These findings are in good agreement with theoretical expectations and provide strong support for using models directly incorporating crossed fiber populations in future studies on chiasmal connectivity (Pestilli et al., 2014; Tournier et al., 2008; Wedeen et al., 2008; Tournier et al., 2012).

4.3. Choice of model parameters and optimal filtering results

We tested only a few filtering methods, not exhaustively as this was not a primary goal of our study. Specifically, two methods were used with default parameters, without optimizing the parameters for the properties of the diffusion data at hand, these methods were LiFE and SIFT2. The COMMIT method was used with two types of parameters (we changed the kernel used for predicting the diffusion, see SZB and SB results). Our results show that the non-optimized methods can return a higher NRMSE in fitting the data, optimized methods instead can fit the data better. As a result of the better fit to the data, filtering improved and allowed higher detection of group differences, i.e. higher AUC-values as compared to the unfiltered tractograms. Even though a full-comparison of all the filtering methods goes beyond the scope of the current work, the results demonstrate that no filtering method is good or bad per-se. Instead careful attention must be taken to assure that the method used in a study achieves a good fit to the diffusion signal, before interpreting and evaluating the results.

4.4. Limitations

The study is mainly limited by the challenges posed by the diffusion-weighted imaging of the optic chiasm. Specifically, the small size of the optic chiasm and its location in a highly heterogeneous brain region impact on the quality of dMRI images and subsequent analysis stages, such as tractography. While the design of our acquisition protocol and preprocessing pipeline allowed us to address those challenges, we note that this study aspect may be further improved in the future with emerging methods (Bastiani et al., 2019). In the present work, we provide proof-of-principle results for the potential to identify crossing abnormalities in the chiasm. Our study was limited in the number of participants, and it is possible that future studies with higher participant numbers will allow for refined ROC-analyses and thus suggest diagnostic criteria with higher classification accuracy. For example, in our case, doubling the sample size, would have allowed us to divide the data into a “training” and “test” set to cross-validate the ROC analysis (Pestilli et al., 2014; Rokem et al., 2015; Pestilli 2015). Unfortunately, no datasets of similar quality and scope are currently openly available to perform additional analyses. Such lack of data speaks to the importance of the promotion of open sharing of data and algorithms to advance methods development and scientific understanding (Avesani et al., 2019; Gorgolewski et al., 2017, 2016).

4.5. Practical relevance

A key objective of our study was to explore the efficacy of dMRI-based assessment of chiasm integrity and hence its potential as a diagnostic. This is particularly relevant as the identification of chiasmatic abnormalities is a key for the correct diagnosis, especially in phenotypes of albinism with mild pigmentation defects (Montoliu et al., 2014). Functional tests established for this purpose (Apkarian et al., 1983; von dem Hagen et al., 2008) have the disadvantage that they require visual stimulation which in turn relies on the cooperation of the often severely visually impaired participants. While procedures based on purely anatomical MRI procedures do not allow for an individualized identification (Schmitz et al., 2003), our results indicate that dMRI combined with CSD modeling might be able to fill this gap. In fact, as suggested above, testing a greater sample of participants is now required. Although the protocol used in the study is clinically suboptimal due to its length (dMRI and fMRI protocols being, respectively, ~45 and ~25 min long), the use of simultaneous multi-slice EPI and limiting acquisition of opposing phase-encoding direction to b0 vol only will shorten dMRI protocol by factor 3–4, i.e., to 10–15 min. The full scanning session, including localizer and acquisition of T1-weighted image, would in that case take no longer than an hour.

5. Conclusions

We investigated the application of state-of-the-art dMRI to detect optic chiasm abnormalities and report CSD-based models to identify abnormalities with high accuracy (AUC = =0.75) and to correlate well with functional (fMRI) measures of the optic nerve misrouting (R^2 = =0.83). The classification accuracy (AUC = =0.92), as well as veridicality of estimates of crossing strength can be further improved by the application of filtering techniques with optimized parameters (in our case COMMIT-SZB). dMRI combined with CSD-modeling and filtering techniques therefore appear to offer promising approaches for the individualized identification of chiasmatic abnormalities. Moreover, our investigations highlight the great value of the optic chiasm as a test-bed for dMRI methods-optimization. In order to further support these activities, we are in the process of making the data set publicly available for the benefit of the general neuroimaging community.

Declaration of Competing Interest

None.

Acknowledgments

The authors thank the study participants. This work was supported by European Union's Horizon 2020 research and innovation programme under the Marie Sklodowska-Curie grant agreement (No. 641805) and by the German Research Foundation (DFG, HO 2002 10-3) to M.B.H. F.P. was supported by NSF IIS-1636893, NSF BCS-1734853, NSF AOC 1916518, NSF IIS 1912270, NIH NIBIB 1R01EB029272-01 a Microsoft Investigator Fellowship, Microsoft Azure, Google Cloud Platform, and the Indiana University Areas of Emergent Research initiative “Learning: Brains, Machines, Children.”

Supplementary materials

Supplementary material associated with this article can be found, in the online version, at doi:10.1016/j.nicl.2019.102055.

References

Ahmadi, K., Fracasso, A., van Dijk, J.A., Kruijt, C., van Genderen, M., Genderen, Mv., Dumoulin, S.O., Hoffmann, M.B., 2019. Altered organization of the visual cortex in FHONDA syndrome. Neuroimage 190 (April), 224–231.

Ahmadi, K., Herbik, A., Wagner, M., Kanowski, M., Thieme, H., Hoffmann, M.B., 2019b. Population receptive field and connectivity properties of the early visual cortex in human albinism. Neuroimage 202 (August), 116105.

Alexander, D.C., Barker, G.J., Arridge, S.R., 2002. Detection and modeling of non-gaussian apparent diffusion coefficient profiles in human brain data. Magnetic Resonance in Medicine 48 (2), 331–340.

Andersson, J.L.R., Skare, S., Ashburner, J., 2003. How to correct susceptibility distortions in spin-echo echo-planar images: application to diffusion tensor imaging. Neuroimage 20 (2), 870–888.

Andersson, J.L.R., Sotiropoulos, S.N., 2016. An integrated approach to correction for off-Resonance effects and subject movement in diffusion MR imaging. Neuroimage 125 (January), 1063–1078.

Apkarian, P., Reits, D., Spekreijse, H., Van Dorp, D., 1983. A decisive electrophysiological test for human Albinism. Electroencephalogr Clin. Neurophysiol. 55 (5), 513–531.

Ather, S., Proudlock, F.A., Welton, T., Morgan, P.S., Sheth, V., Gottlob, I., Dineen, R.A., 2019. “Aberrant visual pathway development in albinism: from retina to cortex. Hum. Brain Mapp. 40 (3), 777–788.

Avesani, P., McPherson, B., Hayashi, S., Cesar, F., Robert Henschel, C., Garyfallidis, E., Kitchell, L., et al., 2019. The open diffusion data derivatives, brain data upcycling via integrated publishing of derivatives and reproducible open cloud services. Sci Data 6

(1), 69.
Bach, M., 1996. The freiburg visual acuity test–automatic measurement of visual acuity. Optometry Vis. Sci. 73 (1), 49–53.
Basser, P.J., Mattiello, J., LeBihan, D., 1994. MR diffusion tensor spectroscopy and imaging. Biophys. J. 66 (1), 259–267.
Bastiani, M., Andersson, J.L.R., Cordero-Grande, L., Murgasova, M., Hutter, J., Price, A.N., Makropoulos, A., et al., 2019. Automated processing pipeline for neonatal diffusion mri in the developing human connectome project. Neuroimage 185 (January), 750–763.
Caiafa, C.F., Pestilli, F., 2017. Multidimensional encoding of brain connectomes. Sci. Rep. 7, 11491. https://doi.org/10.1038/s41598-017-09250-w.
Caruyer, E., Lenglet, C., Sapiro, G., Deriche, R., 2013. Design of multishell sampling schemes with uniform coverage in diffusion MRI. Magnetic Resonance in Medicine 69 (6), 1534–1540.
Daducci, A., Palù, A.D., Lemkaddem, A., Thiran, J.-P., 2015. COMMIT: convex optimization modeling for microstructure informed tractography. IEEE Trans. Med. Imaging 34 (1), 246–257.
Daducci, A., Palu, A.D., Lemkaddem, A., Thiran, J.-P., 2013. A convex optimization framework for global tractography. In: 2013 IEEE 10th International Symposium on Biomedical Imaging, . https://doi.org/10.1109/isbi.2013.6556527.
Descoteaux, M., Angelino, E., Fitzgibbons, S., Deriche, R., 2006. Apparent diffusion coefficients from high angular resolution diffusion imaging: estimation and applications. Magnetic Resonance in Medicine 56 (2), 395–410.
Descoteaux, M., Deriche, R., Bihan, D.L., Mangin, J.-F., Poupon, C., 2011. Multiple Q-Shell diffusion propagator imaging. Med. Image Anal. 15 (4), 603–621.
Donzis, P.B., Rappazzo, J.A., Burde, R.M., Gordon, M., 1983. Effect of binocular variations of snellen's visual acuity on titmus stereoacuity. Arch. Ophthalmol. 101 (6), 930–932.
Gorgolewski, K.J., Alfaro-Almagro, F., Auer, T., Bellec, P., Capotă, M., Mallar Chakravarty, M., Churchill, N.W., et al., 2017. BIDS apps: improving ease of use, accessibility, and reproducibility of neuroimaging data analysis methods. PLoS Comput. Biol. 13 (3), e1005209.
Gorgolewski, K.J., Auer, T., Calhoun, V.D., Cameron Craddock, R., Das, S., Duff, E.P., Flandin, G., et al., 2016. The brain imaging data structure, a format for organizing and describing outputs of neuroimaging experiments. Sci. Data 3 (June), 160044.
Guillery, R.W., 1986. Neural abnormalities of albinos. Trends Neurosci. https://doi.org/10.1016/0166-2236(86)90115-3.
Hoffmann, M.B., Dumoulin, S.O., 2015. Congenital visual pathway abnormalities: a window onto cortical stability and plasticity. Trends Neurosci. 38 (1), 55–65.
Hoffmann, M.B., Lorenz, B., Morland, A.B., Schmidtborn, L.C., 2005. Misrouting of the optic nerves in albinism: estimation of the extent with visual evoked potentials. Invest. Ophthalmol. Vis. Sci. 46 (10), 3892–3898.
Hoffmann, M.B., Tolhurst, D.J., Moore, A.T., Morland, A.B., 2003. Organization of the visual cortex in human albinism. The Journal of Neuroscience: The Official Journal of the Society for Neuroscience 23 (26), 8921–8930.
Jeurissen, B., Leemans, A., Tournier, J.-D., Jones, D.K., Sijbers, J., 2013. Investigating the prevalence of complex fiber configurations in white matter tissue with diffusion magnetic resonance imaging. Hum. Brain Mapp 34 (11), 2747–2766.
Jeurissen, B., Tournier, J.-D., Dhollander, T., Connelly, A., Sijbers, J., 2014. Multi-tissue constrained spherical deconvolution for improved analysis of multi-shell diffusion mri data. Neuroimage 103 (December), 411–426.
Jones, D.K., 2008. Tractography gone wild: probabilistic fibre tracking using the wild bootstrap with diffusion tensor MRI. IEEE Trans Med Imaging 27 (9), 1268–1274.
Jones, D.K., Knösche, T.R., Turner, R., 2013. White matter integrity, fiber count, and other fallacies: the do's and don'ts of diffusion MRI. Neuroimage 73 (June), 239–254.
Kellner, E., Dhital, B., Kiselev, V.G., Reisert, M., 2015. Gibbs-Ringing artifact removal based on local subvoxel-shifts. Magnetic Resonance in Medicine 76 (5), 1574–1581.
Kupfer, C., Chumbley, L., Downer, J.C., 1967. Quantitative histology of optic nerve, optic tract and lateral geniculate nucleus of man. J. Anat. 101 (Pt 3), 393–401.
Lang, J.I., Lang, T.J., 1988. Eye screening with the lang stereotest. Am. Orthopt. J. 38 (1), 48–50.
Montoliu, L., Grønskov, K., Wei, A.-H., Martínez-García, M., Fernández, A., Arveiler, B., Morice-Picard, F., et al., 2014. Increasing the complexity: new genes and new types of albinism. Pigment Cell Melanoma Res. 27 (1), 11–18.
Morland, A.B., Hoffmann, M.B., Neveu, M., Holder, G.E., 2002. Abnormal visual projection in a human albino studied with functional magnetic resonance imaging and visual evoked potentials. J. Neurol. Neurosurg. Psychiatr. 72 (4), 523–526.
Mugler 3rd, J.P., Brookeman, J.R., 1990. Three-Dimensional magnetization-prepared rapid gradient-echo imaging (3D MP RAGE). Magnetic Resonance in Medicine 15 (1), 152–157.
Oouchi, H., Yamada, K., Sakai, K., Kizu, O., Kubota, T., Ito, H., Nishimura, T., 2007. Diffusion anisotropy measurement of brain white matter is affected by voxel size: underestimation occurs in areas with crossing fibers. AJNR Am J Neuroradiol 28 (6), 1102–1106.
Panagiotaki, E., Schneider, T., Siow, B., Hall, M.G., Lythgoe, M.F., Alexander, D.C., 2012. Compartment models of the diffusion MR signal in brain white matter: a taxonomy and comparison. Neuroimage 59 (3), 2241–2254.
Patenaude, B., Smith, S.M., Kennedy, D.N., Jenkinson, M., 2011. A Bayesian model of shape and appearance for subcortical brain segmentation. Neuroimage 56 (3), 907–922.
Pestilli, F., 2015. Test-Retest measurements and digital validation for in vivo neuroscience. Sci. Data 2, 140057. https://doi.org/10.1038/sdata.2014.57.
Pestilli, F., Yeatman, J.D., Rokem, A., Kay, K.N., Wandell, B.A., 2014a. Evaluation and statistical inference for human connectomes. Nat. Methods 11 (10), 1058–1063.
Pestilli, F., Yeatman, J., Rokem, A., Kay, K., Takemura, H., Wandell, B., 2014b. LiFE: linear fascicle evaluation a new technology to study visual connectomes. J. Vis. 14 (10), 1122.
Petros, T.J., Rebsam, A., Mason, C.A., 2008. Retinal axon growth at the optic chiasm: to cross or not to cross. Annu. Rev. Neurosci. 31, 295–315.
Prieur, D.S., Rebsam, A., 2017. Retinal axon guidance at the midline: chiasmatic misrouting and consequences. Dev Neurobiol 77 (7), 844–860.
Roebroeck, A., Galuske, R., Formisano, E., Chiry, O., Bratzke, H., Ronen, I., Kim, D.-S., Goebel, R., 2008. High-Resolution diffusion tensor imaging and tractography of the human optic chiasm at 9.4 T. Neuroimage 39 (1), 157–168.
Rokem, A., Takemura, H., Andrew, S.B., Scherf, K.S., Behrmann, M., Wandell, B.A., Ione, F., Bridge, H., Pestilli, F., 2017. The visual white matter: the application of diffusion MRI and fiber tractography to vision science. J. Vis. 17 (2), 4.
Rokem, A., Yeatman, J.D., Pestilli, F., Kay, K.N., Mezer, A., Stefan van der, W., Wandell, B.A., 2015. Evaluating the accuracy of diffusion mri models in white matter. PLoS One 10 (4), e0123272.
Schmitz, B., Schaefer, T., Christoph, Mck., Reith, W., Backens, M., Käsmann-Kellner, B., 2003. Configuration of the optic chiasm in humans with albinism as revealed by magnetic resonance imaging. Invest. Ophthalmol. Vis. Sci. 44 (1), 16–21.
Smith, R.E., Tournier, J.-D., Calamante, F., Connelly, A., 2012. Anatomically-Constrained tractography: improved diffusion mri streamlines tractography through effective use of anatomical information. Neuroimage 62 (3), 1924–1938.
Smith, R.E., Tournier, J.-D., Calamante, F., Connelly, A., 2015. SIFT2: enabling dense quantitative assessment of brain white matter connectivity using streamlines tractography. Neuroimage 119 (October), 338–351.
Smith, S.M., Jenkinson, M., Woolrich, M.W., Beckmann, C.F., Behrens, T.E.J., Johansen-Berg, H., Bannister, P.R., et al., 2004. Advances in functional and structural MR image analysis and implementation as FSL. Neuroimage 23 (Suppl 1), S208–S219.
Sotiropoulos, S.N., Jbabdi, S., Xu, J., Andersson, J.L., Moeller, S., Auerbach, E.J., Glasser, M.F., et al., 2013. Advances in diffusion MRI acquisition and processing in the human connectome project. Neuroimage 80 (October), 125–143.
Staempfli, P., Rienmueller, A., Reischauer, C., Valavanis, A., Boesiger, P., Kollias, S., 2007. Reconstruction of the human visual system based on DTI fiber tracking. J. Magnet. Reson. Imaging 26 (4), 886–893.
Stejskal, E.O., Tanner, J.E., 1965. Spin diffusion measurements: spin echoes in the presence of a time-dependent field gradient. J. Chem. Phys. https://doi.org/10.1063/1.1695690.
Takemura, H., Caiafa, C.F., Wandell, B.A., Pestilli, F., 2016. Ensemble tractography. PLoS Comput. Biol. 12 (2), e1004692.
Tournier, J.-D., Calamante, F., Connelly, A., 2010. Improved probabilistic streamlines tractography by 2nd order integration over fibre orientation distributions. In: Proceedings of the International Society for Magnetic Resonance in Medicine, pp. 1670.
Tournier, J.-Donald., Calamante, F., Connelly, A., 2007. Robust determination of the fibre orientation distribution in diffusion MRI: non-Negativity constrained super-resolved spherical deconvolution. Neuroimage 35 (4), 1459–1472.
Tournier, J.-Donald., Calamante, F., Connelly, A., 2012. MRtrix: diffusion tractography in crossing fiber regions. Int. J. Imaging Syst. Technol. https://doi.org/10.1002/ima.22005.
Tournier, J.-D., Calamante, F., Connelly, A., 2013. Determination of the appropriate b value and number of gradient directions for high-angular-resolution diffusion-weighted imaging. NMR Biomed. 26 (12), 1775–1786.
Tournier, J.-Donald., Yeh, C.-H., Calamante, F., Cho, K.-H., Connelly, A., Lin, C.-Po., 2008. Resolving crossing fibres using constrained spherical deconvolution: validation using diffusion-weighted imaging phantom data. Neuroimage 42 (2), 617–625.
Tuch, D.S., 2004. Q-Ball imaging. Magne. Reson. Med. 52 (6), 1358–1372.
Tuch, D.S., Reese, T.G., Wiegell, M.R., Makris, N., Belliveau, J.W., Wedeen, V.J., 2002. High angular resolution diffusion imaging reveals intravoxel white matter fiber heterogeneity. Magnet. Reson. Med 48 (4), 577–582.
Tustison, N.J., Avants, B.B., Cook, P.A., Zheng, Y., Egan, A., Yushkevich, P.A., Gee, J.C., 2010. N4ITK: improved N3 bias correction. IEEE Trans. Med. Imaging 29 (6), 1310–1320.
Veraart, J., Fieremans, E., Novikov, D.S., 2016a. Diffusion MRI noise mapping using random matrix theory. Magnet. Reson. Med. 76 (5), 1582–1593.
Veraart, J., Novikov, D.S., Christiaens, D., Ades-Aron, B., Sijbers, J., Fieremans, E., 2016b. Denoising of diffusion MRI using random matrix theory. Neuroimage 142 (November), 394–406.
von dem Hagen, E.A.H., Houston, G.C., Hoffmann, M.B., Jeffery, G., Morland, A.B., 2005. Retinal abnormalities in human albinism translate into a reduction of grey matter in the occipital cortex. Eur. J. Neurosci. https://doi.org/10.1111/j.1460-9568.2005.04433.x.
von dem Hagen, E.A.H., Houston, G.C., Hoffmann, M.B., Morland, A.B., 2007. Pigmentation predicts the shift in the line of decussation in humans with albinism. Eur. J. Neurosci. https://doi.org/10.1111/j.1460-9568.2007.05303.x.
von dem Hagen, E.A.H., Michael, B.H., Antony, B.M., 2008. Identifying human albinism: a comparison of VEP and fMRI. Investig. Opthalmol. Vis. Sci. https://doi.org/10.1167/iovs.07-0458.
Wandell, B.A., Chial, S., Backus, B.T., 2000. Visualization and measurement of the cortical surface. J. Cogn. Neurosci. 12 (5), 739–752.
Wedeen, V.J., Hagmann, P., Tseng, W.-Y.I., Reese, T.G., Weisskoff, R.M., 2005. Mapping complex tissue architecture with diffusion spectrum magnetic resonance imaging. Magnet. Reson. Med. 54 (6), 1377–1386.
Wedeen, V.J., Wang, R.P., Schmahmann, J.D., Benner, T., Tseng, W.Y.I., Dai, G., Pandya, D.N., Hagmann, P., D'Arceuil, H., de Crespigny, A.J., 2008. Diffusion spectrum magnetic resonance imaging (DSI) tractography of crossing fibers. Neuroimage 41 (4), 1267–1277.
Wiegell, M.R., Larsson, H.B., Wedeen, V.J., 2000. Fiber crossing in human brain depicted with diffusion tensor MR imaging. Radiology 217 (3), 897–903.

Chapter 7

Triple visual hemifield maps in a case of optic chiasm hypoplasia

This chapter contains the permitted reprint of the study **"Triple visual hemifield maps in a case of optic chiasm hypoplasia"** published in *Neuroimage*:

Ahmadi, K., Fracasso, A., Puzniak, R. J., Gouws, A. D., Yakupov, R., Speck, O., Kaufmann, J., Pestilli, F., Dumoulin, S. O., Morland, A. B., and Hoffmann, M. B. (July 2020). "Triple visual hemifield maps in a case of optic chiasm hypoplasia". In: *NeuroImage* 215, p. 116822. DOI: 10.1016/j.neuroimage.2020.116822

NeuroImage 215 (2020) 116822

Contents lists available at ScienceDirect

NeuroImage

journal homepage: www.elsevier.com/locate/neuroimage

Triple visual hemifield maps in a case of optic chiasm hypoplasia

Khazar Ahmadi [a,b], Alessio Fracasso [c,d,e,f,1], Robert J. Puzniak [a,1], Andre D. Gouws [g], Renat Yakupov [h,i], Oliver Speck [h,i,j,k], Joern Kaufmann [l], Franco Pestilli [m], Serge O. Dumoulin [c,e,n], Antony B. Morland [g,o], Michael B. Hoffmann [a,k,*]

[a] Department of Ophthalmology, Otto-von-Guericke University, Magdeburg, 39120, Germany
[b] Clinical Memory Research Unit, Department of Clinical Sciences, Lund University, Lund, 22362, Sweden
[c] Department of Experimental Psychology, Helmholtz Institute, Utrecht University, Utrecht, 3584 CS, the Netherlands
[d] Department of Radiology, University Medical Center Utrecht, Utrecht, 3584 CX, the Netherlands
[e] Spinoza Centre for Neuroimaging, Amsterdam, 1105 BK, the Netherlands
[f] Institute of Neuroscience and Psychology, University of Glasgow, Glasgow, G12 8QB, UK
[g] Department of Psychology, York Neuroimaging Centre, University of York, York, YO10 5NY, UK
[h] Department of Biomedical Magnetic Resonance, Institute for Physics, Otto-von-Guericke University, Magdeburg, 39120, Germany
[i] German Center for Neurodegenerative Diseases, Magdeburg, 39120, Germany
[j] Leibniz Institute for Neurobiology, Magdeburg, 39118, Germany
[k] Center for Behavioral Brain Sciences, Magdeburg, 39106, Germany
[l] Department of Neurology, Otto-von-Guericke-University, Magdeburg, 39120, Germany
[m] Department of Psychological and Brain Sciences, Indiana University, Bloomington, IN, 1101 E, USA
[n] Department of Experimental and Applied Psychology, VU University Amsterdam, Amsterdam, 1081 BT, the Netherlands
[o] Centre for Neuroscience, Hull-York Medical School, University of York, York, YO10 5DD, UK

ARTICLE INFO

Keywords:
DWI
fMRI
Optic chiasm
Plasticity
Retinotopy
Visual cortex

ABSTRACT

In humans, each hemisphere comprises an overlay of two visuotopic maps of the contralateral visual field, one from each eye. Is the capacity of the visual cortex limited to these two maps or are plastic mechanisms available to host more maps? We determined the cortical organization of the visual field maps in a rare individual with chiasma hypoplasia, where visual cortex plasticity is challenged to accommodate three hemifield maps. Using high-resolution fMRI at 7T and diffusion-weighted MRI at 3T, we found three hemiretinal inputs, instead of the normal two, to converge onto the left hemisphere. fMRI-based population receptive field mapping of the left V1–V3 at 3T revealed three superimposed hemifield representations in the left visual cortex, i.e. two representations of opposing visual hemifields from the left eye and one right hemifield representation from the right eye. We conclude that developmental plasticity including the re-wiring of local intra- and cortico-cortical connections is pivotal to support the coexistence and functioning of three hemifield maps within one hemisphere.

1. Introduction

Topographic maps of the contralateral visual field are instrumental for the functionality of the human visual cortex and are considered a core principle of the notion of hemispheric specialization (Huberman et al., 2008; Wandell et al., 2007). A fundamental prerequisite for the formation of these maps is the partial decussation of the optic nerves at the optic chiasm. Here, the fate of axons from the eyes is decided such that axons from the nasal retina cross the midline and project to the contralateral hemisphere, while fibers from the temporal retina remain uncrossed and project ipsilaterally. As a consequence of this partial decussation, each hemisphere receives binocular input from the contralateral visual field. While acquired damage to the optic chiasm results in bitemporal hemianopia (Weber and Landau, 2013), congenital chiasma malformations leave major aspects of visual function intact (Hoffmann et al., 2007; Hoffmann and Dumoulin, 2015; Klemen et al., 2012). This renders these conditions invaluable models to study the foundations of visual pathway formation and the scope of its plasticity in humans.

In individuals affected with congenital chiasmatic abnormalities [absence of optic nerve crossing in achiasma and hemihydranencephaly

* Corresponding author. Department of Ophthalmology, Otto-von-Guericke University, Leipziger Str. 44, 39120, Magdeburg, Germany.
E-mail address: michael.hoffmann@med.ovgu.de (M.B. Hoffmann).
[1] These authors contributed equally.

https://doi.org/10.1016/j.neuroimage.2020.116822
Received 30 August 2019; Received in revised form 27 February 2020; Accepted 2 April 2020
Available online 8 April 2020

(Apkarian et al., 1994; Fracasso et al., 2016; Hoffmann et al., 2012; Muckli et al., 2009; Victor et al., 2000) or enhanced crossing in FHONDA and albinism (Ahmadi et al., 2019; Apkarian et al., 1983; Hoffmann et al., 2003; von dem Hagen et al., 2008)], the visual cortex receives erroneous input from the ipsilateral visual field in addition to the normal input from the contralateral visual field. This results, at the macroscopic scale, in two superimposed retinotopic maps of opposing hemifields in V1 (Ahmadi et al., 2019; Bao et al., 2015; Davies-Thompson et al., 2013; Hoffmann et al., 2012, 2003; Kaule et al., 2014; Muckli et al., 2009). Remarkably, at the mesoscopic scale, these maps are interdigitated and form hemifield dominance domains (Olman et al., 2016), that are reminiscent of the ocular dominance domains in the normal visual system. It appears therefore that the reassignment of ocular dominance domains to hemifield dominance domains is a simple mechanism to accommodate two hemifield maps, either two representations of one visual hemifield via binocular input in normal vision or two representations of opposing hemifields via monocular input in congenital chiasma malformations (Hoffmann and Dumoulin, 2015).

These observations prompt the important question, whether V1 is limited to hosting two hemifield maps, or whether the scope of plasticity in human V1 allows for the accommodation of even more maps. To address this question, we determined the cortical organization in an individual with chiasma hypoplasia whose misrouting pattern deviated from the typical hallmark of complete achiasma, i.e., the entire absence of crossing projections. In fact, the clinical spectrum of congenital achiasma ranges between the complete absence of the optic chiasm and consequently an absence of crossing nasal fibers i.e., complete achiasma, to a hypoplastic optic chiasm with a reduction of crossing nasal fibers (Sami et al., 2005). This is depicted as a schematic in Fig. 1, which juxtaposes control, complete achiasma, and the case of chiasma hypoplasia investigated in the present study.

The mechanism of reassigning ocular dominance domains alone would suggest that only two inputs can be accommodated, so any additional input would necessarily need to engage further plastic mechanisms to establish a useful visual representation. The condition of chiasma hypoplasia provides the opportunity to explore the limits of plasticity in V1 and beyond.

Three types of investigations were performed using 3 and 7 T MRI: (i) diffusion-weighted imaging (DWI) to specify the projection error of the optic nerves at the optic chiasm, (ii) population receptive field (pRF) mapping (Ahmadi et al., 2019; Dumoulin and Wandell, 2008) to determine the cortical visual field maps, and (iii) high-resolution fMRI. Our results demonstrate that maps from three hemifields can be accommodated within a single V1. We propose that mechanisms of developmental plasticity that are exceeding the simple reassignment of ocular dominance domains to hemifield dominance domains enable these three maps to be hosted in V1.

2. Materials and methods

2.1. Case description

A 26-year-old female with **c**hiasma **hypo**plasia ('CHP') participated in the study. Her best-corrected decimal visual acuity (Snellen acuity) was 0.63 (20/32) for the dominant right eye and 0.25 (20/80) for the left eye. She had moderate vertical nystagmus, strabismus [alternating strabismus, esotropia (5°), and vertical deviation (7°) with alternating suppression of each eye] and no stereoscopic vision. Humphrey-like visual field testing revealed normal visual fields in both eyes. Decussation anomalies were confirmed with visual evoked potentials (VEPs) and T1-weighted MRI at the age of 22. She reported an otherwise normal developmental and medical history and there was no family history of ophthalmological or neurological disorders. MRI measurements on CHP were performed at two sites. CHP was first scanned at Magdeburg University, Germany, at the age of 24. In two consecutive days, she underwent high-resolution fMRI at 7T and DWI scanning sessions at 3T. Due to limited availability of CHP, pRF mapping data were acquired two years later at York Neuroimaging Center, UK, at 3T.

2.2. Control Participants

12 respective control participants were also included in the current study. The first four controls (C1 – C4; mean age = 31, range = 25–49 years, 2 females) took part in a pRF mapping session at 3T while the other eight controls (C5 – C12, mean age = 29, range = 22–52 years, 6 females) participated in the DWI sessions. The last control participant (C12) also underwent high-resolution fMRI at 7T. All experiments on controls were conducted in Magdeburg. Informed written consent was obtained from all participants prior to the study investigations. The procedures followed the tenets of the declaration of Helsinki and the respective protocols were approved by the ethical committees of the University of Magdeburg and York Neuroimaging Centre.

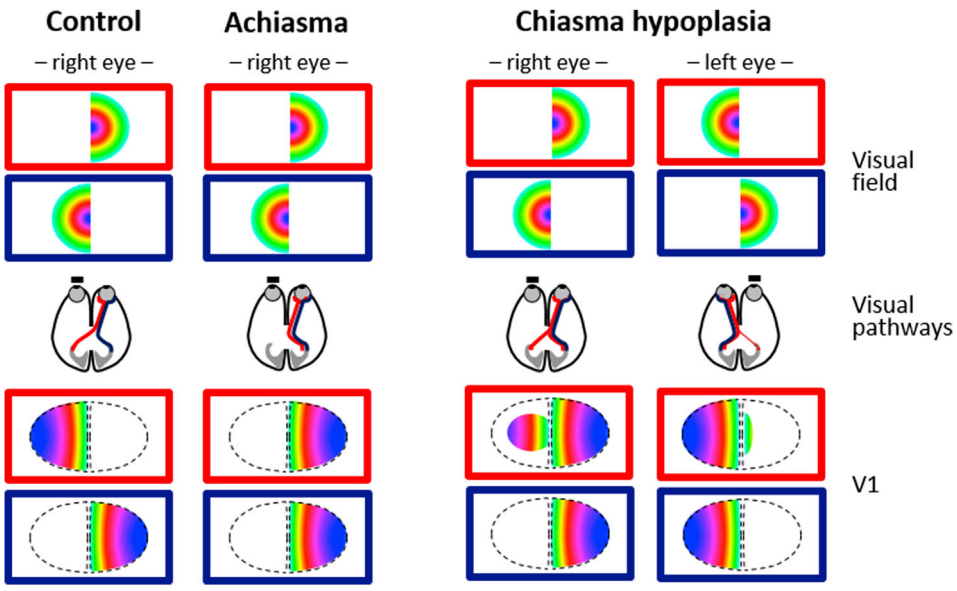

Fig. 1. Schematic optic nerve projections and eccentricity representations in V1 for control, achiasma, and chiasma hypoplasia. Control (right eye): the nasal (red) and temporal (blue) retinal fibers of the right eye project to the left and right hemispheres respectively (frame color follows fiber color coding). Consequently, the eccentricity representations reside in the V1 contralateral to the respective hemifield. **Achiasma (right eye):** Due to the complete absence of crossing nasal fibers, the right V1 is organized as a cortical overlay of orderly eccentricity maps from both the contra- and ipsilateral hemifields. **Chiasma hypoplasia (right and left eyes):** Similar to complete achiasma, the predominance of non-crossing nasal fibers leads to the superimposed eccentricity maps of opposing hemifields in V1. In contrast to complete achiasma, however, there is a portion of crossing nasal fibers resulting in a residual representation of the contralateral hemifield via the contralateral eye in V1. As a consequence, each hemisphere receives not only input from the ipsilateral, but also some input from the contralateral eye.

2.3. High-resolution fMRI

Visual stimulation: Visual stimuli were presented by back-projection onto a screen with a resolution of 1920 X 1080 pixels and viewed at a distance of 100 cm via an angled mirror. Presentation software package (Neurobehavioral Systems, Berkeley, CA, USA) was used to control stimulus presentation. The stimuli extended ±12.9° by ± 7.4° of visual angle from the center of the screen and comprised bilateral, contrast reversing (8 reversals per second) black and white checkerboards with 24 segments and 26 rings (mean luminance 62 cd/m^2, contrast 99%). A block design, alternating between the two eyes was selected. It consisted of 14 checkerboard presentation blocks (7 blocks per eye), each of which lasted for 12 s and was followed by a rest block (mean luminance gray background) with the same duration. The presentation blocks were preceded by an additional rest block of 12 s for dummy stimulation. Participants wore a custom-made manually operated shutter that allowed monocular viewing through either the left or right eye. They fixated a central fixation cross, which changed its color 1 s after initiation of each rest block, lasting for 23 s (11 s of the rest block plus 12 s of the next presentation block). The participants were requested to occlude the right eye and view the stimuli with the left eye for a green fixation cross, and vice versa for a red one. An MRI-compatible camera was used to view the dominant eye, to ensure that the participants were doing the task correctly.

MRI acquisition: For functional imaging, T2*-weighted volumes were acquired using a 2D gradient-echo EPI sequence with a 7T whole body MRI scanner (Siemens Healthineers, Erlangen, Germany) using a 32 channel head coil (Nova Medical, Wilmington, MA) with the following acquisition parameters: TR | TE = 3000 | 22 ms, flip angle = 90°, FOV = 169 (right-left) × 130 (anterior-posterior) × 27 (feet-head) mm^3, acceleration factor (r) = 4 with GRAPPA reconstruction, phase-encoding direction = right-left, phase partial Fourier = 5/8, bandwidth (BW) = 1086 Hz/px, echo-spacing = 1.13 ms and voxel size = 0.65 x 0.65 × 0.65 mm^3. Forty-one oblique axial slices were acquired for the duration of 348 s with 116 time frames, of which the first four were discarded. The slice placement for the functional volumes covered a portion of the occipital cortex parallel to the calcarine sulcus. Foam padding was used to minimize head motion. Four runs of bilateral stimulation were performed for each participant in a single session.

A high-resolution anatomical volume was obtained using a 3D T1-weighted MPRAGE sequence (TR | TE | TI = 2500 | 2.76 | 1050 ms, total duration = 14:14 min, flip angle = 5°, FOV: 350 × 263 × 350 mm^3, and voxel size = 0.65 × 0.65 × 0.65 mm^3). In addition, a proton density weighted volume without the inversion module (identical parameters except for TR = 1820 ms and total duration = 5:33 min) was acquired to correct for receive coil biases (Van de Moortele et al., 2009).

Data analysis: To obtain an inhomogeneity corrected anatomical volume, the T1-weighted MPRAGE reference volume was divided by the proton density weighted volume. Gray and white matter (GM/WM) were segmented based on the resulting anatomical volume in MIPAV (https://mipav.cit.nih.gov/) using the TOADS/CRUISE algorithm (Bazin and Pham, 2007; Han et al., 2004). Manual editing was performed in ITK-GRAY (https://web.stanford.edu/group/vista/cgi-bin/wiki/index.php/ItkGray) to minimize the segmentation error. An equi-volume distance map was employed (Waehnert et al., 2014) to build a coordinate system along the cortical depth, taking the local curvature into account.

The functional data were corrected for motion artifacts and spatial distortion using MCFLIRT function of FSL (https://www.fmrib.ox.ac.uk/fsl) and a point spread function (PSF) mapping method (In and Speck, 2012) respectively. Motion and distortion corrected data were then analyzed using AFNI (https://afni.nimh.nih.gov/afni). Time series were averaged across repetitions for each participant to increase the signal-to-noise ratio (SNR). Afterwards, the averaged functional volume was aligned to the T1-weighted anatomical volume using an affine transformation. The alignment was performed in three steps: First, the T1-weighted anatomy and the averaged EPI were clipped in the anterior-posterior direction, leaving only the occipito-temporal cortex. A good starting point was provided by centering the functional volume on the anatomy using the respective centers of mass. Next, the averaged functional volume was affinely aligned to the T1-weighted volume via AFNI's 'align_epi_anat.py' with the local Pearson's coefficient (LPC) cost function (Saad et al., 2009), using the two-pass option. This procedure blurs the functional volume and initially allows for large rotation and shift, and then refines the alignment by an affine transformation. Finally, the resulting alignment was further improved via 3dAllineate, using the one-pass option. In this step, the functional volume is not blurred. Only a small amount of shift and rotation is allowed, using an affine transformation that is obtained by concatenating the transformation matrices generated in previous steps (Fracasso et al., 2018; Klein et al., 2018).

A general linear model (GLM) was used to analyze the functional data. For each voxel, the percentage of BOLD signal changes to stimulation of the left and right eye was estimated via 3dDeconvolve function of AFNI. Nuisance regressors were modelled using polynomials up to the second order to remove any linear and quadratic trends. The GLM analysis was performed on the native EPI space. The obtained GLM maps (F-maps and beta-coefficient-maps) were co-registered to the T1-weighted space using the affine transformation matrix estimated in the alignment step. Multiple comparisons were corrected using false discovery rate (FDR) with a q value of 0.045. For each of the cortical layers, a 3D mesh was generated using AFNI's IsoSurface function.

2.4. Diffusion-weighted imaging

MRI acquisition: DWI data were acquired using a 3T MAGNETOM Prisma syngo MR D13D scanner (Siemens Healthineers, Erlangen, Germany) with a 64 channel head coil. MRI acquisition was initiated by a localizer scan, followed by a T1-weighted and two diffusion-weighted scans. All data were collected during a single scanning session. The T1-weighted volume was obtained in sagittal orientation using a 3D-MPRAGE sequence (TE | TR = 4.46 | 2600 ms, TI = 1100 ms, flip angle = 7°, resolution = 0.9 x 0.9 × 0.9 mm^3, FoV = 230 × 230 mm^2, image matrix = 256 × 256 x 176, acquisition time (TA) = 11:06 min). The first diffusion-weighted scan was acquired with Echo-Planar Imaging (EPI) with the following parameters: b-value = 1600 s/mm^2, TR | TE = 9400 | 64.0 ms, voxel size = 1.5 x 1.5 × 1.5 mm^3, phase-encoding direction = anterior to posterior, FoV = 220 × 220 mm^2, and TA = 22:24 min. Scanning was performed with 128 unique gradient directions, thus the obtained diffusion-weighted data can be described as High Angular Resolution Diffusion Imaging (HARDI) data (Tuch et al., 2002). Gradient tables were generated using E. Caruyer's tool for q-space sampling (Caruyer et al., 2013). Diffusion-weighted volumes were evenly intersected by 10 non-diffusion weighted volumes for the purpose of motion correction. The second diffusion-weighted scan was acquired with identical parameters except for reversed phase-encoding direction in comparison to the preceding scan, i.e., posterior to anterior direction. Acquisition of two diffusion-weighted scans with opposite phase-encoding directions enhances the correction of susceptibility-induced geometric distortion (Andersson et al., 2003) and improves the SNR of the total DWI data.

Data analysis: Conversion of DICOM images to NIFTI format, denoising of the DWI data and removal of Gibbs ringing were performed with MRtrix 3.0 (http://www.mrtrix.org/). FSL was employed for the correction of susceptibility-induced geometric distortions, eddy current distortions, and motion artifacts. The bias field in the DWI data was corrected using ANTS (http://stnava.github.io/ANTs/). Afterwards, DWI data were co-registered to the T1-weighted volume, which was aligned beforehand to Anterior Commissure – Posterior Commissure line, via mrDiffusion (https://github.com/vistalab/vistasoft/tree/master/mrDiffusion). The T1-weighted volume was automatically segmented using FIRST function of FSL. Subsequently, manual editing was performed to mitigate segmentation errors in the region of the optic chiasm.

Each voxel of the preprocessed DWI data was modelled using the Constrained Spherical Deconvolution (CSD) approach (Tournier et al.,

2008), which is particularly sensitive when resolving populations of crossing fibers, like those observed in the optic chiasm, and benefits from the high angular resolution of HARDI data. The application of the CSD model involved the estimation of single fiber response function with Tournier's algorithm (Tournier et al., 2013) for maximum harmonic order (Lmax = 6) and the estimation of fiber orientation distribution functions (Jeurissen et al., 2014) for 3 different maximum harmonic orders i.e. Lmax = 6, 8 and 10. Four ROIs were manually drawn on the T1-weighted volume, two covering cross-sections of the two optic nerves, and the other two covering cross-sections of the two optic tracts. The ROIs were placed as close to the optic chiasm as possible, but did not intersect it. Each ROI had a width of 3 voxels (anterior-posterior) to assure proper streamline termination during tractography. Fiber tracking was performed between the ROIs of the two optic nerves as seeds and the ROIs of the two optic tracts as targets, resulting in 4 connectivity pairs (2 ipsilateral and 2 contralateral fiber bundles). Tracking was done in two directions i.e. from seed to target ROI and backwards to ensure the indifference of the results to direction of tracking. The corresponding generated connectivity pairs were subsequently merged together. The tracking employed an ensemble tractography (ET) framework (Takemura et al., 2016), where tracking is performed several times, each time for a different set of parameters. As such, the bias in the outcome tracts, caused by parameter selection, is avoided. The tracking was performed with the probabilistic tracking algorithm iFOD2 (Tournier et al., 2010) using unique combinations of 2 different fractional anisotropy (FA) thresholds (FA = 0.04 and 0.08), 3 maximum curvature angles (30°, 45°, 60°), and 3 CSD models estimated for different maximum harmonic orders (L_{max} = 6, 8, 10) for each of 139,000 seeding attempts. Additionally, tractography employed an anatomically-constrained tractography (ACT) approach (Smith et al., 2012), which constrains tractography with anatomical priors derived from the anatomical image using white/gray matter, subcortical gray matter and CSF masks obtained with FSL's FIRST function. As a result of the tractography, 4 streamline groups corresponding to 4 distinct connectivity pairs were obtained. The proportion of streamlines in each group was subsequently used as an estimate of the connectivity strength in the optic chiasm.

2.5. Population receptive field (pRF) and connective field (CF) modeling

Visual stimulation: Visual stimuli consisted of drifting bar apertures (stimulus size in York and Magdeburg: 11° and 10° radius, respectively), exposing a moving high-contrast checkerboard pattern (Dumoulin and Wandell, 2008) at four different directions i.e. upward, downward, left and right. The bars were presented to each eye separately within a mask, covering either the left or the right hemifields for stimulation of either the nasal or the temporal retina in separate experiments. The width of the bars subtended one-quarter of the stimulus radius. Each pass of the bars lasted for 30 s, followed by a mean luminance block (zero contrast) of 30 s. The stimuli were generated in MATLAB (Mathworks, Natick, MA, USA) using the Psychtoolbox (Brainard, 1997; Pelli, 1997) and rear-projected onto a screen (screen resolution in York and Magdeburg: 1920 x 1080 and 1140 x 780 pixels, respectively) inside the magnet bore. In York, CHP viewed the screen at a distance of 57 cm via an angled, front-silvered mirror whereas the eye to screen distance in Magdeburg was 35 cm. Participants were required to fixate a centered dot and to report color changes between red and green by means of a button press.

MRI acquisition: Identical 3T Prisma scanners (Siemens Healthineers, Erlangen, Germany) were used at both sites. At York Neuroimaging Center, functional T2*-weighted volumes were acquired with a 64 channel head coil. A total of 30 EPI slices were obtained within a FOV of 192 mm, with 3 x 3 × 3 mm^3 voxels (TR | TE = 1500 | 26 ms and flip angle = 80°). Each functional scan comprised 168 time frames, lasting for 252 s. The first eight time-frames (12 s) were removed to allow magnetization to reach a steady-state. Foam padding was used to minimize head motion. Additionally, a T1-weighted anatomical volume was acquired at a resolution of 1 x 1 × 1 mm^3 (TR | TE = 2500 | 42.26 ms and flip angle = 7°). Eight functional scans were obtained in a single session (4 scans per eye). The right eye was stimulated during the first 4 runs while the left eye was patched. The stimulation of each of the left and right hemifields was repeated twice in a counterbalanced manner. After a short break in the scanning, the left eye was stimulated while the right eye was occluded. The same stimulation procedure was performed for the left eye. At Magdeburg University, functional images (TR | TE = 1500 | 30 ms and flip angle = 70°) were acquired at a resolution of 2.5 x 2.5 × 2.5 mm^3 with 54 axial slices, using a 64 channel head coil. Every functional scan had 168 time frames (252 s). In addition, a high resolution whole-brain anatomical volume (voxel size = 0.9 x 0.9 × 0.9 mm^3, TR | TE = 2600 | 4.46 ms, and flip angle = 7°) was obtained. Foam padding limited the head movements. In each session, left and right hemifield stimulation conditions were performed monocularly and repeated six times (three repetitions per hemifield).

Data analysis: The same analysis pipeline was used for data sets acquired in both sites. The T1-weighted anatomical volume was automatically segmented using the recon-all function of FreeSurfer (https://surfer.nmr.mgh.harvard.edu). The cortical surface was reconstructed at the white/gray matter boundary and rendered as a smoothed 3D mesh (Wandell et al., 2000). The MCFLIRT function of FSL was used for motion correction of the functional data. Motion corrected data were then analyzed using freely available Vistasoft software package for MATLAB (https://github.com/vistalab/vistasoft). Time series for the same conditions were averaged together for each participant to increase the SNR. Afterwards, the averaged functional image was co-registered to the anatomical scan using a combination of Vistasoft and Kendrick Kay's alignment tools (https://github.com/kendrickkay/alignvolumedata). Visual areas were mapped using the population receptive field (pRF) modeling (Dumoulin and Wandell, 2008). Briefly, the BOLD (blood oxygen level dependent) response of each voxel was predicted using a 2D-Gaussian model of the neuronal populations defined by three stimulus-referred parameters i.e. x0, y0, σ where x0 and y0 are the coordinates of the receptive field center and σ is it's spread (Dumoulin and Wandell, 2008; Fracasso et al., 2016; Harvey and Dumoulin, 2011). The predicted BOLD signal was then calculated by convolution of the stimulus sequence for the respective pRF-model and its three parameters with the canonical hemodynamic response function (Friston et al., 1998). The optimal pRF parameters were found by minimizing the sum of squared errors (RSS) between the predicted and observed BOLD time-course. For all subsequent analyses including derivation of the polar angle and eccentricity maps, required for the delineation of the visual areas, and the visualization on the inflated cortical surface, only the voxels were included whose pRF fits exceeded 15% of the variance explained.

The connective field parameters were estimated from the fMRI time-series, using CF modeling method that predicts the neuronal activity in one brain area with reference to aggregate activity in another area (Haak et al., 2013). The BOLD response in each voxel of a target ROI i.e. V2 or V3, was predicted with a symmetrical, circular 2D Gaussian CF model folded to follow the cortical surface of the source ROI, i.e. V1. The CF model was defined by two parameters i.e. Gaussian position and spread across the cortical surface. The optimal CF parameters were determined by minimizing the residual sum of squares between the predicted, and the observed time-series. For this purpose, many fMRI time-series predictions were generated by changing the CF positions across all voxel positions and Gaussian spread values on the surface of the source ROI. Best models were selected when the explained variance in the fMRI time-series survived a threshold of 15%.

2.6. 2.6 Visual field testing

We simulated the Humphrey visual field testing using PsychoPy (https://www.psychopy.org) on a calibrated CRT monitor (22-inch Mitsubishi, 2070SB at 85 Hz). Background luminance was set to 10 cd/m^2, equal to 30 dB. Goldmann size III stimuli i.e., white circular patches (0.43° diameter) were displayed for 235 ms and placed at 54 locations

according to the Humphrey 24-2 standard test. In addition, four stimuli were placed at 12, 15, 18, and 21° into the temporal field along the horizontal meridian in order to capture the blind spot. The detection threshold was tested in both eyes with one-up-one down staircase procedure with a minimum of 30 trials per location. Responses were within 800 ms after the stimulus presentation. An initial adaptive staircase with 4 dB/2 dB step sizes was used to coarsely estimate the threshold at 16 locations in the visual field (4 in each visual quadrant), starting at the maximum gun value. Subsequently, a second adaptive staircase with finer step sizes (minimum 0.25 dB) was used to more accurately find the threshold starting at a gun value of 25% of the maximum (35 cd/m^2).

3. Results

3.1. Atypical lateralization pattern revealed by high-resolution fMRI data

High-resolution fMRI at 7T was used to evaluate the cortical lateralization pattern in response to bilateral contrast reversing black and white checkerboards presented to each eye separately (see Methods). In a neuro-typical visual system, bilateral stimulation of each eye leads to bihemispheric activation (Figure S1). In CHP, however, bilateral stimulation of the left eye yielded predominant responses on the ipsilateral occipital cortex i.e. on the left hemisphere, and only a marginal activation was observed on the contralateral hemisphere (Fig. 2A). In contrast, considerable bilateral activation was found during bilateral stimulation of the right eye (Fig. 2B). It should be noted that regardless of the stimulated eye, the contralateral activity in CHP was weaker compared to the control participant (the ratio of contralaterally activated voxels to all active i.e. ipsilateral plus contralateral voxels for left and right eye stimulation, respectively in CHP: 5.4% and 20.1%, and in control: 51.3% and 50.6%). Nonetheless, the robust activation on the left hemisphere upon the stimulation of the right eye in CHP indicated that part of the nasal afferents decussate at the chiasm and project to the contralateral hemisphere. This revealed that her misrouting pattern is distinct from complete achiasma where bilateral stimulation of each eye results in complete ipsilateral activation.

3.2. Optic nerve misrouting revealed with DWI

The above results predicted that the proportion of crossing fibers from the right eye would exceed that from the left eye. More direct evidence for this specific misrouting of the optic nerves in CHP was provided by a quantitative assessment of the streamlines at the optic chiasm based on DWI data (see Methods). For CHP and 8 individuals of a control cohort, a total of four ROIs were selected, one in each of the two optic nerves and one in each of the two optic tracts, to identify streamlines connecting each optic nerve with the (i) ipsilateral and (ii) contralateral optic tract, i.e. uncrossed and crossed projections.

The results are presented in Table 1. The proportion of the uncrossed, i.e. ipsilateral, projections was similar for the right and left optic nerves in CHP and within the ranges observed in controls though not between the first and third quartiles. In contrast, the proportion of the crossed, i.e. contralateral, projections was far greater for the right than for the left eye in CHP, exceeding the observed range for the right eye in controls (see Table 1). This underscores the asymmetric distribution of crossing

Table 1
Comparison of ipsi- and contralateral streamlines between right and left eye of CHP and controls. It should be noted, that the values indicate the proportion of ipsilateral streamlines of each eye relative to all ipsilateral streamlines, and the proportion of contralateral streamlines of each eye relative to all contralateral streamlines; i.e., the values are not the proportion of ipsilateral or contralateral projections relative to all streamlines.

		Ipsilateral streamlines per eye normalized to all ipsilateral streamlines		Contralateral streamlines per eye normalized to all contralateral streamlines	
		right eye	left eye	right eye	left eye
CHP	Value	42%	58%	73%	27%
Controls	Values range	40–68%	32–60%	39–68%	32–61%
	Median	54%	46%	48%	52%
	1st and 3rd quartile	47 and 58%	43 and 53%	42 and 59%	41 and 58%

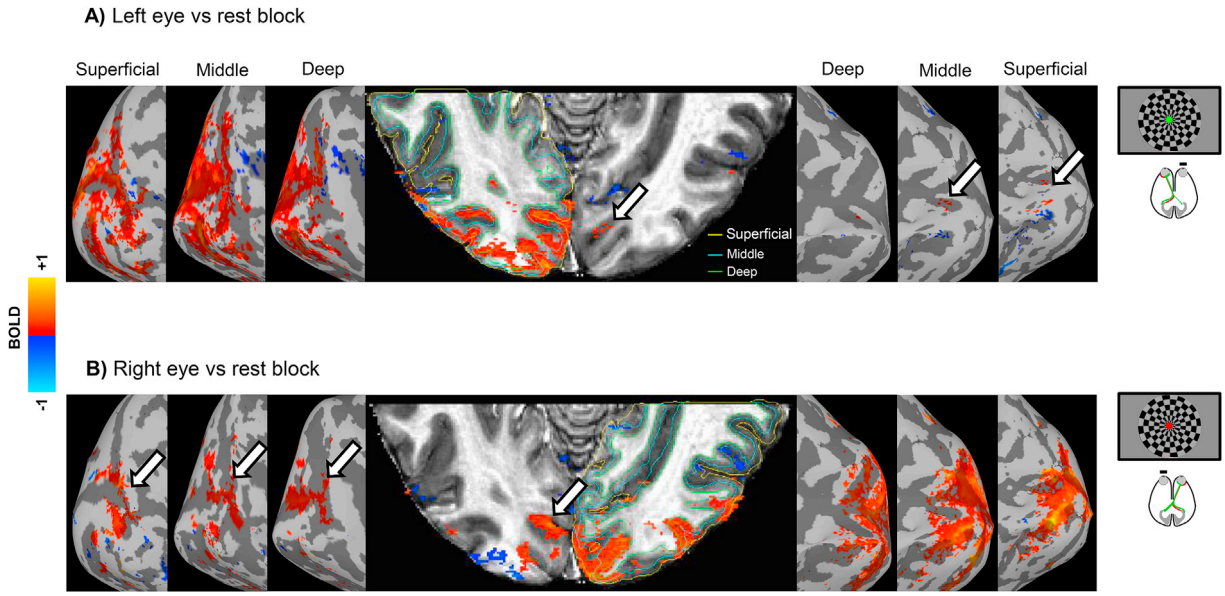

Fig. 2. Cortical response lateralization during bilateral stimulation of each eye in CHP. The cortical activation is projected onto a clipped anatomical image of the occipital cortex and onto the inflated cortical surfaces of the deep, middle, and superficial layers. **A)** Left eye stimulation vs rest elicits predominantly unilateral activation on the ipsilateral hemisphere with a small residual activation on the contralateral hemisphere, indicated by white arrows. **B)** Right eye stimulation vs rest elicits bilateral activation, i.e. on the ipsilateral hemisphere and also on part of the contralateral hemisphere (white arrows). The activation maps consist of signal amplitude expressed as the β coefficient from the GLM thresholded by cluster size and F statistic (cluster = 20, threshold by F = 10.477 and 10.040 for **A** and **B**, respectively, $p < 0.002$, corrected). Note that the cortical surfaces are generated from different cortical depths. Consequently, they look different, delimit to different volumes and have different number of nodes.

afferents at the optic chiasm in CHP, which is in accordance with the above fMRI findings. A 3D rendering of the tracked streamlines is illustrated in Fig. 3.

The proportion of the contra- and ipsilateral streamlines in CHP was further compared to all controls as well as an individual with complete achiasma and a cohort of 9 albinotic participants whose tractography results were extracted from a previous study (Puzniak et al., 2019). As expected, the crossing at the optic chiasm in CHP was lower than the controls and the cohort with albinism and higher than the participant with complete achiasma (see Figure S2).

3.3. Three overlaid hemifield representations revealed by pRF mapping

Based on the response lateralization pattern observed in the high-resolution fMRI data, we speculated that a significant part of the visual cortex on the left occipital lobe receives input from three hemiretinae, from the two hemiretinae of the ipsilateral, i.e. left, eye and from the nasal hemiretina of the contralateral, i.e. right eye. To test this hypothesis and to determine the specific mapping of the three inputs, pRF mapping (Dumoulin and Wandell, 2008) was performed during monocular stimulation of each eye and hemifield separately (see Methods). In the control participant, visuotopic maps of each hemifield were found on the contralateral hemisphere (Fig. 4). Remarkably, stimulation of the left eye in CHP revealed orderly organized eccentricity and polar angle maps of both ipsi- and contralateral hemifields on the left hemisphere across the three early visual areas (V1–V3; Fig. 5 A & B). Left and right hemifield representations were superimposed within each visual area in a mirror-symmetrical manner, in accordance with previous reports of complete achiasma (Hoffmann et al., 2012; Kaule et al., 2014). There was a small normal representation along the horizontal meridian on the contralateral, i.e. right, hemisphere (Fig. 5B).

For hemifield mapping of the right eye in CHP, a similar picture was obtained, i.e. mirror-symmetrical superposition of orderly visuotopic maps of opposing hemifields (Fig. 5 C & D). Importantly, the residual normal representation from the right eye was much more extensive than that from the left eye (Fig. 5C), which is consistent with the above high-resolution fMRI at 7T and DWI findings. The activation patterns measured at 7T (Fig. 2B), specifically in the middle and superficial layers, largely correspond to the residual representation from the right eye observed in Fig. 5C. It should be noted that there is stronger contralateral activity from the right eye for 7T compared to 3T fMRI, likely due to enhanced SNR for the former. This might also be the cause of the emergence of response signature in the dorsal portions of the early visual cortex for the 7T data. Importantly, the residual normal representation on the left hemisphere appeared to be superimposed onto the other two maps from the left eye (Fig. 5 A & B). As shown in Fig. 5C, the residual normal representation of the right hemifield covered a large part of V1 and spanned the entire polar angle range, from the lower vertical meridian in the dorsal portion of V1, through the horizontal and to the upper vertical meridian in the ventral portion of V1 and thus followed the normal retinotopic pattern. The observed retinotopic pattern of this residual input was not restricted to V1 and partially spread to V2 and V3.

In conclusion, we found a superposition of three retinotopic representations i.e., two representations from opposing visual hemifields mediated by the left eye plus an additional representation of the contralateral hemifield from the right eye, in the left hemisphere of CHP. This is in contrast to the retinotopic organization of the neuro-typical visual system where each hemifield is represented on the contralateral hemisphere (Fig. 4). A summary of this finding is provided in Fig. 6 which illustrates the co-localization of three retinotopic representations in the left visual cortex of CHP. Furthermore, the comparison of the eccentricity values between the representations of the i) right vs left hemifields of the left eye, ii) right hemifield of the left vs right hemifield of the right eye, and iii) right hemifield of the right eye vs left hemifield of the left eye revealed a good alignment of the three retinotopic representations within the area of overlap in the left V1 ($R^2 = 0.81$, 0.15, and 0.16 respectively, $p < 0.00001$ for all three comparisons; see Figure S3). The lower R^2 values observed for the two later comparisons might be associated with a slight shift in the eccentricity maps as evident in Fig. 5B and C, which could be attributed to the noise intrusion in the data, possibly due to imperfect fixation. As the circular nature of the polar angle values is a confound of this analysis, it was only performed for the eccentricity values.

3.4. Responsivity of the visual cortex receiving triple hemifield input

The above findings prompted the question of the functional characteristics of these maps in V1 and beyond. To compare the activation of the early visual cortex across the three hemifield-mapping conditions and to assess how the activation is propagated from V1 to V2 and V3, we determined the area of activated cortex in the early areas of the left hemisphere of CHP. As a reference, we used the condition of contralateral hemifield mapping via the left, i.e. ipsilateral, eye (normal input) for normalization and thus determined the relative activated area for both ipsilateral hemifield mapping via the left eye (abnormal input) and contralateral hemifield mapping via the right eye (residual normal input). The normal and abnormal inputs from the left eye activate a similar expanse of V1, V2 and V3. In contrast, the residual normal input from the right eye activates smaller proportions of V1, V3, and specifically V2 (Fig. 7A).

Subsequently, we obtained a measure of the reliability of the input for the ROIs that comprise the overlay of the three hemifield representations

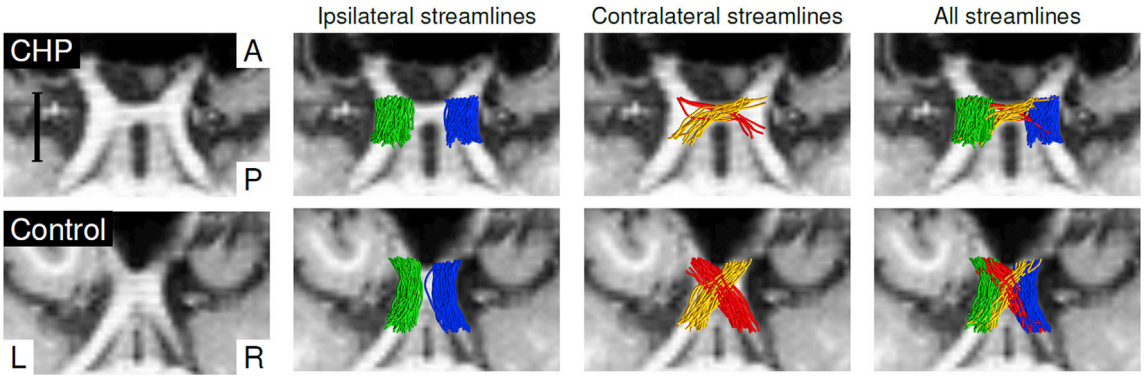

Fig. 3. Tractography of the optic chiasm. Axial slices without and with tractography overlay. The scale bar represents 1 cm. L-R and A-P stand for left-right and anterior-posterior directions, respectively. **Top row)** in CHP, the ipsilaterally projecting streamlines (blue and green for right and left optic nerve, respectively) are largely symmetrically distributed, while there is a predominance of contralaterally projecting streamlines for the right compared to the left optic nerve (yellow and red, respectively). **Bottom row)** in the control participant, both ipsi- and contralaterally projecting streamlines of the right and left optic nerves are largely symmetrically distributed. For clarity, only 0.25% of the generated streamlines are rendered.

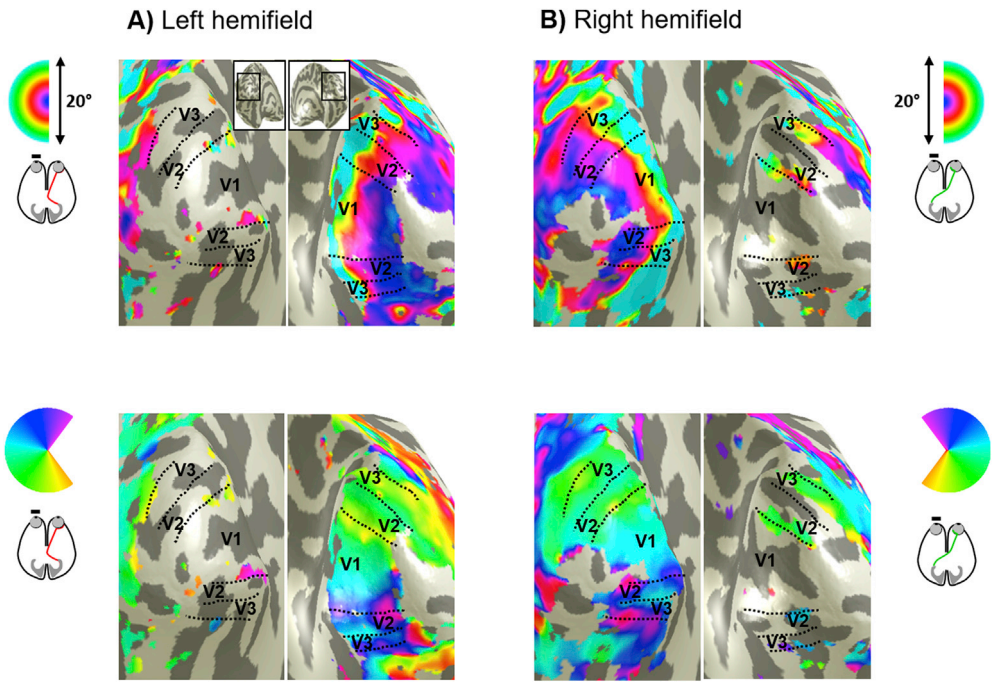

Fig. 4. Visual field representations for unilateral stimulation of the right eye in a control participant. Eccentricity (top row) and polar angle maps (bottom row) on the inflated occipital cortex for left **(A)** and right **(B)** hemifield stimulation. In both cases, orderly eccentricity and polar angle maps were obtained predominantly on the hemisphere contralateral to the stimulated hemifield. Residual ipsilateral representations of the vertical meridians and fovea were observed in V1–V3 as reported previously (Hoffmann et al., 2003; Tootell et al., 1998). Note that this residual representation is clearly different from the additional third hemifield map in CHP (Fig. 5C) which is more widespread and follows a retinotopic progression.

(ROI_{3maps}). For this purpose, we determined the goodness of fit of the pRF model, i.e. mean variance explained (VE; Fig. 7B). Although the area of cortex mapping the residual contralateral input of the right eye is smaller, the VE associated with this input does not appear to be markedly reduced compared to those driven by the normal and abnormal inputs of the left eye. These findings indicate the propagation of the triple hemifield input from V1 to the extrastriate cortex. The assessment of pRF-size properties and V1-referred connective field (CF) estimates in V2 and V3 suggest that the cortico-cortical connectivity underlying this propagation might be altered in CHP. This is depicted for the overlap of the three hemifield representations (ROI_{3maps}) in left V1–V3 in Figure S4 together with a detailed account on the respective pRF and CF signatures and their peculiarities in CHP.

Finally, the visual field coverage was assessed with pRF center and coverage plots as depicted in Figures S5 and S6, respectively. The pRF center distributions for the left and right V1 – V3 are presented for all four stimulation conditions for both CHP and a control participant (Figure S5). For the control, pRF centers predominantly cover the contralateral visual field; far less voxels represent the ipsilateral visual field, possibly due to a combination of the residual ipsilateral representation, noise intrusions and modelling limitation (see below). In CHP, the pRF centers of left V1 – V3 were predominantly located on the left and right hemifields following the left and right hemifield stimulation of the left eye, respectively (Figure S5 A, top panels).

For the left hemifield stimulation of the right eye, the pRF centers of the left V1 and V2 were mainly located in the upper left quadrant, whereas the pRF centers of the left V3 were mostly in the right hemifield (Figure S5 A, bottom left panel); as the right hemifield was actually not stimulated here, the latter is taken as an indication of the limitations of the model fit to the actual stimulus time course. Similarly, other ipsilateral extension into the non-stimulated hemifields, are partially due to the use of a circularly symmetric 2D Gaussian for the pRF model. Application of asymmetric models or models with minimal *priori* assumptions might reduce this ipsilateral coverage (Amano et al., 2009; Lee et al., 2013; Zeidman et al., 2018). Importantly, for the right eye's input during right hemifield stimulation, the pRF centers of these areas were primarily located in the right hemifield (Figure S5 A, bottom right panel), which reflects the residual normal input of the right eye to the left V1 (see also the corresponding pRF center values in control, Figure S5 C). This illustrates for the left visual areas in CHP, a combination of the pattern of representations typical of complete achiasma with the additional input from a third representation mediated by the right eye's input. In contrast, CHP's right visual areas are dominated by right eye input mediating representations from both visual hemifields (Figure S5 B, bottom panels), i.e., the typical hallmark of complete achiasma, with only little left eye input from the contralateral hemifield, found specifically a lower quadrant representation (Figure S5 B, top left panel).

The pRF-center findings are complemented by the visual field coverage plots which depict a combination of pRF center and size estimates (Amano et al., 2009). For clarity, only the coverage plots of V1 are presented in Figure S6. In principle, similar results are indicated by both pRF-center and visual field coverage plots. However, due to the incorporation of the pRF-sizes in the coverage plot, their coverage is more extensive than for the pRF center plots. In combination with the large pRF-size estimates for left V1 upon right hemifield stimulation of the right eye (compared to the corresponding pRF sizes for both left and right hemifield stimulation of the left eye, see Figure S4 A), this results in almost full field coverage for this condition. It should be highlighted that since the observed atypicalities in the left V1 do not occur for the coverage maps of the right V1, the inherent constraints of the pRF model should not be regarded as the only explanation. Other reasons, such as elevated noise in the data associated with imperfect fixation, may also lead to the observed ipsilateral extension of the visual field coverage maps.

4. Discussion

In the case of chiasma hypoplasia examined here, input from three visual hemifields converges onto the same cortical area. This puts a critical challenge on the organization of the visual cortex, which normally comprises a retinotopically aligned overlay of only two maps. The current study, therefore, provides novel insights into the scope and mechanisms of human visual system development and plasticity. Using high-resolution fMRI at 7T, DWI and fMRI-based pRF mapping at 3T, we report asymmetrical crossing of the nasal fibers of the two eyes that results in three overlaid representations of opposing hemifields on the left visual cortex. These findings suggest that the scope of cortical plasticity in the human visual system is sufficient to accommodate input from three

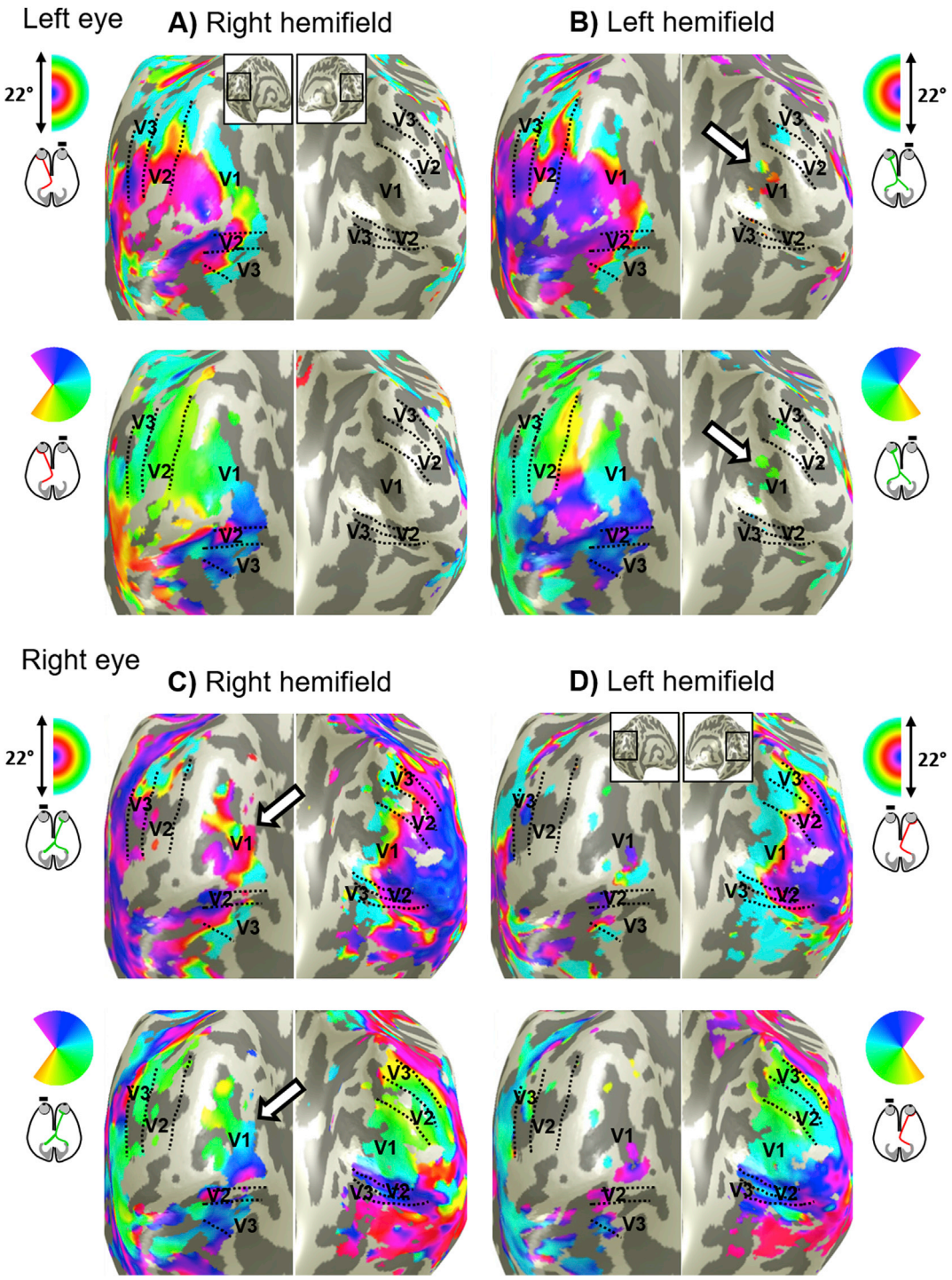

Fig. 5. Visual field representations for hemifield pRF-mapping in CHP for right and left eye stimulation. Eccentricity (top row in each panel) and polar angle (bottom row in each panel) maps are depicted on the inflated occipital cortex of CHP. For left eye stimulation, orderly eccentricity and polar angle maps are obtained on the left hemisphere for both right and left hemifield stimulation **(A, B)** and vice versa for right eye stimulation **(C, D)**. In addition, there is normal input to the hemisphere contralateral to the stimulated eye (white arrows). It is small for left eye stimulation and sizable for right eye stimulation, where it spans the entire polar angle range. The residual ipsilateral activation observed on the left hemisphere during left hemifield stimulation of the right eye **(D)** is reminiscent of the residual ipsilateral representation of the fovea and vertical meridian in controls (see Fig. 4). Furthermore, the considerable activation on the anterior regions of dorsal V3 observed for the aforementioned stimulation condition **(D)** is likely due to the callosal projections leading to binocular interactions at intermediate visual areas, as reported in complete achiasma (Davies-Thompson et al., 2013).

visual hemifields.

The retinotopically registered overlay of the representation of visual hemifields is a key property of the primary visual cortex. Remarkably, this is not only observed in the neuro-typical visual system, where these two maps comprise the binocular input of the contralateral visual hemifield it also holds for conditions with abnormal predominantly monocular input, as achiasma, albinism, or FHONDA (Ahmadi et al., 2019; Hoffmann et al., 2012, 2003). While the two maps segregate into ocular dominance domains in the neuro-typical case, they segregate into hemifield domains (Guillery et al., 1984; Olman et al., 2016) for

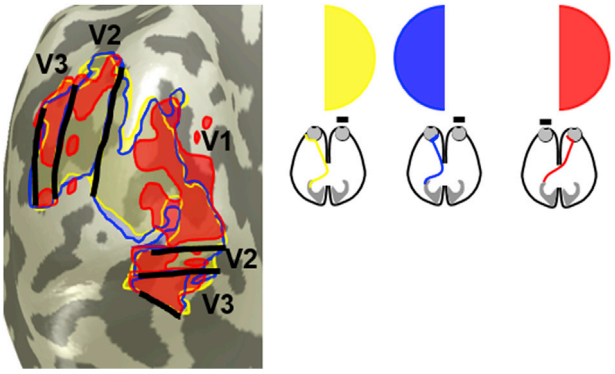

Fig. 6. Overlapping representation of the input from three hemifields in the left occipital lobe of CHP (based on the data shown in Fig. 5). The portions of visual cortex activated by stimulation of the left and right hemifield via the left eye [as typical for complete achiasma (Hoffmann et al., 2012)], colored yellow and blue, and of the right hemifield (as specific to the present case of CHP), colored red, are arranged as transparent overlays and combined into a single inflated representation of the occipital lobe.

conditions with congenital chiasma malformations. This is taken as evidence for largely unaltered geniculo-striate connections despite congenitally abnormal input to the LGN (Hoffmann and Dumoulin, 2015), as summarized in Fig. 8A and B. In fact, it appears that the neuro-typical geniculo-striate projection is in general largely unaffected by enhanced or absent crossing at the optic chiasm as in albinism/FHONDA or achiasma, respectively (Ahmadi et al., 2019; Hoffmann and Dumoulin, 2015). Consequently, we asked which cortical organization pattern would result from such stability in the geniculo-cortical projections in the present case of chiasma hypoplasia, in whom the left V1 receives triple hemifield input. Such an input is expected to result in a combination of the normal organization, i.e. ocular dominance domains (Fig. 8A), and the organization found in complete achiasma, i.e. hemifield domains (Fig. 8B) as depicted in Fig. 8C: the abnormal ipsilateral input from the left nasal hemiretina and the residual normal input from the right nasal hemiretina are expected to converge into the same domain (Fig. 8C). In the absence of geniculo-striate rewiring, the resulting cortical organization pattern is a retinotopic representation of the contralateral visual hemifield, via the left eye, that is interleaved with combined retinotopic representations of the ipsilateral and contralateral hemifield, via the left and right eye respectively. We, therefore, termed it in analogy to the nomenclature introduced previously (Hoffmann and Dumoulin, 2015), 'Interleaved Combined Representation'. In fact, such a pattern would result in the macroscopic cortical mapping we observed in the left occipital lobe. It should be noted though that the domain receiving input from the right visual hemifield, receives input from both eyes, thus reducing the differential activation via the two eyes. Further, we can, at present, not tell whether the neuronal populations representing the right hemifield input from both eyes segregate into distinct neuronal populations, due to the unavailability of data with sufficient resolution. Taken together, stable geniculo-striate projections still hold true even in the presence of triple input as observed in CHP. This conservative projection scheme, therefore, appears to be the most parsimonious concept to explain the cortical maps observed in a set of congenital projection abnormalities of the optic nerves, i.e. for enhanced, reduced or absent crossing.

Remarkably, the triple hemifield input to the left hemisphere affects only, albeit extensively, part of the primary visual cortex. In fact, another part of the visual cortex receives largely exclusive input from both hemiretinae of the left eye, as typical for complete achiasma. As a consequence, there is a coexistence of the 'Interleaved Representation' (Fig. 8B) and 'Interleaved Combined Representation' (Fig. 8C), occupying different regions of the left primary visual cortex. This is in accordance with the reports of animal models of albinism indicating a mixed organization pattern in the primary visual cortex (Cooper and Blasdel, 1980). Taken together, this suggests that the relevant adaptive developmental mechanisms can act locally.

Consistent with the reports on complete achiasma (Davies-Thompson et al., 2013; Hoffmann et al., 2012; Olman et al., 2016; Victor et al., 2000), the participant of the present study made effective use of vision in daily life, including sport activities and reading, and did not present specific visual field defects. Nevertheless quantitative testing is required to assess the behavioral consequences of chiasma hypoplasia and the intactness of the visual perception in CHP. Despite the binocular input to the left visual cortex, the disruption of binocular and stereo-vision is expected in CHP due to vertical and horizontal deviations between the two eyes. This suggests that there is no relevant interaction of the three representations in the left visual cortex.

In analogy to findings in other conditions with chiasma abnormalities (Klemen et al., 2012; Olman et al., 2016; Victor et al., 2000), the three

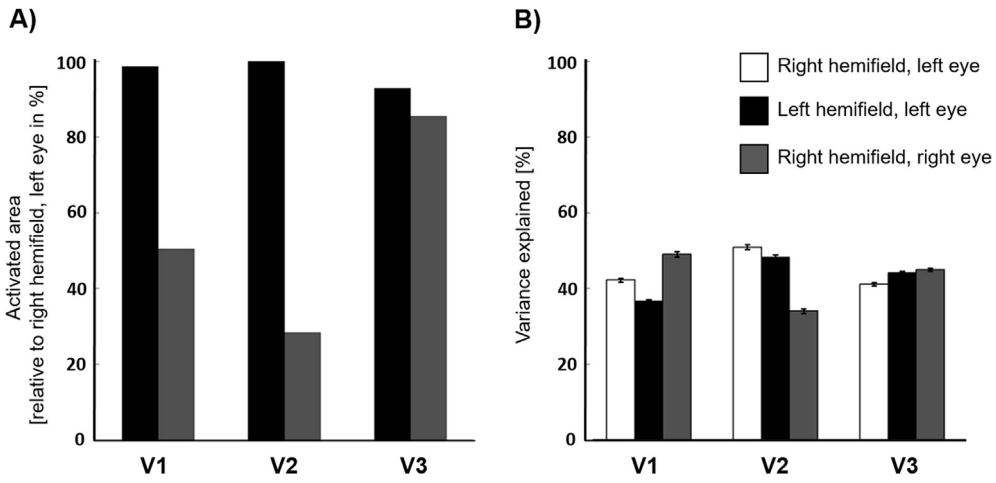

Fig. 7. Activated area and goodness of pRF model fit across left hemisphere V1–V3 of CHP. A) Activated area (normalized with respect to right hemifield, left eye stimulation condition) of left V1–V3 for left hemifield stimulation of the left eye (black bars) and right hemifield stimulation of the right eye (gray bars). For left hemifield stimulation of the left eye, the activated area of the left V1–V3 does not decrease below 92%. For the right hemifield stimulation of the right eye, the relative activated area of V1, V2 and, V3 is smaller, covering 50%, 28%, and 85%, respectively. **B)** Comparison of the goodness of fit, i.e. mean variance explained (VE) ± SEM, of the pRF model between right and left hemifield stimulation of the left eye (white and black bars) and right hemifield stimulation of the right eye (gray bars) in V1–V3 restricted to the overlapping area of the three maps (ROI_{3maps}). The VE for all three maps is relatively similar in V1 and V3 ranging from (49-37%) and (41–45%), respectively. For V2 it is reduced to 34% for the right hemifield right eye condition.

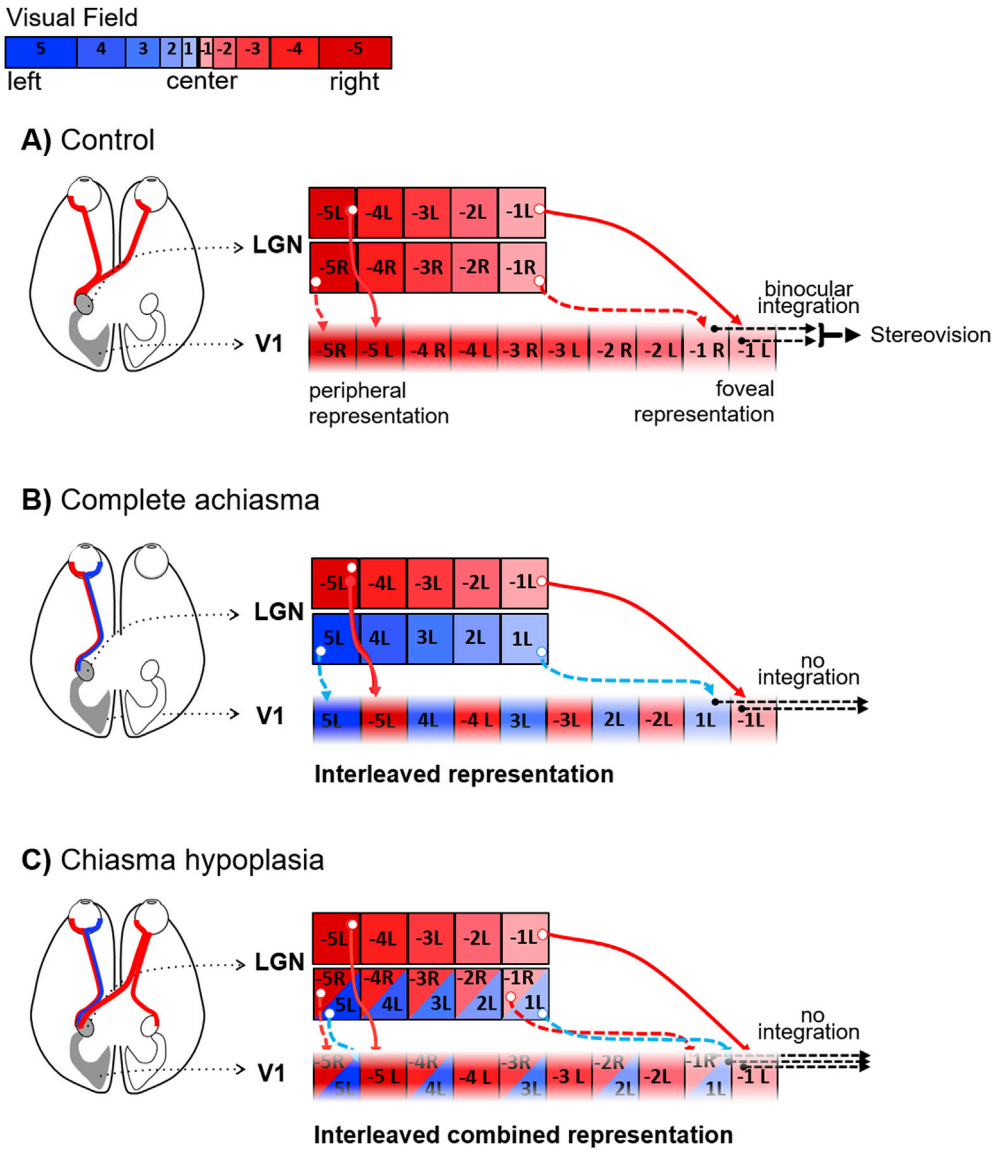

Fig. 8. Schematic of visual field representations in primary visual cortex for control, complete achiasma and chiasma hypoplasia. A) Control. The binocular input to the left LGN is organized as retinotopic maps of the right visual field (color coded red; negative numbers) that are separate for each eye (subscript indicates L – left, R – right eye input; the LGN is schematized as only two LGN layers with input from either eye). The geniculo-striate projections (solid red arrows for the left and dashed red arrows for the right eye input) result in interleaved retinotopic representations of the two eyes in V1. The integration of binocular input from corresponding locations in the contralateral visual field leads to binocular and stereovision. **B)** Complete achiasma. The left LGN receives monocular input from the nasal (blue) and from the temporal (red) hemiretina of the ipsilateral eye (i.e. left the eye, indicated by the subscript L). Consequently, there is in addition to the normal input from the contralateral visual field (red fields with negative numbers) input from the ipsilateral visual field (blue fields with positive numbers). This leads to an interleaved representation of opposing hemifields in V1, which is associated with a conservative, i.e. unchanged, geniculo-striate projection despite the abnormal LGN input (dashed cyan arrows). The absence of integration of the monocular input from opposing visual hemifields counteracts cross-talk of information between the hemifield. **C)** Chiasma hypoplasia. The left LGN receives binocular input from the contralateral visual field (red fields with negative numbers) as well as ipsilateral input (blue fields with positive numbers) only from the left eye. The triple hemifield input to the left LGN is organized as an interleaved representation of the contralateral visual field from the left eye (red fields with negative numbers in separate boxes) and combined representation of opposing hemifields from both eyes (red fields with negative numbers and blue fields with positive numbers in shared boxes). A conservative geniculo-striate projection to V1 would result in an interleaved combined representation pattern, obtained by the combination of cortical organization schemes for the control (A) and complete achiasma (B). Specifically, while the contralateral input of the left eye is incorporated via a separate domain, the contralateral input of the right eye together with the ipsilateral input of the left eye are assumed to be accommodated within a shared domain. Similar to complete achiasma, no integration is expected to occur across the three hemifield representations, supporting independent processing of the three maps.

representations of the hemifields in the left primary visual cortex might drive visual perception independently. Further research addressing the independence of the three different maps is motivated by the current findings. Lack of integration of information across the ocular dominance and/or across the hemifield dominance domains in CHP would require plasticity of the intracortical micro-circuitry to cope with the abnormal visual input and to support independent processing of the three superimposed hemifields (Fig. 8).

Akin to other visual pathway abnormalities, it is therefore assumed that the aberrant representation in CHP is made available for relatively normal visual perception through the interplay of subcortical stability and cortical plasticity. The cortical plasticity might not be confined to changes in the intra-cortical connectivity and, in addition, affect the cortico-cortical connectivity as suggested by changes in pRF and CF size

estimates (Figure S4). It, therefore, appears that the extra-input from the right eye impacts on the cortico-cortical connectivity of the early visual areas in CHP.

Studying visual system abnormalities is a unique approach for advancing our insights into the interplay of pathology and plasticity directly in humans and for gaining an understanding of the underlying developmental principles. A common limitation, however, is the rarity of relevant conditions and hence the limited availability of affected individuals. This also applies to the field of congenital malformations of the optic chiasm. While the well-known enhanced crossing of the optic nerves in albinism is already a rare condition [1.17:000 (Grønskov et al., 2007);], reduced crossing, i.e. achiasma, is much rarer [< 50 cases published worldwide (Hoffmann and Dumoulin, 2015),]. In fact, fMRI-data have been reported in the past two decades for only 6 different individuals (Bao et al., 2015; Davies-Thompson et al., 2013; Hoffmann et al., 2012; Nguyen et al., 2018; Victor et al., 2000). Thus, investigating a subtype of achiasma, i.e. with the specific hypoplasia of the optic chiasm reported in the present study, is an exceptional case. As such, we did not have the opportunity to obtain additional data for this condition, neither from the present nor from other individuals, despite the potentially informative value of e.g. additional high-resolution fMRI data. Another limitation of investigating visual system pathologies is related to fixation instabilities. Particularly, the dependence of the retinotopic data on the fixation stability may be questioned. However, previous studies (Baseler et al., 2002; Levin et al., 2010) have shown that nystagmus and fixation instability result in an enlargement of the pRF sizes without having a major effect on the eccentricity and polar angle maps. The high quality of the retinotopic maps, i.e., systematic response signatures typical of retinotopic maps, in CHP implies sufficiently stable fixation, though it could have been ideal to record the fixation performance in each eye separately.

Furthermore, while the present case is unique, it shares features, previously reported for achiasma, i.e. the retinotopic overlay of opposing visual hemifields (Hoffmann and Dumoulin, 2015). This is taken as an indication of the overall quality of the functional data obtained. Specifically, the data-set allowed reproducing previous results, i.e. orderly eccentricity and polar-angle maps from opposing visual hemifields via the ipsilateral (left) eye, and adding a further feature, i.e. the third input to the left visual cortex via the contralateral (right) eye. Stimulus-induced deviations from central fixation would be expected to be specific to the visual stimuli applied. Importantly, the activation in the cortical region comprising the additional third input was reproducible for different stimulation conditions applied via the right eye, i.e., for bilateral stimulation (Fig. 2B) and for right hemifield mapping (Fig. 5C).

Further, the amount of the overlap between the 3T and 7T data could not be quantified due to inherent differences in data acquisition one of which was the acquisition of 2 distinct anatomical volumes with different spatial resolutions. The visual area boundaries obtained by the pRF mapping could have been projected to the 7T data at the expense of downsampling the high resolution anatomy acquired at 7T. Nonetheless, careful visual inspection suggests a high degree of overlapping activity in cortical regions receiving the additional third input in both stimulation conditions. We conclude that fixation instabilities are a highly unlikely source of the observed cortical triple maps.

It might be argued that the comparison of the observed findings in CHP with strabismic amblyopes with a similar level of visual acuity and strabismus might be more informative than that with healthy controls. However, the effects of amblyopia on the organization of the visual cortex remain controversial. While some studies suggest a shift in ocular dominance of neural activity toward the fellow eye (Goodyear et al., 2002; Crawford and Harwerth, 2004), others have found no alteration or shrinkage of the ocular dominance domains (Horton and Hocking, 1996). Importantly, it has been demonstrated that despite the increased pRF sizes for the amblyopic eye, the retinotopic representations are preserved in strabismic amblyopia (Clavagnier et al., 2015). It is therefore concluded that the interpretation of the observed striking cortical organization in CHP does not hinge on the comparison group.

In addition, a few methodological considerations should be addressed. In the present study, partial Fourier acquisition (Feinberg et al., 1986) was employed in the high-resolution fMRI data. This approach is commonly used to accelerate the acquisition time or shorten the echo train length, albeit at the cost of image blurring (Feinberg et al., 2018). The blurring can be mitigated by use of partial Fourier imaging with a higher factor or with full Fourier acquisition. This results in a prolonged TE, whereas minimal acquisition time and consequently reduced motion artifacts had a higher priority in this experiment. It should also be noted, that the accuracy of the DWI analysis depends on the angle of crossing fibers (Tournier et al., 2008). This limitation is of particular relevance to this study, where the analyzed groups displayed various angles between crossing fibers. To address this issue, the DWI data were collected with the custom protocol designed to resolve crossing fibers [b-value of 1600 s/mm^2 selected according to reported range of 1500–2500 s/mm^2, optimal for resolving two-way crossing (Sotiropoulos et al., 2013); high angular resolution granted by 128 unique gradient directions (Tuch et al., 2002)] and analyzed with the methods ensuring the optimal discrimination between separate fiber populations, such as the Multi-Tissue constrained spherical deconvolution (Jeurissen et al., 2014).

5. Conclusion

Congenital visual pathway abnormalities are powerful models to further our understanding of the scope of developmental stability and plasticity in the human visual system, which may impact on novel therapeutic approaches. Here, we demonstrate that the gross topography of the geniculo-striate projections in CHP remains chiefly unaltered resulting in triple hemifield input to the visual cortex. This reflects an unaltered geniculo-cortical axonal guidance by chemoaffinity gradients (Cang et al., 2005; McLaughlin and O'Leary, 2005), even in the face of severely erroneous input to LGN. The additional input to the left visual cortex is assumed to be incorporated by sharing the same domain between the abnormal input of the left eye and normal input of the right eye. This underlines that intra-cortical plasticity provides sufficient scope to accommodate highly atypical visual input for comparatively normal visual processing.

Author contributions

K.A., A.F., A.D.G., S.O.D., A.B.M., and M.B.H: Conceptualization, K.A., A.F., R.J.P A.D.G., R.Y., O.S., J.K., F.P., and M.B.H: Methodology, K.A., A.F., and R.J.P: Formal Analysis, K.A., A.D.G., A.B.M., and M.B.H: Investigation, K.A., R.J.P: Writing – Original Draft, K.A., A.F., R.J.P., J.K., O.S., F.P., S.O.D., A.B.M., and M.B.H: Writing – Review and Editing, M.B.H: Supervision.

Declaration of competing interest

The authors declare no competing interests.

Acknowledgements

The authors thank the study participants for their patience and cooperation. This work was supported by European Union's Horizon 2020 research and innovation programme under the Marie Sklodowska-Curie grant agreement (No. 641805) to S.O.D, A.B.M and M.B.H, by the German Research Foundation (DFG; HO2002 10-3) to MBH. A.F. was supported by the Biotechnology and Biology research council (BBSRC, grant number: BB/S006605/1).

Appendix A. Supplementary data

Supplementary data to this article can be found online at https://doi.org/10.1016/j.neuroimage.2020.116822.

References

Ahmadi, K., Fracasso, A., van Dijk, J.A., Kruijt, C., van Genderen, M., Dumoulin, S.O., Hoffmann, M.B., 2019. Altered organization of the visual cortex in FHONDA syndrome. NeuroImage, Mapping diseased brains 190, 224–231. https://doi.org/10.1016/j.neuroimage.2018.02.053.

Amano, K., Wandell, B.A., Dumoulin, S.O., 2009. Visual field maps, population receptive field sizes, and visual field coverage in the human MT+ complex. J. Neurophysiol. 102 (5), 2704–2718.

Andersson, J.L., Skare, S., Ashburner, J., 2003. How to correct susceptibility distortions in spin-echo echo-planar images: application to diffusion tensor imaging. Neuroimage 20, 870–888.

Apkarian, P., Bour, L., Barth, P.G., 1994. A unique achiasmatic anomaly detected in non-albinos with misrouted retinal-fugal projections. Eur. J. Neurosci. 6, 501–507.

Apkarian, P., Reits, D., Spekreijse, H., Van Dorp, D., 1983. A decisive electrophysiological test for human albinism. Electroencephalogr. Clin. Neurophysiol. 55, 513–531.

Bao, P., Purington, C.J., Tjan, B.S., 2015. Using an achiasmic human visual system to quantify the relationship between the fMRI BOLD signal and neural response. eLife 4, e09600. https://doi.org/10.7554/eLife.09600.

Baseler, H.A., Brewer, A.A., Sharpe, L.T., Morland, A.B., Jägle, H., Wandell, B.A., 2002. Reorganization of human cortical maps caused by inherited photoreceptor abnormalities. Nat. Neurosci. 5 (4), 364.

Bazin, P.-L., Pham, D.L., 2007. Topology-preserving tissue classification of magnetic resonance brain images. IEEE Trans. Med. Imag. 26, 487–496.

Brainard, D.H., 1997. The psychophysics toolbox. Spat. Vis. 10, 433–436.

Cang, J., Kaneko, M., Yamada, J., Woods, G., Stryker, M.P., Feldheim, D.A., 2005. Ephrin-as guide the formation of functional maps in the visual cortex. Neuron 48, 577–589.

Caruyer, E., Lenglet, C., Sapiro, G., Deriche, R., 2013. Design of multishell sampling schemes with uniform coverage in diffusion MRI. Magn. Reson. Med. 69, 1534–1540.

Clavagnier, S., Dumoulin, S.O., Hess, R.F., 2015. Is the cortical deficit in amblyopia due to reduced cortical magnification, loss of neural resolution, or neural disorganization? J. Neurosci. 35, 14740–14755.

Cooper, M.L., Blasdel, G.G., 1980. Regional variation in the representation of the visual field in the visual cortex of the Siamese cat. J. Comp. Neurol. 193, 237–253.

Crawford, M.L., Harwerth, R.S., 2004. Ocular dominance column width and contrast sensitivity in monkeys reared with strabismus or anisometropia. Invest. Ophthalmol. Vis. Sci. 45 (9), 3036–3042.

Davies-Thompson, J., Scheel, M., Lanyon, L.J., Barton, J.J.S., 2013. Functional organisation of visual pathways in a patient with no optic chiasm. Neuropsychologia 51, 1260–1272. https://doi.org/10.1016/j.neuropsychologia.2013.03.014.

Dumoulin, S.O., Wandell, B.A., 2008. Population receptive field estimates in human visual cortex. Neuroimage 39, 647–660. https://doi.org/10.1016/j.neuroimage.2007.09.034.

Feinberg, D.A., Hale, J.D., Watts, J.C., Kaufman, L., Mark, A., 1986. Halving MR imaging time by conjugation: demonstration at 3.5 kG. Radiology 161 (2), 527–531.

Feinberg, D.A., Vu, A.T., Beckett, A., 2018. Pushing the limits of ultra-high resolution human brain imaging with SMS-EPI demonstrated for columnar level fMRI. Neuroimage 164, 155–163.

Fracasso, A., Koenraads, Y., Porro, G.L., Dumoulin, S.O., 2016. Bilateral population receptive fields in congenital hemihydranencephaly. Ophthalmic Physiol. Optic. 36, 324–334.

Fracasso, A., Luijten, P.R., Dumoulin, S.O., Petridou, N., 2018. Laminar imaging of positive and negative BOLD in human visual cortex at 7 T. Neuroimage 164, 100–111.

Friston, K.J., Fletcher, P., Josephs, O., Holmes, A., Rugg, M.D., Turner, R., 1998. Event-related fMRI: characterizing differential responses. Neuroimage 7, 30–40. https://doi.org/10.1006/nimg.1997.0306.

Goodyear, B.G., Nicolle, D.A., Menon, R.S., 2002. High resolution fMRI of ocular dominance columns within the visual cortex of human amblyopes. Strabismus 10 (2), 129–136.

Grønskov, K., Ek, J., Brondum-Nielsen, K., 2007. Oculocutaneous albinism. Orphanet J. Rare Dis. 2, 43.

Guillery, R.W., Hickey, T.L., Kaas, J.H., Felleman, D.J., Debruyn, E.J., Sparks, D.L., 1984. Abnormal central visual pathways in the brain of an albino green monkey (Cercopithecus aethiops). J. Comp. Neurol. 226, 165–183. https://doi.org/10.1002/cne.902260203.

Haak, K.V., Winawer, J., Harvey, B.M., Renken, R., Dumoulin, S.O., Wandell, B.A., Cornelissen, F.W., 2013. Connective field modeling. Neuroimage 66, 376–384.

Han, X., Pham, D.L., Tosun, D., Rettmann, M.E., Xu, C., Prince, J.L., 2004. CRUISE: cortical reconstruction using implicit surface evolution. Neuroimage 23, 997–1012.

Harvey, B.M., Dumoulin, S.O., 2011. The relationship between cortical magnification factor and population receptive field size in human visual cortex: constancies in cortical architecture. J. Neurosci. Off. J. Soc. Neurosci. 31, 13604–13612. https://doi.org/10.1523/JNEUROSCI.2572-11.2011.

Hoffmann, M.B., Dumoulin, S.O., 2015. Congenital visual pathway abnormalities: a window onto cortical stability and plasticity. Trends Neurosci. 38, 55–65. https://doi.org/10.1016/j.tins.2014.09.005.

Hoffmann, M.B., Kaule, F.R., Levin, N., Masuda, Y., Kumar, A., Gottlob, I., Horiguchi, H., Dougherty, R.F., Stadler, J., Wolynski, B., Speck, O., Kanowski, M., Liao, Y.J., Wandell, B.A., Dumoulin, S.O., 2012. Plasticity and stability of the visual system in human achiasma. Neuron 75, 393–401. https://doi.org/10.1016/j.neuron.2012.05.026.

Hoffmann, M.B., Seufert, P.S., Schmidtborn, L.C., 2007. Perceptual relevance of abnormal visual field representations: static visual field perimetry in human albinism. Br. J. Ophthalmol. 91, 509–513. https://doi.org/10.1136/bjo.2006.094854.

Hoffmann, M.B., Tolhurst, D.J., Moore, A.T., Morland, A.B., 2003. Organization of the visual cortex in human albinism. J. Neurosci. Off. J. Soc. Neurosci. 23, 8921–8930.

Horton, J.C., Hocking, D.R., 1996. Pattern of ocular dominance columns in human striate cortex in strabismic amblyopia. Vis. Neurosci. 13, 787–795.

Huberman, A.D., Feller, M.B., Chapman, B., 2008. Mechanisms underlying development of visual maps and receptive fields. Annu. Rev. Neurosci. 31, 479–509.

In, M.-H., Speck, O., 2012. Highly accelerated PSF-mapping for EPI distortion correction with improved fidelity. Magn. Reson. Mater. Phys. Biol. Med. 25, 183–192.

Jeurissen, B., Tournier, J.-D., Dhollander, T., Connelly, A., Sijbers, J., 2014. Multi-tissue constrained spherical deconvolution for improved analysis of multi-shell diffusion MRI data. Neuroimage 103, 411–426.

Kaule, F.R., Wolynski, B., Gottlob, I., Stadler, J., Speck, O., Kanowski, M., Meltendorf, S., Behrens-Baumann, W., Hoffmann, M.B., 2014. Impact of chiasma opticum malformations on the organization of the human ventral visual cortex. Hum. Brain Mapp. 35, 5093–5105. https://doi.org/10.1002/hbm.22534.

Klein, B.P., Fracasso, A., van Dijk, J.A., Paffen, C.L., Te Pas, S.F., Dumoulin, S.O., 2018. Cortical depth dependent population receptive field attraction by spatial attention in human V1. Neuroimage 176, 301–312.

Klemen, J., Hoffmann, M.B., Chambers, C.D., 2012. Cortical plasticity in the face of congenitally altered input into V1. Cortex J. Devoted Study Nerv. Syst. Behav. 48, 1362–1365. https://doi.org/10.1016/j.cortex.2012.03.012.

Lee, S., Papanikolaou, A., Logothetis, N.K., Smirnakis, S.M., Keliris, G.A., 2013. A new method for estimating population receptive field topography in visual cortex. Neuroimage 81, 144–157.

Levin, N., Dumoulin, S.O., Winawer, J., Dougherty, R.F., Wandell, B.A., 2010. Cortical maps and white matter tracts following long period of visual deprivation and retinal image restoration. Neuron 65 (1), 21–31.

McLaughlin, T., O'Leary, D.D., 2005. Molecular gradients and development of retinotopic maps. Annu. Rev. Neurosci. 28, 327–355.

Muckli, L., Naumer, M.J., Singer, W., 2009. Bilateral visual field maps in a patient with only one hemisphere. Proc. Natl. Acad. Sci. Unit. States Am. 106, 13034–13039. https://doi.org/10.1073/pnas.0809688106.

Nguyen, C.T., Goh, C., Desmond, P., Abel, L.A., Lim, C.H., Symons, R.A., Hardy, T.G., 2018. Congenital achiasma and see-saw nystagmus in VATER syndrome association with hydrocephalus. J. Clin. Neurosci. 51, 63–65.

Olman, C.A., Bao, P., Engel, S.A., Grant, A.N., Purington, C., Qiu, C., Schallmo, M.-P., Tjan, B.S., 2016. Hemifield columns co-opt ocular dominance column structure in human achiasma. Neuroimage.

Pelli, D.G., 1997. The VideoToolbox software for visual psychophysics: transforming numbers into movies. Spat. Vis. 10, 437–442.

Puzniak, R.J., Ahmadi, K., Kaufmann, J., Gouws, A., Morland, A.B., Pestilli, F., Hoffmann, M.B., 2019. Quantifying nerve decussation abnormalities in the optic chiasm. Neuroimage: Clin. https://doi.org/10.1016/j.nicl.2019.102055.

Saad, Z.S., Glen, D.R., Chen, G., Beauchamp, M.S., Desai, R., Cox, R.W., 2009. A new method for improving functional-to-structural MRI alignment using local Pearson correlation. Neuroimage 44, 839–848.

Sami, D.A., Saunders, D., Thompson, D.A., Russell-Eggitt, I.M., Nischal, K.K., Jeffery, G., Dattani, M., Clement, R.A., Liassis, A., Taylor, D.S., 2005. The achiasmia spectrum: congenitally reduced chiasmal decussation. Br. J. Ophthalmol. 89, 1311–1317.

Smith, R.E., Tournier, J.-D., Calamante, F., Connelly, A., 2012. Anatomically-constrained tractography: improved diffusion MRI streamlines tractography through effective use of anatomical information. Neuroimage 62, 1924–1938.

Sotiropoulos, S.N., Jbabdi, S., Xu, J., Andersson, J.L., Moeller, S., Auerbach, E.J., Glasser, M.F., Hernandez, M., Sapiro, G., Jenkinson, M., Feinberg, D.A., 2013. Advances in diffusion MRI acquisition and processing in the human connectome project. Neuroimage 80, 125–143.

Takemura, H., Caiafa, C.F., Wandell, B.A., Pestilli, F., 2016. Ensemble tractography. PLoS Comput. Biol. 12, e1004692.

Tootell, R.B., Mendola, J.D., Hadjikhani, N.K., Liu, A.K., Dale, A.M., 1998. The representation of the ipsilateral visual field in human cerebral cortex. Proc. Natl. Acad. Sci. Unit. States Am. 95, 818–824.

Tournier, J.-D., Calamante, F., Connelly, A., 2013. Determination of the appropriate b value and number of gradient directions for high-angular-resolution diffusion-weighted imaging. NMR Biomed. 26, 1775–1786.

Tournier, J.D., Calamante, F., Connelly, A., 2010. Improved probabilistic streamlines tractography by 2nd order integration over fibre orientation distributions. In: Proceedings of the International Society for Magnetic Resonance in Medicine, p. 1670.

Tournier, J.-D., Yeh, C.-H., Calamante, F., Cho, K.-H., Connelly, A., Lin, C.-P., 2008. Resolving crossing fibres using constrained spherical deconvolution: validation using diffusion-weighted imaging phantom data. Neuroimage 42, 617–625.

Tuch, D.S., Reese, T.G., Wiegell, M.R., Makris, N., Belliveau, J.W., Wedeen, V.J., 2002. High angular resolution diffusion imaging reveals intravoxel white matter fiber heterogeneity. Magn. Reson. Med. Off. J. Int. Soc. Magn. Reson. Med. 48, 577–582.

Van de Moortele, P.-F., Auerbach, E.J., Olman, C., Yacoub, E., Uğurbil, K., Moeller, S., 2009. T1 weighted brain images at 7 Tesla unbiased for Proton Density, T2* contrast

and RF coil receive B1 sensitivity with simultaneous vessel visualization. Neuroimage 46, 432–446.
Victor, J.D., Apkarian, P., Hirsch, J., Conte, M.M., Packard, M., Relkin, N.R., Kim, K.H., Shapley, R.M., 2000. Visual function and brain organization in non-decussating retinal-fugal fibre syndrome. Cereb. Cortex 10, 2–22. N. Y. N 1991.
von dem Hagen, E.A.H., Hoffmann, M.B., Morland, A.B., 2008. Identifying human albinism: a comparison of VEP and fMRI. Invest. Ophthalmol. Vis. Sci. 49, 238–249. https://doi.org/10.1167/iovs.07-0458.
Waehnert, M.D., Dinse, J., Weiss, M., Streicher, M.N., Waehnert, P., Geyer, S., Turner, R., Bazin, P.-L., 2014. Anatomically motivated modeling of cortical laminae. Neuroimage 93, 210–220.
Wandell, B.A., Chial, S., Backus, B.T., 2000. Visualization and measurement of the cortical surface. J. Cognit. Neurosci. 12, 739–752.
Wandell, B.A., Dumoulin, S.O., Brewer, A.A., 2007. Visual field maps in human cortex. Neuron 56, 366–383.
Weber, K.P., Landau, K., 2013. Teaching NeuroImages: mind the gap! Postfixational blindness due to traumatic rupture of the optic chiasm. Neurology 80, e197–e198.
Zeidman, P., Silson, E.H., Schwarzkopf, D.S., Baker, C.I., Penny, W., 2018. Bayesian population receptive field modelling. Neuroimage 180, 173–187.

Chapter 8

Deep learning-based detection of malformed optic chiasms

This chapter contains the permitted reprint of the study **"Deep learning-based detection of malformed optic chiasms from MRI images"** published in *Frontiers in the Neuroscience*:

Puzniak, R. J., Prabhakaran, G. T., and Hoffmann, M. B. (2021). "Deep Learning-Based Detection of Malformed Optic Chiasms From MRI Images". In: *Frontiers in Neuroscience* 15, p. 1332. DOI: 10.3389/fnins.2021.755785

frontiers in Neuroscience

ORIGINAL RESEARCH
published: 25 October 2021
doi: 10.3389/fnins.2021.755785

Deep Learning-Based Detection of Malformed Optic Chiasms From MRI Images

Robert J. Puzniak[1†], Gokulraj T. Prabhakaran[1] and Michael B. Hoffmann[1,2†]*

[1] Visual Processing Lab, Department of Ophthalmology, Otto-von-Guericke-University, Magdeburg, Germany, [2] Center for Behavioral Brain Sciences, Otto-von-Guericke-University, Magdeburg, Germany

Convolutional neural network (CNN) models are of great promise to aid the segmentation and analysis of brain structures. Here, we tested whether CNN trained to segment normal optic chiasms from the T1w magnetic resonance imaging (MRI) image can be also applied to abnormal chiasms, specifically with optic nerve misrouting as typical for human albinism. We performed supervised training of the CNN on the T1w images of control participants (n = 1049) from the Human Connectome Project (HCP) repository and automatically generated algorithm-based optic chiasm masks. The trained CNN was subsequently tested on data of persons with albinism (PWA; n = 9) and controls (n = 8) from the CHIASM repository. The quality of outcome segmentation was assessed *via* the comparison to manually defined optic chiasm masks using the Dice similarity coefficient (DSC). The results revealed contrasting quality of masks obtained for control (mean DSC ± SEM = 0.75 ± 0.03) and PWA data (0.43 ± 0.8, few-corrected p = 0.04). The fact that the CNN recognition of the optic chiasm fails for chiasm abnormalities in PWA underlines the fundamental differences in their spatial features. This finding provides proof of concept for a novel deep-learning-based diagnostics approach of chiasmal misrouting from T1w images, as well as further analyses on chiasmal misrouting and their impact on the structure and function of the visual system.

Keywords: chiasmal malformations, albinism, convolutional neural network, CNN, nerve misrouting, misrouting detection, optic chiasm

OPEN ACCESS

Edited by:
Holly Bridge,
University of Oxford, United Kingdom

Reviewed by:
John Mwangi Wandeto,
Dedan Kimathi University of Technology, Kenya
Denis Scluppeck,
University of Nottingham, United Kingdom

****Correspondence:***
Michael B. Hoffmann
michael.hoffmann@med.ovgu.de

†ORCID:
Robert J. Puzniak
orcid.org/0000-0001-9690-8547
Michael B. Hoffmann
orcid.org/0000-0002-6452-9638

Specialty section:
This article was submitted to Perception Science, a section of the journal Frontiers in Neuroscience

Received: *09 August 2021*
Accepted: *16 September 2021*
Published: *25 October 2021*

Citation:
Puzniak RJ, Prabhakaran GT and Hoffmann MB (2021) Deep Learning-Based Detection of Malformed Optic Chiasms From MRI Images. Front. Neurosci. 15:755785. doi: 10.3389/fnins.2021.755785

INTRODUCTION

The optic chiasm is a key structure in the visual system, where the fate of axons from the retina is decided, such that axons carrying information from the right visual hemifield are guided to the left hemisphere and vice versa. Accordingly, the axons split in the chiasm into two bundles, i.e., axons from the nasal retina that project to the contralateral brain hemisphere (also referred to as "crossing nerves"), and axons from the temporal retina that project to the ipsilateral hemisphere ("non-crossing nerves"). While the normal proportion of axons in the crossing and non-crossing bundle is well established and determined by histological studies to be equal to 53:47, respectively (Kupfer et al., 1967), several congenital disorders are known to affect this arrangement. One example is albinism, where the abnormal development of the visual system (Rebsam et al., 2012) leads to enhanced crossing of the optic nerves at the chiasm resulting in an altered organization of the signal flow in the visual system (Hoffmann et al., 2003). Interestingly, although the altered input to the visual cortex would be expected to fundamentally disrupt signal integration, basic aspects of visual function are preserved, while others (binocular vision, visual acuity, fixation stability) are

reduced (Hoffmann and Dumoulin, 2015). This preservation of basic aspects is likely related to processes of cortical plasticity (Hoffmann et al., 2003; Hoffmann and Dumoulin, 2015; Ahmadi et al., 2019) and as such makes human albinism a unique and powerful model of neuroplasticity, granting insights into the structure–function relationship of the visual system. This kind of analysis, however, requires unambiguous and noninvasive mapping of chiasm's structural features, which is not yet resolved. The first anatomical MRI-based reports (aMRI) of chiasm morphology reported the absence of meaningful anatomical features distinguishing normal and abnormal chiasms (Brodsky et al., 1993). In contrast, two later studies reported differences when comparing chiasm sizes and configurations between controls and people with albinism [PWA; (Schmitz et al., 2003; von dem Hagen et al., 2005)]. Specifically, both studies provided significant evidence of reductions in the width of optic nerves and optic chiasm in PWA, with Schmitz et al. additionally reporting thinner optic nerves and wider angles between optic tracts. Unfortunately, both studies reported group differences but did not explain the aforementioned distinguishing features in the context of diagnostics of chiasmal malformations. Effectively, it is unknown which anatomical features of the chiasm may be employed in an individualized detection of malformations or whether such a detection is possible in the first place. Recently, the application of anatomy-sensitive diffusion MRI (dMRI), capable of estimating the proportion of crossing and non-crossing nerves *via* tractography (Puzniak et al., 2021), has demonstrated chiasmal malformations in albinism at the group level (Ather et al., 2018) with potential for an individualized diagnostic utility (Puzniak et al., 2019). It must be noted, however, that dMRI as compared to aMRI is time consuming at the level of both data acquisition and data analysis. Considering the aforementioned challenges of accurate modeling of chiasmal malformations, it would be of benefit to revisit this issue using models capable of autonomous feature extraction from aMRI data, such as convolutional neural networks [CNNs; (LeCun et al., 1989; Krizhevsky et al., 2012)].

Convolutional neural networks (CNN) are a class of artificial neural networks, i.e., data-driven models inspired by biological systems which are shown to greatly benefit fields relying on computer vision, such as medical imaging (Lundervold and Lundervold, 2019). They are being successfully applied in tasks requiring recognition (segmentation) of brain structures, including the ones involving the optic chiasm (Ibragimov and Xing, 2017; Tong et al., 2018; Chen et al., 2019; Zhu et al., 2019; Duanmu et al., 2020; Mlynarski et al., 2020). This is in particular true for the attempts using MRI data, which have been demonstrated to provide superior contrast and recognition of optic chiasm boundaries compared to other imaging techniques, such as computer tomography (Ibragimov and Xing, 2017; Duanmu et al., 2020). The CNNs, however, are not a universal tool, as their performance is largely dependent on both the quantity and quality of the training data. Consequently, this hinders the development of CNNs in the fields with limited data availability (e.g., due to high data acquisition costs), such as neuroimaging. The above-described limitation is even further augmented in the proposed comparative analysis of normal and abnormal chiasms, where the rarity of albinism [estimated prevalence of albinism equal to 1: 20,000 according to Marçon and Maia (2019)] severely impacts the availability of data from such rare patient groups. These limitations may be counteracted to some degree by known techniques, e.g., transfer learning, allowing to fine-tune existing networks to new data with smaller samples instead of training from scratch. In the present work, we explored the potential of CNNs for the detection of chiasmal abnormalities. For this end, we employed a method that is independent of hardly available, sizable datasets of abnormal chiasms at the expense of interpretability, as discussed in *Limitations*. Specifically, we investigated whether CNNs trained for the purpose of optic chiasm segmentation on control data only, lead to erroneous segmentations for abnormal optic chiasms, e.g., in albinism. Such a differential performance of CNN on normal and abnormal chiasms could be utilized in a quantitative approach for the detection of chiasm abnormalities in albinism and potentially beyond. Currently, albinism diagnosis is based on several morphological and functional features (Hoffmann et al., 2007; Hoffmann and Dumoulin, 2015), with abnormal crossing in the chiasm being one of the major criteria (Kruijt et al., 2018). This is being routinely assessed with functional methods (Hoffmann et al., 2005; von dem Hagen et al., 2008), which are, however, affected by patients' functional limitations, such as low visual acuity or nystagmus as typical for albinism. Although these limitations would be absent for anatomy-based assessments, the only up-to-date successful reported attempt of an individualized detection of the chiasm abnormalities was achieved with dMRI (Puzniak et al., 2019), which required complex and time-consuming data acquisition and analysis extending beyond the clinical standards. Consequently, the successful CNN-based identification of abnormal chiasms *via* aMRI might provide proof of concept for a novel tool which can be applied to diagnostics, e.g., in albinism.

MATERIALS AND METHODS

Rationale

The objective of this study was to investigate the scope of diagnosing chiasmal malformations using the CNN's performance as an indicator. For this purpose, we trained a CNN for the segmentation of normal optic chiasms from T1-weighted (T1w) MRI images. This would ideally be achieved by using already developed networks. However, their lacking validation on external datasets, a common issue in the field of DL (Yao et al., 2020), required the development of a custom new network for this purpose and subsequent testing on MRI images of PWA with malformed chiasms. The accuracy of the CNN, determined *via* the comparison of predicted chiasmal masks with previously hand-curated ground-truth masks, is expected to reveal whether representations of malformed chiasms can be learned from control data only. Consequently, the results provide a deeper understanding on whether malformed chiasms are included in the segmentation of representations learned from the control data. This finding is expected to be of value for the

clinical diagnostics of malformations, as well as basic research on mechanisms guiding malformation of the chiasms.

Workflow

This section details the description of the process, the pipeline, and its components, specifically the type of MRI data employed in the training and testing of the CNN, generation of optic chiasm masks by automatic and manual delineation, data augmentation, CNN training, evaluation of CNN on MRI data of controls and PWA, and the metrics used. The graphical overview of the workflow is provided in **Figure 1**.

MRI Data

T1w anatomical MRI images of the brain were acquired using 3T MRI. The MRI data came from two separate, publicly available datasets and were used in the (i) training and (ii) evaluation of CNN. Specifically, the CNN was (i) trained on the Human Connectome Project (HCP) dataset (Van Essen et al., 2013), containing nearly 1,200 T1w structural MRIs from control participants, and (ii) tested on the CHIASM dataset (Puzniak et al., in revision)[1], a repository containing T1w images of patients with rare chiasmal disorders including PWA (n = 9) and controls (n = 8).

HCP Dataset

The CNN was trained on control T1w images (n = 1049) from the HCP Dataset—Diffusion MRI 3T 1200 Subjects (S1200) Release (Glasser et al., 2013; Van Essen et al., 2013) downloaded from the brainlife.io platform (Avesani et al., 2019)[2]. As detailed in the PreFreeSurfer pipeline from HCP Minimal Preprocessing Pipelines (Glasser et al., 2013), for each subject, the T1w images acquired with native 0.7-mm isotropic resolution were defaced (Milchenko and Marcus, 2013), aligned to MNI152 template space (rigid-body transformation with 6 degrees of freedom), and corrected for readout distortions (van der Kouwe et al., 2008). The preprocessed images were further resampled to 1.25-mm isotropic resolution to match the resolution of the HCP DWI data. Importantly, the downsampling was also a prerequisite for further segmentation of T1w images with FreeSurfer software.

CHIASM Dataset

The performance of the trained CNN was tested on the T1w MRI images of PWA (n = 9) and controls (n = 8) from the CHIASM dataset (Puzniak et al., in revision, see footnote 1) downloaded from the brainlife.io platform (Avesani et al., 2019)[3]. As preprocessing steps, for each subject, T1w images acquired with native resolution of 0.9 mm were defaced, aligned to Anterior Commissure—Posterior Commissure (ACPC) space, and downsampled to 1-mm isotropic voxel (in order to support FreeSurfer segmentation).

[1]Puzniak, R. J., et al. (in revision). CHIASM, The Human Brain Albinism and Achiasma MRI Dataset.

[2]https://brainlife.io/project/5941a225f876b000210c11e5

[3]https://brainlife.io/pub/5dea42a96c0bd9c0508554a2

Optic Chiasm Masks

The T1w MRI images were further used to generate several binary optic chiasm masks through varied approaches. Specifically, this included manually defined ground-truth masks, automatically created masks used for CNN training, and masks of the chiasm computed by the CNN (**Figure 2**). Although automatically created masks from neuroimaging data are known to be of suboptimal quality (as opposed to ones manually defined by experts), we decided for this approach as it enabled us to analyze a wide range of chiasmal morphologies. This is, in fact, a requisite for the CNNs to robustly identify the well-generalizing features of the chiasm. An overview of the employed masks is provided below, followed by detailed descriptions in the subsequent sections:

- X-mask$_{manual}$—optic chiasm mask defined manually on T1w MRI images.
- X-mask$_{atlas-initial}$—optic chiasm mask created by FreeSurfer's atlas-based segmentation of HCP training set (n = 1049) and CHIASM (n = 17) T1w images.
- X-mask$_{atlas-corrected}$—improved optic chiasm masks obtained by correcting X-mask$_{atlas-initial}$ with a custom correction algorithm.
- X-mask$_{CNN}$—optic chiasm mask computed by the CNN from input T1w image. The X-mask$_{NN}$ were generated only for the CHIASM (n = 17) dataset and a subset of HCP datasets (n = 10; HCP test-controls), which were excluded from CNN's training and validation procedure (**Figure 2A**).

Importantly, for the purpose of quality evaluation (see *Computational methods*), the assessed masks were limited only to the axial slices, where the optic chiasm was present, as determined by the X-mask$_{manual}$ (**Figure 2A**). This step was performed to ensure that the evaluation is focused on the optic chiasm only and is not perturbed by neighboring white matter structures, such as optic nerves and tracts.

X-mask$_{manual}$

The X-mask$_{manual}$ were defined in PWA (n = 9; CHIASM albinism) and controls (n = 8; CHIASM controls) from the CHIASM dataset, and 10 HCP test-controls were excluded from CNN training. Specifically, the delineation was performed by a trained researcher in all the T1w image slices with chiasmal presence, as according to the guidelines detailed in (Puzniak et al., in revision, see footnote 1). The X-mask$_{manual}$ were deemed a ground truth and consequently used as reference for the quality assessment of other masks (**Figure 2A**).

X-mask$_{atlas-initial}$

The X-mask$_{atlas-initial}$ were extracted from the existing atlas-based segmentation of the HCP T1w images (Van Essen et al., 2013) processed according to the HCP FreeSurfer pipeline (Glasser et al., 2013) using FreeSurfer v5.2 (Fischl, 2012). Although such atlas-based masks were successfully used in previous studies aiming to accelerate brain segmentation using CNNs (Fedorov et al., 2017a,b; McClure et al., 2019), our comparison of X-mask$_{atlas-initial}$ with X-mask$_{manual}$ revealed a

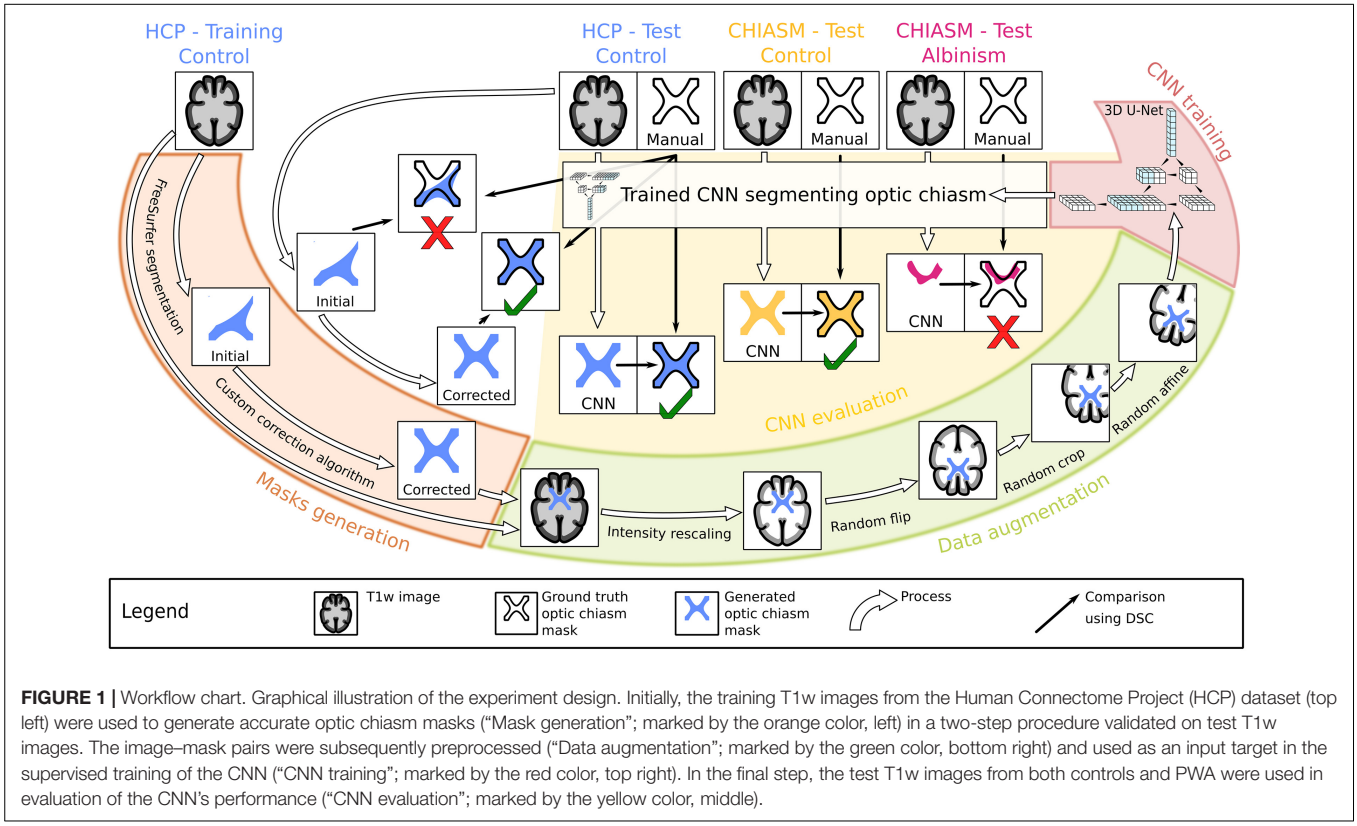

FIGURE 1 | Workflow chart. Graphical illustration of the experiment design. Initially, the training T1w images from the Human Connectome Project (HCP) dataset (top left) were used to generate accurate optic chiasm masks ("Mask generation"; marked by the orange color, left) in a two-step procedure validated on test T1w images. The image–mask pairs were subsequently preprocessed ("Data augmentation"; marked by the green color, bottom right) and used as an input target in the supervised training of the CNN ("CNN training"; marked by the red color, top right). In the final step, the test T1w images from both controls and PWA were used in evaluation of the CNN's performance ("CNN evaluation"; marked by the yellow color, middle).

significantly lower quality of the former (see *Results*), thereby making them (as expected) a suboptimal choice as training data.

X-mask$_{atlas-corrected}$

Although X-mask$_{atlas-initial}$ were found to be of insufficient quality for training, we observed that their shortcomings can be mitigated by incorporating information about voxel intensities in the mask delineation process. This allowed us to formulate the following seven-step algorithm generating a corrected mask, X-mask$_{atlas-corrected}$ from the X-mask$_{atlas-initial}$:

1. Calculate the distribution of intensities of T1w image's voxels within the initial mask, X-mask$_{atlas-initial}$. Notably, apart from optic chiasm's white matter voxels, this will include also false-positive voxels from adjacent tissue.
2. Calculate the 98th percentile of the obtained distribution. This threshold was identified empirically as the one resulting in the optimal separation of hyperintense voxels with blood vessel contributions from the surrounding.
3. Calculate the 66th percentile of the obtained distribution. This threshold was identified empirically as the one resulting in a robust and conservative separation of white matter voxels from partial-volume voxels and surrounding tissue.
4. Binarize a copy of the entire T1w image of the brain, setting all voxels to 0, except for those within the 66-98th percentile range.
5. From the binarized T1w image, extract a bounding box around the initial optic chiasm mask, extended by five voxels in left–right and posterior–anterior directions. This step is intended to exclude neighboring white matter structures which may interfere with step #6 and #7.
6. Extract the biggest cluster of nonzero voxels. This will represent the optic chiasm.
7. Dilate the cluster by one voxel in each direction. The conservatively chosen percentile thresholds, introduced in step #2 and #3, allowed extracting only non-surface voxels of optic chiasm, as they are affected by partial volume. As such, this step allows the possibility to include voxels at the surface.

The quantitative comparison (see *Computational methods*) of outcome for the X-mask$_{atlas-corrected}$ with X-mask$_{manual}$ demonstrated a significantly improved quality of the former (see *Results*) in comparison to X-mask$_{atlas-initial}$. Given this validation, the correction procedure was subsequently performed for all of the HCP X-mask$_{atlas-initial}$, and the resulting X-mask$_{atlas-corrected}$ were used as targets for supervised training of the CNN.

Convolutional Neural Network

This section describes in detail the architecture of the tested CNN, as well as the data preprocessing steps prior to training, training itself, and postprocessing of the output.

Network's Architecture

The developed CNN used a 3D version (Çiçek et al., 2016) of the U-Net architecture (Ronneberger et al., 2015). Although the

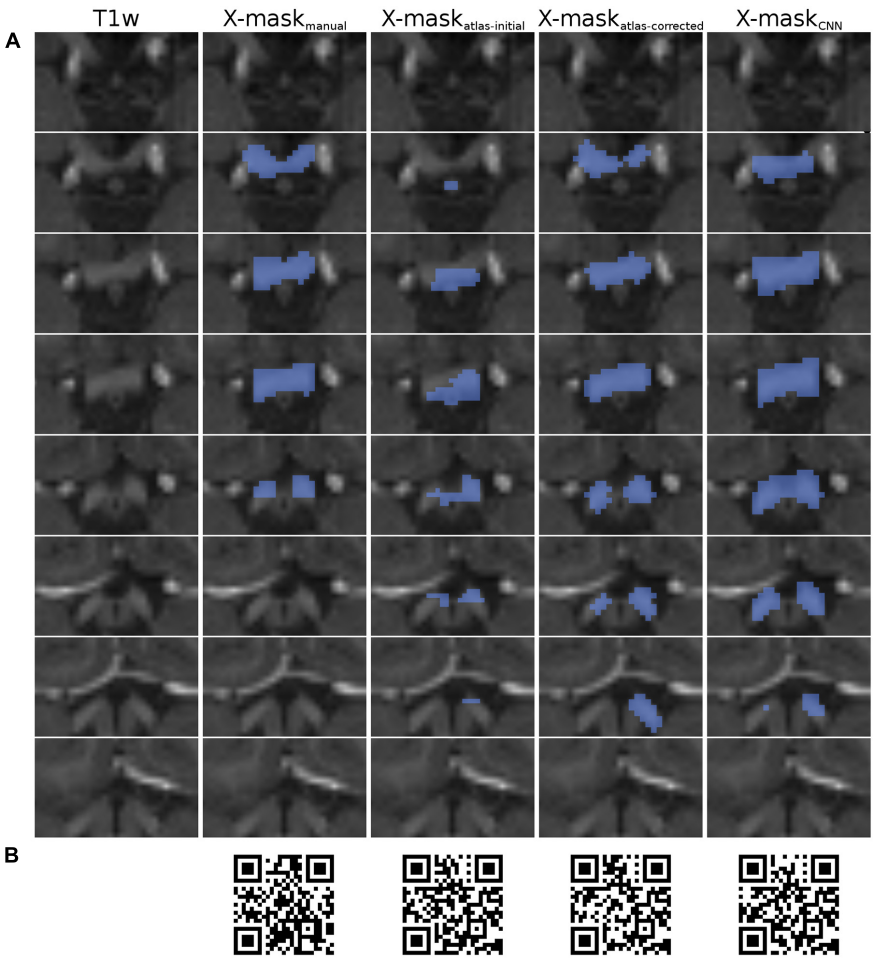

FIGURE 2 | Overview of X-mask from the exemplary HCP dataset (ID 304727). **(A)** Axial slices displaying the optic chiasm region on T1w image (leftmost column). Blue-colored masks superimposed on the T1w slices correspond to, respectively, from left to right: X-mask$_{manual}$, X-mask$_{atlas-initial}$, X-mask$_{atlas-corrected}$, and X-mask$_{CNN}$. The top row displays the most inferior slice, with subsequent rows showing incrementally superior slices. All images are presented in neurological convention. **(B)** QR codes allowing for the inspection of 3D representations of the masks, respectively, from left to right: X-mask$_{manual}$, X-mask$_{atlas-initial}$, X-mask$_{atlas-corrected}$, and X-mask$_{CNN}$.

3D version involves a higher computational load which may limit the upper resolution of processed images, the inclusion of additional dimension was shown to be of significant benefit to the segmentation (Chen et al., 2019; Mlynarski et al., 2020). Another reason for using the U-Net architecture was its reported robustness to jagged boundary-localized errors (Heller et al., 2018), which is a helpful feature in case of training on automatically generated masks.

Specifically, the network consists of analysis (encoding) and synthesis (decoding) paths. The analysis path contains four layers, each containing a standard U-net block [two $3 \times 3 \times 3 \times$ convolutions followed by batch normalization and rectified linear unit (ReLu)] and subsequent $2 \times 2 \times 2$ max pooling (stride of 2). For each subsequent step in the analysis path, the number of feature maps derived from input was doubled in each layer. The synthesis path consists of $2 \times 2 \times 2$ upconvolution followed by a U-net block. Importantly, each decoding layer receives concatenated feature maps from a previous decoding layer and corresponding encoding layer, which allows for preservation of both low- and high-level features. Finally, in the last layer, the two output feature maps (background and target class, here optic chiasm) are being normalized with a voxelwise softmax function. The total number of parameters is 2,206,482.

Data Augmentation

Prior to being fed into the network, the training images and target X-mask$_{atlas-corrected}$ were subjected to the following data augmentation procedure [performed using the TorchIO package (Pérez-García et al., 2021)], respectively:

- Normalization of maximal voxel intensity to 1. This adjusts for varied ranges of intensities between MR images originating from different sources, by rescaling intensities to 0-1 range.

- Random flip along any axis. This accounts for variations in the coordinate systems used for storing MRI images, such as in case of radiological and neurological conventions.
- Random crop to 160 × 160 × 160. This allows for generalization on the incomplete whole-brain data and eases the computational load.
- Random affine (rotation up to 15°, translation up to 20 voxels, bspline interpolation). This accounts for varied orientations and positions of the patient's brain in the scanner space.

Performing these steps on the training data allowed us to enhance CNN's generalization capabilities without resorting to explicit regularization, which has been demonstrated to limit the model's capacity (Hernández-García and König, 2018). This was particularly important considering the misalignment of HCP training images (stored in MNI152 space) and CHIASM testing images (aligned to ACPC space).

Training and Loss Function

The HCP grayscale T1w images (n = 1049) and corresponding X-mask$_{atlas-corrected}$ were divided into training (n = 932, 87.5%; HCP training—controls), validation (n = 107, 10%; HCP validation—controls), and testing (n = 10, 2.5%) subgroups augmented and subsequently fed in batches of 2 to U-Net CNN using the Dice similarity coefficient (see *Computational methods*) loss function and Adam optimizer (Kingma and Ba, 2017) for the purpose of weight updating. The training was performed five times, using different combinations of hyperparameters, specifically the maximal numbers of epochs (13, 15, 30, 40, 100) and learning rates (respectively, 0.0025, 0.0030, 0.0025, 0.0015, and 0.0005). The resulting weights of trained networks were saved and are provided (see *Availability of data and material*).

X-mask$_{CNN}$

The trained CNN returned a grayscale image of the input's size (160 × 160 × 160), where each voxel's intensity depicted the probability of belonging to the optic chiasm (ranging from 0 to 1). This output was turned into a binary optic chiasm mask by thresholding the image to an empirically selected value (here we tested a range of 0.25, 0.50, 0.75, and 1.00 thresholds) and selecting the biggest cluster of nonzero elements present in the image. The quality of final X-mask$_{CNN}$ generated by the tested range of training hyperparameters and threshold values were evaluated against X-mask$_{manual}$ for both HCP test-controls and CHIASM controls datasets (see **Supplementary Material**), with the best-reported performance achieved for 30 epochs, and a learning rate equal to 0.0025 at a threshold of 1.

Computational Methods

The employed computational methods incorporate the quantitative comparison of overlap of two masks by means of the Dice similarity coefficient (specified below), testing of mean equality using t-tests, and a range of classification metrics describing the discrepancy in results.

Dice Similarity Coefficient

In order to measure the quality of optic chiasm masks, we employed the Dice similarity coefficient [DSC; (Dice, 1945; Sørensen, 1948)] statistic, which describes the amount of overlap between two masks, in our case. The DSC ranges from 0 (lack of overlap) to 1 (perfect overlap of identical shapes). Specifically, we calculated the value of DSC between the ground-truth X-mask$_{manual}$ and the candidate X-mask$_{'candidate'}$, where the latter has been previously limited only to axial slices where X-mask$_{manual}$ was present (the excessive voxels were cropped). For brevity, the value of DSC calculated between X-mask$_{manual}$ and candidate X-mask$_{'candidate'}$ is further being denoted to as DSC$_{manual_vs_'candidate'}$, and in case of group-level results, statistics is presented as mean ± standard error of mean (SEM).

Statistical Comparisons

The obtained DSC values, grouped with respect to compared candidate mask group (X-mask$_{initial}$, X-mask$_{atlas-corrected}$, and X-mask$_{CNN}$) and participant group (HCP test-controls, CHIASM controls, and CHIASM albinism), were subjected to statistical testing. All samples were tested for normal distribution using the test by D'Agostino and Pearson (D'Agostino and Pearson, 1973), and for all but one (X-mask$_{atlas-initial}$: HCP test-controls) the null hypothesis of coming from normal distribution could not be rejected. Accordingly, in case of comparison of two normally distributed samples, we used two-tailed, two-sampled t-test at an alpha level of 5%; otherwise, we used the Wilcoxon rank-sum test, which tests the null hypothesis that two samples are drawn from the same distribution. Finally, we controlled for the familywise error (FWE) rate by applying Bonferroni's correction to all calculated p-values.

Classification Metrics

In order to evaluate any potential discrepancy in the X-mask quality obtained for PWA and controls, we classified the obtained DSC$_{manual_vs_CNN}$ using C-support vector classification (C-SVC) model with polynomial kernel (Platt, 1999; Chang and Lin, 2011). The measure of interclass discrepancy was subsequently quantified using well-established machine learning classification metrics, specifically

- $Accuracy = \frac{TP+TN}{TP+TN+FP+FN}$,
- $Precision = \frac{TP}{TP+FP}$,
- $Recall\ (sensitivity) = \frac{TP}{TP+FN}$,
- $Specificity = \frac{TN}{TN+FP}$,

where TP, TN, FP, and FN are, respectively, true positives, true negatives, false positives, and false negatives. Importantly, it should be noted that the classifier has been trained and evaluated on the same data, which is a clearly forbidden practice in case of evaluating a classifiers' performance. Our goal was, however, to quantitatively express the intergroup differences in DSC$_{manual_vs_CNN}$ and the overlap in data points, which is why we decided on such an approach. In line with that purpose, we used the support vector classification model which attempts to maximize the margin around the decision boundary.

TABLE 1 | Mean and standard error of mean of DSC of X-mask and significance of cross-group differences.

Group	X-mask	HCP test-controls			CHIASM controls			CHIASM albinism		
		Atlas-initial	Atlas-corrected	CNN	Atlas-initial	Atlas-corrected	CNN	Atlas-initial	Atlas-corrected	CNN
HCP test-controls	Atlas-initial	57 ± 3 %	$p = 0.025^{1,a}$	75 ± 3 %	n.s.[1,a]	n.s.[b]	79 ± 2 %			
	Atlas-corrected			n.s.[b]			n.s.[c]			
	CNN									
CHIASM controls	Atlas-initial				50 ± 4 %	$p = 0.02^{a}$	28 ± 4 %			
	Atlas-corrected			$p < 0.001^{a}$			$p < 0.001^{b}$	75 ± 3 %		
	CNN									
CHIASM albinism	Atlas-initial							53 ± 5%		
	Atlas-corrected								33 ± 4 %	
	CNN			$p = 0.004^{c}$			$p = 0.04^{c}$		n.s.[b]	44 ± 8%

The diagonal displays the values of DSC of a specific X-mask (atlas-initial, atlas-corrected, CNN) compared to the corresponding X-mask$_{manual}$ (0%: no overlap; 100%: identical masks, i.e., complete overlap) for each of the test groups (10 HCP test-controls, 8 CHIASM controls, and 9 CHIASM PWA). A total of 10 specific statistical tests were performed (corrected for familywise error using Bonferroni's correction): four tests for cross-comparison of quality of X-mask$_{atlas-initial}$ and X-mask$_{atlas-corrected}$ for two control groups (marked by symbol [a]), three tests for comparison of X-mask$_{atlas-corrected}$ with X-mask$_{CNN}$ for all groups (marked by symbol [b]), and three tests for cross-comparisons of X-mask$_{CNN}$ for all groups (marked by symbol [c]). The p-values of the tests (either Wilcoxon rank-sum tests marked by symbol [1], or t-tests) comparing group DSC scores are displayed on the intersection of respective rows and columns (non-significant: n.s.; absence of test: blank cell). Blue color – HCP test-controls, yellow color – CHIASM controls, red color – CHIASM albinism.

[1] Wilcoxon rank-sum tests.

[a] Tests for cross-comparison of quality of X-mask$_{atlas-initial}$ and X-mask$_{atlas-corrected}$ for two control groups.

[b] Tests for comparison of X-mask$_{atlas-corrected}$ with X-mask$_{CNN}$ for all groups.

[c] Tests for cross-comparisons of X-mask$_{CNN}$ for all groups.

RESULTS

This section provides a detailed qualitative and quantitative insight into the two key aspects of our investigation: (i) quality assessment of X-mask$_{atlas-initial}$ and X-mask$_{atlas-corrected}$ and (ii) evaluation of the CNN's performance on the CHIASM dataset. An overview of the quantitative results is given in **Table 1**.

Quality of Optic Chiasm Masks

As detailed in *Methods*, the quality of a candidate mask is determined based on its conformance with the ground-truth masks, i.e., DSC$_{manual_vs_'candidate'}$. The DSC$_{manual_vs_atlas-initial}$ calculated for the 10 HCP test-controls was equal to 57 ± 3% (mean ± SEM). Upon correction of the X-mask$_{atlas-initial}$ with the custom-designed algorithm, the quality of the corrected masks (X-mask$_{atlas-corrected}$) improved significantly (mean DSC$_{manual_vs_atlas-initial}$ and DSC$_{manual_vs_atlas-corrected}$: 57 ± 3% and 75 ± 3%, respectively, FWE corrected p-value = 0.025; see also **Figures 2**, **3** for a quantitative and qualitative account, respectively). These results for the HCP test-controls provide support for the custom mask correction procedure, and as such X-mask$_{atlas-corrected}$. For this reason of better quality, X-mask$_{atlas-corrected}$ were later used for the CNN training.

Although the CNN training was based only on HCP data, the mask correction algorithm was tested also on the CHIASM dataset. The quality of X-mask$_{atlas-initial}$ (DSC$_{manual_vs_atlas-initial}$) of the CHIASM controls compares similarly to the HCP test-controls [HCP vs. CHIASM: 57 ± 3% vs. 50 ± 4 (mean ± SEM); p-value = 1.00]. In contrast, applying the mask correction procedure on the CHIASM data resulted in significantly lower DSC-measures for X-mask$_{atlas-corrected}$ than X-mask$_{atlas-initial}$ (DSC$_{manual_vs_atlas-initial}$ vs. DSC$_{manual_vs_atlas-corrected}$: 50 ± 4% vs. 28 ± 4%; p-value = 0.02; see **Figure 3**). Despite a comparable quality of initial masks, the quality of X-mask$_{atlas-corrected}$ from the CHIASM dataset was reduced compared to the HCP X-mask$_{atlas-corrected}$ [DSC$_{manual_vs_atlas_corrected}$ (HCP vs. CHIASM): 75 ± 3% vs. 28 ± 4%; p-value < 0.001]. The findings reveal the limited generalization of the custom mask correction procedure. It should be noted that this is not of relevance for the hypothesis tested in this study: during training, the CNN is interacting with data and target masks corresponding to the HCP dataset only. Accordingly, while it is critical to ensure the high quality of training X-mask$_{atlas-corrected}$, the CNN itself is agnostic to their derivation process and its limitations on other datasets. This will be proven further in the *Results* section (see *Transferability of CNNs*) where it will be shown that X-mask$_{atlas-corrected}$ and X-mask$_{CNN}$ of CHIASM controls are fundamentally different.

Evaluation of Convolutional Neural Network's Performance on the Testing Data

We calculated the DSC$_{manual_vs_CNN}$ of control (n = 8) and PWA (n = 9) from the CHIASM dataset and HCP test-controls. This allowed us to gain insight into the (i) transferability of CNNs (i.e., how well the CNN performs on data from entirely new sources; for this purpose, we compared the quality of X-mask$_{atlas-corrected}$

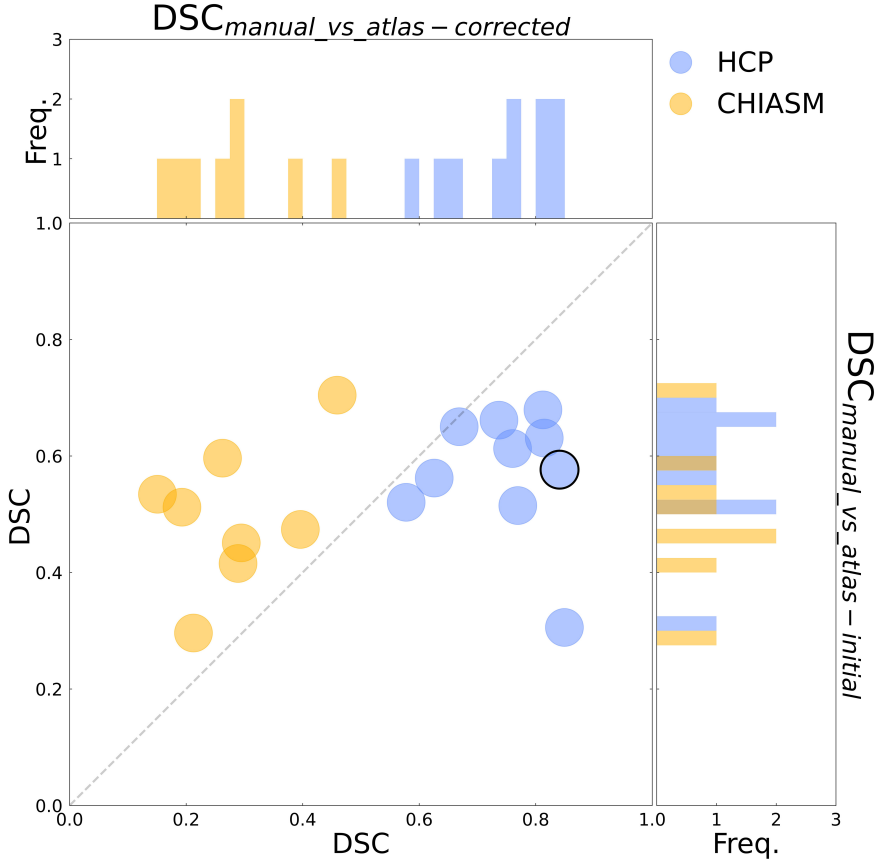

FIGURE 3 | Evaluation of the mask correction procedure. Scatter plot of $DSC_{manual\_vs\_atlas-corrected}$ (x-axis) and $DSC_{manual\_vs\_atlas-initial}$ (y-axis) values for a subset of 10 HCP test-controls and 8 controls from the CHIASM dataset. The values are additionally presented in the form of marginal histograms of the two distributions—$DSC_{manual\_vs\_atlas-corrected}$ (top horizontal) and $DSC_{manual\_vs\_atlas-initial}$ (right vertical). The black contour marks the data point of the representative participant detailed in **Figure 1**.

to X-$mask_{CNN}$) and (ii) differences between optic chiasm masks computed by the CNN for controls and PWA.

(i) Transferability of CNNs. The comparison of $DSC_{manual\_vs\_atlas-corrected}$ with $DSC_{manual\_vs\_CNN}$ performed for the 10 HCP test-controls failed to reveal a statistically significant difference [75 ± 3% and 79 ± 2%, respectively, p-value = 1.00]. This considerably deviated from results obtained for the CHIASM controls, where $DSC_{manual\_vs\_CNN}$ (75 ± 3%) was significantly higher than $DSC_{manual\_vs\_atlas-corrected}$ (28 ± 4%, p-value < 0.001). Interestingly, the values of $DSC_{manual\_vs\_CNN}$ for both HCP test-controls and CHIASM controls were similar (79 ± 2% and 75 ± 3%, respectively; p-value = 1.00). The robust performance of the CNN on the CHIASM dataset reinforces the argument that CNN is agnostic to and does not copy the correction algorithm that generated training X-$mask_{atlas-corrected}$ data (which was shown to fail on the data of CHIASM controls), but rather uses more general and robust processing that is well transferable to datasets different from the training one.

(ii) CNN-computed masks for controls vs. albinism. Comparing the $DSC_{manual\_vs\_CNN}$ between CHIASM controls (75 ± 3%) and albinism participants (44 ± 8%) revealed a significantly lower quality of the latter (p-value = 0.04). These results also applied when substituting the CHIASM controls with the HCP test-controls (79 ± 2%, p-value = 0.004). An overview of the results is displayed in **Figures 4**, **5**.

The observed differentiation between the controls and albinism was further investigated by measuring the performance of a C-SVC model (see *Methods*) applied to CHIASM albinism—CHIASM controls and CHIASM albinism—HCP test-controls data pairs (with PWA as positives and controls as negatives). The results of classification were subsequently evaluated with the metrics specified in *Methods* and detailed in **Table 2**.

The observed discrepancy in values of $DSC_{manual\_vs\_CNN}$ for controls and albinism indicates that malformed chiasms are ill-represented by models "learned" from normal chiasms. This leads to the conclusion that both types of chiasms are described by diverse spatial features. This important

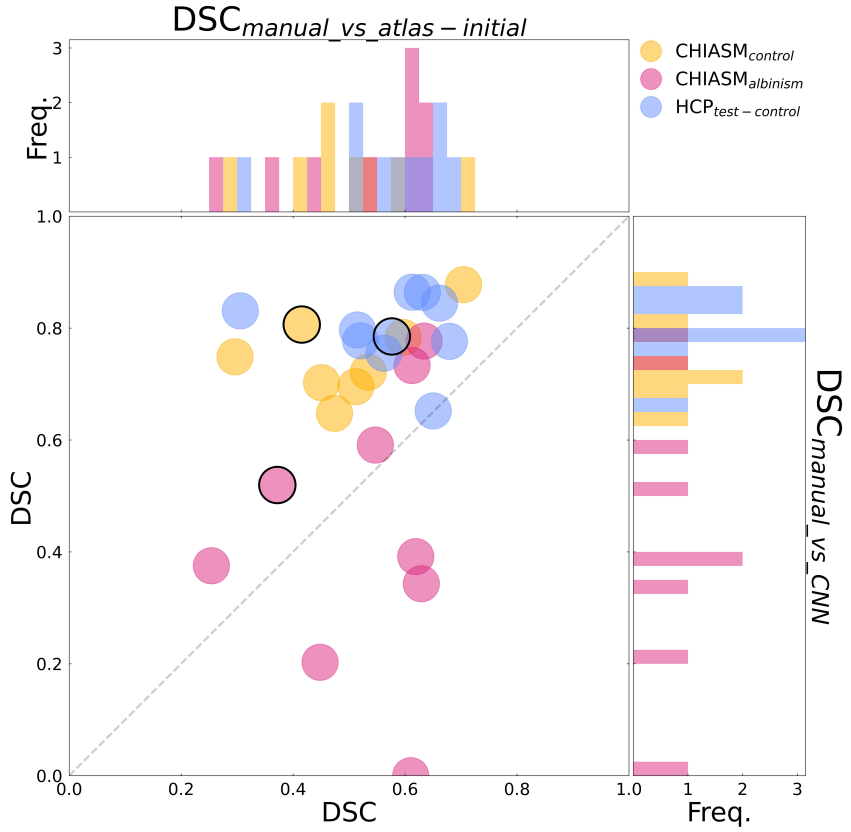

FIGURE 4 | Comparison of quality of X-mask$_{atlas-initial}$ and X-mask$_{CNN}$. Scatter plot of DSC$_{manual_vs_atlas-initial}$ (x-axis) and DSC$_{manual_vs_CNN}$ (y-axis) values for CHIASM albinism (n = 9), CHIASM controls (n = 8), and HCP test-controls (n = 10). The values are additionally presented in the form of marginal histograms of the two distributions—DSC$_{manual_vs_atlas-initial}$ (top horizontal) and DSC$_{manual_vs_CNN}$ (right vertical). The black contours mark the data point of the representative participants, depicted in **Figure 5**. The outlier data point indicating DSC$_{manual_vs_CNN}$ = 0 corresponds to a single case, where the chiasm could not be correctly identified. Specifically, X-mask$_{CNN}$ was defined as a largest cluster of voxels with positive predictions (as output by CNN). In this unique case, however, the largest cluster was located outside the chiasm, in the cerebellum.

observation provides a proof of concept for CNN-based direct classification of chiasms with regard to misrouting. At the same time, it should be noted that due to the limited sample of testing data, it is beyond the scope of the present study to provide an optimal DSC threshold for distinguishing controls from PWA. Given the clinical relevance of a threshold, we emphasize the need for future research to estimate this value through extensive evaluation of multiple datasets from several sources. While such a study is expected to provide the value for the optimal decision boundary (e.g., *via* a receiver operating characteristic curve analysis), the final proposed value should also factorize the consequences of type I and type II errors.

DISCUSSION

We aimed to investigate whether normal optic chiasms and those with misrouting as in albinism are represented by CNNs differently and, if yes, whether such differences could be used in the diagnostics of abnormal chiasms. In order to investigate this, we built and trained a CNN to segment optic chiasms based on control T1w images and algorithm-generated training masks. Our findings of a differential performance of the CNN in predicting normal and abnormal chiasms indeed highlight a potential utility of CNNs in identifying patients with chiasmal abnormalities. In the context of our findings, we intend to discuss two key aspects of our study: (i) use of automated masks in the training of CNN and (ii) application of control chiasms learned by CNN to abnormal cases.

Use of Automated Masks in the Training of CNN

Automatically generated algorithm-based masks are bound to be a suboptimal solution for the purpose of image segmentation as compared to manual segmentations, specifically in medical images. Remarkably, we observed that in the case of a dataset with a specific structure, tailored adjustments can significantly increase the fidelity of automated masks to the ground truth. This strategy is useful in mitigating the disadvantages of a trade-off between mask quality and big sample size, as encountered when using automatically generated training data

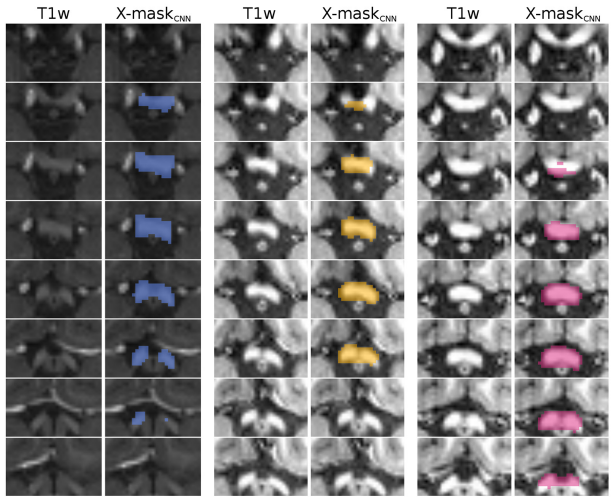

FIGURE 5 | Overview of X-mask$_{CNN}$ from a representative HCP test-control, CHIASM control, and CHIASM albinism participant. Axial slices display the optic chiasm region on the T1w image; blue-, yellow-, and magenta-colored masks show the X-mask$_{CNN}$ defined for the HCP test-control, CHIASM control, and CHIASM albinism participants, respectively (marked by a black edge on **Figure 4**).

(McClure et al., 2019). This is further reinforced by the robust performance of the trained CNN here, demonstrating that the approximate masks despite individual flaws allow for a successful capture of the structure's properties by the neural networks (Heller et al., 2018).

Application of Control Chiasms Learned by Convolutional Neural Network to Abnormal Cases

Finally, the reported results demonstrated that the features of chiasms "learned" by training on control data does not apply to chiasms with enhanced misrouting, as present in albinism. This finding allows for a number of conclusions:

a. The chiasmal misrouting significantly alters the spatial organization of the optic chiasm [supporting the findings of Schmitz et al. (2003) and von dem Hagen et al. (2005)], which thus cannot be represented by data-driven models trained on control data only. Consequently, deep learning frameworks which exclude data of malformed chiasms from the training datasets will not be able to accurately represent them.
b. At the same time, the fundamental differences between CNN representations of normal and abnormal chiasms, as demonstrated by the quantified inaccuracy of masks, indicate the possibility of the identification of chiasmal misrouting from the T1w MRI images. Establishing such a method would provide direct and robust methods for the identification of misrouting in the clinical environment, which in turn is expected to reinforce the diagnostics of albinism. Further studies are needed to explore how our specific findings related to albinism translate to the detection of chiasma abnormalities in general.
c. The distinguished CNN representations of normal and abnormal chiasms are also a promising starting point for further studies addressing the association between chiasm malformations (with its further impact on white matter of visual system) and related reorganization at the level of the visual cortex (Hoffmann and Dumoulin, 2015). Additionally, the complexity of this phenomenon may greatly benefit from more complex methods, such as CNNs.
d. Finally, it should be noted that our current study underlines the general need for public datasets of rare, not infrequently overlooked, patient groups (Puzniak et al., in revision, see footnote 1). This is particularly important in the context of the current influx of deep learning-based tools in the healthcare system, such as CNNs trained to segment organs at risk (including chiasm as well) for therapy planning, which may not be available to rare patient groups not represented in training data. Considering this, the current study highlights the opportunities of improved diagnostics for the example of albinism and is intended to inspire the publication of further datasets to be utilized for the development of robust and transferable neural networks capable of accurate classification of chiasmal abnormalities from T1w MRI images.

TABLE 2 | Accuracy of cross-group classification based on DSC$_{manual_vs_CNN}$.

Metrics	CHIASM albinism vs. CHIASM controls	CHIASM albinism vs. HCP test-controls
Accuracy	0.89	0.84
Precision	0.80	0.82
Recall (sensitivity)	1.00	0.9
Specificity	0.78	0.78

Limitations

The study limitations come from several distinct sources. Firstly, we note the limitations stemming from (i) lack of evidence on specific anatomical biomarkers of chiasmal malformations. Secondly, we acknowledge the limitations caused by data scarcity affecting the (ii) interpretability of the model, (iii) quantity and heterogeneity of the data, and (iv) quality of the data and labels. Finally, we note that the study might be partially affected by unavoidable (v) limitations in the design and training of the CNN.

Identification of Anatomical Biomarkers of Chiasmal Malformations

An important step in the validation of a diagnostic tool is the demonstration of its sensitivity to meaningful individualized biomarkers of the disease. Unfortunately, the evidence for such specific anatomical biomarkers of chiasmal malformations is missing. Although previous studies (Schmitz et al., 2003;

von dem Hagen et al., 2005) provided a list of candidate features distinguishing normal from abnormal chiasms (width of chiasm, optic nerves and optic tracts, angle between optic tracts), none of these features were investigated in the context of individualized diagnostics. This lack of literature on the anatomy-based detection of chiasmal malformations was also the primary reason for the choice of our method here, which aimed at the investigation of the generalized applicability of CNNs for the purpose of detection of chiasmal malformations.

Interpretability of the Convolutional Neural Network

While the missing knowledge on specific relevant anatomical biomarkers of chiasmal misrouting can be retrieved by the identification of features driving the correct diagnostics, this process requires the CNN to be interpretable, i.e., to grant insight into identifying the input features driving the outcome decision. This property is, however, not generally available for all the CNNs but is rather dependent on their task. Specifically, in the case of described segmentation CNN (as chosen in this study to avoid dependence on the scarce data on chiasmal malformations), there are strong limits of the possibilities for visualization of the inference process. This limitation does not apply to the classification CNNs, where several interpretation techniques (Montavon et al., 2018) such as Grad-CAM (Selvaraju et al., 2017) can be implemented. These, however, require extensive datasets. Additionally, as this type of network uses both normal and abnormal data for training, it allows for extensive validation of features that drive the CNN's decision that will lead to understand their placing in the normal–abnormal spectrum. In summary, we note that while the employed approach provides the evidence that certain anatomical biomarkers of chiasmal malformations exist, the next step should involve their identification with a classifying CNN trained on larger datasets comprising both normal and abnormal data.

Quantity and Heterogeneity of the Data

Although our study's design enabled us to take advantage of the massive HCP dataset and train the CNN on much bigger samples than typically used, the rarity of albinism (and other cases of congenital malformations of the chiasm) severely limited the size of the training sample. For the same reasons, we were limited to testing data from only one site, which prevented us from investigation of impact of scanner and data acquisition protocol on the method's outcome. Moreover, this limited our estimates of the accuracy and robustness of the presented method.

Quality of Data and Labels

Although the HCP dataset is well-known for setting standards in MRI data quality assessment, it does not contain any clinical information pertaining to the participants' visual system evaluations. Furthermore, the training dataset might include participants with retinal and/or optic nerve disorders in proportions corresponding to their representation in the real world. This prevalence is, however, not expected to influence the outcome of CNN training, but even if so, this would cause underestimation of our method's performance, rather than overestimation.

Similarly, although the CHIASM datasets provides findings of ophthalmologic examination of included participants, it does not provide information about the types of albinism represented in the dataset (e.g., oculo-cutaneous, ocular albinism).

Finally, the quality of automatically generated training labels is inferior to the ones created manually. Although we provide evidence that this does not impact the general outcome of the study, we acknowledge the use of manually defined labels to be the optimal approach.

Convolutional Neural Network Design and Training

Due to the models' complexity and high dependence on the underlying data, the Deep Learning modeling approach is mainly driven by empirical, rather than theoretical, evidence. Consequently, despite the choice of employing an established 3D U-Net architecture, which was reported to perform well in similar task, we cannot rule out that other architectures would not provide better results. Similarly during CNN training, although we tried several combinations of hyperparameters and reported the ones yielding the best results, it is nearly impossible that we found the globally optimal configuration of the CNN network's parameters.

DATA AVAILABILITY STATEMENT

The datasets presented in this study can be found in online repositories. Specifically, this includes:

- T1w images from the HCP dataset stored on the brainlife.io platform: https://brainlife.io/project/5941a225f876b000210c11e5
- T1w images from the CHIASM dataset stored on the brainlife.io platform: https://brainlife.io/pub/5dea42a96c0bd9c0508554a2
- X-mask$_{manual}$, X-mask$_{atlas-initial}$, X-mask$_{atlas-corrected}$, and X-mask$_{CNN}$ stored on the brainlife.io platform: https://brainlife.io/project/6043cb8966d5ce5fc26f5f73
- The weights of the trained network stored on osf.io platform: https://osf.io/4cvgq/
  The code used in this study for generation of training data, CNN training, analyses, and figures can be found on github.com platform: https://github.com/rjpuzniak/Use-of-deep-learning-based-optic-chiasm-segmentation-for-investigating-visual-system-pathophysiology.

ETHICS STATEMENT

Ethical review and approval was not required for the study on human participants in accordance with

the local legislation and institutional requirements. Written informed consent for participation was not required for this study in accordance with the national legislation and the institutional requirements.

AUTHOR CONTRIBUTIONS

RP and MH designed the study and interpreted the data. RP performed the analysis. RP, GP, and MH wrote the manuscript. All authors contributed to the article and approved the submitted version.

FUNDING

This work was supported by European Union's Horizon 2020 Research and Innovation Program under the Marie Skłodowska-Curie grant agreement (No. 641805) and by the German Research Foundation (DFG, HO 2002 10-3) to MH.

SUPPLEMENTARY MATERIAL

The Supplementary Material for this article can be found online at: https://www.frontiersin.org/articles/10.3389/fnins.2021.755785/full#supplementary-material

REFERENCES

Ahmadi, K., Herbik, A., Wagner, M., Kanowski, M., Thieme, H., and Hoffmann, M. B. (2019). Population receptive field and connectivity properties of the early visual cortex in human albinism. *Neuroimage* 202:116105. doi: 10.1016/j.neuroimage.2019.116105

Ather, S., Proudlock, F. A., Welton, T., Morgan, P. S., Sheth, V., Gottlob, I., et al. (2018). Aberrant visual pathway development in albinism: from retina to cortex. *Hum. Brain Mapp.* 40, 777–788. doi: 10.1002/hbm.24411

Avesani, P., McPherson, B., Hayashi, S., Caiafa, C. F., Henschel, R., Garyfallidis, E., et al. (2019). The open diffusion data derivatives, brain data upcycling via integrated publishing of derivatives and reproducible open cloud services. *Sci. Data* 6:69. doi: 10.1038/s41597-019-0073-y

Brodsky, M. C., Glasier, C. M., and Creel, D. J. (1993). Magnetic resonance imaging of the visual pathways in human albinos. *J. Pediatr. Ophthalmol. Strabismus* 30, 382–385.

Chang, C.-C., and Lin, C.-J. (2011). LIBSVM: a library for support vector machines. *ACM Trans. Intell. Syst. Technol.* 2, 1–27. doi: 10.1145/1961189.1961199

Chen, H., Lu, W., Chen, M., Zhou, L., Timmerman, R., Tu, D., et al. (2019). A recursive ensemble organ segmentation (REOS) framework: application in brain radiotherapy. *Phys. Med. Biol.* 64:025015. doi: 10.1088/1361-6560/aaf83c

Çiçek, Ö, Abdulkadir, A., Lienkamp, S. S., Brox, T., and Ronneberger, O. (2016). "D U-Net: learning dense volumetric segmentation from sparse annotation," in *Medical Image Computing and Computer-Assisted Intervention–MICCAI 2016. (Lecture Notes in Computer Science)*, eds S. Ourselin, L. Joskowicz, M. Sabuncu, G. Unal, and W. Wells (Cham: Springer), 424–432. doi: 10.1007/978-3-319-46723-8_49

D'Agostino, R., and Pearson, E. S. (1973). Tests for departure from normality. Empirical results for the distributions of b2 and ✓ b1. *Biometrika* 60, 613–622. doi: 10.2307/2335012

Dice, L. R. (1945). Measures of the amount of ecologic association between species. *Ecology* 26, 297–302. doi: 10.2307/1932409

Duanmu, H., Kim, J., Kanakaraj, P., Wang, A., Joshua, J., Kong, J., et al. (2020). "Automatic brain organ segmentation with 3D fully convolutional neural network for radiation therapy treatment planning," in *Proceedings of the 2020 IEEE 17th International Symposium on Biomedical Imaging (ISBI)*, Iowa City, IA, 758–762. doi: 10.1109/ISBI45749.2020.9098485

Fedorov, A., Damaraju, E., Calhoun, V., and Plis, S. (2017a). Almost instant brain atlas segmentation for large-scale studies. *arXiv* [Preprint]. Available online at: http://arxiv.org/abs/1711.00457 (accessed March 16, 2021). arXiv:1711.00457 [cs],

Fedorov, A., Johnson, J., Damaraju, E., Ozerin, A., Calhoun, V., and Plis, S. (2017b). "End-to-end learning of brain tissue segmentation from imperfect labeling," in *Proceedings of the 2017 International Joint Conference on Neural Networks (IJCNN)*, Anchorage, AK, 3785–3792. doi: 10.1109/IJCNN.2017.7966333

Fischl, B. (2012). FreeSurfer. *Neuroimage* 62, 774–781. doi: 10.1016/j.neuroimage.2012.01.021

Glasser, M. F., Sotiropoulos, S. N., Wilson, J. A., Coalson, T. S., Fischl, B., Andersson, J. L., et al. (2013). The minimal preprocessing pipelines for the human connectome project. *Neuroimage* 80, 105–124. doi: 10.1016/j.neuroimage.2013.04.127

Heller, N., Dean, J., and Papanikolopoulos, N. (2018). "Imperfect segmentation labels: how much do they matter?," in *Intravascular Imaging and Computer Assisted Stenting and Large-Scale Annotation of Biomedical Data and Expert Label Synthesis. (Lecture Notes in Computer Science)*, eds D. Stoyanov, Z. Taylor, S. Balocco, R. Sznitman, A. Martel, L. Maier-Hein, et al. (Cham: Springer International Publishing), 112–120. doi: 10.1007/978-3-030-01364-6_13

Hernández-García, A., and König, P. (2018). Data augmentation instead of explicit regularization. *arXiv* [Preprint]. arXiv:1806.03852,

Hoffmann, M. B., and Dumoulin, S. O. (2015). Congenital visual pathway abnormalities: a window onto cortical stability and plasticity. *Trends Neurosci.* 38, 55–65. doi: 10.1016/j.tins.2014.09.005

Hoffmann, M. B., Lorenz, B., Morland, A. B., and Schmidtborn, L. C. (2005). Misrouting of the optic nerves in albinism: estimation of the extent with visual evoked potentials. *Invest. Ophthalmol. Vis. Sci.* 46, 3892–3898. doi: 10.1167/iovs.05-0491

Hoffmann, M. B., Schmidtborn, L. C., and Morland, A. B. (2007). Abnormale repräsentationen im visuellen kortex von albinismus-patienten. *Der Ophthalmol.* 104, 666–673. doi: 10.1007/s00347-007-1589-7

Hoffmann, M. B., Tolhurst, D. J., Moore, A. T., and Morland, A. B. (2003). Organization of the visual cortex in human albinism. *J. Neurosci.* 23, 8921–8930. doi: 10.1523/JNEUROSCI.23-26-08921.2003

Ibragimov, B., and Xing, L. (2017). Segmentation of organs-at-risks in head and neck CT images using convolutional neural networks. *Med. Phys.* 44, 547–557. doi: 10.1002/mp.12045

Kingma, D. P., and Ba, J. (2017). Adam: a method for stochastic optimization. *arXiv* [Preprint]. Available online at: http://arxiv.org/abs/1412.6980 (accessed March 4 2021). arXiv:1412.6980 [cs]

Krizhevsky, A., Sutskever, I., and Hinton, G. E. (2012). *ImageNet Classification with Deep Convolutional Neural Networks, Advances in Neural Information Processing Systems, 25*. Available online at: https://proceedings.neurips.cc/paper/2012/file/c399862d3b9d6b76c8436e924a68c45b-Paper.pdf (accessed March 2 2021).

Kruijt, C. C., de Wit, G. C., Bergen, A. A., Florijn, R. J., Schalij-Delfos, N. E., and van Genderen, M. M. (2018). The phenotypic spectrum of albinism. *Ophthalmology* 125, 1953–1960. doi: 10.1016/j.ophtha.2018.08.003

Kupfer, C., Chumbley, L., and Downer, J. C. (1967). Quantitative histology of optic nerve, optic tract and lateral geniculate nucleus of man. *J. Anat.* 101(Pt 3), 393–401.

LeCun, Y., Boser, B., Denker, J. S., Henderson, D., Howard, R. E., Hubbard, W., et al. (1989). Backpropagation applied to handwritten zip code recognition. *Neural Comput.* 1, 541–551. doi: 10.1162/neco.1989.1.4.541

Lundervold, A. S., and Lundervold, A. (2019). An overview of deep learning in medical imaging focusing on MRI. *Z. Med. Phys.* 29, 102–127. doi: 10.1016/j.zemedi.2018.11.002

Marçon, C. R., and Maia, M. (2019). Albinism: epidemiology, genetics, cutaneous characterization, psychosocial factors. *An. Bras. Dermatol.* 94, 503–520. doi: 10.1016/j.abd.2019.09.023

McClure, P., Rho, N., Lee, J. A., Kaczmarzyk, J. R., Zheng, C. Y., Ghosh, S. S., et al. (2019). Knowing what you know in brain segmentation using bayesian deep neural networks. *Front. Neuroinform.* 13:67. doi: 10.3389/fninf.2019.00067

Milchenko, M., and Marcus, D. (2013). Obscuring surface anatomy in volumetric imaging data. *Neuroinformatics* 11, 65–75. doi: 10.1007/s12021-012-9160-3

Mlynarski, P., Delingette, H., Alghamdi, H., Bondiau, P. Y., and Ayache, N. (2020). Anatomically consistent CNN-based segmentation of organs-at-risk in cranial radiotherapy. *J. Med. Imaging* 7:014502. doi: 10.1117/1.JMI.7.1.014502

Montavon, G., Samek, W., and Müller, K.-R. (2018). Methods for interpreting and understanding deep neural networks. *Digit. Signal Process.* 73, 1–15. doi: 10.1016/j.dsp.2017.10.011

Pérez-García, F., Sparks, R., and Ourselin, S. (2021). TorchIO: a Python library for efficient loading, preprocessing, augmentation and patch-based sampling of medical images in deep learning. *arXiv* [Preprint]. Available online at: http://arxiv.org/abs/2003.04696 (accessed 4 March 2021) arXiv:2003.04696 [cs, eess, stat]

Platt, J. C. (1999). "Probabilistic outputs for support vector machines and comparisons to regularized likelihood methods," in *Advances in Large Margin Classifiers*, eds A. J. Smola, P. Bartlett, B. Schölkopf, and D. Schuurmans (Cambridge, MA: MIT Press), 61–74.

Puzniak, R. J., Ahmadi, K., Kaufmann, J., Gouws, A., Morland, A. B., Pestilli, F., et al. (2019). Quantifying nerve decussation abnormalities in the optic chiasm. *Neuroimage Clin.* 24:102055. doi: 10.1016/j.nicl.2019.102055

Puzniak, R. J., Prabhakaran, G. T., Buentjen, L., Schmitt, F. C., and Hoffmann, M. B. (2021). Tracking the visual system—from the optic chiasm to primary visual cortex. *Z. Epileptol.* 34, 57–66. doi: 10.1007/s10309-020-00384-y

Rebsam, A., Bhansali, P., and Mason, C. A. (2012). Eye-specific projections of retinogeniculate axons are altered in albino mice. *J. Neurosci.* 32, 4821–4826. doi: 10.1523/JNEUROSCI.5050-11.2012

Ronneberger, O., Fischer, P., and Brox, T. (2015). "U-Net: convolutional networks for biomedical image segmentation," in *Medical Image Computing and Computer-Assisted Intervention–MICCAI 2015 (Lecture Notes in Computer Science)*, eds N. Navab, J. Hornegger, W. Wells, and A. Frangi (Cham: Springer International Publishing), 234–241. doi: 10.1007/978-3-319-24574-4_28

Schmitz, B., Schaefer, T., Krick, C. M., Reith, W., Backens, M., and Käsmann-Kellner, B. (2003). Configuration of the optic chiasm in humans with albinism as revealed by magnetic resonance imaging. *Invest. Ophthalmol. Vis. Sci.* 44, 16–21. doi: 10.1167/iovs.02-0156

Selvaraju, R. R., Cogswell, M., Das, A., Vedantam, R., Parikh, D., and Batra, D. (2017). "Grad-CAM: visual explanations from deep networks via gradient-based localization," in *Proceedigs of the 2017 IEEE International Conference on Computer Vision (ICCV)*, Venice, 618–626. doi: 10.1109/ICCV.2017.74

Sørensen, T. J. (1948). *A Method of Establishing Groups of Equal Amplitude in Plant Sociology Based on Similarity of Species Content and its Application to Analyses of the Vegetation on Danish Commons*. København: I kommission hos E. Munksgaard.

Tong, N., Gou, S., Yang, S., Ruan, D., and Sheng, K. (2018). Fully automatic multi-organ segmentation for head and neck cancer radiotherapy using shape representation model constrained fully convolutional neural networks. *Med. Phys.* 45, 4558–4567. doi: 10.1002/mp.13147

van der Kouwe, A. J. W., Benner, T., Salat, D. H., and Fischl, B. (2008). Brain morphometry with multiecho MPRAGE. *Neuroimage* 40, 559–569. doi: 10.1016/j.neuroimage.2007.12.025

Van Essen, D. C., Smith, S. M., Barch, D. M., Behrens, T. E. J., Yacoub, E., Uğurbil, K., et al. (2013). The wu-minn human connectome project: an overview. *Neuroimage* 80, 62–79. doi: 10.1016/j.neuroimage.2013.05.041

von dem Hagen, E. A. H., Hoffmann, M. B., and Morland, A. B. (2008). Identifying human albinism: a comparison of VEP and fMRI. *Invest. Ophthalmol. Vis. Sci.* 49, 238–249. doi: 10.1167/iovs.07-0458

von dem Hagen, E. A. H., Houston, G. C., Hoffmann, M. B., Jeffery, G., and Morland, A. B. (2005). Retinal abnormalities in human albinism translate into a reduction of grey matter in the occipital cortex. *Eur. J. Neurosci.* 22, 2475–2480. doi: 10.1111/j.1460-9568.2005.04433.x

Yao, A. D., Cheng, D. L., Pan, I., and Kitamura, F. (2020). Deep learning in neuroradiology: a systematic review of current algorithms and approaches for the new wave of imaging technology. *Radiol. Artif. Intell.* 2:e190026. doi: 10.1148/ryai.2020190026

Zhu, W., Huang, Y., Zeng, L., Chen, X., Liu, Y., Qian, Z., et al. (2019). AnatomyNet: deep learning for fast and fully automated whole-volume segmentation of head and neck anatomy. *Med. Phys.* 46, 576–589. doi: 10.1002/mp.13300

Conflict of Interest: The authors declare that the research was conducted in the absence of any commercial or financial relationships that could be construed as a potential conflict of interest.

Publisher's Note: All claims expressed in this article are solely those of the authors and do not necessarily represent those of their affiliated organizations, or those of the publisher, the editors and the reviewers. Any product that may be evaluated in this article, or claim that may be made by its manufacturer, is not guaranteed or endorsed by the publisher.

Chapter 9

CHIASM, the human brain albinism and achiasma MRI dataset

This chapter contains the permitted reprint of the study **"CHIASM, the human brain albinism and achiasma MRI dataset"** published in *Scientific Data*:

Puzniak, R. J., McPherson, B., Ahmadi, K., Herbik, A., Kaufmann, J., Liebe, T., Gouws, A., Morland, A. B., Gottlob, I., Hoffmann, M. B., and Pestilli, F. (Nov. 2021). "CHIASM, the human brain albinism and achiasma MRI dataset". In: *Scientific Data* 8.1, p. 308. DOI: 10.1038/s41597-021-01080-w

scientific data

OPEN

DATA DESCRIPTOR

CHIASM, the human brain albinism and achiasma MRI dataset

Robert J. Puzniak[1], Brent McPherson[2,10], Khazar Ahmadi[1,10], Anne Herbik[1], Jörn Kaufmann[3], Thomas Liebe[4], Andre Gouws[5], Antony B. Morland[6], Irene Gottlob[7], Michael B. Hoffmann[1,8,11] & Franco Pestilli[9,11] ✉

We describe a collection of T1-, diffusion- and functional T2*-weighted magnetic resonance imaging data from human individuals with albinism and achiasma. This repository can be used as a test-bed to develop and validate tractography methods like diffusion-signal modeling and fiber tracking as well as to investigate the properties of the human visual system in individuals with congenital abnormalities. The MRI data is provided together with tools and files allowing for its preprocessing and analysis, along with the data derivatives such as manually curated masks and regions of interest for performing tractography.

Background & Summary

We present CHIASM, the human brain albinism, and achiasma dataset, a unique collection of magnetic resonance imaging (MRI) data of brains with congenital abnormalities in the visual system. The unique feature of these subjects is the varied amount of crossing found in a specific structure –the optic chiasm– across participants with albinism. More specifically, it is well established[1] that the number of crossing fibers crossing at the human optic chiasma to reach the contralateral brain hemisphere (right and left respectively) varies between certain groups. The percentage of fiber crossing at the chiasm has been reported for normal-sighted (control) participants to be about 53%[2]. In brains affected by albinism instead, the number of crossing fibers at the optic chiasm grows above 53%[3]. Crossing fibers within the optic chiasma in individuals affected by chiasm hypoplasia is lower than 53%[4]. Finally, data from individuals with achiasma have been shown to completely lack neuronal fiber crossing at the optic chiasm[1,5,6].

The data covers four participant groups: the controls (n = 8, Fig. 1a), albinism (n = 9, Fig. 1b), chiasma hypoplasia (n = 1; Fig. 1c) and achiasma (n = 1; Fig. 1d), and comprises three different MRI modalities: (A) T1-weighted (T1w; Fig. 1, top row) images, (B) diffusion-weighted images (DWI, Fig. 1, middle row) and (c) T2*-weighted functional MRI (fMRI; Fig. 1, bottom row) images. More specifically: (A) T1w images are provided together with further derivatives (masks and labels obtained through segmentation, white matter mask manually curated in optic chiasm region), (B) DWI data was acquired using high angular[7,8] and spatial[9–11] resolution and is provided with further derivatives, such as tractography results, (C) fMRI data is provided for the subset of participants from control and albinism groups (n = 4 and n = 6, respectively) and is accompanied with meta-files describing stimulus and acquisition. All the data, both in the raw and preprocessed form are available on the cloud computing platform https://brainlife.io[11] and Github repository https://github.com/rjpuzniak/CHIASM.

[1]Visual Processing Lab, Department of Ophthalmology, Otto-von-Guericke-University, Leipziger-Str. 44 (H. 60B), 39120, Magdeburg, Germany. [2]Pestilli Lab, Department of Psychological and Brain Sciences, Indiana University Bloomington, 1101 E 10th Street, Bloomington, Indiana, 47405, USA. [3]Department of Neurology, Otto-von-Guericke-Universität, Leipziger-Str. 44 (H. 60A/60B), 39120, Magdeburg, Germany. [4]Department of Psychiatry and Psychotherapy, Jena University Hospital, Philosophenweg 3, 07742, Jena, Germany. [5]York Neuroimaging Centre, Department of Psychology, University of York, York, YO10 5DD, United Kingdom. [6]Centre for Neuroscience, Hull-York Medical School, Heslington, York, YO10 5DD, United Kingdom. [7]Department of Neuroscience, Psychology & Behaviour, University of Leicester, University Road, Leicester, LE1 7RH, United Kingdom. [8]Center for Behavioral Brain Sciences, Otto-von-Guericke-Universität, Universitätsplatz 2 (G24-205), 39106, Magdeburg, Germany. [9]Department of Psychology, Center for Perceptual Systems, Center for Theoretical and Computational Neuroscience, Institute for Neuroscience, The University of Texas, 108 E Dean Keeton Street, Austin, Texas, 78712, United States. [10]These authors contributed equally: Brent McPherson and Khazar Ahmadi. [11]These authors jointly supervised this work: Michael B. Hoffmann and Franco Pestilli. ✉e-mail: pestilli@utexas.edu

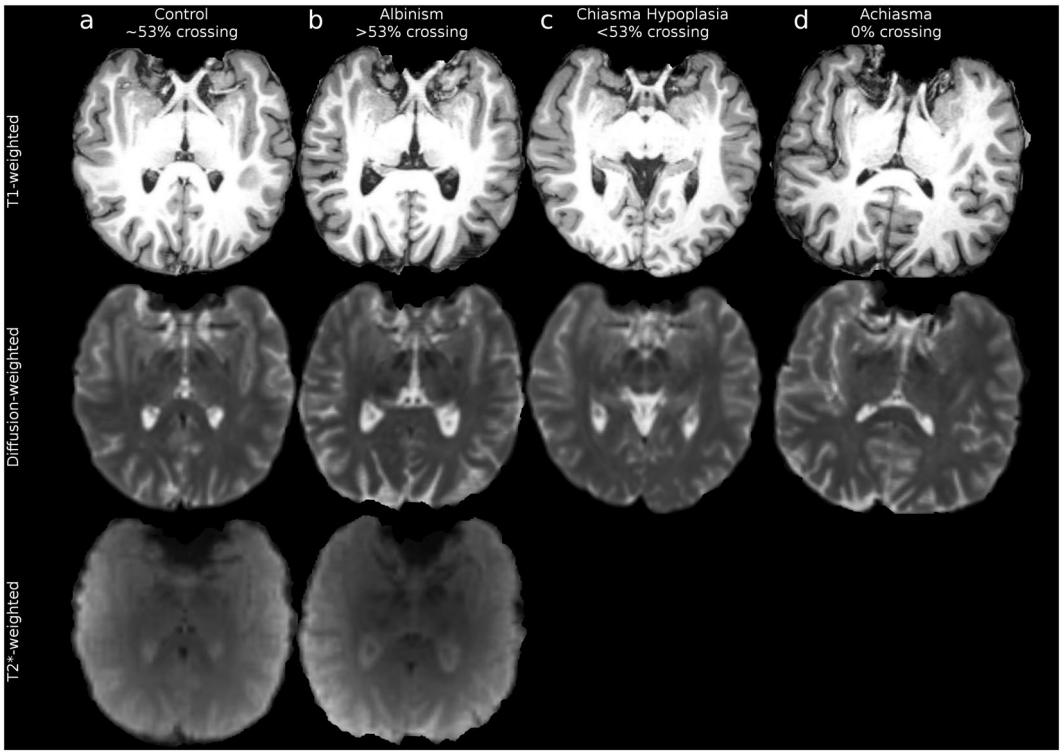

Fig. 1 Overview of structural abnormalities of the optic chiasm and provided MRI data. (**a**) Exemplary control participant (CON1). (**b**) Exemplary participant with albinism (ALB1). (**c**) Participant with chiasma hypoplasia (CHP1). (**d**) Participant with achiasma (ACH1). The fMRI data is not provided due to severe nystagmus and motion compromising the quality of data. Top, middle and bottom rows display respectively T1w, DW, and fMRI data. Images show pseudo-axial views of a T1w image cropped to the brain mask.

The data we present here can be of value to the scientific community for multiple reasons. First, it can serve as a reference dataset to support basic research for clarifying the neuroscientific underpinnings of the different conditions. Currently, there are no reference datasets available covering similar conditions measured with high-resolution DWI data. Second, this dataset can be used by investigators to validate independent results and advance studies on the disease and neuroplasticity mechanisms. This is possible as chiasmal malformations induce abnormal representations within the visual pathways, which are expected to trigger neuroplastic mechanisms e.g. to resolve potential sensory conflicts[1,12–19]. Finally, the dataset presented here can be used to advance tractography methods development. The field of brain tractography has faced a long-lasting challenge commonly referred to as the "crossing fibers problem" or simply CFP[18,20–35]. CFP can lead to poor estimates of the number of crossing fibers through brain regions containing multiple fiber populations[36,37]. It has been established that up to 90% of total brain white matter volume might have crossing fibers[38]. Advancing methods for accurate tracking in regions with crossing fibers is fundamental in clarifying the role of white matter in human health and disease[18,39,40]. As of today, several important approaches to tractography evaluation and validation have been proposed. These approaches can be classified into four primary categories: synthetic phantoms[41,42], physical phantoms[43], biological phantoms[44,45], and statistical[9,32,46–49]. Most of these approaches have helped advance tractography methods, but major challenges remain[30,31,42]. The data made available here opens the possibility to assess crossing strength at the optic chiasm by first using anatomical data (T1w, DWI) to model the crossing at the optic chiasm and cross-validating the proposed findings with functional estimates (fMRI) of misrouting based on the BOLD signal[4,50,51] (see Suppl. Table 1). This provides a unique opportunity for testing novel tractography methods that assess crossing strength by providing an independent modality for their evaluation.

Methods

MRI Data sources. The described MRI data was analyzed in previously published studies[4,50,51], where acquisition protocols and data properties are detailed.

Participants. A single participant with achiasma, a single participant with chiasm hypoplasia, 9 participants with diagnosed albinism, and 8 control participants [no neurological or ophthalmological history; normal visual acuity ($\geq$1.0 with Freiburg Visual Acuity Test[52]) and normal stereo vision[53,54]] were recruited for the MRI measurements. Each participant was instructed about the purpose of the study and the methods involved and gave written informed study participation and data sharing consent. The study was approved by the Ethics Committee of the Otto-von-Guericke University Magdeburg, Magdeburg, Germany. The patients and control participants underwent ophthalmological examination (Suppl. Table 1), which incorporated methods described in[55,56].

MRI Data acquisition. MRI data was acquired with a Siemens MAGNETOM Prisma 3 Tesla scanner with the *Syngo* MR D13D software and a 64-channel head coil. The acquisition protocol for T1w and DW data was initiated by a localizer scan, followed by a whole-brain T1w 3D-MPRAGE scan and two DW scans - respectively with anterior-posterior (A-P) and posterior-anterior (P-A) phase-encoding direction. T1w and DW images were collected during a single continuous scanning session, fMRI data was acquired in separate sessions (patients data was acquired on two consecutive days). T1w images were obtained in sagittal orientation using a 3D-MPRAGE sequence (TE/TR = 4.46/2600 ms, TI = 1100 ms, flip angle = 7°, resolution = $0.9 \times 0.9 \times 0.9$ mm^3, FoV: 230×230 mm^2; image matrix: $256 \times 256 \times 176$, acquisition time = 11 min:06 s[57]) and corrected simultaneously during acquisition for gradient nonlinearity distortions. Each individual's T1w data was screened by a radiologist for unexpected abnormalities present in the data. Apart from the abnormalities given in Methods (Participants), no clinically relevant abnormalities were detected.

DWI were acquired with Echo-Planar Imaging (EPI) sequence (TE/TR = 64.0/9400 ms, b-value 1600 s/mm^2, resolution $1.5 \times 1.5 \times 1.5$ mm^3, FoV 220×220 mm^2, anterior to posterior (A-P) phase-encoding direction, acquisition time = 22 min:24 s, no multi-band). The b-value was chosen with regard to reported optimal values for resolving two-way crossing[58] (1500–2500 s/mm^2). Scans were performed with 128 gradient directions, so the obtained DWI data can be described as High Angular Resolution Diffusion Imaging[7] (HARDI) data. The redundantly high number of gradient directions for the maximal angular contrast provided by a b-value of 1600 s/mm^2 supported residual bootstrapping. This enhanced the effective signal-to-noise ratio (SNR), which is an important feature considering the reduced SNR of the DWI of the optic chiasm. The gradient scheme, initially generated using E. Caruyer's tool for q-space sampling[59] for 3 shells acquisition, was narrowed to the single shell in order to address the acquisition time constraints. DW volumes were evenly intersected by 10 non-diffusion weighted (b-value = 0, hereafter referred to as b0) volumes for the purpose of motion correction. The second DW series were acquired with reversed phase-encoding direction in comparison to the previous scan, specifically posterior to anterior (P-A). Apart from that, all scan parameters were identical to ones corresponding to the preceding acquisition. Acquisition of two DW series with opposite phase-encoding directions enhanced the correction of geometrically induced distortions[60]. Furthermore, the additional scans improve the signal-to-noise ratio (SNR) of the total DWI data.

fMRI data was acquired from 4 controls and 6 participants with albinism (see Suppl. Tables 1 and 2) with T2*-weighted EPI sequence (TE/TR = 30.0/1500 ms, flip angle = 70°, resolution $2.5 \times 2.5 \times 2.5$ mm^3, FoV 210×210 mm^2, acquired with multi-band and in-plane acceleration factor = 2) during visual stimulation. Visual stimulation was performed in either the left, right or both visual hemifields in separate runs. A single repetition comprised 168 volumes acquired within 252 seconds. Each of these three stimulation conditions was repeated three times, resulting in a total of nine functional runs acquired within a single session. The visual stimulation is detailed in[51]. Briefly, it employed a moving high-contrast checkerboard pattern[61] presented within the aperture of a drifting bar (width: 2.5°) within a circular aperture (radius: 10°). The bar aperture was moving in four directions (upwards, downwards, left, and right) across the stimulus window in 20 evenly spaced steps within 30 s. The sequence of the visual stimulation runs was interspersed by equally long (30 s) mean luminance blocks with zero contrast. The stimuli, generated with Psychtoolbox[62,63] in MATLAB (Mathworks, Natick, MA, USA), were projected onto a screen (resolution 1140×780 pixels) placed at the magnet bore. The participants viewed the stimuli monocularly with their dominant eye (see Suppl. Tables 1 and 2) via an angled mirror at a distance of 35 centimeters, and were instructed to fixate on a central dot and respond with a button press to dot color changes.

Data preprocessing. Data preprocessing was mainly performed online, using web services available on the brainlife.io platform (https://brainlife.io), with a few exceptional steps done offline. The source code for the Apps used for online preprocessing is to be found at https://github.com/brainlife. The offline preprocessing involved conversion of DICOM data to NIfTI format, data anonymization, and, in the case of DW data, correction of gradient nonlinearity distortions and alignment to T1w image. The scripts for all of the offline preprocessing steps are available on https://github.com/rjpuzniak/CHIASM. Data preprocessing was meant to provide minimally processed data and standardized T1w, DWI, and fMRI data files.

The following software packages were used for data preprocessing: MRtrix[28,64], FMRIB's FSL[65–67], ANTs[68,69], FreeSurfer[70], dcm2niix[71], MIPAV[72], VISTASOFT package (including mrVista and mrDiffusion tools; https://github.com/vistalab/vistasoft), AFNI[73], fMRIPrep[74], Mindboogle[75], Nipype[76], Nilearn[77] and Human Connectome Project gradunwarp package (https://github.com/Washington-University/gradunwarp). The computing environment of the brainlife.io uses Docker (https://docker.com) as well as Singularity containers (https://sylabs.io/singularity/ and https://singularity.lbl.gov).

Preprocessing of the T1w data. In the offline preprocessing steps, T1w images were converted into the NIfTI format using *dcm2niix*[71] and subsequently anonymized through the removal of facial features using *mri_deface* algorithm[78] from FreeSurfer 6.0.0. Anonymized T1w images were aligned to the Anterior Commissure - Posterior Commissure (ACPC) plane using the mrAnatAverageAcPcNifti.m command from mrDiffusion package (https://github.com/vistalab/vistasoft/wiki/ACPC-alignment). The outcome T1w images were used as the reference image for the coregistration of DWI. Further, T1w images were automatically segmented into five-tissue-type (cerebrospinal fluid, white, grey, and subcortical grey matter, and eventual pathological tissue; 5TT) segmented images[79] through the use of commands from FSL 6.0.3[65,80–82]. Finally, the T1w data was uploaded to brainlife.io, where it was segmented once again using FreeSurfer 7.1.1 (Fig. 2a, top row). Detailed information about the preprocessing code is provided in the Code Availability section (Table 1).

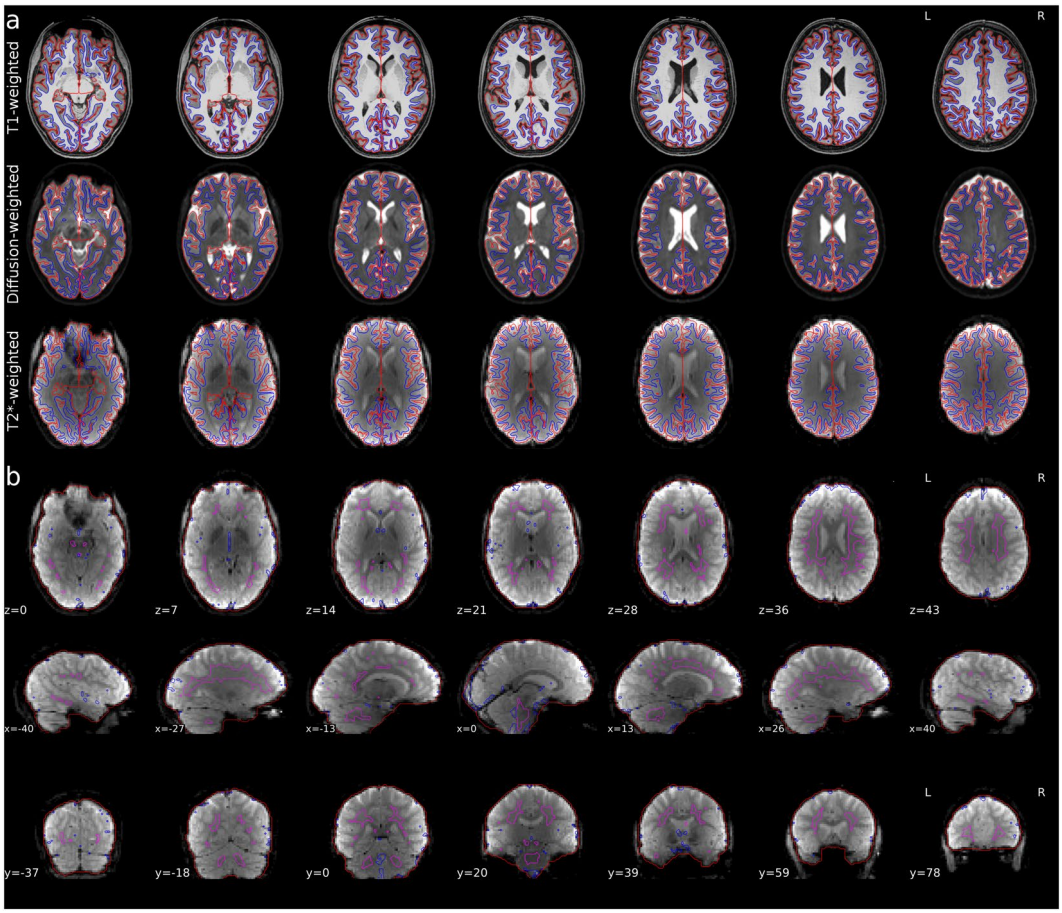

Fig. 2 Qualitative overview of preprocessing for a representative participant (CON1). (**a**) Axial view of surfaces of white and pial matter (blue and red color, respectively) overlaid on T1w (top row), non-diffusion weighted (b0; middle row) and fMRI (T2*; bottom row) images. (**b**) Axial (top row), sagittal (middle row) and coronal (bottom row) views of fMRI images. The red contour marks brain mask estimated from BOLD signal, magenta contour marks combined CSD and WM masks, where voxels with partial GM volume were removed, blue contour marks the top 2% most variable voxels within brain mask.

Preprocessing step	Software/Tool	Software website/App
1. DICOM conversion	dcm2niix	http://people.cas.sc.edu/rorden/mricron/dcm2nii.html
2. Anonymization	FreeSurfer 6.0.0/mri_deface	https://surfer.nmr.mgh.harvard.edu/fswiki/mri_deface
3. ACPC Alignment	mrDiffusion/mrAnatAverageAcPcNifti	https://github.com/vistalab/vistasoft
4. Tissue Segmentation	MRtrix 3.0/5ttgen	https://www.mrtrix.org
5. Tissue segmentation	FreeSurfer 7.1.1/recon-all	https://surfer.nmr.mgh.harvard.edu
		https://doi.org/10.25663/brainlife.app.462[124]

Table 1. List of preprocessing steps applied to the T1w images, together with web links to relevant software and, if available, brainlife.io Apps. Web services used to process that are available for reuse on https://brainlife.io/apps.

Preprocessing of the DWI data. The DICOM DWI data preprocessing followed the well-established outline proposed by the Human Connectome Project (HCP) consortium[83]. Initially, DW files were converted offline into NIfTI format using *dcm2niix* and uploaded to brainlife.io. Next, the DWI data was corrected online for the Rician noise using *dwidenoise*[84,85] and for Gibbs ringing using *mrdegibbs*[86] commands from MRtrix 3.0. The following step of preprocessing involved estimation of the susceptibility-induced off-resonance field in the DW data with FSL's *topup* command[60,65] using two DW series with opposite phase encoding directions. The output of *topup* was subsequently fed to *eddy* command[87] in order to correct for susceptibility- and eddy current-induced off-resonance field, as well as the motion correction. The *topup* and *eddy* command were implemented through *dwifslpreproc* command from MRtrix 3.0, which final output was a single file containing the corrected DW series. In the final online preprocessing step, the data was corrected for the field biases using *dwibiascorrect* from MRtrix 3.0, which, in turn, used the N4 algorithm from ANTS[88] in order to estimate the MR field inhomogeneity. At this stage, the DWI data were downloaded and corrected in an offline mode for the gradient nonlinearities

Preprocessing step	Software/Tool	Software website/App
1. DICOM conversion	dcm2niix	http://people.cas.sc.edu/rorden/mricron/dcm2nii.html
2. Denoising	MRtrix 3.0/dwidenoise	https://www.mrtrix.org
		https://doi.org/10.25663/bl.app.68125
3. Removal of Gibbs ringing	MRtrix 3.0/mrdegibbs	https://www.mrtrix.org
		https://doi.org/10.25663/bl.app.68[125]
4. Geometrical distortions corrections	FSL/topup	https://fsl.fmrib.ox.ac.uk/fsl/fslwiki
		https://doi.org/10.25663/bl.app.68[125]
5. Eddy currents distortions corrections	FSL / eddy	https://fsl.fmrib.ox.ac.uk/fsl/fslwiki
		https://doi.org/10.25663/bl.app.68[125]
6. Correction for head motion	FSL/eddy	https://fsl.fmrib.ox.ac.uk/fsl/fslwiki
		https://doi.org/10.25663/bl.app.68[125]
7. Correction for bias field	MRtrix 3.0/dwibiascorrect	https://www.mrtrix.org
		https://doi.org/10.25663/bl.app.68[125]
8. Correction for gradient nonlinearities	gradunwarp/gradunwarp	https://github.com/Washington-University/gradunwarp
9. Coregistration to T1w image & Rotation of b-vectors	FSL/epi_reg & flirt MRtrix/mrresize HCP Pipelines/rotate_bvecs	https://fsl.fmrib.ox.ac.uk/fsl/fslwiki
		https://www.mrtrix.org
		https://github.com/Washington-University/HCPpipelines/blob/master/global/scripts/Rotate_bvecs.sh

Table 2. List of preprocessing steps applied to the DW images, together with web links to relevant software and, if available, brainlife.io Apps. Web services used to process that are available for reuse on https://brainlife.io/apps.

distortions. This step involved using the *gradunwarp* package and information about Legendre coefficients in spherical harmonics for the scanner's gradient coil, provided by the vendor (stored in the https://github.com/rjpuzniak/CHIASM repository). As for the final step of preprocessing, the DWI data was coregistered to T1w data using the Boundary-Based Registration (Fig. 2a, middle row). At first, the transformation matrix from DWI to T1w image space was estimated with the *epi_reg* command from FLIRT[89–91], a part of FSL 6.0.3 package. The transformation matrix was subsequently applied to DWI data by the *flirt* command from the same package, and to the corresponding b-vectors by shell script from HCP repository (https://github.com/Washington-University/HCPpipelines/blob/master/global/scripts/Rotate_bvecs.sh). The resulting data, in NIfTI format, have been uploaded to brainlife.io and were published as a preprocessed DW data set. Detailed information about the preprocessing code is provided in the Code Availability section (Table 2).

Preprocessing of the fMRI data. The fMRI data was converted into NIfTI format using dcm2niix. Subsequent preprocessing was performed online using two Apps wrapping the fMRIPrep tool[74]: *fMRIPrep - Surface output*[92] (which output data as the surface vertices) and *fMRIPrep - Volume output*[93] (which output data in volumetric format). The preprocessing, in both cases, involved correction for susceptibility distortions using *antsRegistration* from ANTs 2.3.3, registration to T1w image using *bbregister* command from FreeSurfer 6.0.1 (Fig. 2a, bottom row), slice-time correction using *3dTshift* from AFNI and correction for head-motion. Additionally, the BOLD (blood-oxygen-level-dependent) data was subject to Component-Based Noise Correction (CompCor)[94], which uses information principal components from noise-driven regions (defined as top 2% variable voxels in BOLD image; Fig. 2b, blue contour) in order to reduce the standard deviation of resting-state BOLD data. The noise-driven regions selection was limited only to voxels not affected by gray matter partial volume (Fig. 2b, pink contour). The output files created during preprocessing with *fMRIPrep* Apps are described in detail in section Data Records. Detailed information about the preprocessing pipeline is provided in the HTML report files generated by fMRIPrep application in the Data Records, while the code is provided in the Code Availability section (Table 3).

Drawing of the optic chiasm mask. Due to the limited accuracy of the automatically generated optic chiasm mask (Fig. 3a), manual segmentation was necessary to ensure the proper anatomical definition of the structures in each participant. The procedure comprised the following steps:

1) Initial segmentation of voxels unambiguously belonging to the optic chiasm (i.e. outer voxels affected by partial volume effects were excluded). This segmentation was performed only in an axial view and was done in multiple slices covering optic nerves, optic chiasm,and optic tract.
2) Second step where voxels affected by partial volume effects, previously omitted, were included. The two main criteria for the inclusion of candidate voxels were (a) relative intensity (compared to neighboring voxels identified in the previous step) and the coherence/continuity of the optic chiasm structure (already defined by voxels selected in the previous step).
3) A third and final step involved corrections performed in axial, coronal, and sagittal views at the same time. The main criterion here was to assure the continuous borders.

The outcome masks covered posterior optic nerves, whole optic chiasm, and anterior optic tracts (Fig. 3b) and were used for correction of white matter definition in previously generated 5TT masks. The corrected white

Preprocessing step	Software/Tool	Software website/App
1. DICOM conversion	MRtrix 3.0/mrconvert	https://www.mrtrix.org
2. Geometrical distortions corrections	ANTS 2.3.3/antsRegistration	http://stnava.github.io/ANTs/
		https://doi.org/10.25663/brainlife.app.160[93].
		https://doi.org/10.25663/brainlife.app.267[92]
3. Registration to T1w image	FreeSurfer 7.1.1/bbregister	https://surfer.nmr.mgh.harvard.edu/.
		https://doi.org/10.25663/brainlife.app.160[93]
		https://doi.org/10.25663/brainlife.app.267[92]
4. Slice-time correction	AFNI/3dTshift	https://afni.nimh.nih.gov/
		https://doi.org/10.25663/brainlife.app.160[93]
		https://doi.org/10.25663/brainlife.app.267[92]
5. Motion correction	FSL 5.0.9/mcflirt	https://fsl.fmrib.ox.ac.uk/fsl/fslwiki
		https://doi.org/10.25663/brainlife.app.160[93]
		https://doi.org/10.25663/brainlife.app.267[92]
6. Removal of physiological noise	CompCor	https://doi.org/10.25663/brainlife.app.160[93]
		https://doi.org/10.25663/brainlife.app.267[92]

Table 3. List of preprocessing steps applied to the fMRI images, together with web links to relevant software and, if available, brainlife.io Apps. Web services used to process that are available for reuse on https://brainlife.io/apps.

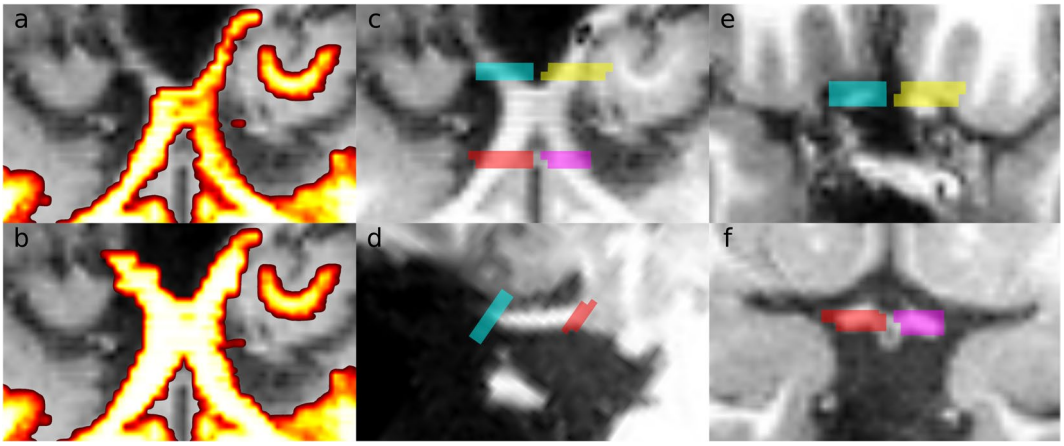

Fig. 3 Masks and regions of interest used to define the location of the optic chiasm, tract, and nerve. Left-hand column, the pseudo-axial view of the anatomical image of exemplary control participant (CON6) and overlaid optic-chiasm white matter mask before (**a**) and after (**b**) manual correction. Middle column, four representative ROIs covering the optic nerves and optic tracts in pseudo-axial (**c**) and sagittal (**d**) view. Right-hand column, four representative ROIs covering a cross-section of optic nerves (**e**) and optic tracts (**f**) in pseudo-coronal view.

matter masks were extracted from 5TT images using *mrconvert* command, transformed to the space of T1w image (in order to ensure matching of QForm and SForm transformation matrices) with *flirt* command from FSL and *mrconvert* commands from MRtrix, and uploaded to the brainlife.io. Detailed information about the code for preprocessing can be found in the Code Availability section (Table 4).

Drawing regions of interest in the optic chiasm. Four ROIs were manually drawn and curated in each participant (Fig. 3c) on the T1w images. These ROIs identified the anterior and posterior aspects of the optic chiasm in each individual. The two anterior ROIs identified the location of the left and right optic nerve (Fig. 3c,e, yellow, and magenta). The posterior ROIs identified the left and right optic tract (Fig. 3c,f, cyan, and red). Once created, ROIs were transformed to the space of T1w image with *mrconvert* and *mrtransform* and thresholded with *mrthreshold* commands from MRtrix (in order to remove interpolation artifacts) and uploaded to the brainlife.io. Detailed information about the code for preprocessing can be found in the Code Availability section (Table 4).

Diffusion signal reconstruction, tractography, and statistical evaluation. The whole-brain tractography was performed using MRtrix 0.2.12[64]. The tractography was based on diffusion tensor (DT) and constrained spherical deconvolution (CSD) models and was performed using both deterministic and probabilistic methods[25,28,95–99]. The DT model was used for deterministic tracking, in the case of CSD both deterministic and probabilistic tracking was applied. The tractography utilized Anatomically-Constrained Tractography[79], where the tracking was restricted to gray matter-white matter boundary from the newly created FreeSurfer 7.1.1 segmentation of the provided T1w image to ensure the agreement of the obtained tracks with the underlying anatomical

Preprocessing step	Software/Tool	Software source/App
1. Alignment of the custom mask to T1w image	FSL/flirt	https://www.mrtrix.org
2. Alignment of the ROIs to T1w image	MRtrix/mrtransform	https://www.mrtrix.org
3. Removal of interpolation artifacts	MRtrix/mrthreshold	https://www.mrtrix.org

Table 4. List of preprocessing steps applied to the custom white matter masks and ROIS, together with web links to relevant software and, if available, brainlife.io Apps. Web services used to process that are available for reuse on https://brainlife.io/apps.

structure. Additionally, an Ensemble Tractography[100] framework was used, which negates bias of different parameter options in tractography by merging results of several tracking approaches, with each generating tracks with different properties[18,41,101–104]. Merging all tractograms mitigates the bias introduced from the variability of individual tractography parameters. Adhering to this, the final tractogram consisted of streamlines generated using: (A) deterministic tracking[97] based on Diffusion Tensor[95,105], (B) deterministic tracking[25] based on Constrained Spherical Deconvolution model[106] (CSD), and (C) probabilistic CSD-based tracking using iFOD2 algorithm[28]. The tractography was performed for several harmonic orders L = 2, 4, 6, 8, 10, 12, which were estimated using *dwi2reponse tournier*[107] and *dwi2fod msmt_csd*[108] commands from MRtrix 3.0. The full set of parameters guiding tractography is as follows: step size 0.15 mm for (A) and (B), 0.75 mm for (C); minimal length 7.5 mm, maximal length 200 mm, maximum angle between consecutive steps 5, 10, 20, 40, 80°, 15,000 fibers per parameters combination. The tracking has been performed using *Ensemble Tracking (dwi)*[109] brainlife.io application.

The whole-brain tractogram was evaluated and optimized using the Linear Fasiscle Evaluation method[9,49] (LiFE). Over the course of the evaluation process, every streamline is assigned a weight indicating its unique contribution in explaining the measured diffusion signal based on a tensor fit of the preprocessed diffusion data. Streamlines with non-zero weights are deemed as significant, while others are being discarded. The brainlife.io application implementing LiFE evaluation[9] can be found at[110].

Data Records

The data includes T1w, DW, and (if available) fMRI images of: single participant with achiasma (ACH1), single participant with chiasma hypoplasia (CHP1), 9 participants with albinism (ALB1 - ALB9) and 8 control participants (CON1 - CON8). The data from control participants are provided under an open license. To assure anonymity of the participants with clinical conditions, their data are made available upon direct request (as regulated by the Data Use Agreement, Suppl. Box 1).

The data is publicly accessible via brainlife.io platform[11] at https://doi.org/10.25663/brainlife.pub.9[111]. When downloaded, the files are organized as defined by brainlife.io DataTypes (https://brainlife.io/docs/user/datatypes/ and https://brainlife.io/datatypes), and, if applicable, as the most updated version of the Brain Imaging Data Structure specification[112] (BIDS). Due to the developmental nature of the BIDS format, at the present time, it does not support all the data derivative types presented here; the data records detailed below are presented according to brainlife.io Data Types. The data files stored for each subject on brainlife.io can be divided into three general categories: (A) source data, which consist of anonymized and aligned to the anterior commissure - posterior commissure (AC-PC) space T1w image, raw DW and fMRI data in NIfTI format, (B) preprocessed data, which consist of preprocessed DW and fMRI data, as described in Data Preprocessing section and (C) data derivatives, as described in Data Derivatives section. Additionally, the fMRI NIfTI data stored on brainlife.io are provided together with (D) MrVista.mat files (further referred to as "fMRI meta-files"), which are necessary for the analysis of the former. Those files are stored in a separate Open Science Framework (OSF) repository: https://doi.org/10.17605/osf.io/XZ29Q[113] and are described in detail in the 'fMRI meta-files' section.

Source data. Source data (raw) files consist of two DWI datasets, one T1w set per participant, and, in the case of 6 participants from the albinism group and 4 controls, fMRI T2*-weighted images.

DW source data. Source DWI data covers two DW series acquired with opposite phase encoding directions (PEDs) - Anterior-Posterior (AP, Box 1a) and Posterior-Anterior (PA, Box 1b), as indicated by the tags.

Box 1 Organization of the DW source data files according to the brainlife.io Data Types. (**a**) DW data files corresponding to acquisition with AP PED, (**b**) DW data files corresponding to acquisition with PA PED.

```
(a) proj-5ddfa986936ca339b1c5f455/sub-{}/dt-neuro-dwi.tag-raw.tag-AP.
    tag-normalized.tag-single_shell.id-{}/
       dwi.bvals
       dwi.bvecs
       dwi.nii.gz
       _info.json
(b) proj-5ddfa986936ca339b1c5f455/sub-{}/dt-neuro-dwi.tag-raw.tag-PA.
    tag-normalized.tag-single_shell.id-{}/
    dwi.bvals
      dwi.bvecs
      dwi.nii.gz
      _info.json
```

fMRI source data. The source fMRI data is available for 6 participants with albinism (ALB1, ALB5, ALB6, ALB7, ALB8 and ALB9) and 4 controls (CON1, CON2, CON3 and CON8) and incorporates BOLD series acquired in 6 runs (3 runs corresponding to monocular stimulation of right visual hemifield, and 3 runs for left), except for ALB5 (3 runs for right and 2 for left hemifield) and CON1 (2 runs for right and 3 for left hemifield). Importantly, the fMRI files for the participant are stored in separate sessions (e.g. CON1/run4, Box 2).

Box 2 Organization of the fMRI source data files according to the brainlife.io Data Types.

```
proj-5ddfa986936ca339b1c5f455/sub-{}.ses-run{}/dt-neuro-func-task.tag-
raw.tag-retinotopy.id-{}/
     bold.nii.gz
     _info.json
```

T1w source data. Source T1w images (already anonymized and aligned to ACPC plane) were uploaded to participant's main folder (e.g. CON1/, Box 3a), and, if applicable, all fMRI sessions (e.g. CON1/run4, CON1/run5 etc., Box 3b).

Box 3 Organization of the T1w source data files according to the brainlife.io Data Types. (**a**) T1w images uploaded to participant's main folder, (**b**) T1w images uploaded to all folders corresponding to separate fMRI sessions.

```
(a) proj-5ddfa986936ca339b1c5f455/sub-{}/dt-neuro-anat-t1w.tag-ACPC.
    id-{}/
      T1.nii.gz
      _info.json
(b) proj-5ddfa986936ca339b1c5f455/sub-{}.ses-run{}/dt-neuro-anat-t1w.
    tag-ACPC.id-{}/
      T1.nii.gz
      _info.json
```

Preprocessed data. Preprocessed files are divided into 2 main categories: DW and fMRI files. The former are stored in each participant's main folder, whereas fMRI files, if provided, are stored in folders corresponding to separate sessions.

DW preprocessed data. Preprocessed DW data consists of two files, tagged as "preprocessed" and "clean". The 'preprocessed' tag marks the data (Box 4), which has been processed online, but lacks correction for gradient nonlinearity distortions and was not aligned to T1w image (those last two steps were performed offline) - the details are described in the "Data preprocessing" section.

Box 4 Organization of the preprocessed DW data files, tagged as "preprocessed", according to the brainlife.io Data Types.

```
proj-5ddfa986936ca339b1c5f455/sub-{}/dt-neuro-dwi.tag-raw.tag-AP.
tag-normalized.tag-single_shell.tag-preprocessed.id-{}/
    dwi.bvals
    dwi.bvecs
    dwi.nii.gz
    _info.json
```

The "clean" tag marks the data which has been completely preprocessed and aligned to T1w image (Box 5). Consequently, the files tagged as "clean" are recommended for further analyses.

Box 5 Organization of the preprocessed DW data files, tagged as "clean", according to the brainlife.io Data Types.

```
proj-5ddfa986936ca339b1c5f455/sub-{}/dt-neuro-dwi.tag-clean.tag-ACPC.
tag-normalized.tag-single_shell.id-{}/
    dwi.bvals
    dwi.bvecs
    dwi.nii.gz
    _info.json
```

fMRI preprocessed data. fMRI data processing was performed both for surface and volume representations of the data, and in both cases several output files were created.

In case of surface output[92], the output files consist of surface vertices (3D mesh), for pial and white matter, as well as inflated representation, defined for both hemispheres (Box 6a), surface data in NIfTI format containing measures at each vertices (Box 6b), surface time series data in CIFTI format (Box 6c), HTML preprocessing report (Box 6d), volumetric mask of brain (Box 6e) and confounds (nuisance regressors) representing fluctuations with a potential non-neuronal origin, identified using CompCor (Box 6f).

Box 6 Organization of the fMRI preprocessed data files (surface output) according to the brainlife.io Data Types. (**a**) surface vertices (3D mesh), for pial and white matter, as well as inflated representation, defined for both hemispheres, (**b**) surface data in NIfTI format containing measures at each vertices, (**c**) surface time series data in CIFTI format, (**d**) HTML preprocessing report, (**e**) volumetric mask of brain and (**f**) confounds (nuisance regressors) representing fluctuations with a potential non-neuronal origin, identified using CompCor.

```
(a) proj-5ddfa986936ca339b1c5f455/sub-{}.ses-run{}/dt-neuro-surface-vertices.id-{}/
      _info.json
      left/
            inflated.gii
            pial.gii
            white.gii
      right/
            inflated.gii
            pial.gii
            White.gii
(b) proj-5ddfa986936ca339b1c5f455/sub-{}.ses-run{}/dt-neuro-surface-data.id-{}/
      _info.json
      left.gii
      Right.gii
(c) proj-5ddfa986936ca339b1c5f455/sub-{}.ses-run{}/dt-neuro-cifti.tag-dtseries.id-{}/
      cifti.nii
      _info.json
(d) proj-5ddfa986936ca339b1c5f455/sub-{}.ses-run{}/dt-report-html.tag-fmriprep.id-{}/
      html/
            sub-{}/
                  figures/
                        …
            sub-{}.html
      _info.json
(e) proj-5ddfa986936ca339b1c5f455/sub-{}.ses-run{}/dt-neuro-mask.tag-anat.tag-brain.id-{}/
      _info.json
      Mask.nii.gz
(f) proj-5ddfa986936ca339b1c5f455/sub-{}.ses-run{}/dt-neuro-func-regressors.id-{}/
      _info.json
      regressors.json
      regressors.tsv
```

Volumetric preprocessing output[93] shares a majority of files with surface preprocessing (Box 6c–f), except for files containing data in surface representation (Box 6a,b). Furthermore, two additional files are included in the volumetric input: brain mask based on BOLD image (Box 7a) and volumetric BOLD image (Box 7b).

Box 7 Organization of the additional fMRI preprocessed data files (volume output), with regard to files from surface output, according to the brainlife.io Data Types. (**a**) brain mask based on BOLD image and (**b**) volumetric BOLD image.

```
(a) proj-5ddfa986936ca339b1c5f455/sub-{}.ses-run{}/dt-neuro-mask.tag-brain.tag-bold.tag-func.id-{}/
      _info.json
      mask.nii.gz
(b) proj-5ddfa986936ca339b1c5f455/sub-{}.ses-run{}/dt-neuro-func-task.tag-raw.tag-retinotopy.tag-preprocessed.id-{}/
      bold.nii.gz
      _info.json
```

Data derivatives. Provided data derivatives consist of manually curated and automatically generated white matter masks, custom ROIs, T1w image segmentation, tractograms, and filtered tractograms.

Manually curated and automatically generated masks. White matter masks manually curated in the optic chiasm region (Fig. 3b; creation described in "Data preprocessing" section) sampled to match the original T1w image resolution (Box 8):

Box 8 Organization of the data files of manually curated optic chiasm masks according to the brainlife.io Data Types.

```
proj-5ddfa986936ca339b1c5f455/sub-{}/dt-neuro-mask.id-{}/
      _info.json
      mask.nii.gz
```

Additional white matter mask (created from FreeSurfer segmentation of white matter), generated by brainlife.io App performing tractography[109] (Box 9):

Box 9 Organization of the data files of automatically generated optic chiasm masks according to the brainlife.io Data Types.

```
proj-5ddfa986936ca339b1c5f455/sub-{}/dt-neuro-mask.tag-white_matter.
tag-anat.id-{}/
      _info.json
      mask.nii.gz
```

Custom ROIs. We provide a set of four masks covering the left and right optic nerve and left and right optic tract (Fig. 3e). ROIs (Box 10) are provided as individual NIfTI files containing the left and right optic tract (OT) and the left and right optic nerve (ON). Data in the files contain a '1' for each voxel within the ROIs, 0 otherwise. These ROIs can be used for tracking start-end.

Box 10 Organization of the data files of custom ROIs covering optic nerves and optic tracts according to the brainlife.io Data Types.

```
proj-5ddfa986936ca339b1c5f455/sub-{}/dt-neuro-rois/tag-aligned.id-{}/
    _info.json
      rois/
      {}-left_ON.nii.gz
      {}-left_OT.nii.gz
      {}-right_ON.nii.gz
      {}-right_OT.nii.gz
```

T1w image segmentation. A FreeSurfer (v 7.1.1.) segmentation of T1w image, which was generated as a part of data preprocessing (see section "Data preprocessing") and was used in tractography (Box 11a) and fMRI data preprocessing (Box 11b) is provided exclusively in brainlife.io Data Types format.

Box 11 Organization of the T1w segmentation data files (generated by the FreeSurfer) according to the brainlife.io Data Types. Data files used for (**a**) tractography and (**b**) fMRI data preprocessing purposes.

```
(a) proj-5ddfa986936ca339b1c5f455/sub-{}/dt-neuro-freesurfer.tag-ACPC.
    id-{}/
      _info.json
      output/
         label/
         mri/
         scripts/
       stats/
         surf/
         tmp/
         touch/
         trash/
(b) proj-5ddfa986936ca339b1c5f455/sub-{}.ses-run{}/dt-neuro-freesurfer.
    tag-ACPC.id-{}/
      _info.json
      output/
         label/
         mri/
         scripts/
         stats/
         surf/
         tmp/
         touch/
         trash/
```

Tractograms and filtering results. The results of tractography performed for the purpose of technical validation of the DW data (Box 12a) and results of its filtering with LiFE (Box 12b) are provided as part of the repository:

Box 12 Organization of the tractography data according to brainlife.io Data Types. (**a**) outcome tractogram generated for the purpose of technical validation and (**b**) results of its filtering with LiFE algorithm.

```
(a) proj-5ddfa986936ca339b1c5f455/sub-{}/dt-neuro-track-tck.tag-ensem-
    ble.id-{}/
      Track.tck
(b) proj-5ddfa986936ca339b1c5f455/sub-{}/dt-neuro-life-tck.tag-ensemble.
    id-{}/
      Track.tck
```

fMRI meta-files. fMRI meta-files (for a subset of 6 albinism and 4 control participants, for which fMRI source data are provided) are available on the Open Science Framework (OSF) platform: https://doi.org/10.17605/osf.io/XZ29Q[113]. The files are in MATLAB format.mat and provide all the necessary information for performing the retinotopy data analysis using the MrVista package (https://github.com/vistalab/vistasoft). For each participant there is a total of 6 files: description of visual stimulus presented during left and right visual hemifield stimulation (Box 13a,b, respectively), full information about the acquisition parameters, participant's response and stimulus for left and right visual hemifield stimulation (Box 13c,d, respectively; this also includes contents of visual stimulus corresponding to given hemifield stimulation as in Box 13a,b, respectively), file containing all parameters necessary for initialization of session in MrVista (such as paths to files required in analysis; Box 13e) and mrSession file storing all information about the analysis (Box 13f):

Box 13 Organization of the fMRI meta-files stored on OSF repository. Description of visual stimulus presented during (**a**) left and (**b**) right visual hemifield stimulation, full information about the acquisition parameters, participant's response and stimulus for (**c**) left and (**d**) right visual hemifield stimulation [this also includes contents of visual stimulus corresponding to left and right hemifield stimulation as in (**a**) and (**b**), respectively], (**e**) file containing all parameters necessary for initialization of session in MrVista (such as paths to files required in analysis) and (**f**) mrSession file storing all information about the analysis).

```
(a) {}/{}_images_left_images.mat
(b) {}/{}_images_right_images.mat
(c) {}/{}_params_left_mod.mat
(d) {}/{}_params_right_mod.mat
(e) {}/{}_mrInit_params.mat
(f) {}/{}_mrSession.mat
```

Technical Validation

This section provides a quality assessment of the published DW and fMRI data and is based on a previously published approach[11] comprising qualitative and quantitative measures.

Qualitative assessment. The qualitative assessment involves (A) demonstration of the quality of alignment between anatomical, DWI, and fMRI images, and (B) demonstration of reconstruction of diffusion signal and tractography in the optic chiasm.

Registration of anatomical, DW, and fMRI data. A critical step in data preprocessing is to obtain the precise alignment between images of various modalities (T1w, DWI, and fMRI images; for a detailed description see Methods). The quality of registration is demonstrated by overlaying FreeSurfer's 7.1.1 segmentation contours of white and pial matter (Fig. 2a; blue and red colors, respectively) on top of T1w image (from which they were derived; Fig. 2a, top row), DWI (Fig. 2a, middle row) and BOLD image (Fig. 2a, bottom row) for a representative participant (CON1).

Diffusion signal reconstruction and tractography in the optic chiasm. Considering the role of optic chiasm malformations as a major factor driving group differences, the quality assessment included diffusion signal modeling and tractography in this structure. Figure 4a displays representative optic chiasms in the T1w images, next to aligned dMRI b0 images (Fig. 4b). The DWI signal in each voxel was modeled using a CSD[106,114] model in a process where an estimated single fiber response (SFR; $L_{max} = 6$) was used as a deconvolution kernel in the process of calculating the fiber orientation distribution function[20] (FOD; $L_{max} = 12$) from acquired DWI. Figure 4c demonstrates the fit of calculated FOD in an optic chiasm region. Figure 4d demonstrates tracking results in the region of the optic chiasm. Presented results are limited only to probabilistic CSD-based tractography (iFOD2 algorithm, step size = 0.75 mm, FOD cutoff amplitude = 0.06, maximum angle between successive steps = 45°) based on already calculated ODFs ($L_{max} = 12$; Fig. 4c), which was done between pairs of ROIs and within manually corrected white matter mask defined in the Data derivatives paragraph of the Methods section. For the purpose of clarity, only 0.25% of the total number of generated streamlines is displayed.

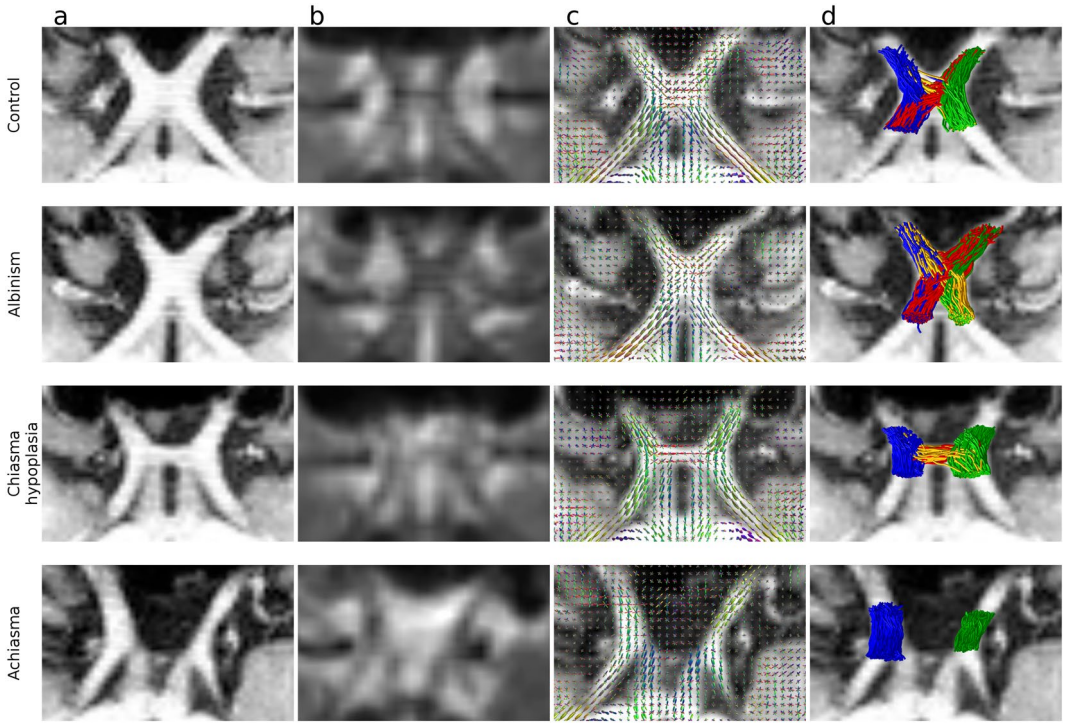

Fig. 4 Diffusion signal reconstruction and tractography. The rows correspond to exemplary participants representing, respectively from top to bottom: control (CON1), albinism (ALB1), chiasma hypoplasia (CHP1) and achiasma (ACH1). (**a**) Pseudo-axial view of T1w image of the optic chiasm. (**b**) Pseudo-axial view of b0 image of the optic chiasm. (**c**) Pseudo-axial view of the anatomical image with overlaid estimated fiber orientation distribution function (FOD; $L_{max} = 12$). (**d**) Pseudo-axial view of an anatomical image with overlaid results of tractography performed between pairs of ROIs defined in Methods.

Quantitative assessment. The quantitative validation includes (A) assessment of participants' motion during DW data acquisition, (B) SNR in raw and preprocessed DW images, (C) modeling of DW data, (D) tractography, (E) temporal SNR of fMRI data, and (F) pRF-mapping.

Participant's motion during DW data acquisition. The participants' motion in DWI has been calculated for concatenated AP and PA series (acquired subsequently during a single scanning session, see Methods) by calculating the RMS of each voxels' displacement using the *Eddy* command from FSL. The displacement calculation used the first acquired voxels as a reference for all volumes and included only voxels within the brain mask. The slow, yet steadily increasing drift visible for all participants (Fig. 5a) can be well tracked with b0 images intersecting DW series, which benefited motion correction. While, the lowest RMS was observed for the control group (which can be justified by the inclusion of trained control participants, well accustomed to MRI scanning), no proof for inequality of mean displacement RMS between participants with albinism and controls was found (Student's t-test p-value = 0.11). It should be noted that the increased motion shown by achiasmatic participant ACH1 matches the observations from the fMRI scanning session, where the data had to be discarded due to extensive motion.

The output data of *eddy* describing motion for each participant is available online on the Github repository (https://github.com/rjpuzniak/CHIASM/tree/main/Plots/Fig.5_Motion), where it is provided together with the MATLAB code of Fig. 5a.

SNR in DW data. In order to evaluate the quality of the DWI data, the signal-to-noise ratio (SNR) of raw and preprocessed images was measured. The computations were performed for b0 (Fig. 5b) and diffusion-weighted (along with X-, Y- and Z-axis; Suppl. Fig. 1) for corpus callosum and optic chiasm voxels. Specifically, the SNR was defined as the mean ratio of the signal in voxels (from the selected structure) to standard deviation of noise (measured in voxels outside the brain), as described in[37,115]. In the case of the corpus callosum, the SNR was calculated separately for b0 images of two raw DW series (one with AP PED and one with opposite PA PED) and for the fully preprocessed DW image ("corrected"). As expected, the comparable SNR of corrected images is increased while the preprocessing (unwarping) is performed (Fig. 5b).

Comparable analysis of SNR in optic chiasm was obstructed by the severe geometry-induced distortions present in this region, which introduce spatial warping of the chiasm. Although theoretically this problem can be addressed by using new sets of optic chiasm masks (created separately for images warped in AP and PA directions), drawing new masks on top of DW images in heavily distorted regions is practically extremely challenging and is highly likely to introduce inaccuracies. Instead, the SNR was calculated for the fully preprocessed

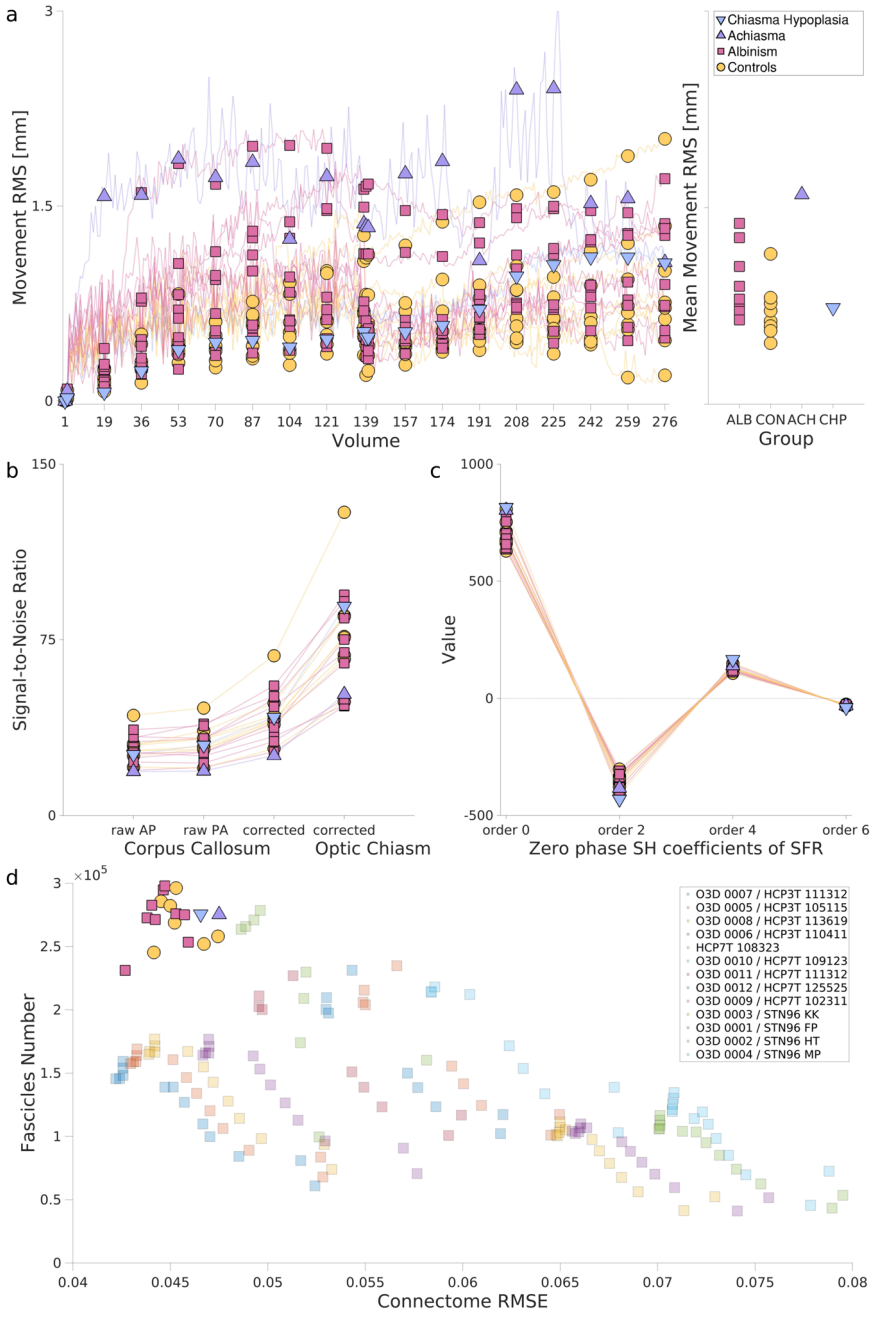

Fig. 5 Quantitative assessment of motion, SNR, and modeling of DW data, as well as the quality of derived tractograms. (**a**) Left plot displays motion in the DW volumes (expressed as Root Mean Square of voxel displacements within brain mask, calculated with respect to the first volume) where 138 volumes with AP PED were followed by 138 volumes with opposite PED. Markers indicate the values calculated for the b0 volumes. The right-hand plot displays the mean motion RMS calculated for each participant. The color code and markers shape correspond to groups: orange circle - control, magenta square - albinism, violet up-pointing triangle - achiasma, blue down-pointing triangle - chiasma hypoplasia. (**b**) SNR in b0 images for each participant calculated from callosal voxels (selected from raw AP PED DW series, raw PA PED DW series, and corrected DWI) and optic chiasm (only for corrected DWI). (**c**) Values of zero phase (m = 0) coefficients of SFR calculated for each participant. (**d**) Results of evaluation of tractogram using LiFE method. Y-axis displays the number of fascicles remaining after filtering with LiFE, x-axis displays voxel-wise error between original signal and the one predicted from optimized tractograms. The bright markers correspond to the published datasets, while the dimmed display results for representative datasets from other publicly available DW repositories (such as 3T and 7T HCP datasets).

(corrected) DWI images, where the optic chiasm mask was cropped from a manually curated white matter mask (Fig. 5b). The observed higher SNR in optic chiasm (compared to corpus callosum) could be due to multiple reasons that were not tested by the authors. We speculate that it might be the result of using a 64-channel Radio

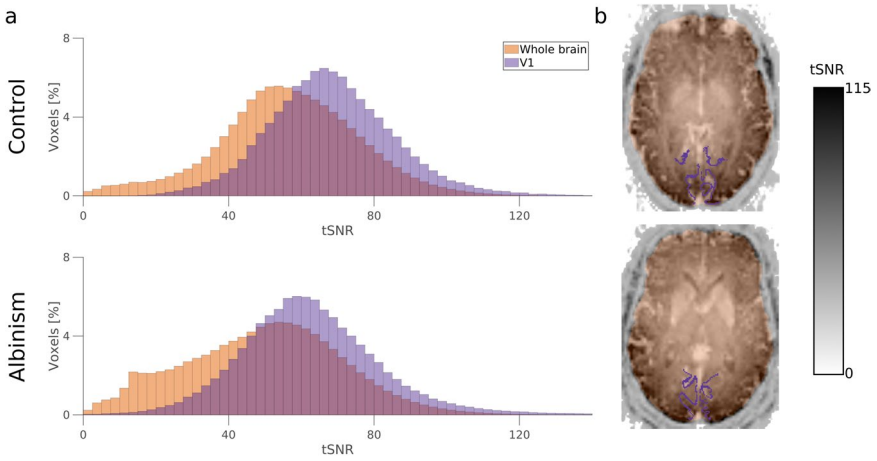

Fig. 6 BOLD image temporal SNR in V1 and whole-brain volume. (**a**) Histograms of tSNR calculated in whole brain volume (orange) and V1 region (defined according to Benson's atlas; violet). (**b**) Whole brain (orange) and V1 (violet) masks overlaid on maps of tSNR calculated for representative participants (top - control participant CON1, bottom - participant with albinism ALB1).

Frequency coil, which measures stronger signals from peripheral brain regions in comparison to deeper regions such as the corpus callosum. The brainlife.io application implementing the SNR computation in the corpus callosum can be found at[116] which follows the outlined SNR calculation strategy presented in[37,115].

Coefficients of the single fiber response (SFR) function. The quality of modeling of DWI was assessed by plotting the zero phase coefficient of the SFR function (calculated for $L_{max} = 6$ with *dwi2response* command from MRtrix, which used a iterative algorithm for SFR voxels selection and response function estimation;[107] Fig. 5c). The observed plot is in agreement with theoretical expectations, where successive non-zero (even) terms are of opposite signs and of decreasing absolute value.

Quality of tractography. Finally, the quality of the created tractogram has been assessed with the LiFE algorithm (see Diffusion signal reconstruction, tractography and statistical evaluation in Methods). Figure 5d demonstrates the correlation between the number of fascicles of non-zero weights (y-axis) and Connectome Root Mean Square Error (RMSE;[9,103]). The data points for all CHIASM participants demonstrate a high number of weighted fascicles (positively contributing to measured signal, y-axis on Fig. 5d) combined with a low connectome's RMSE (measuring the discrepancy between signal predicted from weighted fascicles and measured signal, y-axis). Those measures replicate previous findings of high-quality diffusion scans (HCP/O3D[11,117]).

tSNR of fMRI data. The quality of fMRI images was assessed using a temporal SNR (tSNR) measure (Fig. 6). Specifically, the tSNR in the BOLD images was calculated for two areas - whole brain volume (derived from BOLD images with *fMRIPrep - Volume Output*[93] App) and primary visual cortex (V1) mask derived from T1w image using Benson's atlas[118–120]. The tSNR has been calculated using the code provided in[121] (https://github.com/psychoinformatics-de/studyforrest-data-aligned). The mean values of tSNR calculated for participants with albinism and controls (51.0 and 57.7, respectively) correspond well to the tSNR previously reported for voxel volumes of 16.625 mm^3 [122].

Population Receptive Fields (pRF) Mapping. The pRF-mapping data derivatives and methods were described in a previous publication[51]. Briefly: The pRF sizes and positions can be estimated from the fMRI data and visual stimulus position time course. The BOLD response of each voxel can be predicted using a circular 2D-Gaussian model of the neuronal populations receptive field defined by three stimulus-referred parameters i.e. x0, y0, σ where x0 and y0 are the coordinates of the receptive field center and σ is it's spread[61]. The predicted BOLD signal can be calculated by convolution of the stimulus sequence for the respective pRF-model and its three parameters with the canonical hemodynamic response function[123]. Based on this, the optimal pRF parameters can be found by minimizing the residual sum of squared errors (RSS) between the predicted and observed BOLD time-course. Only voxels will be retained whose explained variance exceeded a threshold of 15%.

Usage Notes

This data is organized according to BIDS standard[112], whenever applicable (additionally, in all cases the data is organized according to brainlife.io Data Types), and are stored in documented standard NIfTI format. The data is to be accessed at the brainlife.io computing platform either by (A) the web interface of brainlife.io and/or (B) a command-line interface (https://github.com/brainlife/cli). CLI offers means to query and download partial or full data. This utility is further expanded when using a web interface, which in addition to selection and download of data allows for online processing with provided brainlife.io Apps Table 5.

Type	Preprocessing step	URL to code
T1w	1. DICOM conversion	—
	2. Anonymization	—
	3. ACPC Alignment	—
	4. Tissue Segmentation	—
	5. Tissue segmentation	https://github.com/brainlife/app-freesurfer/tree/7.1.1
DWI	1. DICOM conversion	https://github.com/rjpuzniak/CHIASM/blob/main/Uploading_and_Preprocessing/Diffusion_and_T1-weighted_data/1_Upload_raw_DW_T1w.sh
	2. Denoising	https://github.com/brain-life/app-mrtrix3-preproc
	3. Removal of Gibbs ringing	https://github.com/brain-life/app-mrtrix3-preproc
	4. Eddy currents distortions corrections	https://github.com/brain-life/app-mrtrix3-preproc
	5. Geometrical distortions corrections	https://github.com/brain-life/app-mrtrix3-preproc
	6. Correction for head motion	https://github.com/brain-life/app-mrtrix3-preproc
	7. Correction for bias field	https://github.com/brain-life/app-mrtrix3-preproc
	8. Correction for gradient nonlinearities	https://github.com/rjpuzniak/CHIASM/blob/main/Uploading_and_Preprocessing/Diffusion_and_T1-weighted_data/2_Apply_GNC.sh
	9. Coregistration to T1w image & Rotation of b-vectors	https://github.com/rjpuzniak/CHIASM/blob/main/Uploading_and_Preprocessing/Diffusion_and_T1-weighted_data/3_Align_DW_to_T1w.sh
fMRI	1. DICOM conversion	https://github.com/rjpuzniak/CHIASM/blob/main/Uploading_and_Preprocessing/fMRI/1_Extract_anonymize_upload_fMRI_data.sh
	2. Geometrical distortions corrections	https://github.com/brainlife/app-fmriprep/tree/20.2.1
	3. Registration to T1w image	https://github.com/brainlife/app-fmriprep/tree/20.2.1
	4. Slice-time correction	https://github.com/brainlife/app-fmriprep/tree/20.2.1
	5. Motion correction	https://github.com/brainlife/app-fmriprep/tree/20.2.1
	6. Removal of physiological noise	https://github.com/brainlife/app-fmriprep/tree/20.2.1
Masks and ROIs	1. Alignment of the custom mask to T1w image	https://github.com/rjpuzniak/CHIASM/blob/main/Uploading_and_Preprocessing/ROIs_and_Mask/1_Align_anonymize_upload_ROIs.sh
	2. Alignment of the ROIs to T1w image	https://github.com/rjpuzniak/CHIASM/blob/main/Uploading_and_Preprocessing/ROIs_and_Mask/1_Align_anonymize_upload_ROIs.sh
	3. Removal of interpolation artifacts	https://github.com/rjpuzniak/CHIASM/blob/main/Uploading_and_Preprocessing/ROIs_and_Mask/1_Align_anonymize_upload_ROIs.sh

Table 5. Code implementing each processing step. Code implementing the processing pipeline is available on https://github.com/rjpuzniak/CHIASM.

Code availability

The processing was performed mainly using brainlife.io services (https://brainlife.io/apps), which together with the code are available online. The offline preprocessing was performed with freely accessible neuroimaging tools. The preprocessing steps, together with the references to the Software/Apps are provided separately for the T1w, DW, fMRI data, and hand-curated ROIs and mask (Tables 1–4, respectively). The web links to source code are provided separately in the Table 5.

Received: 17 June 2020; Accepted: 11 October 2021;
Published online: 26 November 2021

References

1. Hoffmann, M. B. & Dumoulin, S. O. Congenital visual pathway abnormalities: a window onto cortical stability and plasticity. *Trends Neurosci.* **38**, 55–65 (2015).
2. Kupfer, C., Chumbley, L. & Downer, J. C. Quantitative histology of optic nerve, optic tract and lateral geniculate nucleus of man. *J. Anat.* **101**, 393–401 (1967).
3. Hoffmann, M. B., Lorenz, B., Morland, A. B. & Schmidtborn, L. C. Misrouting of the Optic Nerves in Albinism: Estimation of the Extent with Visual Evoked Potentials. *Invest. Ophthalmol. Vis. Sci.* **46**, 3892–3898 (2005).
4. Ahmadi, K. *et al.* Triple visual hemifield maps in a case of optic chiasm hypoplasia. *NeuroImage* **215**, 116822 (2020).
5. Hoffmann, M. B. *et al.* Plasticity and stability of the visual system in human achiasma. *Neuron* **75**, 393–401 (2012).

6. Davies-Thompson, J., Scheel, M., Lanyon, L. J. & Barton, J. J. S. Functional organisation of visual pathways in a patient with no optic chiasm. *Neuropsychologia* **51**, 1260–1272 (2013).
7. Tuch, D. S. *et al*. High angular resolution diffusion imaging reveals intravoxel white matter fiber heterogeneity. *Magn. Reson. Med.* **48**, 577–582 (2002).
8. Frank, L. R. Characterization of anisotropy in high angular resolution diffusion-weighted MRI. *Magn. Reson. Med.* **47**, 1083–1099 (2002).
9. Caiafa, C. F. & Pestilli, F. Multidimensional encoding of brain connectomes. *Sci. Rep.* **7**, 11491 (2017).
10. Wu, X. *et al*. High-resolution whole-brain diffusion MRI at 7T using radiofrequency parallel transmission. *Magn. Reson. Med.* **80**, 1857–1870 (2018).
11. Avesani, P. *et al*. The open diffusion data derivatives, brain data upcycling via integrated publishing of derivatives and reproducible open cloud services. *Sci. Data* **6**, 69 (2019).
12. Guillery, R. W. Neural abnormalities of albinos. *Trends Neurosci.* **9**, 364–367 (1986).
13. Morland, A. B., Baseler, H. A., Hoffmann, M. B., Sharpe, L. T. & Wandell, B. A. Abnormal retinotopic representations in human visual cortex revealed by fMRI. *Acta Psychol. (Amst.)* **107**, 229–247 (2001).
14. Hagen, E. A. H. von dem, Houston, G. C., Hoffmann, M. B., Jeffery, G. & Morland, A. B. Retinal abnormalities in human albinism translate into a reduction of grey matter in the occipital cortex. *Eur. J. Neurosci.* **22**, 2475–2480 (2005).
15. Bridge, H. *et al*. Changes in brain morphology in albinism reflect reduced visual acuity. *Cortex* **56**, 64–72 (2014).
16. Ogawa, S. *et al*. White matter consequences of retinal receptor and ganglion cell damage. *Invest. Ophthalmol. Vis. Sci.* **55**, 6976–6986 (2014).
17. Allen, B., Spiegel, D. P., Thompson, B., Pestilli, F. & Rokers, B. Altered white matter in early visual pathways of humans with amblyopia. *Vision Res.* **114**, 48–55 (2015).
18. Rokem, A. *et al*. The visual white matter: The application of diffusion MRI and fiber tractography to vision science. *J. Vis.* **17**, 4 (2017).
19. Yoshimine, S. *et al*. Age-related macular degeneration affects the optic radiation white matter projecting to locations of retinal damage. *Brain Struct. Funct.* **223**, 3889–3900 (2018).
20. Tournier, J.-D., Calamante, F., Gadian, D. G. & Connelly, A. Direct estimation of the fiber orientation density function from diffusion-weighted MRI data using spherical deconvolution. *NeuroImage* **23**, 1176–1185 (2004).
21. Anderson, A. W. Measurement of fiber orientation distributions using high angular resolution diffusion imaging. *Magn. Reson. Med.* **54**, 1194–1206 (2005).
22. Peled, S., Friman, O., Jolesz, F. & Westin, C.-F. Geometrically Constrained Two-Tensor Model for Crossing Tracts in DWI. *Magn. Reson. Imaging* **24**, 1263–1270 (2006).
23. Staempfli, P. *et al*. Resolving fiber crossing using advanced fast marching tractography based on diffusion tensor imaging. *NeuroImage* **30**, 110–120 (2006).
24. Descoteaux, M., Angelino, E., Fitzgibbons, S. & Deriche, R. Regularized, fast, and robust analytical Q-ball imaging. *Magn. Reson. Med.* **58**, 497–510 (2007).
25. Descoteaux, M., Deriche, R., Knosche, T. R. & Anwander, A. Deterministic and Probabilistic Tractography Based on Complex Fibre Orientation Distributions. *IEEE Trans. Med. Imaging* **28**, 269–286 (2009).
26. Wedeen, V. J. *et al*. Diffusion spectrum magnetic resonance imaging (DSI) tractography of crossing fibers. *NeuroImage* **41**, 1267–1277 (2008).
27. Dell'Acqua, F. *et al*. A modified damped Richardson–Lucy algorithm to reduce isotropic background effects in spherical deconvolution. *NeuroImage* **49**, 1446–1458 (2010).
28. Tournier, J.-D., Calamante, F. & Connelly, A. MRtrix: Diffusion tractography in crossing fiber regions. *Int. J. Imaging Syst. Technol.* **22**, 53–66 (2012).
29. Cheng, J., Deriche, R., Jiang, T., Shen, D. & Yap, P.-T. Non-Negative Spherical Deconvolution (NNSD) for estimation of fiber Orientation Distribution Function in single-/multi-shell diffusion MRI. *NeuroImage* **101**, 750–764 (2014).
30. Thomas, C. *et al*. Anatomical accuracy of brain connections derived from diffusion MRI tractography is inherently limited. *Proc. Natl. Acad. Sci.* **111**, 16574–16579 (2014).
31. Reveley, C. *et al*. Superficial white matter fiber systems impede detection of long-range cortical connections in diffusion MR tractography. *Proc. Natl. Acad. Sci.* **112**, E2820–E2828 (2015).
32. Rokem, A. *et al*. Evaluating the Accuracy of Diffusion MRI Models in White Matter. *PLOS ONE* **10**, e0123272 (2015).
33. Shi, Y. & Toga, A. W. Connectome imaging for mapping human brain pathways. *Mol. Psychiatry* **22**, 1230–1240 (2017).
34. Aydogan, D. B. *et al*. When tractography meets tracer injections: a systematic study of trends and variation sources of diffusion-based connectivity. *Brain Struct. Funct.* **223**, 2841–2858 (2018).
35. Schilling, K. G. *et al*. Limits to anatomical accuracy of diffusion tractography using modern approaches. *NeuroImage* **185**, 1–11 (2019).
36. Oouchi, H. *et al*. Diffusion Anisotropy Measurement of Brain White Matter Is Affected by Voxel Size: Underestimation Occurs in Areas with Crossing Fibers. *Am. J. Neuroradiol.* **28**, 1102–1106 (2007).
37. Jones, D. K., Knösche, T. R. & Turner, R. White matter integrity, fiber count, and other fallacies: The do's and don'ts of diffusion MRI. *NeuroImage* **73**, 239–254 (2013).
38. Jeurissen, B., Leemans, A., Tournier, J., Jones, D. K. & Sijbers, J. Investigating the prevalence of complex fiber configurations in white matter tissue with diffusion magnetic resonance imaging. *Hum. Brain Mapp.* **34**, 2747–2766 (2012).
39. Wandell, B. A. Clarifying Human White Matter. *Annu. Rev. Neurosci.* **39**, 103–128 (2016).
40. Pestilli, F. Human white matter and knowledge representation. *PLoS Biol.* **16** (2018).
41. Fillard, P. *et al*. Quantitative evaluation of 10 tractography algorithms on a realistic diffusion MR phantom. *NeuroImage* **56**, 220–234 (2011).
42. Maier-Hein, K. H. *et al*. The challenge of mapping the human connectome based on diffusion tractography. *Nat. Commun.* **8**, 1349 (2017).
43. Perrin, M. *et al*. Validation of q-ball imaging with a diffusion fibre-crossing phantom on a clinical scanner. *Philos. Trans. R. Soc. B Biol. Sci.* **360**, 881–891 (2005).
44. Roebroeck, A. *et al*. High-resolution diffusion tensor imaging and tractography of the human optic chiasm at 9.4 T. *NeuroImage* **39**, 157–168 (2008).
45. Spees, W. M. *et al*. MRI-based assessment of function and dysfunction in myelinated axons. *Proc. Natl. Acad. Sci.* **115**, E10225–E10234 (2018).
46. Daducci, A., Palù, A. D., Lemkaddem, A. & Thiran, J. A convex optimization framework for global tractography. in *2013 IEEE 10th International Symposium on Biomedical Imaging* 524–527, https://doi.org/10.1109/ISBI.2013.6556527 (2013).
47. Daducci, A., Dal Palù, A., Lemkaddem, A. & Thiran, J.-P. COMMIT: Convex optimization modeling for microstructure informed tractography. *IEEE Trans. Med. Imaging* **34**, 246–257 (2015).
48. Smith, R. E., Tournier, J.-D., Calamante, F. & Connelly, A. SIFT: Spherical-deconvolution informed filtering of tractograms. *NeuroImage* **67**, 298–312 (2013).
49. Pestilli, F. *et al*. LiFE: Linear Fascicle Evaluation a new technology to study visual connectomes. *J. Vis.* **14**, 1122–1122 (2014).

50. Puzniak, R. J. *et al*. Quantifying nerve decussation abnormalities in the optic chiasm. *NeuroImage Clin.* **24**, 102055 (2019).
51. Ahmadi, K. *et al*. Population receptive field and connectivity properties of the early visual cortex in human albinism. *NeuroImage* **202**, 116105 (2019).
52. Bach, M. The Freiburg Visual Acuity test–automatic measurement of visual acuity. *Optom. Vis. Sci. Off. Publ. Am. Acad. Optom.* **73**, 49–53 (1996).
53. Donzis, P. B., Rappazzo, J. A., Bürde, R. M. & Gordon, M. Effect of Binocular Variations of Snellen's Visual Acuity on Titmus Stereoacuity. *Arch. Ophthalmol.* **101**, 930–932 (1983).
54. Lang, J. I. & Lang, T. J. Eye Screening with the Lang Stereotest. *Am. Orthopt. J.* **38**, 48–50 (1988).
55. Schmitz, B. *et al*. Configuration of the Optic Chiasm in Humans with Albinism as Revealed by Magnetic Resonance Imaging. *Invest. Ophthalmol. Vis. Sci.* **44**, 16–21 (2003).
56. Hoffmann, M. B. *et al*. Visual Pathways in Humans With Ephrin-B1 Deficiency Associated With the Cranio-Fronto-Nasal Syndrome. *Invest. Ophthalmol. Vis. Sci.* **56**, 7427–7437 (2015).
57. Mugler, J. P. & Brookeman, J. R. Three-dimensional magnetization-prepared rapid gradient-echo imaging (3D MP RAGE). *Magn. Reson. Med.* **15**, 152–157 (1990).
58. Sotiropoulos, S. N. *et al*. Advances in diffusion MRI acquisition and processing in the Human Connectome Project. *NeuroImage* **80**, 125–143 (2013).
59. Caruyer, E., Lenglet, C., Sapiro, G. & Deriche, R. Design of Multishell Sampling Schemes with Uniform Coverage in Diffusion MRI. *Magn. Reson. Med.* **69**, 1534–1540 (2013).
60. Andersson, J. L. R., Skare, S. & Ashburner, J. How to correct susceptibility distortions in spin-echo echo-planar images: application to diffusion tensor imaging. *NeuroImage* **20**, 870–888 (2003).
61. Dumoulin, S. O. & Wandell, B. A. Population receptive field estimates in human visual cortex. *NeuroImage* **39**, 647–660 (2008).
62. Brainard, D. H. The Psychophysics Toolbox. *Spat. Vis.* **10**, 433–436 (1997).
63. Pelli, D. G. The VideoToolbox software for visual psychophysics: transforming numbers into movies. *Spat. Vis.* **10**, 437–442 (1997).
64. Tournier, J.-D. *et al*. MRtrix3: A fast, flexible and open software framework for medical image processing and visualisation. *NeuroImage* **202**, 116137 (2019).
65. Smith, S. M. *et al*. Advances in functional and structural MR image analysis and implementation as FSL. *NeuroImage* **23**, S208–S219 (2004).
66. Woolrich, M. W. *et al*. Bayesian analysis of neuroimaging data in FSL. *NeuroImage* **45**, S173–S186 (2009).
67. Jenkinson, M., Beckmann, C. F., Behrens, T. E. J., Woolrich, M. W. & Smith, S. M. FSL. *NeuroImage* **62**, 782–790 (2012).
68. Avants, B. B. *et al*. The optimal template effect in hippocampus studies of diseased populations. *NeuroImage* **49**, 2457–2466 (2010).
69. Avants, B. B. *et al*. A reproducible evaluation of ANTs similarity metric performance in brain image registration. *NeuroImage* **54**, 2033–2044 (2011).
70. Fischl, B. FreeSurfer. *NeuroImage* **62**, 774–781 (2012).
71. Rorden, C. & Brett, M. Stereotaxic display of brain lesions. *Behav. Neurol.* **12**, 191–200 (2000).
72. McAuliffe, M. J. *et al*. Medical Image Processing, Analysis and Visualization in clinical research. in *Proceedings 14th IEEE Symposium on Computer-Based Medical Systems. CBMS 2001* 381–386, https://doi.org/10.1109/CBMS.2001.941749 (2001).
73. Cox, R. W. AFNI: software for analysis and visualization of functional magnetic resonance neuroimages. *Comput. Biomed. Res. Int. J.* **29**, 162–173 (1996).
74. Esteban, O. *et al*. fMRIPrep: a robust preprocessing pipeline for functional MRI. *Nat. Methods* **16**, 111–116 (2019).
75. Klein, A. *et al*. Mindboggling morphometry of human brains. *PLOS Comput. Biol.* **13**, e1005350 (2017).
76. Gorgolewski, K. *et al*. Nipype: A Flexible, Lightweight and Extensible Neuroimaging Data Processing Framework in Python. *Front. Neuroinformatics* **5** (2011).
77. Abraham, A. *et al*. Machine learning for neuroimaging with scikit-learn. *Front. Neuroinformatics* **8** (2014).
78. Bischoff-Grethe, A. *et al*. A technique for the deidentification of structural brain MR images. *Hum. Brain Mapp.* **28**, 892–903 (2007).
79. Smith, R. E., Tournier, J.-D., Calamante, F. & Connelly, A. Anatomically-constrained tractography: Improved diffusion MRI streamlines tractography through effective use of anatomical information. *NeuroImage* **62**, 1924–1938 (2012).
80. Zhang, Y., Brady, M. & Smith, S. Segmentation of brain MR images through a hidden Markov random field model and the expectation-maximization algorithm. *IEEE Trans. Med. Imaging* **20**, 45–57 (2001).
81. Smith, S. M. Fast robust automated brain extraction. *Hum. Brain Mapp.* **17**, 143–155 (2002).
82. Patenaude, B., Smith, S. M., Kennedy, D. N. & Jenkinson, M. A Bayesian model of shape and appearance for subcortical brain segmentation. *NeuroImage* **56**, 907–922 (2011).
83. Glasser, M. F. *et al*. The minimal preprocessing pipelines for the Human Connectome Project. *NeuroImage* **80**, 105–124 (2013).
84. Veraart, J. *et al*. Denoising of diffusion MRI using random matrix theory. *NeuroImage* **142**, 394–406 (2016).
85. Veraart, J., Fieremans, E. & Novikov, D. S. Diffusion MRI noise mapping using random matrix theory. *Magn. Reson. Med.* **76**, 1582–1593 (2016).
86. Kellner, E., Dhital, B., Kiselev, V. G. & Reisert, M. Gibbs-ringing artifact removal based on local subvoxel-shifts. *Magn. Reson. Med.* **76**, 1574–1581 (2016).
87. Andersson, J. L. R. & Sotiropoulos, S. N. An integrated approach to correction for off-resonance effects and subject movement in diffusion MR imaging. *NeuroImage* **125**, 1063–1078 (2016).
88. Tustison, N. J. *et al*. N4ITK: Improved N3 Bias Correction. *IEEE Trans. Med. Imaging* **29**, 1310–1320 (2010).
89. Jenkinson, M. & Smith, S. A global optimisation method for robust affine registration of brain images. *Med. Image Anal.* **5**, 143–156 (2001).
90. Jenkinson, M., Bannister, P., Brady, M. & Smith, S. Improved Optimization for the Robust and Accurate Linear Registration and Motion Correction of Brain Images. *NeuroImage* **17**, 825–841 (2002).
91. Greve, D. N. & Fischl, B. Accurate and robust brain image alignment using boundary-based registration. *NeuroImage* **48**, 63–72 (2009).
92. Levitas, D., Hunt, D., Faskowitz, J. & Hayashi, S. fMRIPrep - Surface Output. *brainlife.io* https://doi.org/10.25663/brainlife.app.267 (2019).
93. Levitas, D., Hunt, D., Faskowitz, J. & Hayashi, S. fMRIPrep - Volume Output. *brainlife.io* https://doi.org/10.25663/brainlife.app.160 (2019).
94. Behzadi, Y., Restom, K., Liau, J. & Liu, T. T. A component based noise correction method (CompCor) for BOLD and perfusion based fMRI. *NeuroImage* **37**, 90–101 (2007).
95. Basser, P. J., Pajevic, S., Pierpaoli, C., Duda, J. & Aldroubi, A. *In vivo* fiber tractography using DT-MRI data. *Magn. Reson. Med.* **44**, 625–632 (2000).
96. Tuch, D. S., Belliveau, J. W. & Wedeen, V. J. A Path Integral Approach to White Matter Tractography. in *Proceedings of the 8th Annual Meeting of ISMRM* **791** (2000).
97. Lazar, M. *et al*. White matter tractography using diffusion tensor deflection. *Hum. Brain Mapp.* **18**, 306–321 (2003).

98. Behrens, T. E. J., Berg, H. J., Jbabdi, S., Rushworth, M. F. S. & Woolrich, M. W. Probabilistic diffusion tractography with multiple fibre orientations: What can we gain? *NeuroImage* **34**, 144–155 (2007).
99. Sherbondy, A. J., Dougherty, R. F., Napel, S. & Wandell, B. A. Identifying the human optic radiation using diffusion imaging and fiber tractography. *J. Vis.* **8**, 12.1–1211 (2008).
100. Takemura, H., Caiafa, C. F., Wandell, B. A. & Pestilli, F. Ensemble Tractography. *PLOS Comput. Biol.* **12**, e1004692 (2016).
101. Bastiani, M., Shah, N. J., Goebel, R. & Roebroeck, A. Human cortical connectome reconstruction from diffusion weighted MRI: The effect of tractography algorithm. *NeuroImage* **62**, 1732–1749 (2012).
102. Côté, M.-A. *et al*. Tractometer: Towards validation of tractography pipelines. *Med. Image Anal.* **17**, 844–857 (2013).
103. Pestilli, F., Yeatman, J. D., Rokem, A., Kay, K. N. & Wandell, B. A. Evaluation and statistical inference for living connectomes. *Nat. Methods* **11**, 1058–1063 (2014).
104. Neher, P. F., Descoteaux, M., Houde, J.-C., Stieltjes, B. & Maier-Hein, K. H. Strengths and weaknesses of state of the art fiber tractography pipelines – A comprehensive *in-vivo* and phantom evaluation study using Tractometer. *Med. Image Anal.* **26**, 287–305 (2015).
105. Basser, P. J. & Pierpaoli, C. Microstructural and physiological features of tissues elucidated by quantitative-diffusion-tensor MRI. *J. Magn. Reson. B* **111**, 209–219 (1996).
106. Tournier, J.-D., Calamante, F. & Connelly, A. Robust determination of the fibre orientation distribution in diffusion MRI: Non-negativity constrained super-resolved spherical deconvolution. *NeuroImage* **35**, 1459–1472 (2007).
107. Tournier, J.-D., Calamante, F. & Connelly, A. Determination of the appropriate b value and number of gradient directions for high-angular-resolution diffusion-weighted imaging. *NMR Biomed.* **26**, 1775–1786 (2013).
108. Jeurissen, B., Tournier, J.-D., Dhollander, T., Connelly, A. & Sijbers, J. Multi-tissue constrained spherical deconvolution for improved analysis of multi-shell diffusion MRI data. *NeuroImage* **103**, 411–426 (2014).
109. Hayashi, S., Kitchell, L., McPherson, B. & Caron, B. Ensemble Tracking (dwi). *brainlife.io* https://doi.org/10.25663/bl.app.103 (2018).
110. Caron, B., Pestilli, F., Berto, G. & Hayashi, S. LiFE (dwi). *brainlife.io* https://doi.org/10.25663/bl.app.104 (2018).
111. Puzniak, R., McPherson, B. & Pestilli, F. The human brain albinism and achiasma dataset: A biological testbed for the crossing-fibers problem with ground truth. *brainlife.io* https://doi.org/10.25663/brainlife.pub.9 (2019).
112. Gorgolewski, K. J. *et al*. The brain imaging data structure, a format for organizing and describing outputs of neuroimaging experiments. *Sci. Data* **3**, 160044 (2016).
113. Puzniak, R. & Pestilli, F. CHIASM, the human brain albinism and achiasma MRI dataset. *Open Science Framework* https://doi.org/10.17605/osf.io/XZ29Q (2021).
114. Descoteaux, M., Angelino, E., Fitzgibbons, S. & Deriche, R. Apparent diffusion coefficients from high angular resolution diffusion imaging: estimation and applications. *Magn. Reson. Med.* **56**, 395–410 (2006).
115. Descoteaux, M., Deriche, R., Le Bihan, D., Mangin, J.-F. & Poupon, C. Multiple q-shell diffusion propagator imaging. *Med. Image Anal.* **15**, 603–621 (2011).
116. Hunt, D. Compute SNR on Corpus Callosum. *brainlife.io* https://doi.org/10.25663/brainlife.app.120 (2018).
117. Van Essen, D. C. *et al*. The WU-Minn Human Connectome Project: an overview. *NeuroImage* **80**, 62–79 (2013).
118. Benson, N. C. *et al*. The Retinotopic Organization of Striate Cortex Is Well Predicted by Surface Topology. *Curr. Biol.* **22**, 2081–2085 (2012).
119. Benson, N. C., Butt, O. H., Brainard, D. H. & Aguirre, G. K. Correction of Distortion in Flattened Representations of the Cortical Surface Allows Prediction of V1-V3 Functional Organization from Anatomy. *PLOS Comput. Biol.* **10**, e1003538 (2014).
120. Benson, N. C. & Winawer, J. Bayesian analysis of retinotopic maps. *eLife* **7**, e40224 (2018).
121. Sengupta, A. *et al*. A studyforrest extension, retinotopic mapping and localization of higher visual areas. *Sci. Data* **3**, 160093 (2016).
122. Triantafyllou, C. *et al*. Comparison of physiological noise at 1.5 T, 3 T and 7 T and optimization of fMRI acquisition parameters. *NeuroImage* **26**, 243–250 (2005).
123. Friston, K. J. *et al*. Event-Related fMRI: Characterizing Differential Responses. *NeuroImage* **7**, 30–40 (1998).
124. Hayashi, S. Freesurfer 7.1.1. *brainlife.io* https://doi.org/10.25663/brainlife.app.462 (2020).
125. McPherson, B. mrtrix3 preprocess. *brainlife.io* https://doi.org/10.25663/bl.app.68 (2018).

Acknowledgements

R.J.P., K.A., and M.B.H. were supported by the European Union's Horizon 2020 research and innovation program under the Marie Skłodowska-Curie grant agreement No. 641805 and by the German research foundation (DFG; HO2002/10-3). B.M. was partially supported by NIH 5T32MH103213-05 to William Hetrick. NSF IIS 1636893, NSF IIS 1912270, NIH NIBIB 1R01EB029272, NSF BCS 1734853 and a Microsoft Faculty Fellowship granted to F.P. We thank all participants in the project for their time and effort. We thank Soichi Hayashi for support with uploading the data on brainlife.io, and Denise Scheermann and Martin Kanowski for their contribution in the data acquisition.

Author contributions

J.K., K.A., R.J.P., A.H., M.B.H., A.G., A.B.M., and I.G. acquired the data. T.L. performed screening of the data. R.J.P., B.M., F.P. and M.B.H. processed the data. R.J.P., J.K., B.M., M.B.H., and F.P. wrote the manuscript.

Competing interests

The authors declare no competing interests.

Additional information

Supplementary information The online version contains supplementary material available at https://doi.org/10.1038/s41597-021-01080-w.

Correspondence and requests for materials should be addressed to F.P.

Reprints and permissions information is available at www.nature.com/reprints.

Publisher's note Springer Nature remains neutral with regard to jurisdictional claims in published maps and institutional affiliations.

Chapter 10

General Discussion

Despite the relevance of chiasmal malformations for clinical and scientific studies, their potential remains still untapped. One of the major causes of this situation are the challenges in imaging the chiasm, which is further enhanced by the scarcity of the data and general lack of awareness about congenital chiasmal disorders and their impact on individuals. The main objective of my work was to facilitate the recognition of the importance of albinism and achiasma by clinical and scientific communities, which is hoped to benefit both the patients (by development of diagnostic methods) and the general society (by improvement of understanding of brain functioning). Subchapter 10.1 (Summary of main contributions) provides detailed description of my contributions, which is summarized in the final subchapter 10.2 (Concluding remarks).

10.1 Summary of main contributions

My contributions to research on and understanding chiasmal malformations can be in principle divided in two categories. The first includes novel scientific findings, which were focused on the imaging methods enabling detection and quantification of chiasmal misrouting. Specifically, those include:

- development of dMRI pipeline aimed at quantification of nerve misrouting in the chiasm – subchapter 10.1.2 (dMRI-based quantification of abnormal chiasmal crossing),
- confirmation of asymmetrical projections from eyes to brain in a case study on chiasmal hypoplasia – subchapter 10.1.3 (Further applications of developed dMRI-based framework),
- application of DL methods for detection of malformations directly from anatomical MRI images – subchapter 10.1.4 (DL-based detection of chiasmal malformations).

The second category covers contribution of knowledge and data to the general scientific community, specifically:

- communication of knowledge on dMRI imaging and tractography of the visual system – subchapter 10.1.1 (Recommendations for tractography of the visual system),
- sharing of the highly uncommon MRI data on chiasmal malformations with the scientific community – subchapter 10.1.5 (Publication of MRI data on congenital chiasmal disorders).

10.1.1 Recommendations for tractography of the visual system

Although the incorporation of dMRI in the studies provides considerable advantages, the utility of this approach is partially limited by the complexity of the analysis. This, combined with limitations of imaging particular brain structures or systems may pose a considerable obstacle in establishing dMRI-based study. In acknowledgement of this issue, I have first-authored a review article (chapter 5) with recommendations for a dMRI-based tractography of the visual system for the purpose of epilepsy surgery (Nilsson et al., 2007; Chen et al., 2009; Winston et al., 2011; Schmitt et al., 2014; James et al., 2015) and research (McDonald et al., 2008; Diehl et al., 2010). Specifically, the review has listed the recommended modalities to be acquired during data acquisition (T1w and dMRI images, as well as proton density maps) and discussed approaches to data acquisition – either through scanning with carefully chosen sets of parameters (Jones et al., 2013; Soares et al., 2013; Tournier et al., 2013), or by accessing public datasets (Van Essen et al., 2013). Furthermore, it provided a comprehensive list of tools for dMRI analysis which covered both standard analysis software, such as MRtrix (Tournier et al., 2012; Tournier et al., 2019) or FSL (Smith et al., 2001; Jenkinson et al., 2012), as well as newly emerging online services for neuroimaging (Avesani et al., 2019). Furtherly, the review provided an insight into the most common distortions present in dMRI data and suggested correction methods and packages (Andersson et al., 2003; Andersson and Skare, 2012). These widely applicable recommendations were followed by a detailed discussion on tractography of the visual system. Specifically, this section covered delineation of structures of visual system (Fischl, 2012), modelling of dMRI signal with DT (Basser et al., 1994) and CSD models (Tournier et al., 2004; Tournier et al., 2007), discussion on tractography types [deterministic (Basser et al., 2000) and probabilistic (Jones, 2008)], algorithms [e.g. iFOD2 (Tournier et al., 2010)] and further approaches and parameters relevant for the outcome of tractography. Finally, the review presented a discussion on the methods for post-processing of tractography results, such as Linear Fascicle Evaluation [LiFE; (Pestilli et al., 2014; Caiafa and Pestilli, 2017)] or Convex Optimization Modeling for Microstructure Informed Tractography [COMMIT; (Daducci et al., 2015)].

The main objective of this review was to raise awareness about the benefits of the dMRI and tractography in the clinical and research routines, as well as to provide the readers with knowledge and sources enabling establishing their own dMRI analysis. Importantly, although the review was primarily focused on the epilepsy, the recommended approaches and good practices are well applicable to wide range of studies utilizing anatomical information about the brain. As such, the review is expected to facilitate a wide community of clinicians and researchers in incorporation of dMRI-based analysis and tractography in the ongoing and future research.

10.1.2 dMRI-based quantification of abnormal chiasmal crossing

Considering that congenital chiasmal disorders primarily affect the crossing of the nerves in the chiasm, with the subsequent reorganization of visual system being the secondary effect, the dMRI-based tractography would be expected to be particularly well suited for the quantification of changes in the chiasm. In order to investigate the efficiency of this approach and potential for diagnostics, I have explored the sensitivity of dMRI-based tractography to abnormal connectivity patterns, as observed in the chiasm of PWA. Specifically, I aimed to: (i) evaluate and test advanced dMRI methods on the chiasms with varied connectivity pattern, as observed in controls

and PWA, (ii) probe whether such biological models can be treated as robust biological models of crossing fibers and (iii) evaluate dMRI as a tool for clinical diagnostics of albinism.

In order to achieve these goals I acquired MRI data (T1w and dMRI) from a group of controls (n=8) and PWA (n=9). Furthermore, I designed a preprocessing pipeline that used a range of methods (MRtrix, FSL, FreeSurfer, ANTS and MATLAB's package MrDiffusion) in order to achieve the optimal distortion correction and co-registration of T1- and diffusion-weighted data. Importantly, preprocessing of the data also involved manual definition and correction of ROIs necessary for the successful tractography within the chiasm. Afterwards, I have modeled the dMRI data using a conventional DT model [in order to compare results with previous dMRI investigations of chiasmal connectivity (Roebroeck et al., 2008; Ather et al., 2018)] and advanced CSD model recognized for its sensitivity to populations of crossing fibers. In the next step, I have performed ROI-to-ROI tractography to reconstruct 4 distinct groups of fibers that form the chiasm. Notably, the tractography was repeated twice, separately for DT and CSD models, and adhered to Ensemble Tractography (Takemura et al., 2016); multiple repetitions of tractography with different conditions to avoid bias choice of parameters] and Anatomically-Constrained Tractography [(Smith et al., 2012); limiting the tractography to white matter only] approaches. Finally, I have tested the impact of tractography post-processing methods on the final results by filtering the obtained tractograms with several different methods. The results of the analysis were expressed by an ID parameter, which denoted the percentage of crossing fibers in the reconstructed 4 groups of streamlines.

The results of the analysis based on DT model revealed a significant difference between IDs calculated for albinism and control groups (mean $\pm$ SEM: 41$\pm$40% and 6$\pm$4%, respectively; p=0.014), as well as lower ROC AUC of 0.61. The CSD approach, expected to perform better, provided a more pronounced cross-group difference (mean ID of 41$\pm$15% for albinism and 19$\pm$6% for controls, p=0.0009) as well as higher ROC AUC of 0.75. Furtherly, in order to validate dMRI-based estimates of crossing, I have compared them to fMRI-based estimates of chiasmal misrouting calculated for the same patients in a separate study (Ahmadi et al., 2019b). Importantly, the results for the CSD model demonstrated a significant positive correlation with the fMRI-based estimates (R^2=0.83, p=0.012), while DT model showed a non-significant trend of positive correlation (R^2=0.05, p=0.052). Finally, the application of tractography post-processing methods revealed preservation of group-level differences in the IDs between controls and PWA, as well as improved separation of data points reaching a ROC AUC in the range of of 0.92-0.94 (though surprisingly they did not increase a correlation between dMRI and fMRI estimates).

The above results provide relevant insights for the general dMRI, as well as the goals of the study:

(i) The study demonstrated that careful choice of methods, models (specifically CSD) and application of post-processing improves the performance of dMRI-based analysis in the region of crossing fibers. As such, this bears important message for future dMRI studies of the brain.

(ii) The robustness of results observed for the various approaches employed in the study indicates that chiasmal malformations can be reliably used as a general biological model of crossing fibers with gradable degrees of crossing. Such a model is expected to highly benefit development and validation of future

tractography algorithms (which is still necessary, considering that even in the case of best configuration the calculated IDs were falling short of ground truth known from histological studies).

(iii) The achieved ROC AUC of greater than 0.90 indicates the potential of dMRI-based methods in the detection of chiasmal misrouting from anatomical images. This provides a foundation for a novel method for diagnostics of achiasma and albinism, which is not dependable on patient's visual functions or attention.

As such, the presented study increased the knowledge about advantages and limitations of dMRI and paved a way for a novel method of diagnostics of chiasmal malformations.

10.1.3 Further applications of developed dMRI-based framework

In addition to the detection of enhanced crossing, qualitative dMRI can be also used to assess the brain's connectivity. Consequently, dMRI can be used for cross-validation of functional studies, which was the primary motivation for its application in the below described study on chiasmal hypoplasia. Specifically, I used the previously established dMRI framework to assess the possible asymmetries in the contralateral projection from the eyes. This investigation that while the contribution of the right and left eye to ipsilateral (non-crossing) streamlines (42 and 58%, respectively) was within the range observed in controls (40–68% and 32–60%, respectively), the proportion of contralateral (crossed) streamlines was greater for right eye than for the left (73 and 27%, respectively; with the values for controls in range of 39–68% and 32–61%, respectively).

The results of dMRI analysis confirmed the existence of residual connectivity in the chiasm and furthermore prove the asymmetry of the contralateral projections. These findings provided an important cross-validation for the findings of the conducted fMRI analysis, which ultimately demonstrated, previously unseen, presence of 3 superimposed hemifield representations in the visual cortex. While this finding itself bears important consequences for our understanding of V1's plasticity, the main importance of my contribution was the demonstration of the robustness, capabilities and applications of the dMRI-based tractography framework I have established.

10.1.4 DL-based detection of chiasmal malformations

Although the dMRI-based diagnostics of chiasmal misrouting demonstrated promising results, the applicability of such as approach in clinical environment is severely limited by the high cost of required dMRI data acquisition. This observation motivated me to research the possibilities of detection of chiasmal malformations from clinically common T1w images with the DL methods. To investigate this approach I have performed an experiment designed to reveal whether CNN models are sufficiently sensitive to detect differences between normal and malformed chiasms (as captured on T1w images) and whether those differences can be leveraged in the future diagnostics. Specifically, I have trained a CNN for segmentation of the chiasm from the T1-weighted images of control population. This training has been performed in a supervised manner on T1-weighted images of controls from HCP dataset (Van Essen et al., 2013), which was paired with the corresponding set of automatically generated, binary optic chiasm mask The trained network was subsequently deployed on a test subset of controls from HCP dataset, and a group of

controls and PWA from the CHIASM dataset I've published (chapter 9). The accuracy of the CNN was assessed by comparison of the predicted optic chiasm mask to the manually defined ground truth masks with the DSC (denoting the range of overlap, with 0 being lack of overlap and 100% being complete overlap). Importantly, while the results indicated a similar performance of the CNN in case of controls from HCP and CHIASM datasets (mean $\pm$ SEM of DSC equal to 79$\pm$2% and 75$\pm$3%, respectively, FWE-corrected p-value of 1.0), the accuracy of the masks obtained for PWA was significantly lower (44$\pm$8%, with comparisons against HCP and CHIASM controls yielding FWE-corrected p-values of 0.004 and 0.04, respectively). The separation of data points was further evaluated with the ROC AUC which returned an accuracy of 0.89 (PWA vs controls from CHIASM dataset), and 0.84 (PWA vs controls from HCP dataset).

In summary, the performed analysis revealed a fundamental difference in the way the CNN process normal and abnormal optic chiasm represented on T1-weighted images. This provides a critical proof-of-concept for DL-based detection of chiasmal malformations, which is an inexpensive method that uses data standardly used in clinics. As such, such a method can be applied in addition to already existing investigations using T1w images, as well as can be retrospectively run on data acquired in the past. At the same time, the reported findings emphasize the need of inclusion of data from rare patient groups in development of data-driven methods in healthcare, to ensure robust performance of developed tools for the general population.

10.1.5 Publication of MRI data on congenital chiasmal disorders

One of the main hurdles in a scientific and clinical research on chiasmal malformations is limited access to data, which is a consequence of is their rarity. This problem is even more expressed in the light of expansion of data-driven DL models (Lundervold and Lundervold, 2019), which performance strictly depends on training data. In order to facilitate further scientific and clinical research on congenital chiasmal disorders I have released the first public MRI dataset on congenital chiasmal disorders. Specifically, the published dataset included T1w and dMRI data from a controls (n=8), PWA (n=9), chiasm hypoplasia (n=1) and achiasma (n=1). Additionally, the shared data included fMRI data from a subset of 4 controls and 6 participants with albinism which contained recordings of the cortical response to the monocular stimulation of both eyes, as well as white matter masks that were manually corrected in the region of optic chiasm and manually drawn ROIs used for the purpose of tractography in the optic chiasm. The published data has been anonymized, subjected to through quality assessment and uploaded on the neuroscientific cloud computing platform brainlife.io (Avesani et al., 2019), where it is available together with a wide range of service that can be used for online preprocessing and further analysis.

This contribution is expected to increase general recognition of the congenital chiasmal disorders, as well as to facilitate a wide range of studies benefiting from this high quality multi-modal MRI data of the very rare participants. In particular, this dataset is expected to be used by the vision scientist, scientists researching the neuroplasticity, developers of the tools and methods for the tractography, as well as clinicians and researchers researching diagnostics of chiasmal abnormalities, as well as general DL-based tools in healthcare.

10.2 Concluding remarks

The presented projects represent the frontiers of research on structural imaging of the chiasmal malformations and provided valuable information about both their nature, as well as capabilities of imaging methods applied to this problem. But even more importantly, those contributions pave the way for future developments in this field, as well as provide means to facilitate this process. As such, I hope that:

- The published work will help in increasing the visibility of congenital chiasmal malformations in the scientific and general community,
- The congenital chiasmal malformations will become more commonly recognized as a unique window granting insights into brain plasticity and in future will help unravel the big mystery of neuroplasticity, learning and degeneration,
- The published data will facilitate further clinical and research studies focused on this subject, in particular the data-driven DL models, thus enabling them to support rare patients' group which may be otherwise omitted.

But foremost, I hope that my work will make the life of people with achiasma and albinism better.

List of Abbreviations

aMRI	**a**natomical **M**agnetic **R**esonance **I**maging
ANN	**A**rtificial **N**eural **N**etwork
AUC	**A**rea **U**nder **C**urve
CNN	**C**onvolutional **N**eural **N**etwork
COMMIT	**C**onvex **O**ptimization **M**odeling for **M**icrostructure **I**nformed **T**ractoraphy
CSD	**C**onstrained **S**pherical **D**econvolution
CT	**C**omputed **T**omography
dMRI	**d**iffusion **M**agnetic **R**esonance **I**maging
DSC	**D**ice **S**imilarity **C**oefficient
DT	**D**iffusion **T**ensor
FHONDA	**F**ovea **H**ypoplasia, **O**ptic **N**erve **D**ecussation defect **A**nterior segment syndrome
FWE	**F**amily-**W**ise **E**rror
fMRI	**f**unctional **M**agnetic **R**esonance **I**maging
HCP	**H**uman **C**onnectome **P**roject
LGN	**L**ateral **G**eniculate **N**ucleus
LiFE	**L**inear **F**ascicle **E**valuation
MRI	**M**agnetic **R**esonance **I**maging
OA	**O**cular **A**lbinism
OCA	**O**culo**c**utaneous **A**lbinism
PWA	**P**eople **W**ith **A**lbinism
RGC	**R**etinal **G**anglion **C**ells
ROC	**R**eceiver **O**perator **C**haracteristics
ROI	**R**egion **O**f **I**nterest
SIFT	**S**pherical-deconvolution **I**nformed **F**iltering of **T**ractograms
T1w	**T**1-**w**eighted
V1	Primary **V**isual Cortex
VEP	**V**isual **E**voked **P**otentials

Physical Constants

gyromagnetic ratio of proton $\gamma_{proton} = 267.522\,187\,44(11) \times 10^6\,\mathrm{rad\,s^{-1}\,T^{-1}}$

List of Symbols

$\mathbf{B}$	magnetic flux density	T	$(\mathrm{kg\,s^{-2}\,A^{-1}})$
$\mathbf{M}$	magnetization		$(\mathrm{A\,m^{-1}})$
f	frequency	Hz	$(\mathrm{s^{-1}})$
γ	gyromagnetic ratio		$(\mathrm{rad\,s^{-1}\,T^{-1}})$

Bibliography

Abadi, R. and Pascal, E. (Jan. 1989). "The recognition and management of albinism". In: *Ophthalmic & Physiological Optics: The Journal of the British College of Ophthalmic Opticians (Optometrists)* 9.1, pp. 3–15. DOI: 10.1111/j.1475-1313.1989.tb00797.x.

Adams, D. R., Menezes, S., Jauregui, R., Valivullah, Z. M., Power, B., Abraham, M., Jeffrey, B. G., Garced, A., Alur, R. P., Cunningham, D., Wiggs, E., Merideth, M. A., Chiang, P.-W., Bernstein, S., Ito, S., Wakamatsu, K., Jack, R. M., Introne, W. J., Gahl, W. A., and Brooks, B. P. (Mar. 2019). "One-year pilot study on the effects of nitisinone on melanin in patients with OCA-1B". In: *JCI Insight* 4.2. DOI: 10.1172/jci.insight.124387.

Ahmadi, K., Fracasso, A., Dijk, J. A. van, Kruijt, C., Genderen, M. van, Dumoulin, S. O., and Hoffmann, M. B. (Apr. 2019a). "Altered organization of the visual cortex in FHONDA syndrome". In: *NeuroImage*. Mapping diseased brains 190, pp. 224–231. DOI: 10.1016/j.neuroimage.2018.02.053.

Ahmadi, K., Fracasso, A., Puzniak, R. J., Gouws, A. D., Yakupov, R., Speck, O., Kaufmann, J., Pestilli, F., Dumoulin, S. O., Morland, A. B., and Hoffmann, M. B. (July 2020). "Triple visual hemifield maps in a case of optic chiasm hypoplasia". In: *NeuroImage* 215, p. 116822. DOI: 10.1016/j.neuroimage.2020.116822.

Ahmadi, K., Herbik, A., Wagner, M., Kanowski, M., Thieme, H., and Hoffmann, M. B. (Nov. 2019b). "Population receptive field and connectivity properties of the early visual cortex in human albinism". In: *NeuroImage* 202, p. 116105. DOI: 10.1016/j.neuroimage.2019.116105.

Al-Araimi, M., Pal, B., Poulter, J. A., Genderen, M. M. van, Carr, I., Cudrnak, T., Brown, L., Sheridan, E., Mohamed, M. D., Bradbury, J., Ali, M., Inglehearn, C. F., and Toomes, C. (Nov. 2013). "A new recessively inherited disorder composed of foveal hypoplasia, optic nerve decussation defects and anterior segment dysgenesis maps to chromosome 16q23.3-24.1". In: *Molecular Vision* 19, pp. 2165–2172.

Andersson, J. L. R. and Skare, S. (Sept. 2012). "Image Distortion and Its Correction in Diffusion MRI". In: *Diffusion MRITheory, Methods, and Applications*. Oxford, UK: Oxford University Press. DOI: 10.1093/med/9780195369779.003.0017.

Andersson, J. L. R., Skare, S., and Ashburner, J. (Oct. 2003). "How to correct susceptibility distortions in spin-echo echo-planar images: application to diffusion tensor imaging". In: *NeuroImage* 20.2, pp. 870–888. DOI: 10.1016/S1053-8119(03)00336-7.

Apkarian, P., Bour, L., and Barth, P. G. (Mar. 1994). "A unique achiasmatic anomaly detected in non-albinos with misrouted retinal-fugal projections". In: *The European Journal of Neuroscience* 6.3, pp. 501–507. DOI: 10.1111/j.1460-9568.1994.tb00293.x.

Apkarian, P. and Bour, L. J. (Sept. 2001). "See-saw nystagmus and congenital nystagmus identified in the non-decussating retinal-fugal fiber syndrome". In: *Strabismus* 9.3, pp. 143–163. DOI: 10.1076/stra.9.3.143.6761.

Apkarian, P., Bour, L. J., Barth, P. G., Wenniger-Prick, L., and Verbeeten, B. (Oct. 1995). "Non-decussating retinal-fugal fibre syndrome. An inborn achiasmatic

malformation associated with visuotopic misrouting, visual evoked potential ipsilateral asymmetry and nystagmus". In: *Brain: A Journal of Neurology* 118 (Pt 5), pp. 1195–1216. DOI: 10.1093/brain/118.5.1195.

Arveiler, B., Michaud, V., and Lasseaux, E. (July 2020). "Albinism: An Underdiagnosed Condition". In: *Journal of Investigative Dermatology* 140.7, pp. 1449–1451. DOI: 10.1016/j.jid.2019.12.010.

Assaf, Y. and Basser, P. J. (Aug. 2005). "Composite hindered and restricted model of diffusion (CHARMED) MR imaging of the human brain". In: *NeuroImage* 27.1, pp. 48–58. DOI: 10.1016/j.neuroimage.2005.03.042.

Ather, S., Proudlock, F. A., Welton, T., Morgan, P. S., Sheth, V., Gottlob, I., and Dineen, R. A. (Dec. 2018). "Aberrant visual pathway development in albinism: From retina to cortex". In: *Human Brain Mapping* 40.3, pp. 777–788. DOI: 10.1002/hbm.24411.

Atkinson, J. (Mar. 1992). "Early visual development: Differential functioning of parvocellular and magnocellular pathways". In: *Eye* 6.2, pp. 129–135. DOI: 10.1038/eye.1992.28.

Avesani, P., McPherson, B., Hayashi, S., Caiafa, C. F., Henschel, R., Garyfallidis, E., Kitchell, L., Bullock, D., Patterson, A., Olivetti, E., Sporns, O., Saykin, A. J., Wang, L., Dinov, I., Hancock, D., Caron, B., Qian, Y., and Pestilli, F. (May 2019). "The open diffusion data derivatives, brain data upcycling via integrated publishing of derivatives and reproducible open cloud services". In: *Scientific Data* 6.1, p. 69. DOI: 10.1038/s41597-019-0073-y.

Baker, G. E. and Reese, B. E. (Apr. 1993). "Chiasmatic course of temporal retinal axons in the developing ferret". In: *The Journal of Comparative Neurology* 330.1, pp. 95–104. DOI: 10.1002/cne.903300108.

Bammer, R. (Mar. 2003). "Basic principles of diffusion-weighted imaging". In: *European Journal of Radiology* 45.3, pp. 169–184. DOI: 10.1016/S0720-048X(02)00303-0.

Bao, P., Purington, C. J., and Tjan, B. S. (2015). "Using an achiasmic human visual system to quantify the relationship between the fMRI BOLD signal and neural response". In: *eLife* 4, e09600. DOI: 10.7554/eLife.09600.

Basser, P. J., Mattiello, J., and Lebihan, D. (Mar. 1994). "Estimation of the Effective Self-Diffusion Tensor from the NMR Spin Echo". In: *Journal of Magnetic Resonance, Series B* 103.3, pp. 247–254. DOI: 10.1006/jmrb.1994.1037.

Basser, P. J., Pajevic, S., Pierpaoli, C., Duda, J., and Aldroubi, A. (Oct. 2000). "In vivo fiber tractography using DT-MRI data". In: *Magnetic Resonance in Medicine* 44.4, pp. 625–632. DOI: 10.1002/1522-2594(200010)44:4<625::aid-mrm17>3.0.co;2-o.

Basser, P. J. and Pierpaoli, C. (June 1996). "Microstructural and physiological features of tissues elucidated by quantitative-diffusion-tensor MRI". In: *Journal of Magnetic Resonance. Series B* 111.3, pp. 209–219. DOI: 10.1006/jmrb.1996.0086.

Bhansali, P., Rayport, I., Rebsam, A., and Mason, C. (May 2014). "Delayed neurogenesis leads to altered specification of ventrotemporal retinal ganglion cells in albino mice". In: *Neural Development* 9, p. 11. DOI: 10.1186/1749-8104-9-11.

Bischoff-Grethe, A., Ozyurt, I. B., Busa, E., Quinn, B. T., Fennema-Notestine, C., Clark, C. P., Morris, S., Bondi, M. W., Jernigan, T. L., Dale, A. M., Brown, G. G., and Fischl, B. (Feb. 2007). "A technique for the deidentification of structural brain MR images". In: *Human Brain Mapping* 28.9, pp. 892–903. DOI: 10.1002/hbm.20312.

Bloch, F. (Oct. 1946). "Nuclear Induction". In: *Physical Review* 70.7-8, pp. 460–474. DOI: 10.1103/PhysRev.70.460.

Boltzmann, L. (1868). *Studien über das Gleichgewicht der lebendigen Kraft zwischen bewegten materiellen Punkten*. Wien: K.k. Hof- und Staatsdruckerei.

Brett, M., Johnsrude, I. S., and Owen, A. M. (Mar. 2002). "The problem of functional localization in the human brain". In: *Nature Reviews Neuroscience* 3.3, pp. 243–249. DOI: 10.1038/nrn756.

Bridge, H., Hagen, E. A. H. von dem, Davies, G., Chambers, C., Gouws, A., Hoffmann, M., and Morland, A. B. (July 2014). "Changes in brain morphology in albinism reflect reduced visual acuity". In: *Cortex*. The clinical neuroanatomy of the occipital lobes 56, pp. 64–72. DOI: 10.1016/j.cortex.2012.08.010.

Brodsky, M. C., Glasier, C. M., and Creel, D. J. (Dec. 1993). "Magnetic resonance imaging of the visual pathways in human albinos". In: *Journal of Pediatric Ophthalmology and Strabismus* 30.6, pp. 382–385.

Brown, T. B., Mann, B., Ryder, N., Subbiah, M., Kaplan, J., Dhariwal, P., Neelakantan, A., Shyam, P., Sastry, G., Askell, A., Agarwal, S., Herbert-Voss, A., Krueger, G., Henighan, T., Child, R., Ramesh, A., Ziegler, D. M., Wu, J., Winter, C., Hesse, C., Chen, M., Sigler, E., Litwin, M., Gray, S., Chess, B., Clark, J., Berner, C., McCandlish, S., Radford, A., Sutskever, I., and Amodei, D. (July 2020). "Language Models are Few-Shot Learners". In: *arXiv:2005.14165 [cs]*.

Caiafa, C. F. and Pestilli, F. (Sept. 2017). "Multidimensional encoding of brain connectomes". In: *Scientific Reports* 7.1, p. 11491. DOI: 10.1038/s41598-017-09250-w.

Cajal, S. Ramón y (1910). *Manual de histología normal: y de técnica micrográfica para uso de estudiantes*. Madrid: Imprenta y Librería de Nicolás Moya.

Carvalho, J., Invernizzi, A., Ahmadi, K., Hoffmann, M. B., Renken, R. J., and Cornelissen, F. W. (Apr. 2020). "Micro-probing enables fine-grained mapping of neuronal populations using fMRI". In: *NeuroImage* 209, p. 116423. DOI: 10.1016/j.neuroimage.2019.116423.

Chacko, L. W. (Aug. 1948). "The laminar pattern of the lateral geniculate body in the primates". In: *Journal of Neurology, Neurosurgery, and Psychiatry* 11.3, pp. 211–224. DOI: 10.1136/jnnp.11.3.211.

Chen, X., Weigel, D., Ganslandt, O., Buchfelder, M., and Nimsky, C. (Apr. 2009). "Prediction of visual field deficits by diffusion tensor imaging in temporal lobe epilepsy surgery". In: *NeuroImage* 45.2, pp. 286–297. DOI: 10.1016/j.neuroimage.2008.11.038.

Cramer, S. F. (Feb. 1991). "The origin of epidermal melanocytes. Implications for the histogenesis of nevi and melanomas". In: *Archives of Pathology & Laboratory Medicine* 115.2, pp. 115–119.

Currie, S., Hoggard, N., Craven, I. J., Hadjivassiliou, M., and Wilkinson, I. D. (Apr. 2013). "Understanding MRI: basic MR physics for physicians". In: *Postgraduate Medical Journal* 89.1050, pp. 209–223. DOI: 10.1136/postgradmedj-2012-131342.

Cybenko, G. (Dec. 1989). "Approximation by superpositions of a sigmoidal function". In: *Mathematics of Control, Signals and Systems* 2.4, pp. 303–314. DOI: 10.1007/BF02551274.

Daducci, A., Dal Palù, A., Lemkaddem, A., and Thiran, J.-P. (Jan. 2015). "COMMIT: Convex optimization modeling for microstructure informed tractography". In: *IEEE transactions on medical imaging* 34.1, pp. 246–257. DOI: 10.1109/TMI.2014.2352414.

Daniels, D. L., Herfkins, R., Gager, W. E., Meyer, G. A., Koehler, P. R., Williams, A. L., and Haughton, V. M. (July 1984). "Magnetic resonance imaging of the optic nerves and chiasm". In: *Radiology* 152.1, pp. 79–83. DOI: 10.1148/radiology.152.1.6729139.

Davies-Thompson, J., Scheel, M., Jane Lanyon, L., and Sinclair Barton, J. J. (June 2013). "Functional organisation of visual pathways in a patient with no optic chiasm". In: *Neuropsychologia* 51.7, pp. 1260–1272. DOI: 10.1016/j.neuropsychologia.2013.03.014.

De Moraes, C. G. (July 2013). "Anatomy of the visual pathways". In: *Journal of Glaucoma* 22 Suppl 5, S2–7. DOI: 10.1097/IJG.0b013e3182934978.

Descoteaux, M., Deriche, R., Knosche, T. R., and Anwander, A. (Feb. 2009). "Deterministic and Probabilistic Tractography Based on Complex Fibre Orientation Distributions". In: *IEEE Transactions on Medical Imaging* 28.2, pp. 269–286. DOI: 10.1109/TMI.2008.2004424.

Descoteaux, M., Angelino, E., Fitzgibbons, S., and Deriche, R. (2007). "Regularized, fast, and robust analytical Q-ball imaging". In: *Magnetic Resonance in Medicine* 58.3, pp. 497–510. DOI: https://doi.org/10.1002/mrm.21277.

Dhollander, T., Clemente, A., Singh, M., Boonstra, F., Civier, O., Duque, J. D., Egorova, N., Enticott, P., Fuelscher, I., Gajamange, S., Genc, S., Gottlieb, E., Hyde, C., Imms, P., Kelly, C., Kirkovski, M., Kolbe, S., Liang, X., Malhotra, A., Mito, R., Poudel, G., Silk, T. J., Vaughan, D. N., Zanin, J., Raffelt, D., and Caeyenberghs, K. (Nov. 2021). "Fixel-based Analysis of Diffusion MRI: Methods, Applications, Challenges and Opportunities". In: *NeuroImage* 241, p. 118417. DOI: 10.1016/j.neuroimage.2021.118417.

Diehl, B., Tkach, J., Piao, Z., Ruggieri, P., LaPresto, E., Liu, P., Fisher, E., Bingaman, W., and Najm, I. (Aug. 2010). "Diffusion tensor imaging in patients with focal epilepsy due to cortical dysplasia in the temporo-occipital region: Electro-clinico-pathological correlations". In: *Epilepsy Research* 90.3, pp. 178–187. DOI: 10.1016/j.eplepsyres.2010.03.006.

Duanmu, H., Kim, J., Kanakaraj, P., Wang, A., Joshua, J., Kong, J., and Wang, F. (Apr. 2020). "Automatic Brain Organ Segmentation with 3D Fully Convolutional Neural Network for Radiation Therapy Treatment Planning". In: *2020 IEEE 17th International Symposium on Biomedical Imaging (ISBI)*, pp. 758–762. DOI: 10.1109/ISBI45749.2020.9098485.

Einstein, A. (Jan. 1956). *Investigations on the Theory of the Brownian Movement*. Courier Corporation.

Elster, A. D. (2021). *MRI Questions & Answers; MR imaging physics & technology*.

Erskine, L. and Herrera, E. (Dec. 2014). "Connecting the Retina to the Brain". In: *ASN NEURO* 6.6, p. 1759091414562107. DOI: 10.1177/1759091414562107.

Federico, J. R. and Krishnamurthy, K. (2021). "Albinism". In: *StatPearls*. Treasure Island (FL): StatPearls Publishing.

Fischl, B. (Aug. 2012). "FreeSurfer". In: *NeuroImage*. 20 YEARS OF fMRI 62.2, pp. 774–781. DOI: 10.1016/j.neuroimage.2012.01.021.

Frisch, R. and Stern, O. (Jan. 1933). "Über die magnetische Ablenkung von Wasserstoffmolekülen und das magnetische Moment des Protons. I". In: *Zeitschrift für Physik* 85.1, pp. 4–16. DOI: 10.1007/BF01330773.

Frisén, L. and Glansholm, A. (July 1975). "Optical and neural resolution in peripheral vision". In: *Investigative Ophthalmology* 14.7, pp. 528–536.

Fukushima, K. (Apr. 1980). "Neocognitron: A self-organizing neural network model for a mechanism of pattern recognition unaffected by shift in position". In: *Biological Cybernetics* 36.4, pp. 193–202. DOI: 10.1007/BF00344251.

Glasser, M. F., Sotiropoulos, S. N., Wilson, J. A., Coalson, T. S., Fischl, B., Andersson, J. L., Xu, J., Jbabdi, S., Webster, M., Polimeni, J. R., Van Essen, D. C., and Jenkinson, M. (Oct. 2013). "The minimal preprocessing pipelines for the Human

Connectome Project". In: *NeuroImage*. Mapping the Connectome 80, pp. 105–124. DOI: 10.1016/j.neuroimage.2013.04.127.

Güler, A. D., Ecker, J. L., Lall, G. S., Haq, S., Altimus, C. M., Liao, H.-W., Barnard, A. R., Cahill, H., Badea, T. C., Zhao, H., Hankins, M. W., Berson, D. M., Lucas, R. J., Yau, K.-W., and Hattar, S. (May 2008). "Melanopsin cells are the principal conduits for rod–cone input to non-image-forming vision". In: *Nature* 453.7191, pp. 102–105. DOI: 10.1038/nature06829.

Gregor, Z. (Aug. 1978). "The perifoveal vasculature in albinism". In: *The British Journal of Ophthalmology* 62.8, pp. 554–557. DOI: 10.1136/bjo.62.8.554.

Guillery, R. W., Hickey, T. L., Kaas, J. H., Felleman, D. J., Debruyn, E. J., and Sparks, D. L. (June 1984). "Abnormal central visual pathways in the brain of an albino green monkey (Cercopithecus aethiops)". In: *The Journal of Comparative Neurology* 226.2, pp. 165–183. DOI: 10.1002/cne.902260203.

Guillery, R. W., Okoro, A. N., and Witkop, C. J. (Oct. 1975). "Abnormal visual pathways in the brain of a human albino". In: *Brain Research* 96.2, pp. 373–377. DOI: 10.1016/0006-8993(75)90750-7.

Hagen, E. A. H. v. d., Hoffmann, M. B., and Morland, A. B. (Jan. 2008). "Identifying Human Albinism: A Comparison of VEP and fMRI". In: *Investigative Ophthalmology & Visual Science* 49.1, pp. 238–249. DOI: 10.1167/iovs.07-0458.

Hagen, E. A. H. v. d., Houston, G. C., Hoffmann, M. B., Jeffery, G., and Morland, A. B. (2005). "Retinal abnormalities in human albinism translate into a reduction of grey matter in the occipital cortex". In: *European Journal of Neuroscience* 22.10, pp. 2475–2480. DOI: https://doi.org/10.1111/j.1460-9568.2005.04433.x.

Hahn, E. L. (Nov. 1950). "Spin Echoes". In: *Physical Review* 80.4, pp. 580–594. DOI: 10.1103/PhysRev.80.580.

Hanson, L. G. (2008). "Is quantum mechanics necessary for understanding magnetic resonance?" In: *Concepts in Magnetic Resonance Part A* 32A.5, pp. 329–340. DOI: 10.1002/cmr.a.20123.

Hebb, D. O. (1949). *The organization of behavior; a neuropsychological theory*. The organization of behavior; a neuropsychological theory. Oxford, England: Wiley.

Hendrickson, A. (2005). "Organization of the Adult Primate Fovea". In: *Macular Degeneration*. Ed. by P. L. Penfold and J. M. Provis. Berlin, Heidelberg: Springer, pp. 1–23. DOI: 10.1007/3-540-26977-0_1.

Hodgkins, P., Lees, M., Lawson, J., Reardon, W., Leitch, J., Thorogood, P., Winter, R. M., and Taylor, D. S. (Mar. 1998). "Optic disc anomalies and frontonasal dysplasia". In: *The British Journal of Ophthalmology* 82.3, pp. 290–293. DOI: 10.1136/bjo.82.3.290.

Hoffmann, M., Kaule, F., Levin, N., Masuda, Y., Kumar, A., Gottlob, I., Horiguchi, H., Dougherty, R., Stadler, J., Wolynski, B., Speck, O., Kanowski, M., Liao, Y., Wandell, B., and Dumoulin, S. (Aug. 2012). "Plasticity and stability of the visual system in human achiasma". In: *Neuron* 75.3, pp. 393–401. DOI: 10.1016/j.neuron.2012.05.026.

Hoffmann, M. B., Choritz, L., Thieme, H., Prabhakaran, G. T., and Puzniak, R. J. (Sept. 2021). "[Neuro-computational approaches for objective assessment of visual function]". In: *Der Ophthalmologe: Zeitschrift Der Deutschen Ophthalmologischen Gesellschaft* 118.9, pp. 900–906. DOI: 10.1007/s00347-021-01404-6.

Hoffmann, M. B. and Dumoulin, S. O. (Jan. 2015). "Congenital visual pathway abnormalities: a window onto cortical stability and plasticity". In: *Trends in Neurosciences* 38.1, pp. 55–65. DOI: 10.1016/j.tins.2014.09.005.

Hoffmann, M. B., Lorenz, B., Morland, A. B., and Schmidtborn, L. C. (Oct. 2005). "Misrouting of the Optic Nerves in Albinism: Estimation of the Extent with Visual Evoked Potentials". In: *Investigative Ophthalmology & Visual Science* 46.10, pp. 3892–3898. DOI: 10.1167/iovs.05-0491.

Hoffmann, M. B., Thieme, H., Liedecke, K., Meltendorf, S., Zenker, M., and Wieland, I. (Nov. 2015). "Visual Pathways in Humans With Ephrin-B1 Deficiency Associated With the Cranio-Fronto-Nasal Syndrome". In: *Investigative Ophthalmology & Visual Science* 56.12, pp. 7427–7437. DOI: 10.1167/iovs.15-17705.

Hoffmann, M. B., Tolhurst, D. J., Moore, A. T., and Morland, A. B. (Oct. 2003). "Organization of the Visual Cortex in Human Albinism". In: *Journal of Neuroscience* 23.26, pp. 8921–8930. DOI: 10.1523/JNEUROSCI.23-26-08921.2003.

Horton, J. C. and Hoyt, W. F. (June 1991). "The Representation of the Visual Field in Human Striate Cortex: A Revision of the Classic Holmes Map". In: *Archives of Ophthalmology* 109.6, pp. 816–824. DOI: 10.1001/archopht.1991.01080060080030.

Hrabe, J., Kaur, G., and Guilfoyle, D. N. (2007). "Principles and limitations of NMR diffusion measurements". In: *Journal of Medical Physics / Association of Medical Physicists of India* 32.1, pp. 34–42. DOI: 10.4103/0971-6203.31148.

Hubel, D. H. and Wiesel, T. N. (1959). "Receptive fields of single neurones in the cat's striate cortex". In: *The Journal of Physiology* 148.3, pp. 574–591. DOI: 10.1113/jphysiol.1959.sp006308.

— (1968). "Receptive fields and functional architecture of monkey striate cortex". In: *The Journal of Physiology* 195.1, pp. 215–243. DOI: 10.1113/jphysiol.1968.sp008455.

— (Dec. 1972). "Laminar and columnar distribution of geniculo-cortical fibers in the macaque monkey". In: *The Journal of Comparative Neurology* 146.4, pp. 421–450. DOI: 10.1002/cne.901460402.

Ibragimov, B. and Xing, L. (Feb. 2017). "Segmentation of organs-at-risks in head and neck CT images using convolutional neural networks". In: *Medical Physics* 44.2, pp. 547–557. DOI: 10.1002/mp.12045.

Ilia, M. and Jeffery, G. (Mar. 1999). "Retinal mitosis is regulated by dopa, a melanin precursor that may influence the time at which cells exit the cell cycle: analysis of patterns of cell production in pigmented and albino retinae". In: *The Journal of Comparative Neurology* 405.3, pp. 394–405. DOI: 10.1002/(sici)1096-9861(19990315)405:3<394::aid-cne9>3.0.co;2-y.

Inouye, T. (1909). *Die Sehstorungen bei Schussverletzungen der kortikalen Sehsphare. Nach Beobachtungen an Verwundeten der letzten japanischen Kreige.* Leipzig : Engelmann.

Isambert, A., Dhermain, F., Bidault, F., Commowick, O., Bondiau, P.-Y., Malandain, G., and Lefkopoulos, D. (Apr. 2008). "Evaluation of an atlas-based automatic segmentation software for the delineation of brain organs at risk in a radiation therapy clinical context". In: *Radiotherapy and Oncology: Journal of the European Society for Therapeutic Radiology and Oncology* 87.1, pp. 93–99. DOI: 10.1016/j.radonc.2007.11.030.

James, J. S., Radhakrishnan, A., Thomas, B., Madhusoodanan, M., Kesavadas, C., Abraham, M., Menon, R., Rathore, C., and Vilanilam, G. (Feb. 2015). "Diffusion tensor imaging tractography of Meyer's loop in planning resective surgery for drug-resistant temporal lobe epilepsy". In: *Epilepsy Research* 110, pp. 95–104. DOI: 10.1016/j.eplepsyres.2014.11.020.

Jansonius, N. M., Vliet, T. M. van der, Cornelissen, F. W., Pott, J. W., and Kooijman, A. C. (Mar. 2001). "A girl without a chiasm: electrophysiologic and MRI evidence for the absence of crossing optic nerve fibers in a girl with a congenital

nystagmus". In: *Journal of Neuro-Ophthalmology: The Official Journal of the North American Neuro-Ophthalmology Society* 21.1, pp. 26–29. DOI: 10.1097/00041327-200103000-00007.

Jbabdi, S., Sotiropoulos, S. N., Savio, A. M., Graña, M., and Behrens, T. E. (Dec. 2012). "Model-based analysis of multi-shell diffusion MR data for tractography: How to get over fitting problems". In: *Magnetic resonance in medicine : official journal of the Society of Magnetic Resonance in Medicine / Society of Magnetic Resonance in Medicine* 68.6, pp. 1846–1855. DOI: 10.1002/mrm.24204.

Jenkinson, M., Beckmann, C. F., Behrens, T. E. J., Woolrich, M. W., and Smith, S. M. (Aug. 2012). "FSL". In: *NeuroImage*. 20 YEARS OF fMRI 62.2, pp. 782–790. DOI: 10.1016/j.neuroimage.2011.09.015.

Jeong, Y. U., Yoo, S., Kim, Y.-H., and Shim, W. H. (Dec. 2020). "De-Identification of Facial Features in Magnetic Resonance Images: Software Development Using Deep Learning Technology". In: *Journal of Medical Internet Research* 22.12, e22739. DOI: 10.2196/22739.

Jeurissen, B., Leemans, A., Tournier, J., Jones, D. K., and Sijbers, J. (May 2012). "Investigating the prevalence of complex fiber configurations in white matter tissue with diffusion magnetic resonance imaging". In: *Human Brain Mapping* 34.11, pp. 2747–2766. DOI: 10.1002/hbm.22099.

Jones, D. K. (Sept. 2008). "Tractography gone wild: probabilistic fibre tracking using the wild bootstrap with diffusion tensor MRI". In: *IEEE transactions on medical imaging* 27.9, pp. 1268–1274. DOI: 10.1109/TMI.2008.922191.

Jones, D. K., Knösche, T. R., and Turner, R. (June 2013). "White matter integrity, fiber count, and other fallacies: The do's and don'ts of diffusion MRI". In: *NeuroImage* 73, pp. 239–254. DOI: 10.1016/j.neuroimage.2012.06.081.

Jovicich, J., Czanner, S., Greve, D., Haley, E., Kouwe, A. van der, Gollub, R., Kennedy, D., Schmitt, F., Brown, G., Macfall, J., Fischl, B., and Dale, A. (Apr. 2006). "Reliability in multi-site structural MRI studies: effects of gradient non-linearity correction on phantom and human data". In: *NeuroImage* 30.2, pp. 436–443. DOI: 10.1016/j.neuroimage.2005.09.046.

Kandel, E. R., Schwartz, J. H., and Jessell, T. M., eds. (1991). *Principles of Neural Science*. Third. New York: Elsevier.

Kaule, F. R., Wolynski, B., Gottlob, I., Stadler, J., Speck, O., Kanowski, M., Meltendorf, S., Behrens-Baumann, W., and Hoffmann, M. B. (Oct. 2014). "Impact of chiasma opticum malformations on the organization of the human ventral visual cortex". In: *Human Brain Mapping* 35.10, pp. 5093–5105. DOI: 10.1002/hbm.22534.

Kelts, E. A. (2010). "The basic anatomy of the optic nerve and visual system (or, why Thoreau was wrong)". In: *NeuroRehabilitation* 27.3, pp. 217–222. DOI: 10.3233/NRE-2010-0600.

Kim, U. S., Mahroo, O. A., Mollon, J. D., and Yu-Wai-Man, P. (2021). "Retinal Ganglion Cells—Diversity of Cell Types and Clinical Relevance". In: *Frontiers in Neurology* 12, p. 635. DOI: 10.3389/fneur.2021.661938.

Kinnear, P. E., Jay, B., and Witkop, C. J. (Oct. 1985). "Albinism". In: *Survey of Ophthalmology* 30.2, pp. 75–101. DOI: 10.1016/0039-6257(85)90077-3.

Klemen, J., Hoffmann, M. B., and Chambers, C. (Nov. 2012). "Cortical plasticity in the face of congenitally altered input into V1". In: *Cortex* 48.10, pp. 1362–1365. DOI: 10.1016/j.cortex.2012.03.012.

Kolb, H., Fernandez, E., and Nelson, R., eds. (1995). *Webvision: The Organization of the Retina and Visual System*. Salt Lake City (UT): University of Utah Health Sciences Center.

Korff, C. M., Apkarian, P., Bour, L. J., Meuli, R., Verrey, J.-D., and Roulet Perez, E. (Aug. 2003). "Isolated absence of optic chiasm revealed by congenital nystagmus, MRI and VEPs". In: *Neuropediatrics* 34.4, pp. 219–223. DOI: 10.1055/s-2003-42214.

Kralj-Hans, I., Tibber, M., Jeffery, G., and Mobbs, P. (Jan. 2006). "Differential effect of dopamine on mitosis in early postnatal albino and pigmented rat retinae". In: *Journal of Neurobiology* 66.1, pp. 47–55. DOI: 10.1002/neu.20200.

Krizhevsky, A., Sutskever, I., and Hinton, G. E. (2012). "ImageNet Classification with Deep Convolutional Neural Networks". In: *Advances in Neural Information Processing Systems* 25.

Kruijt, B., Franssen, L., Prick, L. J. J. M., Vliet, J. M. J. van, and Berg, T. J. T. P. van den (May 2011). "Ocular Straylight in Albinism". In: *Optometry and Vision Science* 88.5, E585. DOI: 10.1097/OPX.0b013e318212071e.

Kruijt, C. C., Wit, G. C. d., Bergen, A. A., Florijn, R. J., Schalij-Delfos, N. E., and Genderen, M. M. v. (Dec. 2018). "The Phenotypic Spectrum of Albinism". In: *Ophthalmology* 125.12, pp. 1953–1960. DOI: 10.1016/j.ophtha.2018.08.003.

Kupfer, C, Chumbley, L, and Downer, J. C. (June 1967). "Quantitative histology of optic nerve, optic tract and lateral geniculate nucleus of man." In: *Journal of Anatomy* 101.Pt 3, pp. 393–401.

Lasseaux, E., Plaisant, C., Michaud, V., Pennamen, P., Trimouille, A., Gaston, L., Monfermé, S., Lacombe, D., Rooryck, C., Morice-Picard, F., and Arveiler, B. (2018). "Molecular characterization of a series of 990 index patients with albinism". In: *Pigment Cell & Melanoma Research* 31.4, pp. 466–474. DOI: 10.1111/pcmr.12688.

Lauterbur, P. C. (Mar. 1973). "Image Formation by Induced Local Interactions: Examples Employing Nuclear Magnetic Resonance". In: *Nature* 242.5394, pp. 190–191. DOI: 10.1038/242190a0.

Le Bihan, D. (June 1990). "IVIM method measures diffusion and perfusion". In: *Diagnostic Imaging* 12.6, pp. 133, 136.

LeCun, Y., Boser, B., Denker, J. S., Henderson, D., Howard, R. E., Hubbard, W., and Jackel, L. D. (Dec. 1989). "Backpropagation Applied to Handwritten Zip Code Recognition". In: *Neural Computation* 1.4, pp. 541–551. DOI: 10.1162/neco.1989.1.4.541.

LeCun, Y., Bottou, L., Bengio, Y., and Haffner, P. (Nov. 1998). "Gradient-based learning applied to document recognition". In: *Proceedings of the IEEE* 86.11, pp. 2278–2324. DOI: 10.1109/5.726791.

Lecun, Y. (1985). "Une procedure d'apprentissage pour reseau a seuil asymmetrique (A learning scheme for asymmetric threshold networks)". In: *Proceedings of Cognitiva 85, Paris, France*, pp. 599–604.

Leventhal, A. G. and Creel, D. J. (Mar. 1985). "Retinal projections and functional architecture of cortical areas 17 and 18 in the tyrosinase-negative albino cat". In: *The Journal of Neuroscience: The Official Journal of the Society for Neuroscience* 5.3, pp. 795–807.

Lundervold, A. S. and Lundervold, A. (May 2019). "An overview of deep learning in medical imaging focusing on MRI". In: *Zeitschrift Fur Medizinische Physik* 29.2, pp. 102–127. DOI: 10.1016/j.zemedi.2018.11.002.

Marçon, C. R. and Maia, M. (Sept. 2019). "Albinism: epidemiology, genetics, cutaneous characterization, psychosocial factors". In: *Anais Brasileiros de Dermatologia* 94.5, pp. 503–520. DOI: 10.1016/j.abd.2019.09.023.

Mazziotta, J., Toga, A., Evans, A., Fox, P., Lancaster, J., Zilles, K., Woods, R., Paus, T., Simpson, G., Pike, B., Holmes, C., Collins, L., Thompson, P., MacDonald,

D., Iacoboni, M., Schormann, T., Amunts, K., Palomero-Gallagher, N., Geyer, S., Parsons, L., Narr, K., Kabani, N., Le Goualher, G., Boomsma, D., Cannon, T., Kawashima, R., and Mazoyer, B. (Aug. 2001). "A probabilistic atlas and reference system for the human brain: International Consortium for Brain Mapping (ICBM)". In: *Philosophical Transactions of the Royal Society of London. Series B, Biological Sciences* 356.1412, pp. 1293–1322. DOI: 10.1098/rstb.2001.0915.

McCafferty, B. K., Wilk, M. A., McAllister, J. T., Stepien, K. E., Dubis, A. M., Brilliant, M. H., Anderson, J. L., Carroll, J., and Summers, C. G. (2015). "Clinical Insights Into Foveal Morphology in Albinism". In: *Journal of pediatric ophthalmology and strabismus* 52.3, pp. 167–172. DOI: 10.3928/01913913-20150427-06.

McCulloch, W. S. and Pitts, W. (Dec. 1943). "A logical calculus of the ideas immanent in nervous activity". In: *The bulletin of mathematical biophysics* 5.4, pp. 115–133. DOI: 10.1007/BF02478259.

McDonald, C. R., Ahmadi, M. E., Hagler, D. J., Tecoma, E. S., Iragui, V. J., Gharapetian, L., Dale, A. M., and Halgren, E. (Dec. 2008). "Diffusion tensor imaging correlates of memory and language impairments in temporal lobe epilepsy". In: *Neurology* 71.23, pp. 1869–1876. DOI: 10.1212/01.wnl.0000327824.05348.3b.

Mcketton, L., Kelly, K. R., and Schneider, K. A. (Aug. 2014). "Abnormal lateral geniculate nucleus and optic chiasm in human albinism". In: *The Journal of Comparative Neurology* 522.11, pp. 2680–2687. DOI: 10.1002/cne.23565.

Minsky, M. and Papert, S. A. (Jan. 1969). *Perceptrons: An Introduction to Computational Geometry*. Cambridge, MA, USA: MIT Press.

Mishkin, M., Ungerleider, L. G., and Macko, K. A. (Jan. 1983). "Object vision and spatial vision: two cortical pathways". In: *Trends in Neurosciences* 6, pp. 414–417. DOI: 10.1016/0166-2236(83)90190-X.

Mohammad, S., Gottlob, I., Sheth, V., Pilat, A., Lee, H., Pollheimer, E., and Proudlock, F. A. (July 2015). "Characterization of Abnormal Optic Nerve Head Morphology in Albinism Using Optical Coherence Tomography". In: *Investigative Ophthalmology & Visual Science* 56.8, pp. 4611–4618. DOI: 10.1167/iovs.15-16856.

Montoliu, L., Grønskov, K., Wei, A.-H., Martínez-García, M., Fernández, A., Arveiler, B., Morice-Picard, F., Riazuddin, S., Suzuki, T., Ahmed, Z. M., Rosenberg, T., and Li, W. (Jan. 2014). "Increasing the complexity: new genes and new types of albinism". In: *Pigment Cell & Melanoma Research* 27.1, pp. 11–18. DOI: 10.1111/pcmr.12167.

Mori, S. and Zhang, J. (Sept. 2006). "Principles of Diffusion Tensor Imaging and Its Applications to Basic Neuroscience Research". In: *Neuron* 51.5, pp. 527–539. DOI: 10.1016/j.neuron.2006.08.012.

Mori, S. and Zijl, P. C. M. van (Dec. 2002). "Fiber tracking: principles and strategies - a technical review". In: *NMR in biomedicine* 15.7-8, pp. 468–480. DOI: 10.1002/nbm.781.

Mueller, B. A., Lim, K. O., Hemmy, L., and Camchong, J. (Sept. 2015). "Diffusion MRI and its role in neuropsychology". In: *Neuropsychology review* 25.3, pp. 250–271. DOI: 10.1007/s11065-015-9291-z.

Nilsson, D., Starck, G., Ljungberg, M., Ribbelin, S., Jönsson, L., Malmgren, K., and Rydenhag, B. (Oct. 2007). "Intersubject variability in the anterior extent of the optic radiation assessed by tractography". In: *Epilepsy Research* 77.1, pp. 11–16. DOI: 10.1016/j.eplepsyres.2007.07.012.

Oetting, W. S., Summers, C. G., and King, R. A. (1994). "Albinism and the associated ocular defects". In: *Metabolic, Pediatric, and Systemic Ophthalmology (New York, N.Y.: 1985)* 17.1-4, pp. 5–9.

Ogden, T. E. (Jan. 1984). "Nerve fiber layer of the primate retina: morphometric analysis". In: *Investigative Ophthalmology & Visual Science* 25.1, pp. 19–29.

O'Mahony, N., Campbell, S., Carvalho, A., Harapanahalli, S., Hernandez, G. V., Krpalkova, L., Riordan, D., and Walsh, J. (2020). "Deep Learning vs. Traditional Computer Vision". In: *Advances in Computer Vision*. Ed. by K. Arai and S. Kapoor. Vol. 943. Cham: Springer International Publishing, pp. 128–144. DOI: 10.1007/978-3-030-17795-9_10.

Oouchi, H., Yamada, K., Sakai, K., Kizu, O., Kubota, T., Ito, H., and Nishimura, T. (June 2007). "Diffusion Anisotropy Measurement of Brain White Matter Is Affected by Voxel Size: Underestimation Occurs in Areas with Crossing Fibers". In: *American Journal of Neuroradiology* 28.6, pp. 1102–1106. DOI: 10.3174/ajnr.A0488.

Pal, B., Mohamed, M. D., Keen, T. J., Williams, G. A., Bradbury, J. A., Sheridan, E., and Inglehearn, C. F. (Oct. 2004). "A new phenotype of recessively inherited foveal hypoplasia and anterior segment dysgenesis maps to a locus on chromosome 16q23.2–24.2." In: *Journal of Medical Genetics* 41.10, pp. 772–777. DOI: 10.1136/jmg.2004.020040.

Park, K.-A. and Oh, S. Y. (Feb. 2013). "Clinical characteristics of high grade foveal hypoplasia". In: *International Ophthalmology* 33.1, pp. 9–14. DOI: 10.1007/s10792-012-9664-8.

Parravano, J. G., Toledo, A, and Kucharczyk, W (Sept. 1993). "Dimensions of the optic nerves, chiasm, and tracts: MR quantitative comparison between patients with optic atrophy and normals". In: *Journal of computer assisted tomography* 17.5, pp. 688–690. DOI: 10.1097/00004728-199309000-00003.

Pestilli, F., Yeatman, J., Rokem, A., Kay, K., Takemura, H., and Wandell, B. (Aug. 2014). "LiFE: Linear Fascicle Evaluation a new technology to study visual connectomes". In: *Journal of Vision* 14.10, pp. 1122–1122. DOI: 10.1167/14.10.1122.

Poldrack, R. A., Mumford, J. A., Schonberg, T., Kalar, D., Barman, B., and Yarkoni, T. (2012). "Discovering relations between mind, brain, and mental disorders using topic mapping". In: *PLoS computational biology* 8.10, e1002707. DOI: 10.1371/journal.pcbi.1002707.

Pooley, R. A. (July 2005). "Fundamental Physics of MR Imaging". In: *RadioGraphics* 25.4, pp. 1087–1099. DOI: 10.1148/rg.254055027.

Poulter, J., Al-Araimi, M., Conte, I., van Genderen, M., Sheridan, E., Carr, I., Parry, D., Shires, M., Carrella, S., Bradbury, J., Khan, K., Lakeman, P., Sergouniotis, P., Webster, A., Moore, A., Pal, B., Mohamed, M., Venkataramana, A., Ramprasad, V., Shetty, R., Saktivel, M., Kumaramanickavel, G., Tan, A., Mackey, D., Hewitt, A., Banfi, S., Ali, M., Inglehearn, C., and Toomes, C. (Dec. 2013). "Recessive Mutations in SLC38A8 Cause Foveal Hypoplasia and Optic Nerve Misrouting without Albinism". In: *American Journal of Human Genetics* 93.6, pp. 1143–1150. DOI: 10.1016/j.ajhg.2013.11.002.

Prieur, D. S. and Rebsam, A. (July 2017). "Retinal axon guidance at the midline: Chiasmatic misrouting and consequences". In: *Developmental Neurobiology* 77.7, pp. 844–860. DOI: 10.1002/dneu.22473.

Provis, J. M. and Hendrickson, A. E. (Apr. 2008). "The foveal avascular region of developing human retina". In: *Archives of Ophthalmology (Chicago, Ill.: 1960)* 126.4, pp. 507–511. DOI: 10.1001/archopht.126.4.507.

Purington, C., Bao, P., and Tjan, B. S. (Aug. 2012). "Visual cortex representation of achiasmic retinal inputs". In: *Journal of Vision* 12.9, p. 788. DOI: 10.1167/12.9.788.

Puzniak, R. J., Ahmadi, K., Kaufmann, J., Gouws, A., Morland, A. B., Pestilli, F., and Hoffmann, M. B. (Jan. 2019). "Quantifying nerve decussation abnormalities in

the optic chiasm". In: *NeuroImage: Clinical* 24, p. 102055. DOI: 10.1016/j.nicl.2019.102055.

Puzniak, R. J., McPherson, B., Ahmadi, K., Herbik, A., Kaufmann, J., Liebe, T., Gouws, A., Morland, A. B., Gottlob, I., Hoffmann, M. B., and Pestilli, F. (Nov. 2021a). "CHIASM, the human brain albinism and achiasma MRI dataset". In: *Scientific Data* 8.1, p. 308. DOI: 10.1038/s41597-021-01080-w.

Puzniak, R. J., Prabhakaran, G. T., Buentjen, L., Schmitt, F. C., and Hoffmann, M. B. (Feb. 2021b). "Tracking the visual system—from the optic chiasm to primary visual cortex". In: *Zeitschrift für Epileptologie* 34.1, pp. 57–66. DOI: 10.1007/s10309-020-00384-y.

Puzniak, R. J., Prabhakaran, G. T., and Hoffmann, M. B. (2021c). "Deep Learning-Based Detection of Malformed Optic Chiasms From MRI Images". In: *Frontiers in Neuroscience* 15, p. 1332. DOI: 10.3389/fnins.2021.755785.

Rabi, I. I., Zacharias, J. R., Millman, S., and Kusch, P. (Feb. 1938). "A New Method of Measuring Nuclear Magnetic Moment". In: *Physical Review* 53.4, pp. 318–318. DOI: 10.1103/PhysRev.53.318.

Rachel, R. A., Dölen, G., Hayes, N. L., Lu, A., Erskine, L., Nowakowski, R. S., and Mason, C. A. (June 2002). "Spatiotemporal Features of Early Neuronogenesis Differ in Wild-Type and Albino Mouse Retina". In: *The Journal of Neuroscience* 22.11, pp. 4249–4263. DOI: 10.1523/JNEUROSCI.22-11-04249.2002.

Ravindra, V. and Grama, A. (Aug. 2019). "De-anonymization Attacks on Neuroimaging Datasets". In: *arXiv:1908.03260 [cs, eess, q-bio]*.

Reveley, C., Seth, A. K., Pierpaoli, C., Silva, A. C., Yu, D., Saunders, R. C., Leopold, D. A., and Ye, F. Q. (May 2015). "Superficial white matter fiber systems impede detection of long-range cortical connections in diffusion MR tractography". In: *Proceedings of the National Academy of Sciences* 112.21, E2820–E2828. DOI: 10.1073/pnas.1418198112.

Riesenhuber, M. and Poggio, T. (Nov. 1999). "Hierarchical models of object recognition in cortex". In: *Nature Neuroscience* 2.11, pp. 1019–1025. DOI: 10.1038/14819.

Rimmer, A. (Oct. 2017). "Radiologist shortage leaves patient care at risk, warns royal college". In: *BMJ* 359, j4683. DOI: 10.1136/bmj.j4683.

Robbins, H. (2007). "A Stochastic Approximation Method". In: DOI: 10.1214/AOMS/1177729586.

Rodieck, R. W. (1998). *The first steps in seeing*. The first steps in seeing. Sunderland, MA, US: Sinauer Associates.

Roebroeck, A., Galuske, R., Formisano, E., Chiry, O., Bratzke, H., Ronen, I., Kim, D.-s., and Goebel, R. (Jan. 2008). "High-resolution diffusion tensor imaging and tractography of the human optic chiasm at 9.4 T". In: *NeuroImage* 39.1, pp. 157–168. DOI: 10.1016/j.neuroimage.2007.08.015.

Rokem, A., Takemura, H., Bock, A. S., Scherf, K. S., Behrmann, M., Wandell, B. A., Fine, I., Bridge, H., and Pestilli, F. (Feb. 2017). "The visual white matter: The application of diffusion MRI and fiber tractography to vision science". In: *Journal of Vision* 17.2, p. 4. DOI: 10.1167/17.2.4.

Rosenblatt, F. (Mar. 1961). *PRINCIPLES OF NEURODYNAMICS. PERCEPTRONS AND THE THEORY OF BRAIN MECHANISMS*. Tech. rep. CORNELL AERONAUTICAL LAB INC BUFFALO NY.

Rovamo, J. and Virsu, V. (Nov. 1979). "An estimation and application of the human cortical magnification factor". In: *Experimental Brain Research* 37.3, pp. 495–510. DOI: 10.1007/BF00236819.

Rumelhart, D. E., Hinton, G. E., and Williams, R. J. (Oct. 1986). "Learning representations by back-propagating errors". In: *Nature* 323.6088, pp. 533–536. DOI: 10.1038/323533a0.

Sacks, O. (1987). *The man who mistook his wife for a hat and other clinical tales*. 1st Perennial Library ed. New York: Perennial Library.

Sami, D. A., Saunders, D., Thompson, D. A., Russell-Eggitt, I. M., Nischal, K. K., Jeffery, G., Dattani, M., Clement, R. A., Liassis, A., and Taylor, D. S. (Oct. 2005). "The achiasmia spectrum: congenitally reduced chiasmal decussation". In: *British Journal of Ophthalmology* 89.10, pp. 1311–1317. DOI: 10.1136/bjo.2005.068171.

Scheinfeld, N. S. (Dec. 2003). "Syndromic albinism: a review of genetics and phenotypes". In: *Dermatology Online Journal* 9.5, p. 5.

Schmitt, F. C., Kaufmann, J., Hoffmann, M. B., Tempelmann, C., Kluge, C., Rampp, S., Voges, J., Heinze, H. J., Buentjen, L., and Grueschow, M. (May 2014). "Case Report: Practicability of functionally based tractography of the optic radiation during presurgical epilepsy work up". In: *Neuroscience Letters* 568, pp. 56–61. DOI: 10.1016/j.neulet.2014.03.049.

Schmitz, B., Käsmann-Kellner, B., Schäfer, T., Krick, C. M., Grön, G., Backens, M., and Reith, W. (Sept. 2004). "Monocular visual activation patterns in albinism as revealed by functional magnetic resonance imaging". In: *Human Brain Mapping* 23.1, pp. 40–52. DOI: 10.1002/hbm.20046.

Schmitz, B., Schaefer, T., Krick, C. M., Reith, W., Backens, M., and Käsmann-Kellner, B. (Jan. 2003). "Configuration of the Optic Chiasm in Humans with Albinism as Revealed by Magnetic Resonance Imaging". In: *Investigative Ophthalmology & Visual Science* 44.1, pp. 16–21. DOI: 10.1167/iovs.02-0156.

Schneider, K. A., Richter, M. C., and Kastner, S. (Oct. 2004). "Retinotopic Organization and Functional Subdivisions of the Human Lateral Geniculate Nucleus: A High-Resolution Functional Magnetic Resonance Imaging Study". In: *Journal of Neuroscience* 24.41, pp. 8975–8985. DOI: 10.1523/JNEUROSCI.2413-04.2004.

Seth, A., Culverwell, J., Walkowicz, M., Toro, S., Rick, J. M., Neuhauss, S. C. F., Varga, Z. M., and Karlstrom, R. O. (Feb. 2006). "belladonna/(lhx2) is required for neural patterning and midline axon guidance in the zebrafish forebrain". In: *Development (Cambridge, England)* 133.4, pp. 725–735. DOI: 10.1242/dev.02244.

Shatz, C. J. (Sept. 1992). "The developing brain". In: *Scientific American* 267.3, pp. 60–67. DOI: 10.1038/scientificamerican0992-60.

Smith, R. E., Tournier, J.-D., Calamante, F., and Connelly, A. (Sept. 2012). "Anatomically-constrained tractography: Improved diffusion MRI streamlines tractography through effective use of anatomical information". In: *NeuroImage* 62.3, pp. 1924–1938. DOI: 10.1016/j.neuroimage.2012.06.005.

Smith, S., Bannister, P. R., Beckmann, C., Brady, M., Clare, S., Flitney, D., Hansen, P., Jenkinson, M., Leibovici, D., Ripley, B., Woolrich, M., and Zhang, Y. (June 2001). "FSL: New tools for functional and structural brain image analysis". In: *NeuroImage*. Originally published as Volume 13, Number 6, Part 2 13.6, Supplement, p. 249. DOI: 10.1016/S1053-8119(01)91592-7.

Smith, S. M. (Sept. 2002). "Fast robust automated brain extraction". In: *Human Brain Mapping* 17.3, pp. 143–155. DOI: 10.1002/hbm.10062.

Smith, S. M., Jenkinson, M., Johansen-Berg, H., Rueckert, D., Nichols, T. E., Mackay, C. E., Watkins, K. E., Ciccarelli, O., Cader, M. Z., Matthews, P. M., and Behrens, T. E. J. (July 2006). "Tract-based spatial statistics: voxelwise analysis of multi-subject diffusion data". In: *NeuroImage* 31.4, pp. 1487–1505. DOI: 10.1016/j.neuroimage.2006.02.024.

Soares, J. M., Magalhães, R., Moreira, P. S., Sousa, A., Ganz, E., Sampaio, A., Alves, V., Marques, P., and Sousa, N. (2016). "A Hitchhiker's Guide to Functional Magnetic Resonance Imaging". In: *Frontiers in Neuroscience* 10, p. 515. DOI: 10.3389/fnins.2016.00515.

Soares, J., Marques, P., Alves, V., and Sousa, N. (2013). "A hitchhiker's guide to diffusion tensor imaging". In: *Frontiers in Neuroscience* 7, p. 31. DOI: 10.3389/fnins.2013.00031.

Staempfli, P., Jaermann, T., Crelier, G. R., Kollias, S., Valavanis, A., and Boesiger, P. (Mar. 2006). "Resolving fiber crossing using advanced fast marching tractography based on diffusion tensor imaging". In: *NeuroImage* 30.1, pp. 110–120. DOI: 10.1016/j.neuroimage.2005.09.027.

Stehling, M. K., Turner, R., and Mansfield, P. (Oct. 1991). "Echo-planar imaging: magnetic resonance imaging in a fraction of a second". In: *Science (New York, N.Y.)* 254.5028, pp. 43–50. DOI: 10.1126/science.1925560.

Stejskal, E. O. and Tanner, J. E. (Jan. 1965). "Spin Diffusion Measurements: Spin Echoes in the Presence of a Time-Dependent Field Gradient". In: *The Journal of Chemical Physics* 42.1, pp. 288–292. DOI: 10.1063/1.1695690.

Takemura, H., Caiafa, C. F., Wandell, B. A., and Pestilli, F. (Feb. 2016). "Ensemble Tractography". In: *PLOS Computational Biology* 12.2, e1004692. DOI: 10.1371/journal.pcbi.1004692.

Talairach, J., Rayport, M., and Tournoux, P. (1997). *Co-planar stereotaxic atlas of the human brain: 3-dimensional proportional system: an approach to cerebral imaging*. Stuttgart: Thieme.

Taylor, D. (Oct. 2007). "Developmental abnormalities of the optic nerve and chiasm". In: *Eye* 21.10, pp. 1271–1284. DOI: 10.1038/sj.eye.6702851.

Thomas, C., Ye, F. Q., Irfanoglu, M. O., Modi, P., Saleem, K. S., Leopold, D. A., and Pierpaoli, C. (Nov. 2014). "Anatomical accuracy of brain connections derived from diffusion MRI tractography is inherently limited". In: *Proceedings of the National Academy of Sciences* 111.46, pp. 16574–16579. DOI: 10.1073/pnas.1405672111.

Thompson, D. A., Kriss, A., Chong, K., Harris, C., Russell-Eggitt, I., Shawkat, F., Neville, B. G., Aclimandos, W., and Taylor, D. S. (Dec. 1999). "Visual-evoked potential evidence of chiasmal hypoplasia". In: *Ophthalmology* 106.12, pp. 2354–2361. DOI: 10.1016/S0161-6420(99)90539-0.

Torrey, H. C. (Nov. 1956). "Bloch Equations with Diffusion Terms". In: *Physical Review* 104.3, pp. 563–565. DOI: 10.1103/PhysRev.104.563.

Tournier, J.-D., Calamante, F, and Connelly, A (2010). "Improved probabilistic streamlines tractography by 2nd order integration over fibre orientation distributions". In: *Proceedings of the International Society for Magnetic Resonance in Medicine*, p. 1670.

Tournier, J.-D., Calamante, F., and Connelly, A. (May 2007). "Robust determination of the fibre orientation distribution in diffusion MRI: Non-negativity constrained super-resolved spherical deconvolution". In: *NeuroImage* 35.4, pp. 1459–1472. DOI: 10.1016/j.neuroimage.2007.02.016.

Tournier, J.-D., Calamante, F., and Connelly, A. (2012). "MRtrix: Diffusion tractography in crossing fiber regions". In: *International Journal of Imaging Systems and Technology* 22.1, pp. 53–66. DOI: https://doi.org/10.1002/ima.22005.

Tournier, J.-D., Calamante, F., and Connelly, A. (Dec. 2013). "Determination of the appropriate b value and number of gradient directions for high-angular-resolution diffusion-weighted imaging". In: *NMR in biomedicine* 26.12, pp. 1775–1786. DOI: 10.1002/nbm.3017.

Tournier, J. D., Calamante, F., Gadian, D. G., and Connelly, A. (Nov. 2004). "Direct estimation of the fiber orientation density function from diffusion-weighted MRI data using spherical deconvolution". In: *NeuroImage* 23.3, pp. 1176–1185. DOI: 10.1016/j.neuroimage.2004.07.037.

Tournier, J.-D., Smith, R., Raffelt, D., Tabbara, R., Dhollander, T., Pietsch, M., Christiaens, D., Jeurissen, B., Yeh, C.-H., and Connelly, A. (Nov. 2019). "MRtrix3: A fast, flexible and open software framework for medical image processing and visualisation". In: *NeuroImage* 202, p. 116137. DOI: 10.1016/j.neuroimage.2019.116137.

Tournier, J.-D., Mori, S., and Leemans, A. (2011). "Diffusion tensor imaging and beyond". In: *Magnetic Resonance in Medicine* 65.6, pp. 1532–1556. DOI: 10.1002/mrm.22924.

Tuch, D. S. (2004). "Q-ball imaging". In: *Magnetic Resonance in Medicine* 52.6, pp. 1358–1372. DOI: 10.1002/mrm.20279.

Tuch, D. S., Reese, T. G., Wiegell, M. R., Makris, N., Belliveau, J. W., and Wedeen, V. J. (2002). "High angular resolution diffusion imaging reveals intravoxel white matter fiber heterogeneity". In: *Magnetic Resonance in Medicine* 48.4, pp. 577–582. DOI: https://doi.org/10.1002/mrm.10268.

Van Essen, D. C., Smith, S. M., Barch, D. M., Behrens, T. E. J., Yacoub, E., Ugurbil, K., and WU-Minn HCP Consortium (Oct. 2013). "The WU-Minn Human Connectome Project: an overview". In: *NeuroImage* 80, pp. 62–79. DOI: 10.1016/j.neuroimage.2013.05.041.

Vaswani, A., Shazeer, N., Parmar, N., Uszkoreit, J., Jones, L., Gomez, A. N., Kaiser, L., and Polosukhin, I. (June 2017). "Attention Is All You Need". In.

Vicente-Saez, R. and Martinez-Fuentes, C. (July 2018). "Open Science now: A systematic literature review for an integrated definition". In: *Journal of Business Research* 88, pp. 428–436. DOI: 10.1016/j.jbusres.2017.12.043.

Victor, J. D., Apkarian, P., Hirsch, J., Conte, M. M., Packard, M., Relkin, N. R., Kim, K. H., and Shapley, R. M. (Jan. 2000). "Visual function and brain organization in non-decussating retinal-fugal fibre syndrome". In: *Cerebral Cortex (New York, N.Y.: 1991)* 10.1, pp. 2–22. DOI: 10.1093/cercor/10.1.2.

Videira, I. F. d. S., Moura, D. F. L., and Magina, S. (Feb. 2013). "Mechanisms regulating melanogenesis". In: *Anais Brasileiros De Dermatologia* 88.1, pp. 76–83. DOI: 10.1590/s0365-05962013000100009.

Wagner, A. L., Murtagh, F. R., Hazlett, K. S., and Arrington, J. A. (Apr. 1997). "Measurement of the normal optic chiasm on coronal MR images". In: *AJNR. American journal of neuroradiology* 18.4, pp. 723–726.

Wald, G. (Aug. 1968). "The Molecular Basis of Visual Excitation". In: *Nature* 219.5156, pp. 800–807. DOI: 10.1038/219800a0.

Wandell, B. A., Dumoulin, S. O., and Brewer, A. A. (Oct. 2007). "Visual Field Maps in Human Cortex". In: *Neuron* 56.2, pp. 366–383. DOI: 10.1016/j.neuron.2007.10.012.

Wedeen, V. J., Wang, R. P., Schmahmann, J. D., Benner, T., Tseng, W. Y. I., Dai, G., Pandya, D. N., Hagmann, P., D'Arceuil, H., and Crespigny, A. J. de (July 2008). "Diffusion spectrum magnetic resonance imaging (DSI) tractography of crossing fibers". In: *NeuroImage* 41.4, pp. 1267–1277. DOI: 10.1016/j.neuroimage.2008.03.036.

Williams, R. W., Hogan, D., and Garraghty, P. E. (Feb. 1994). "Target recognition and visual maps in the thalamus of achiasmatic dogs". In: *Nature* 367.6464, pp. 637–639. DOI: 10.1038/367637a0.

Winston, G. P., Mancini, L., Stretton, J., Ashmore, J., Symms, M. R., Duncan, J. S., and Yousry, T. A. (Nov. 2011). "Diffusion tensor imaging tractography of the optic radiation for epilepsy surgical planning: A comparison of two methods". In: *Epilepsy Research* 97.1, pp. 124–132. DOI: 10.1016/j.eplepsyres.2011.07.019.

Wolynski, B., Kanowski, M., Meltendorf, S., Behrens-Baumann, W., and Hoffmann, M. B. (Nov. 2010). "Self-organisation in the human visual system–visuo-motor processing with congenitally abnormal V1 input". In: *Neuropsychologia* 48.13, pp. 3834–3845. DOI: 10.1016/j.neuropsychologia.2010.09.011.

Appendix A

Publications

* Puzniak, R. J., Ahmadi, K., Kaufmann, J., Gouws, A., Morland, A. B., Pestilli, F., and Hoffmann, M. B. (Jan. 2019). "Quantifying nerve decussation abnormalities in the optic chiasm". In: *NeuroImage: Clinical* 24, p. 102055. DOI: 10.1016/j.nicl.2019.102055

* Ahmadi, K., Fracasso, A., Puzniak, R. J., Gouws, A. D., Yakupov, R., Speck, O., Kaufmann, J., Pestilli, F., Dumoulin, S. O., Morland, A. B., and Hoffmann, M. B. (July 2020). "Triple visual hemifield maps in a case of optic chiasm hypoplasia". In: *NeuroImage* 215, p. 116822. DOI: 10.1016/j.neuroimage.2020.116822

* Puzniak, R. J., Prabhakaran, G. T., Buentjen, L., Schmitt, F. C., and Hoffmann, M. B. (Feb. 2021). "Tracking the visual system—from the optic chiasm to primary visual cortex". In: *Zeitschrift für Epileptologie* 34.1, pp. 57–66. DOI: 10.1007/s10309-020-00384-y

Hoffmann, M. B., Choritz, L., Thieme, H., Prabhakaran, G. T., and Puzniak, R. J. (Sept. 2021). "[Neuro-computational approaches for objective assessment of visual function]". In: *Der Ophthalmologe: Zeitschrift Der Deutschen Ophthalmologischen Gesellschaft* 118.9, pp. 900–906. DOI: 10.1007/s00347-021-01404-6

* Puzniak, R. J., Prabhakaran, G. T., and Hoffmann, M. B. (2021). "Deep Learning-Based Detection of Malformed Optic Chiasms From MRI Images". In: *Frontiers in Neuroscience* 15, p. 1332. DOI: 10.3389/fnins.2021.755785

* Puzniak, R. J., McPherson, B., Ahmadi, K., Herbik, A., Kaufmann, J., Liebe, T., Gouws, A., Morland, A. B., Gottlob, I., Hoffmann, M. B., and Pestilli, F. (Nov. 2021). "CHIASM, the human brain albinism and achiasma MRI dataset". In: *Scientific Data* 8.1, p. 308. DOI: 10.1038/s41597-021-01080-w

* Publications presented in this thesis.

Appendix B

Conference Contributions

2021

Puzniak, R. J., McPherson, B., Ahmadi, K., Herbik, A., Kaufmann, J., Liebe, T., Gouws, A., Morland, A. B., Gottlob, I., Hoffmann, M. B., and Pestilli, F. (Sep. 2021). "CHIASM, the human brain albinism and achiasma MRI dataset". [Oral presentation]. In: *Big Data Neuroscience Workshop 2021: Organized by the Advanced Computational Neuroscience Network*

Puzniak, R. J., Prabhakaran, G. T., and Hoffmann, M. B. (Jul. 2021). "Identification of chiasmal malformations with deep learning anomaly detection". [Poster presentation]. In: *Doctoral Symposium of Medical Imaging with Deep Learning 2021 conference*

Puzniak, R. J., McPherson, B., Ahmadi, K., Herbik, A., Kaufmann, J., Liebe, T., Gouws, A., Morland, A. B., Gottlob, I., Hoffmann, M. B., and Pestilli, F. (May 2021). "CHIASM, the human brain albinism and achiasma MRI dataset". [Poster presentation]. In: *Vision Sciences Society 2021 conference*

Puzniak, R. J. and Hoffmann, M. B. (Apr. 2021). "Identification of chiasmal malformations with deep learning anomaly detection". [Poster presentation]. In: *Interdisciplinary College Spring School 2021*

2020

Puzniak, R. J., Ahmadi, K., Kaufmann, J., Gouws, A., Morland, A. B., Pestilli, F., and Hoffmann, M. B. (Nov. 2020). "Advanced imaging of the optic chiasm and its relevance for albinism diagnostics". [Oral presentation]. In: 5^{th} *European Days of Albinism 2020*

2019

Puzniak, R. J., Ahmadi, K., Kaufmann, J., Gouws, A., Morland, A. B., Pestilli, F., and Hoffmann, M. B. (Sep. 2019). "Diffusion MRI detects structural abnormalities in optic chiasm". [Poster presentation]. In: *International Conference on Brain Plasticity: Molecules, Cells and Behaviour 2019*

Puzniak, R. J., Ahmadi, K., Kaufmann, J., Gouws, A., Morland, A. B., Pestilli, F., and Hoffmann, M. B. (Jun. 2019). "Diffusion MRI detects structural abnormalities in optic chiasm". [Poster presentation]. In: *Organization for Human Brain Mapping 2019 conference*

2018

Puzniak, R. J., Ahmadi, K., Kaufmann, J., Gouws, A., Morland, A. B., Pestilli, F., and Hoffmann, M. B. (Nov. 2018). "Quantification of nerve decussation abnormalities in optic chiasm". [Oral presentation]. In: *Aspects of Neuroscience conference 2018*

Puzniak, R. J., Ahmadi, K., Kaufmann, J., Gouws, A., Morland, A. B., Pestilli, F., and Hoffmann, M. B. (Feb. 2018). "Diffusion MRI of congenitally abnormal optic chiams". [Poster presentation]. In: *NextGenVis dissemination conference 2018*

2017

Puzniak, R. J., Kaufmann, J., Pestilli, F., and Hoffmann, M. B. (Nov. 2017). "Quantification of nerve decussation abnormalities at the optic chiasm". [Poster presentation]. In: *Computational Brain Connectivity Mapping Winter School 2017*

Appendix C

Declaration of Honor

I hereby declare that I prepared this thesis without impermissible help of third parties and that none other than the indicated tools have been used; all sources of information are clearly marked, including my own publications.

In particular I have not consciously:

- Fabricated data or rejected undesired results
- Misused statistical methods with the aim of drawing other conclusions than those warranted by the available data
- Plagiarized external data or publications
- Presented the results of other researchers in a distorted way

I am aware that violations of copyright may lead to injunction and damage claims of the author and also to prosecution by the law enforcement authorities.

I hereby agree that the thesis may be reviewed for plagiarism by mean of electronic data processing.

This work has not yet been submitted as a doctoral thesis in the same or a similar form in Germany or in any other country. It has not yet been published as a whole.

Magdeburg, 28.01.2022

Robert Puzniak